



<https://theses.gla.ac.uk/>

Theses Digitisation:

<https://www.gla.ac.uk/myglasgow/research/enlighten/theses/digitisation/>

This is a digitised version of the original print thesis.

Copyright and moral rights for this work are retained by the author

A copy can be downloaded for personal non-commercial research or study, without prior permission or charge

This work cannot be reproduced or quoted extensively from without first obtaining permission in writing from the author

The content must not be changed in any way or sold commercially in any format or medium without the formal permission of the author

When referring to this work, full bibliographic details including the author, title, awarding institution and date of the thesis must be given

Enlighten: Theses

<https://theses.gla.ac.uk/>  
[research-enlighten@glasgow.ac.uk](mailto:research-enlighten@glasgow.ac.uk)

FACTORS CONTRIBUTING TO  
INCOMPLETE CHARGE COLLECTION IN Si(Li) X-RAY DETECTORS.

Kevin A. Pears B.Sc.

Department of Physics and Astronomy  
The University  
Glasgow G12 8QQ  
Scotland.

Submitted for the degree of Doctor of Philosophy  
in the University of Glasgow.  
September 1990.

ProQuest Number: 11007543

All rights reserved

INFORMATION TO ALL USERS

The quality of this reproduction is dependent upon the quality of the copy submitted.

In the unlikely event that the author did not send a complete manuscript and there are missing pages, these will be noted. Also, if material had to be removed, a note will indicate the deletion.



ProQuest 11007543

Published by ProQuest LLC (2018). Copyright of the Dissertation is held by the Author.

All rights reserved.

This work is protected against unauthorized copying under Title 17, United States Code  
Microform Edition © ProQuest LLC.

ProQuest LLC.  
789 East Eisenhower Parkway  
P.O. Box 1346  
Ann Arbor, MI 48106 – 1346

## Declaration

The work presented in this thesis is work carried out by myself under the guidance of Dr. A J Craven. Certain results are quoted which were obtained from experiments carried out by other researchers, these are appropriately referred to at the relevant sections.

The following papers have been published presenting results mentioned in this thesis.

(1) C P McHardy, A J Craven, K A Pears, B Lowe, W A P Nicholson (1988) "Effects of the electron microscope environment on the performance of Si(Li) detectors" Inst. Phys. Conf. Ser. no. 93 Vol. 1. p. 135.

(2) A J Craven, C P McHardy, K A Pears (1989) "The effect of magnetic fields on incomplete charge collection in Si(Li) x-ray detectors", Ultramicroscopy, **28**, 157.

(3) A J Craven, K A Pears, J-P Chevalier (1989) " The effect of Compton scattering on energy dispersive x-ray spectra" Inst. Phys. Conf. Ser. no. 98 Vol. 1. p. 307.

This thesis or no part of it, has been submitted in any previous application for a degree.

## Contents.

Acknowledgements.

Summary.

Chapter1. Introduction.	1
1.1 The basis for this project.	1
1.2 Aims of this project.	3
1.3 Structuring of this thesis.	5
Chapter 2. Theoretical Considerations.	6
2.1 Introduction.	6
2.2 Characteristic x-ray production.	6
2.3 Auger electrons.	7
2.4 Bremsstrahlung radiation.	8
2.5 Electron generated x-ray spectra.	10
2.6 Cross-sections for bremsstrahlung production.	10
2.7 The interaction of x-rays with matter.	12
2.8 The types of physical interaction.	14
2.9 Absorption coefficients.	16
2.10 Photoelectric absorption coefficients.	17
2.11 Compton absorption cross-sections.	20
2.12 Rayleigh cross-section.	21
2.13 Energy dependence of the interaction processes.	21
2.14 Conclusion.	22
Chapter 3. The Energy Dispersive X-ray Detector.	23
3.1 Introduction.	23
3.2 Schematic over-view of the detector.	24

3.3 Detector fabrication.	24
3.4 Detection process.	27
3.5 Detector electronics.	30
3.6 Detector resolution.	31
3.7 Escape peaks.	33
3.8 Incomplete charge collection.	34
3.9 Detector efficiency.	36
3.10 The Link Analytical AN10000 Analyser.	38
3.11 Summary.	38
Chapter 4. Preliminary Investigation of Thin Film Spectra.	39
4.1 Introduction.	39
4.2 Detector efficiency.	39
4.3 HB5 Scanning transmission electron microscope.	41
4.4 Experimental techniques.	43
4.5 Results and analysis.	45
4.6 Conclusions.	49
Chapter 5. Considerations of the Effect of the Electron Microscope Environment on the Detector Performance.	51
5.1 Introduction.	51
5.2 Differences between Si(Li) x-ray detectors.	51
5.3 Microscope environment.	53
5.4 The effect of a magnetic field.	54
5.5 Effect of irradiation on detector performance.	58
5.6 On the bench performance of the HB5 detector.	59
5.7 Detector irradiation with electrons.	59
5.8 Conclusion.	60
Chapter 6. Effect of High Energy Photons upon Detector Performance.	62
6.1 Introduction.	62

6.2 Effect of high energy photons on the JEM detector.	63
6.3 Investigation of the HB5 detector.	69
6.4 Detector damage as a function of radiation dose.	73
6.5 Field direction in the HB5 objective lens.	73
6.6 Possible mechanisms to explain the damage effects.	75
6.7 Radiation damage in silicon.	76
6.8 The effect of the electric field.	77
6.9 Study of the photon damage on a new detector.	79
6.10 Conclusions	80
Chapter 7. Factors Contributing to the Low Energy Tail.	84
7.1 Introduction.	84
7.2 The effect of Compton scattering in the source.	86
7.3 <u>Bremsstrahlung from the x-ray sources.</u>	90
7.4 <u>The effect of bremsstrahlung escaping from the detector.</u>	94
7.5 Simple model for the ICC in the tail	103
7.6 Investigation of the low energy region of the tail.	106
7.7 Additional artifacts contributing to the tail.	109
7.8 Discussion and conclusions	110
Chapter 8. Conclusions and Future Work.	112
8.1 Introduction.	112
8.2 General conclusions to this project.	112
8.3 Future work.	115
Appendix 1. Specimen Preparation.	117
A1.1 Thin film specimens.	117
A1.2 Fluorescence specimens.	120
Appendix 2. Computation and Software.	121
A2.1 X-ray acquisition hardware.	121

<b>A2.2 Programming on the AN10000.</b>	<b>122</b>
<b>A2.3 Software.</b>	<b>122</b>
<b>Appendix 3. Fluorescence Sources.</b>	<b>125</b>
<b>A3.1 Americium variable x-ray source.</b>	<b>125</b>
<b>A3.2 Iron-55 radioactive source.</b>	<b>126</b>
<b>Appendix 4. Setting up of the Pulse Processor for X-ray Acquisition.</b>	<b>127</b>
<b>A4.1 Introduction.</b>	<b>127</b>
<b>References.</b>	

... ..

... ..

... ..

... ..

## Acknowledgements.

I would like to take the opportunity of thanking all those, who in some way have helped with the work presented in this thesis. First I must thank my academic supervisor Dr. A J Craven for his guidance, constructive criticism and the many hours of useful discussions we had throughout this work. I must also thank Dr. W A P Nicholson for many useful discussions on some of the more practical aspects of this work. I am also indebted to Dr. Nicholson for teaching me the fundamentals required for programming on the AN10000 and for supplying some of the software used within this work. I thank Dr. C P McHardy, formerly of the solid state physics group, for teaching me the basics required to use the HB5 electron microscope. I thank Prof. J N Chapman for reading the experimental chapters and proving some useful suggestions. I am also very grateful to Prof. R P Ferrier, head of department, for providing me with facilities within the solid state group.

I must also thank of my colleagues within the solid state group for additional motivation and occasional help. In particular, Khalid Khan for supplying software which was adapted to my particular requirements. Thanks also to George Sinclair for his help in transferring of this text from a Sinclair Q.L. p.c. onto the Apple Mac. word processor.

I would like to thank all the technicians who have helped with construction and maintenance of equipment, these being; Mr. Andy Young, who helped with the construction of the vacuum evaporator and who repaired numerous items of equipment, Mr. Donald MacDonald who prepared the sputtered thin film specimens. Messrs David Blackwell, John Richardson and Ian Selkirk of the workshop, who made much of the apparatus used in the experimental work. Thanks also to Mrs. Margaret Waterson for tracing several diagrams.

Last but by no least, a special thank you to my parents and my grandparents for their support, encouragement and much needed financial assistance and to my girlfriend Colette for her encouragement during the writing of this thesis.

## Summary.

This project is concerned with a detailed study of the properties and behaviour of lithium drifted silicon Si(Li) energy dispersive x-ray detectors. In particular, the factors which effect their performance in the detection of low energy x-rays. The Si(Li) detectors used in this project were a new generation of detector. These new detectors were known to exhibit an order of magnitude improvement in the low energy tails associated with the detection process. These low energy tails are caused by the effects of incomplete charge collection (ICC) of the charge carriers created during the detection process.

The work discussed in this thesis describes a series of experiments which were performed to primarily investigate why electron generated x-ray spectra obtained from our transmission electron microscope were of a poorer quality, in terms of ICC, than had been predicted by a series of preliminary tests performed with this detector.

Chapter 2 discusses the various theoretical considerations required throughout the project. This includes a brief outline of the processes involved during the detection of x-rays and discusses the various cross-sections involved for these processes. Chapter 3 then discusses the design and operation of the Si(Li) energy dispersive x-ray detector.

Chapter 4 details the preliminary investigation performed to establish the quality of electron generated spectra obtainable with the Si(Li) detector. The quality of the spectra was established by the accuracy of the theoretical background fit obtainable for a particular spectrum. This investigation clearly showed that the spectra were of an inferior quality to that expected.

Chapter's 5 and 6 then detail an investigation into possible reasons to explain why the spectra should have been of such a poor quality. This investigation considers what effects the microscope environment can have on the detectors performance. Whilst in use on the microscope, the detector is immersed in the strong magnetic field from the objective lens ( $\sim 0.3$  T). In addition, the detector is

continually subjected to a high energy irradiation from the x-rays created during the collisions between the electron beam and the specimens. In certain applications it is also possible for electrons to be scattered onto the detector.

Two similar detectors were studied in detail; this allowed direct comparisons of their performances to be made. This investigation revealed that several interesting phenomena occur with these detectors. Both detectors were found to have regions around their circumference in which a high trap density existed (this leading to the creation of excess ICC). However, the nature of these side regions was found to be different for both detectors. In the first detector, the traps were seen to form by themselves. In the second detector, traps were created by high energy irradiation from terbium characteristic photons. These traps were seen to decay with time. However, both detectors were found to behave in the desired manner when collimated down to a small central region. The performance of the first detector was seen to show a marked deterioration, in terms of the level of ICC, during the time this investigation took.

Chapter 7 discusses some of the processes known to be occurring in the detectors which give rise to the low energy tails seen in all spectra. Some of these processes are fundamental and should not be confused with those which give rise to the ICC. The magnitudes of these processes were established whenever possible. This information is valuable to the detector manufacturers who are striving to produce the best detectors that physical constraints will allow. A knowledge of these fundamental limits makes it possible to predict levels in design improvement theoretically possible.

## CHAPTER ONE

### INTRODUCTION

#### 1.1 The basis for this project.

Theoretical background modelling of the bremsstrahlung background from electron generated x-ray spectra has been investigated by many authors (Ware and Reed, 1973; Rao-Sahib and Wittry, 1975; Fiori et al., 1976; Chapman et al., 1983). The basic procedure was to calculate the continuum energy distribution function and combine this with a detector response function. The resulting function could then be subtracted off the real spectrum to leave the characteristic x-ray intensities.

The importance of this theoretical treatment has arisen due to the need for accurate background subtractions particularly in the low energy region of the spectrum. Here, the characteristic x-ray peaks may often overlap one-another due to the small energy differences between them. This results in difficulties since it limits the regions of background over which bremsstrahlung background fitting can be performed. This problem is exasperated when using a windowless detector, since these detectors are able to detect lower energy x-rays than a conventional beryllium window detector.

In this low energy region the bremsstrahlung background is absorbed very easily. This has a major effect in changing the bremsstrahlung background shape in this region. In addition, the background shape can be further complicated by absorption effects in the region around an absorption edge. Absorption corrections are difficult to perform. Self absorption within the specimen is difficult to model due to the lack of accurate knowledge on the specimens geometry and composition. Absorption corrections for the detector's front surface are also required. These are made difficult by the lack of knowledge on the exact nature of this layer. To further complicate matters, the mass absorption coefficients are subject to large uncertainties in the low energy region, thus making accurate absorption corrections even more difficult. In performing

absorption corrections we are essentially working from the basis of a very good guess.

In theory the bremsstrahlung background should contain all the information on the nature of the absorption that the x-ray distribution has undergone. Therefore, an accurate knowledge of the background can be used to give valuable information on the absorption that the x-rays, characteristic and continuum, have undergone before their detection. This information is essential in x-ray analysis in order to be able to correct the intensities of the low energy x-rays. Low energy x-rays suffer very large absorption effects even in very thin absorbing layers and hence their intensities can be underestimated by large amounts.

The work by Chapman et al.(1983) has been used by several authors (Adam, 1985; Steele, 1987; Garratt-Reed, 1987) and has proved very successful when modelling the background in the region between 3 keV to 20 keV. Modelling the background below 3 keV has proved more difficult however. Adam (1985) investigated the ideas proposed by Chapman et al. (1983) and by comparing these with the more exact calculations of Pratt and Tseng and co-workers (1977 et.al.) he suggested that the Chapman model should be able to describe the bremsstrahlung background in the region below 3 keV, to an accuracy better than that obtainable from the experimental data (Gray, 1981). Adam (1985) tried to verify this by experiment but found that the energy dispersive x-ray (EDX) detectors available at the time were not capable of allowing him to justify his conclusions. The detectors were limited in low energy sensitivity because of the low energy tail which is always present in these energy dispersive detectors. This low energy tail, which had been known to exist since the advent of the very first semiconductor particle detectors, was caused by incomplete charge collection (ICC) of carriers within the detector (section 3.8). ICC has been studied during the development of semiconductor particle detectors for the nuclear industry. More recently with the increasing popularity of the lithium drifted silicon Si(Li) x-ray detectors, this study has been extended to consider the low energy region where the effects of ICC are found to be at their worst. Using a high purity germanium detector, Llacer et al. (1977) studied the ICC for different photon energies as a function of the mass absorption coefficient in germanium. This work indicated that the surface of the detector played an important role in the occurrence of the ICC. Photons which were absorbed closest to the detector

† The series E crystals undergo a manufacturing process which leads to significantly lower levels of ICC.

---

surface always exhibited the largest percentage of ICC in their spectra. Craven et al. (1985, 1987) verified this for two different generations of Si(Li) detectors. In this work, Craven proposed a parameterisation which was capable of predicting the variation of the ICC with photon energy and in addition was capable of taking into account the redistribution of the charge over the same energy range. Adam (1985) used this model as a means of overcoming the problems he encountered with the detectors. Although this model predicted many of the features being found in the spectra, it could not predict why a residual "bump-like" artifact was left in each spectrum after the "ICC-modified" background was subtracted. This artifact covered energies from approximately 1.5 to 3 keV, and could not be accounted for using any known spectral artifacts.

The detectors used by Adam were superseded by a new generation of Si(Li) EDX detector, the "Link series E" type detectors. A detector of this kind was studied by Craven et al. (1987). In this study they found that the level of ICC exhibited by these detectors, was an order of magnitude lower than the previous generation. Using this type of detector a more accurate background correction was thought to be possible. However, a preliminary investigation, using a series E type detector, showed that any electron generated spectra obtained with this detector were in fact of a poorer quality than the spectra from the previous generation of detectors. These spectra were seen to exhibit far more ICC than "bench tests" had indicated. This discovery changed the entire direction of this project. It was obviously very important to discover why this detector should behave differently on the microscope than it did during the bench investigations. In addition, it was important to test the performance of similar series E type detectors in order to establish whether or not this detector was characteristic of a typical series E detector.

## 1.2 Aims of this project.

The aim of this project was to establish possible reasons to explain why the electron generated spectra obtained with the new series E detector should be of a poorer quality

than was predicted by our initial tests. This investigation considered what effects the microscope environment had upon the detector's performance. Whilst in operation on the microscope, the detector is continually subjected to the large magnetic field associated with the objective lens and to high energy irradiation by characteristic and bremsstrahlung photons. Any effects that these might cause had to be investigated. This investigation basically involved simulating the microscope environment outside the microscope. This was achieved using a set of permanent magnets to represent the objective lens magnetic field and a radioactive isotope to represent the high energy irradiation.

A comparison of the performance of a similar series E type detector was very important. This would hopefully indicate whether these detectors all behave the same way, or differ from detector to detector. As well as the detector used to collect the electron generated spectra, a second series E type detector existed within our group (referred to as the JEM detector). Although this detector had not been used to acquire spectra on the HB5, it had been frequently used to acquire electron generated spectra on a JEOL JEM 100C electron microscope. This detector was used to begin the investigation of the microscope environment on the detector performance. This was simply because of group commitments which did not allow access to the HB5 detector at that time. However, the favourable results found with this detector lead us to believe that a similar study performed upon the HB5 detector would reveal the information required.

Three other series E detectors were used at some stage during this project. These detectors were generally used for comparison purposes when applicable. This was simply to gain additional information about the properties of the series E detectors.

In order to fully understand the nature of the spectra, in particular the ICC, it is essential to have a good understanding of the variety and magnitudes of the processes which occur within the detector. Work of this kind is very beneficial to the detector manufacturers who are ultimately looking to produce the best detector which the physical constraints will allow. Work concerned with investigating these fundamental detector properties had already been studied within our group (Craven et al., 1985,

1987). An investigation into factors which can contribute to the ICC tail was undertaken. This considered effects such as the Compton effect and the escape of bremsstrahlung radiation from the detector and from the source of x-rays. This study showed that several minor effects are possible, all which lead to additional counts in the tail.

### 1.3 Structuring of this thesis.

Chapter 2 introduces the important theoretical concepts required throughout this thesis. Chapter 3 then discusses in some detail the energy dispersive Si(Li) x-ray detector. The Si(Li) detector is of central importance to this project and therefore requires a detailed review. Chapter 4 deals with the preliminary investigation of thin film specimens on the HB5 electron microscope using the new Link series E detector crystals. The results and conclusions from chapter 4 lead to the next two chapters which are an investigation of possible reasons for the poor quality spectra found in chapter 4. This investigation basically considers what effects the microscope environment has on the detector's performance.

Chapter 7 is a more theoretical chapter dealing with some of the processes known to occur in the detector which contribute to the low energy tail seen on fluoresced spectra. Finally, chapter 8 states the overall conclusions arrived at during this work and talks about any possible future work.

## CHAPTER TWO

### Theoretical Considerations

#### 2.1 Introduction.

This chapter is designed to introduce the theoretical concepts underlying the work of this thesis. The chapter begins with a brief introduction to the physics involved in x-ray production, describing both characteristic and bremsstrahlung x-rays. The cross-sections for the production of these x-rays are then outlined.

The final sections discuss the attenuation and absorption of x-rays. The various types of physical interactions between x-rays and matter are explained. Finally, the important concept of the mass absorption coefficient is introduced and some of the empirical models used are reviewed.

#### 2.2 Characteristic x-ray production.

Characteristic x-rays are so-called because the energies which they exhibit are characteristic of the atoms from which they originate. It is for this reason that characteristic x-rays are so important in elemental analysis. Characteristic x-rays are produced in a process whereby an atom in an excited state returns to its ground state by an internal re-arrangement of its electrons. This re-arrangement involves an ionized electron shell being filled by an electron from a higher energy level making a transition down to this otherwise vacant electron state. The energy for the creation of the x-ray photon arises due to the change in the total energy of the electron making the transition. The amount of energy that any particular photon may have is related to the difference in

energy between the two levels taking part in the transition. Since the different atomic species each have a set of discrete energy levels characteristic of their nuclear charge, photon energies due to transitions between these levels are specific to a particular species. We therefore have a very convenient method for identifying an atom by identifying the x-rays which it emits.

The relationship between x-ray energy and the element from which it originates was first discovered by Moseley (1914) and takes the approximate form

$$E = 3/4.Rhc(Z- \xi)^2 \quad 2.1$$

where R is the Rydberg constant, h is Plancks constant, c is the speed of light in vacuum, Z is the atomic number of the element and  $\xi$  is a constant. An important point to

realise from equation 2.1 is that the energy of the x-rays can be seen to have an approximate  $Z^2$  dependence. This is very important for the elements with very small values of Z, since these photons have very small values of x-ray energy. Such x-rays can be absorbed very easily before arriving at the detector. This causes problems since it effectively sets a low energy detection limit. This idea will be explained in more detail in chapter three.

### 2.3 Auger electrons.

Auger electrons are produced in direct competition to characteristic photons. Here, instead of an x-ray photon escaping the atom, a radiationless transition takes place in which a loosely bound electron is emitted. The energy which would have otherwise been used to create the x-ray photon is used to remove an electron from a loosely bound outer shell. This then leaves the atom doubly ionized with two vacancies still to be filled. De-excitation of an atom can be seen as a complex process where it is

possible to have a cascade of different events taking place sequentially over a very short period of time. As for characteristic x-rays, the Auger electrons have an energy characteristic of the shell from which they have originated.

For the low atomic number elements, the probability for an Auger electron being produced is far higher than for a K series x-ray photon being emitted. The number of photons produced per ionization is known as the fluorescence yield; this is important when calculating the intensity of radiation expected. The fluorescence yield for the K shell,  $\omega_K$ , can be approximated by the equation

$$\omega_K = Z^4 / (a+Z^4) \quad 2.2$$

where  $a = 1.12 \times 10^6$ , Dyson (1973<sup>1</sup>).

#### 2.4 Bremsstrahlung radiation.

Bremsstrahlung or continuum radiation is produced by charged particles when they are accelerated or decelerated by the atoms of a specimen. Classical physics tells us that an accelerated charge emits radiation. This acceleration may be caused, for example, by the deflection of an electron in the field of an atom as the charged particle penetrates matter. Since this acceleration is essentially the ratio of the electrostatic force to the mass, this radiation component is significantly more important for electrons than for heavier particles. The important feature of this process is that the radiation emitted can have any energy up to the energy of the incident electron.

Many studies of bremsstrahlung have been made. These were among the first experiments carried with x-rays after their discovery. Dyson (1973<sup>2</sup>) reviews much of this area in some detail. Some of the more important ideas which have relevance to electron generated x-ray spectra will now be outlined. The intensity of bremsstrahlung

radiation is found to be characteristic of the material from which the radiation emanates, with the intensity being approximately proportional to  $Z^2$  for the material. The bremsstrahlung intensity is also found to be a function of the incident electrons energy.

Bremsstrahlung radiation is emitted non-isotropically and has an angular dependence which is a function of the incident electron's energy. This is very important during elemental analysis with the electron microscope. Here, the bremsstrahlung radiation is an unavoidable consequence of the process. In some microscopes the detector can be positioned at "high take-off angles" where the bremsstrahlung intensity is relatively low. Since the characteristic x-rays are emitted isotropically no characteristic intensity is therefore lost, but the amount of detected bremsstrahlung has been lowered. This has the effect of increasing the "peak-to-background" ratio which is very important when trying to detect an element present at a low concentration. In practice this benefit is often counteracted by the increase in the number of scattered electrons reaching the detector.

The energy distribution for the bremsstrahlung spectrum was considered by Kramers (1923). Kramers obtained an analytical expression for the emitted x-ray intensity in a frequency interval  $d\nu$  as a function of the emitted frequency  $\nu$ . Kramers result has subsequently been expressed as a cross-section differential in photon energy by Lee et al. (1976) where they obtained

$$\beta_0^2 k / Z^2 \cdot d\sigma / dk = 16\pi r_0^2 / (137.3\sqrt{3}) \quad 2.3$$

where  $\beta_0 = v/c$ ,  $k$  is the electrons momentum and  $r_0$  is the classical electron radius. Kramers result is still used by workers in microanalysis to obtain an approximate idea of the bremsstrahlung intensity.

## 2.5 Electron generated x-ray spectra.

As mentioned in section 2.3, the production of characteristic x-rays relies on the atom being ionized. There are many different ways in which atoms can be ionized, the important ones in this work being, ionization by fast electrons or x-rays.

X-ray generation in the electron microscope relies on the interaction of the incident electrons with the specimen. The probability of such an ionizing event is governed by the ionization cross-section  $\sigma_i$ . The most commonly used approach for calculating the ionization cross-section of inner atomic shells follows from the original work of Bethe (1930). The basic form of the cross section derived by Bethe is

$$\sigma_i = 6.51 \times 10^{-20} \cdot (n \cdot b_n / U \cdot E_0) \cdot \ln(c_n \cdot U) \quad \text{barns} \quad 2.4$$

where  $n$  is the number of electrons in the particular shell or subshell,  $b_n$  and  $c_n$  are constants for the shell,  $U$  is the overvoltage,  $E_0/E_B$ , where  $E_0$  is the energy of the electron beam and  $E_B$  is the ionization energy for the shell.

## 2.6 Cross-sections for bremsstrahlung production.

Cross-sections for bremsstrahlung radiation need to be both relativistic, because of the high energy electrons and have to be angularly dependent to account for the non-isotropic nature of the radiation. Various quantum mechanical treatments for bremsstrahlung production have been developed in which the relativistic and angular corrections have been incorporated. The basis of all quantum mechanical treatments is to consider a radiative transition of an electron between two states in the continuum with the emission of a bremsstrahlung photon. By making use of time dependent

perturbation theory a differential cross-section is obtained in the form

$$d^3\sigma_b = \sigma(k, \Omega_k, \Omega_p, \mathbf{j}) dk d\Omega_k d\Omega_p = (137 r_o^2 p E_o E k) / (2\pi)^4 p_o \int_{\tau} [\psi_f^* \mathbf{j} \cdot \alpha \exp(-im_o c \mathbf{k} \cdot \mathbf{r} / h) \psi_i d\tau]^2 dk d\Omega_k d\Omega_p \quad 2.5$$

where  $k$  and  $\mathbf{k}$  are the energy and momentum of the emitted photon in  $m_o c^2$  and  $m_o c$  units,  $E_o$  and  $E$  are the initial and final total energy of the electron in a collision, in  $m_o c^2$  units,  $p_o$  and  $p$  are the initial and final momentum of an electron in a collision, in  $m_o c$  units,  $r_o$  is the classical radius of an electron,  $m_o$  is the rest mass of an electron,  $\psi_i$  and  $\psi_f$  are the initial and final wavefunctions,  $\alpha$  is the Dirac matrix and  $\mathbf{j}$  is the polarization direction of the emitted photon. This is the differential cross-section for the emission of a photon with energy between  $k$  and  $k+dk$  into an element of solid angle  $d\Omega_k$  whilst the electron is scattered into an element of solid angle  $d\Omega_p$ .

It is from an equation similar to 2.5 that all quantum mechanical evaluations of bremsstrahlung production begin. The principal problem is the evaluation of the matrix element which ideally involves the use of "exact" wavefunctions to describe the electron in a screened nuclear field. At present there are no solutions in a closed form of the Dirac wave equation for an electron in a Coulomb field and for this reason various approximate wavefunctions and procedures have been developed. There are two commonly used approaches for the derivation of the bremsstrahlung cross-section, those of Sommerfeld (1931) and Bethe and Heitler (1934). Chapman et al. (1983) have compared these two theories and have found that a modified theory of Bethe and Heitler, MBH (Koch and Motz, 1959) appears to best represent the bremsstrahlung cross-sections obtained by Pratt and co-workers (1977) who have performed exact numerical calculations on equation 2.5. In the same work, Chapman also compared the MBH theory with experimental data in the range 3-30 keV. This indicated that for incident electron energies greater than 40keV, photon energies less than 30 keV and for targets with  $Z$  less than 50, there was a very close agreement between the MBH, the

exact calculations and their experimental observations. In a subsequent paper, Chapman et al (1984) state that the accuracy of the MBH equation should be better than 5% for the range specified above.

Adam (1986) has made a comparison of the MBH and the calculations of Pratt and Tseng (1980) for photon energies down to 0 keV. Unfortunately the data set provided by the exact calculations is far from complete. However, from the data available, Adam was able to conclude: for the parameters of interest for our electron microscope (  $\theta_0 = 100.5^\circ$  (see fig. 4.3), accelerating voltage,  $T_0 = 100$  keV) the MBH and the exact calculations are accurate to within 3% for elements with  $Z < 30$ . In this comparison the values for the cross-sections were scaled at 20 keV and with the difference being taken over the region 0 to 10 keV. As  $Z$  increases the divergence between the two steadily increases, but this is only to be expected since the MBH is based upon the Born approximation.

$$Ze^2/hv_0 \ll 1 \quad \text{and} \quad Ze^2/hv \ll 1 \quad 2.6$$

where  $v_0$  and  $v$  are the velocities of the incoming and outgoing electron. According to Adam this level of difference between the MBH and the exact calculations would probably not be noticed since Gray (1981) quotes an experimental accuracy of 5% in this region.

## 2.7 The interaction of x-rays and matter.

An accurate knowledge of the interaction of x-ray radiation with matter is essential if experiments are to be fully understood and appreciated. The basis of all measurements on the attenuation of x-rays is the fact that the intensity of radiation decreases as it passes through material in such a way that for a small thickness  $dx$ , the

change in intensity  $dI$  is proportional to the thickness and to the incident intensity  $I$ . That is

$$dI = -\mu \cdot I dx \quad 2.7$$

where  $\mu$  is the proportionality constant known as the linear attenuation coefficient or the attenuation cross-section. If the radiation is homogeneous,  $\mu$  is a constant and integration yields

$$I / I_0 = \exp(-\mu x). \quad 2.8$$

This is Beer's Law and gives the intensity of radiation  $I$  after a beam of initial intensity  $I_0$  has traversed a thickness  $x$  of a particular material. The linear attenuation coefficient  $\mu$  can be shown to be the product of the number of atoms per unit volume,  $n$  and the removal or interaction cross-section per atom,  $\sigma$ ,  $\text{cm}^2/\text{atom}$

$$\mu = n \cdot \sigma \quad \text{cm}^{-1} \quad 2.9$$

this may also be written

$$\mu = (N_A/A) \sigma \cdot \rho \quad \text{cm}^{-1} \quad 2.10$$

where  $N_A$  is Avogadro's number  $A$  is the atomic weight and  $\rho$  is the density. Because the interaction cross-section is unaffected by the density of the interacting medium, it is convenient to define the idea of the mass attenuation coefficient  $\mu/\rho$ . This is the form in which attenuation coefficients are normally quoted.

## 2.8 The types of physical interactions.

In the energy range being dealt with in this work, 0 to 100 keV, there are three types of interaction possible between the radiation and matter:

(1) The Photoelectric effect: In this type of interaction the photon gives up all its energy to a single electron. Part of the energy is required to overcome the electrons binding energy to the atom and the remainder is given the electron as kinetic energy. The energy of the photoelectron can be expressed by the equation

$$E_{pe} = h\nu - E_B \quad 2.11$$

where  $E_B$  is the binding energy of a particular energy shell. Multielectron atoms contain many electron shells of different energies; any of these can undergo a photoelectric event providing the photon energy is sufficient to overcome the binding energy of the shell.

Photoelectric absorption occurs most readily when the photon energy is comparable to the binding energy of a particular shell. As the energy of the photons increase the photoelectric cross-sections decrease. This can be seen in fig. 2.1 where a graph of the photoelectric cross-section versus energy is plotted for silicon. The major feature of the graph can be seen as the sharp rise in the cross-section at the point known as the K shell absorption edge. Absorption edges signify the point at which an incident photon has just enough energy to ionize a more tightly bound shell; this allows more electrons to act as absorbers, hence the abrupt rise in the value for the cross-section.

(2) The Compton effect: In this type of interaction, a photon is scattered by an electron, the photon travelling off in an arbitrary direction with decreased energy while the scattering electron recoils with the remainder of the energy. If the incident photons energy is large compared to the binding energy of the scattering electron then the

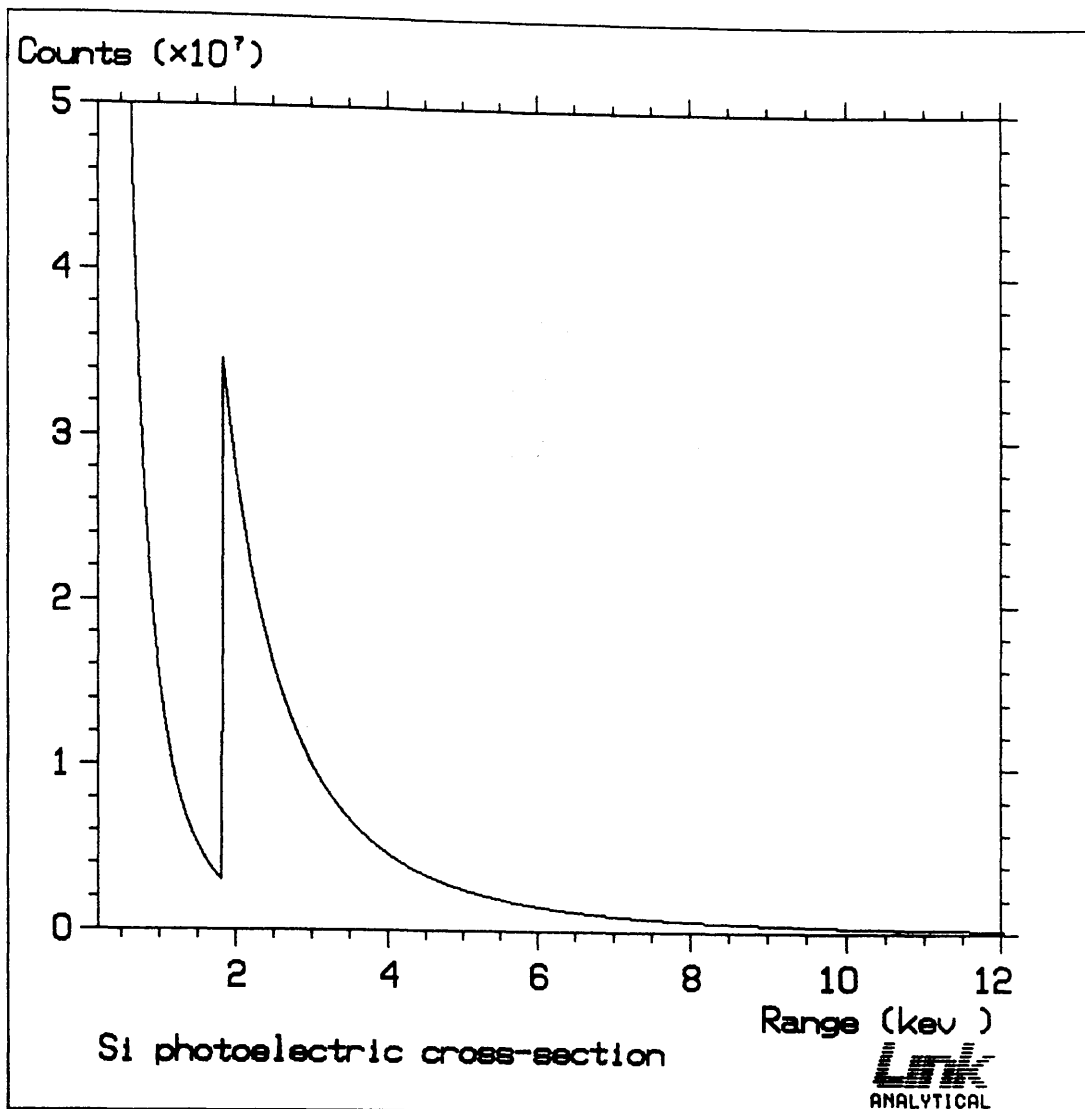


Fig. 2.1 Photoelectric cross-section versus photon energy for silicon

electron may be considered to be free. This situation is more amenable to exact theoretical treatment and the principle of conservation of momentum can be applied to the electron and the incident and scattered photon in order to ascertain the division of energy between the photon and electron. Figure 2.2 shows a classical interpretation of the situation, from this diagram it can be shown that the energy of the scattered photon is

$$h\nu' = h\nu / (1 + \alpha(1 - \cos\theta)) \quad 2.12$$

where  $\theta$  is the scattering angle of the photon,  $\alpha = (h\nu/m_0c^2)$  and  $m_0$  is the rest mass of the electron. From this equation it can be shown that the energy loss is greatest for  $180^\circ$  scatter i.e. a photon back scattering along the incident direction. Also, as the energy of the incident photon increases the energy loss at each particular scattering angle also increases. For example, a 10 keV photon scattering at  $180^\circ$  is reduced to 9.62 keV whereas a 100 keV photon scattering at the same angle is reduced to 71.76 keV.

Finally, it is important to clarify one point from above. The "free electron" approach which is used in defining equation 2.12 is only an approximation and only strictly holds when the energy of the incident photon is very large compared to the binding energy of the struck electron. For lower energy photons the momentum of the scattering electron has to be considered and the energy losses associated with the scattering events cover a wide band of energies.

(3) Rayleigh scattering: In this interaction the incident photon is scattered elastically by the atom without any loss of energy. Interactions of this kind contribute to the linear attenuation coefficient since photons are scattered out of the direct beam.

The three interaction processes act independently of each other so that the linear

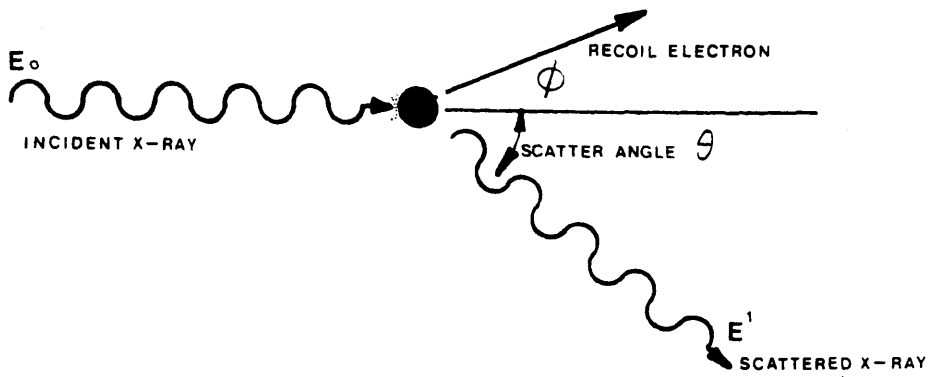


Fig. 2.2 Classical interpretation of Compton scattering.

attenuation coefficient can be written as the sum of three constituent attenuation coefficients

$$\mu = \tau + \sigma_C + \sigma_R \quad 2.13$$

where  $\tau$  is the photoelectric absorption coefficient,  $\sigma_C$  is the Compton attenuation cross-section, and  $\sigma_R$  is the Rayleigh attenuation cross-section.

## 2.9 Absorption coefficients.

Attenuation coefficients are obtained by considering all the interactions between the radiation and the interacting matter. However, under certain circumstances, for example where the energies involved are limited to a fairly narrow range, then it is usual to separate the two processes of absorption and scattering. The Compton effect, for example, results in the initial photon being scattered through an angle  $\theta$  with a reduced energy, whilst at the same time the "scattering electron" travels off at a related angle  $\phi$  with the remainder of the energy. The Compton attenuation cross-section mentioned above is in fact made up from two partial cross-sections, which correspond to the proportions of energy absorbed and scattered respectively.

$$\sigma_C = {}_a\sigma_C + {}_s\sigma_C \quad 2.14$$

With this in mind a new "absorption" coefficient can be defined; here we are only interested in the proportion of the incident energy absorbed. This absorption coefficient will therefore be the sum of the absorption cross-sections for photoelectric absorption and for Compton absorption.

$$\mu_a = \tau + \sigma_C \quad 2.15$$

Since the reduction of intensity is determined by the quantity of matter traversed by the incident beam, the absorber thickness is often expressed on a mass basis, in grams per cm<sup>2</sup>. Consequently a mass absorption coefficient  $\mu/\rho$  (cm<sup>2</sup>/g) can be defined, where  $\rho$  is the density of the absorber. The mass absorption coefficient is found to be approximately independent of the physical state of the material (Evans, 1958). For photons of low energies, equation 2.15 can usually be regarded as being equal to the photoelectric absorption coefficient alone. It is only when the energy of the incident photons exceeds 30 keV that the Compton effect begins to play any significant role. Thus it is  $\tau/\rho$  which will be used throughout the remainder of this thesis whenever any absorption calculations are being referred to.

## 2.10 Photoelectric absorption coefficients.

Many analyses of photoelectric processes have been made but exact solutions of the equations are both difficult and require long computational time since the Dirac relativistic equation for a bound electron must be used. It is therefore more usual to use approximations to simplify matters somewhat. These approximations include the use of hydrogen-like wavefunctions with a schematic treatment of the screening effects and the use of non-relativistic quantum mechanics for the motion of the electron. A very good review of these and other various theoretical approaches can be found in White (1952). A fairly comprehensive review of some of the other approaches used can be found in Davisson and Evans (1952). Often quoted, especially in the older literature, is the crude approximation

$$\mu/\rho = C.Z^4 / (h\nu)^3 \quad 2.16$$

where C is a constant calculated for the region of interest.

Many empirical models have been suggested for calculation of mass absorption coefficients, these include those by Siegbahn (1914) and Richtmyer (1921) and all generally start from an expression of the following type

$$\mu/\rho = C. \lambda^m.Z^n + b \quad 2.17$$

where C,m and n are parameters which vary between the absorption edges and b is a scattering coefficient required to meet the experimental data.

Victoreen (1943) developed an empirical equation for photoelectric absorption coefficients in the energy range 1 keV to 1 MeV. In his paper Victoreen starts with the empirical formula of equation 2.17 and uses the Compton cross-section of Klein and Nishina (1929) to take account of the scattering. By using the experimental data of the time, Victoreen arrives at the empirical expression

$$\mu/\rho = \alpha Z^2.\lambda^3.(2Z/A) - \beta Z^5.\lambda^4.(2Z/A) + {}_e\sigma.N_0.Z/A \quad 2.18$$

where  $\alpha$  and  $\beta$  are polynomials in Z,  $N_0$  is the number of atoms per unit volume,  ${}_e\sigma$  is the Compton cross-section per electron, the other symbols all have the usual meanings.

Heinrich (1966) starts from an initial expression similar to Victoreen and simplifies the equation to

$$\mu/\rho = C.Z^3 . \lambda^n \quad 2.19$$

where C and n are the parameters which vary between the absorption edges. From this expression, the mass absorption coefficients are calculated between the various absorption edges by varying the coefficients and exponents to fit the experimental data.

Springer and Nolan (1976) followed the Heinrich work very closely and suggested slight improvements to render this approach more accurate. These mass absorption coefficients were used quite successfully within our research group for several years.

Each of the models and subsequent absorption coefficients mentioned so far suffer from the same low energy unreliability. The reason for this was partly due to a lack of good experimental data in this region and partly due to an inherent lacking in the particular models. More recently, Heinrich (1987) has published a new model in which he claims to have overcome the low energy limitations inherent to all the previous models. This new model expresses the mass absorption coefficients as

$$\mu/\rho(E) = C.Z^4/A.(12397/E)^n.(1-\exp[(E+b)/a]) \quad 2.20$$

where E is the energy of the photon and C, n, a and b are parameters which vary with the atomic number of the absorber in the regions between the absorption edges. The values for the various coefficients, which are all polynomials in Z were obtained by reference to experimental data where possible. Where no experimental data was available theoretical values were chosen. Khan and Nicholson (1989) have compared these absorption coefficients to those of Springer and Nolan. In this work they found that the values of Heinrich, which are numerically larger than those of Springer and Nolan, vary quite significantly below 3 keV. However, the Heinrich values appear to give a better estimate of the "true" mass absorption coefficient values. This claim is partially backed up by experiment. Absorption corrections made for the beryllium window on the EDX detector predict a 9  $\mu\text{m}$  beryllium thickness. This has been verified over a wide range of specimen thicknesses and is thought to be fairly accurate. Previous work carried out within our group using the Springer and Nolan coefficients always predicted a beryllium thickness of around 11  $\mu\text{m}$  (Adam, 1986). The manufacturers of the detectors quote a nominal beryllium thickness of 8  $\mu\text{m}$ . Values near to this thickness are now being predicted by the Heinrich coefficients for the

experimental results obtained. In addition, Nicholson (1988) has shown that an accurate Si(Li) detector thickness of 3mm can be predicted. The Springer and Nolan mass absorption coefficients previously used always predicted a crystal thickness of around 2.6 mm.

### 2.11 Compton absorption cross-sections.

By considering solutions to the Dirac equation, Klein and Nishina (1929) carried out a quantum mechanical treatment for photon scattering from a free electron and were able to obtain an expression for the differential collision cross-section for unpolarised radiation

$$d_e\sigma(\theta) = r_o/2 \cdot d\Omega \cdot (v'/v)^2 \cdot (v/v' + v'/v \cdot \sin^2\theta) \text{ cm}^2/\text{electron} \quad 2.21$$

where  $r_o$  is the classical electron radius and  $d\Omega$  is the solid angle. By substituting for  $v/v'$  in terms of  $\theta$  and photon energy  $h\nu = \alpha(m_o c^2)$  we get the equivalent relationship

$$d_e\sigma(\theta) = r_o \cdot d\Omega \left[ \frac{1}{(1 + \alpha(1 - \cos\theta))} \right]^2 \cdot \left( \frac{1 + \cos^2\theta}{2} \right) \times \left\{ 1 + \frac{\alpha^2(1 - \cos\theta)^2}{(1 + \cos^2\theta)(1 + \alpha(1 - \cos\theta))} \right\} \text{ cm}^2/\text{electron} \quad 2.22$$

where  $d_e\sigma(\theta)$  is the cross-section for the number of photons scattered into the solid angle  $d\Omega$  in the direction  $\theta$ .

The important features of equation 2.22 can be seen in figure 2.3 from which it is seen that for small values of  $\alpha$ , the cross-section falls with increasing angle  $\theta$ , reaching a minimum around  $90^\circ$  before rising again.

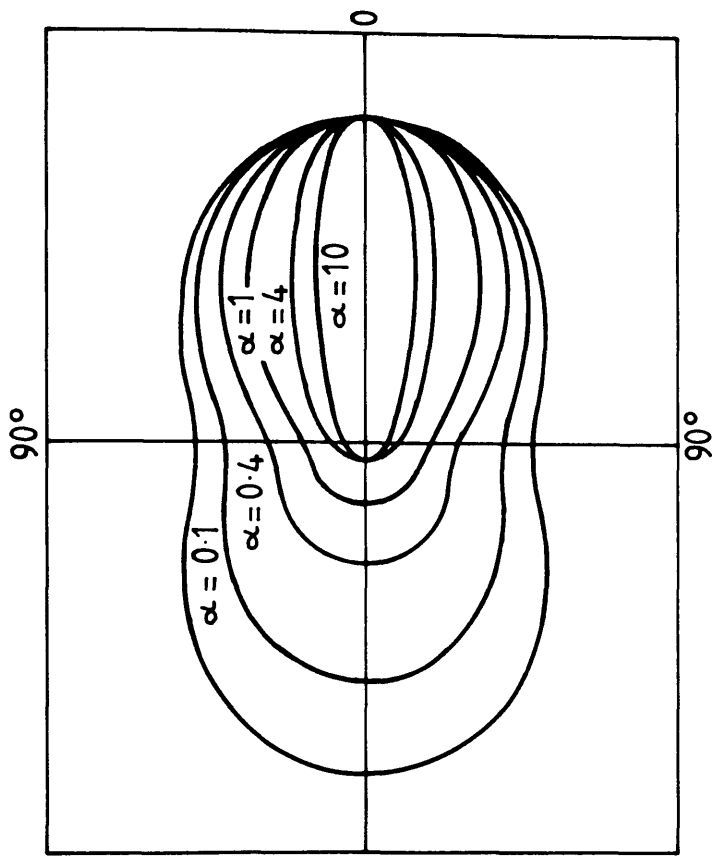


Fig. 2.3 Compton cross-section versus scattering angle, Evans (1958).

## 2.12 Rayleigh cross-sections.

In Rayleigh scattering, the entire atom is considered to be involved in the scattering process. All the electrons of the atom are considered to be forced into vibration at the frequency of the incident radiation. The scattering cross-section per electron has little meaning in such a situation, so we speak of an atomic scattering cross-section

$$\sigma_R = 8\pi \cdot r_o^2 \cdot f^2(\theta) / 3 \quad \text{cm}^2/\text{atom} \quad 2.23$$

where  $f(\theta)$  is the atomic scattering factor and is a function of angle.

Being an elastic process Rayleigh scattering does not play that significant a role in the work being outlined within this thesis. Rayleigh scattering could essentially lead to the loss of photons from the detector after an initial interaction with the detector itself, or can lead to transmitted photons scattering back into the crystal.

## 2.13 Energy dependence of the interaction processes.

Figure 2.4 shows a plot of percentage total cross-section versus energy for the three interaction processes in the 0 to 40 keV range for aluminium. Here we see that the photoelectric effect is the dominant process in the low energy region below 20 keV. However, beyond this point the photo cross-section drops steadily whilst the Compton and Rayleigh cross-sections both begin to play a far more significant role. As photon energies increase the photoelectric effect no longer dominates and eventually the three interactions occur with almost equal probability. As the photon energy continues to increase, the photoelectric effect eventually becomes insignificant as Compton scattering and the high energy phenomenon of pair production begin to dominate.

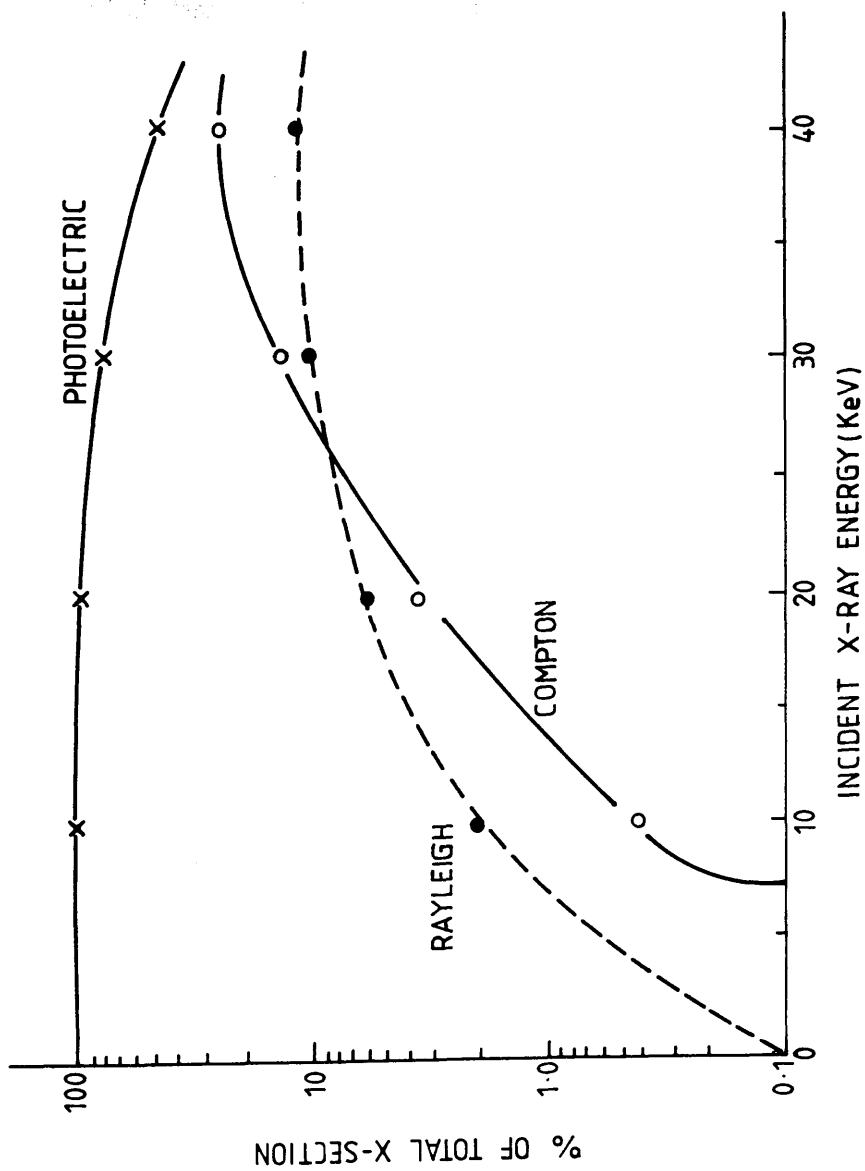


Fig. 2.4 Percentage total cross-section versus energy for the three interaction processes.

## 2.14 Conclusions.

This chapter has introduced most of the important theoretical considerations required throughout this thesis. In the next chapter the energy dispersive x-ray detector will be introduced. The important features will be described in some detail with certain other theoretical ideas being introduced as they become necessary.

## CHAPTER THREE

### The Si(Li) Energy Dispersive X-Ray Detector.

#### 3.1 Introduction.

With the Si(Li) energy dispersive detector playing such an important role in this project, it is necessary to look rather carefully into the way this detector works. This is important so that its performance can be fully appreciated whilst in operation either on the microscope or on the bench. The various sections in this chapter break down the detector into various blocks which can be used to describe its operation. Firstly, section 3.2 gives a general over-view of the detector and detection process so that the ideas developed in the subsequent sections will be more apparent. Section 3.3 looks at how the detector is fabricated, with the important design features being explained in detail. Section 3.4 describes the physics behind the detection process. A detailed knowledge of the physical processes occurring within the detector are essential if we aim to fully understand the nature of the spectra obtained. The next section briefly introduces the pulse processor and the electronics behind the detectors operation. The detector resolution and electronic noise are then explained; these have an important role in determining the shape and width of the observed peaks. The next two sections look at some of the typical spectral artifacts found with these type of detectors. Finally in this chapter, the detector efficiency is discussed. Detector efficiency is very important in the detection of low energy x-rays since it effectively sets the limit to what can be detected. In this section windowless detectors are conveniently introduced and some of the problems which these type of detectors give rise to are then outlined.

### 3.2 Schematic over view of the detector.

The Si(Li) x-ray detector is essentially a reverse biased  $p^+i-n^+$  diode (Haller, 1982). The silicon crystal which constitutes this diode is kept under vacuum and maintained at liquid nitrogen temperature. This low temperature is required to minimise electronic noise in the system and to minimise the reverse current flowing in the diode. A thin foil of beryllium is used as an entrance window through which x-rays must pass before being detected. This window is required to maintain the vacuum and to isolate the crystal from any potential contaminants.

X-rays incident upon the detector are absorbed through photoelectric capture or by the Compton effect. The excited silicon atoms decay by the emission of either an Auger electron or a photon, this photon being subsequently absorbed in a similar way to the initial x-ray. This process creates high energy electrons within the detector. These electrons dissipate their energy by scattering inelastically within the crystal, in doing so they create a series of electron-hole pairs. Ideally, the number of electron-hole pairs created per photon is characteristic of the incident photons energy.

The reverse bias applied across the crystal results in there being a very high electric field in the large intrinsic region. This electric field sweeps the carriers to either end of the crystal, those arriving at the rear contact, the electrons, are collected and fed to the gate electrode of a field effect transistor (FET). This FET is the input stage of a charge sensitive preamplifier. This preamplifier produces a voltage pulse which is characteristic of the charge collected by the detector. These voltages are subsequently processed by a pulse processor before being digitised and sent to a multichannel analyser for counting.

### 3.3 Detector fabrication.

Exact details of how detector crystals are fabricated are kept secret by the particular manufacturer. However, the general principles behind the construction are well known and are now outlined. Additional details can be found in Bertolini and Coche (1968).

In designing a detector crystal the major aim of the manufacturer is to achieve as large an intrinsic region as possible. This intrinsic region is where the majority of the photons are absorbed, the thicker it can be fabricated then the greater is the detectors efficiency at detecting high energy photons. This intrinsic region is required to minimize the number of carriers lost by trapping or recombination as the electrons and holes are swept through the crystal to the collection electrodes.

All crystals start life as a piece of very high purity silicon. Unfortunately a small concentration of impurities and defects will still exist within the silicon rendering it p-type. To compensate for these impurities, lithium ions are diffused into the crystal. Lithium is an interstitial donor and has a very high diffusion constant for silicon. The lithium diffusion usually takes place at a temperature of 100°C and with an applied voltage of greater than 500V (Link detector information manual). The bias is applied in such a direction as to help the lithium ions move through the crystal. As the lithium ions migrate through the crystal they seek out the impurity atoms and electrically pair. The net result of this lithium diffusion is to change the p-type silicon to the intrinsic variety. Once the lithium diffusion has taken place, electrical contacts are applied to the surfaces of the crystal. These consist of a thin gold film, typically 20 nm thick which is applied to the front surface forming an ohmic contact. The back surface has a lithium diffused contact with an additional gold ohmic contact applied. The surfaces are then treated to minimise any surface leakage currents which may arise (Link detector information manual). Lithium drifted crystals of this kind have be kept at liquid nitrogen temperature whilst in operation; this is to minimise the reverse current associated with such a diode. This also helps prevent the lithium ions further diffusing within the crystal under the action of the applied field. With the bias removed the detector can be warmed up to room temperature quite safely (Lowe, 1988). However, under no circumstances should the bias be applied if the crystal is at room temperature, since the large reverse current can destroy the FET. Warming the crystal to room temperature in this manner can be used as a means of annealing out defects within the crystal.

Figure 3.1(a) shows a schematic of a detector crystal as supplied by Link Analytical. An important design feature that can be seen from the diagram is that the

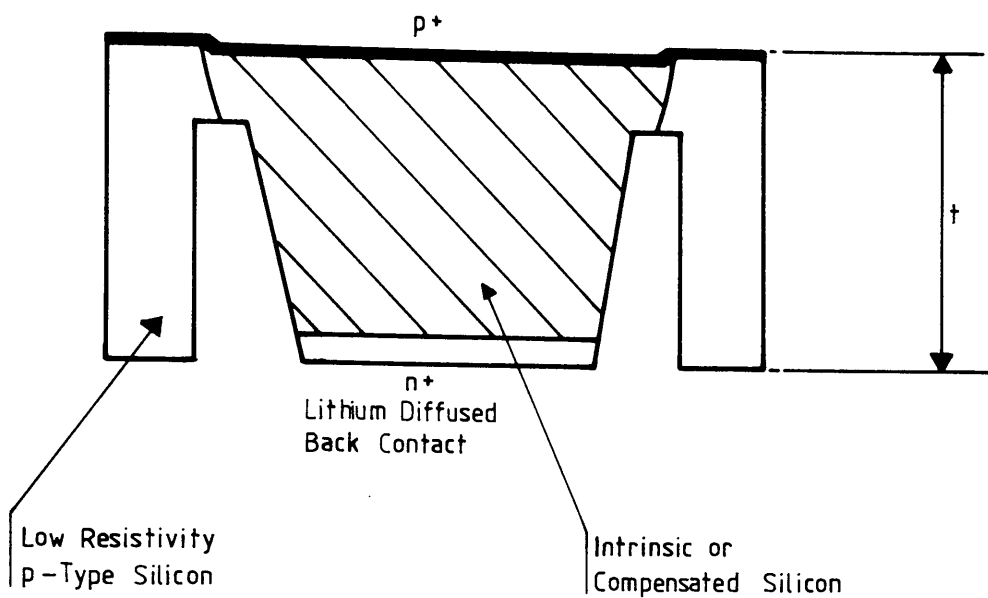


Fig. 3.1a Schematic of a Link Si(Li) detector crystal.

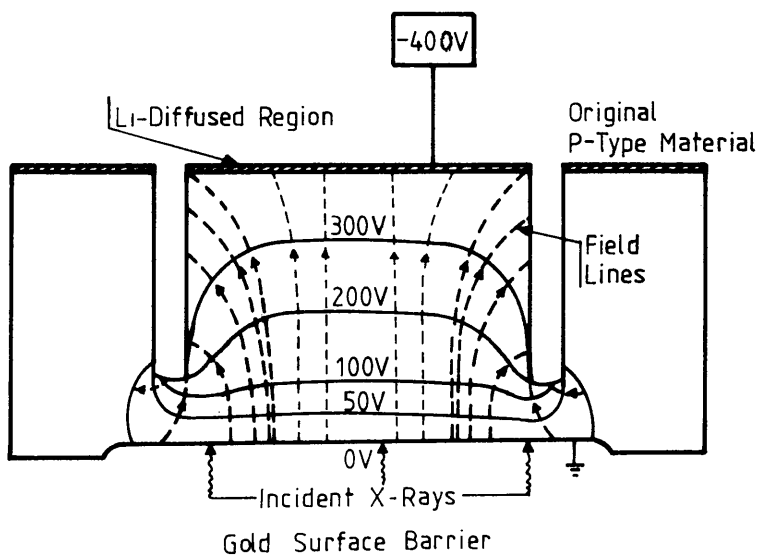


Fig. 3.1b Typical field lines associated with the biasing, Goulding (1977).

crystal is manufactured with a grooved geometry. This groove serves as a means of minimising the surface leakage current flowing in the exposed walls of the intrinsic region. It also modulates the surface charge density on these surfaces in such a way as to give the best possible field shape inside the crystal (Link detector information manual). Typical field lines associated with a reverse bias of 400 V are indicated in fig. 3.1(b) (Goulding, 1977). At the periphery of the crystal the electric field is weaker than in the centre, this can cause problems with trapping and surface charging (Lowe, 1989).

Crystals are generally manufactured in a variety of sizes. However, it is the active area, i.e. the area of crystal exposed to the x-rays, that is important. Active areas of 10 and 30 mm<sup>2</sup> are the most common size of crystal produced. The active area is set by the initial size of the silicon wafer and by an internal collimator, usually made from aluminium or tantalum.

The Si(Li) crystals are then assembled with the other components to produce a complete detector. Figure 3.2 (a) shows a schematic of a finished detector. Figure 3.2 (b) shows a close-up of the front of the detector. Here the beryllium window, internal collimator and crystal can be seen clearly. Within the detector housing, the crystal is kept at liquid nitrogen temperature by connecting the crystal/FET to a large reservoir of liquid nitrogen. This is done using the thermal properties of a copper rod, known as the cold finger. The entire assembly is kept under vacuum by the pumping action of molecular sieve which is kept in the cryostat housing and cooled by the nitrogen.

The entrance window, beryllium or otherwise, has to be very thin to minimise any absorption effects. Absorption in the window does however pose a problem since it effectively sets a cut-off in energy below which no photon energies can be detected. With the current thickness of beryllium being used ( $\sim 8\mu\text{m}$ ) the detection of characteristic x-rays from elements below sodium is not usually possible. Due to this effect different types of material have been used to replace the beryllium type windows. Manufacturers such as Link, Kevex and Tracor Northern have marketed detectors with a so-called ultra thin window (UTW). These have the effect of extending the low energy efficiency so that elements down to carbon can be detected. At present Kevex

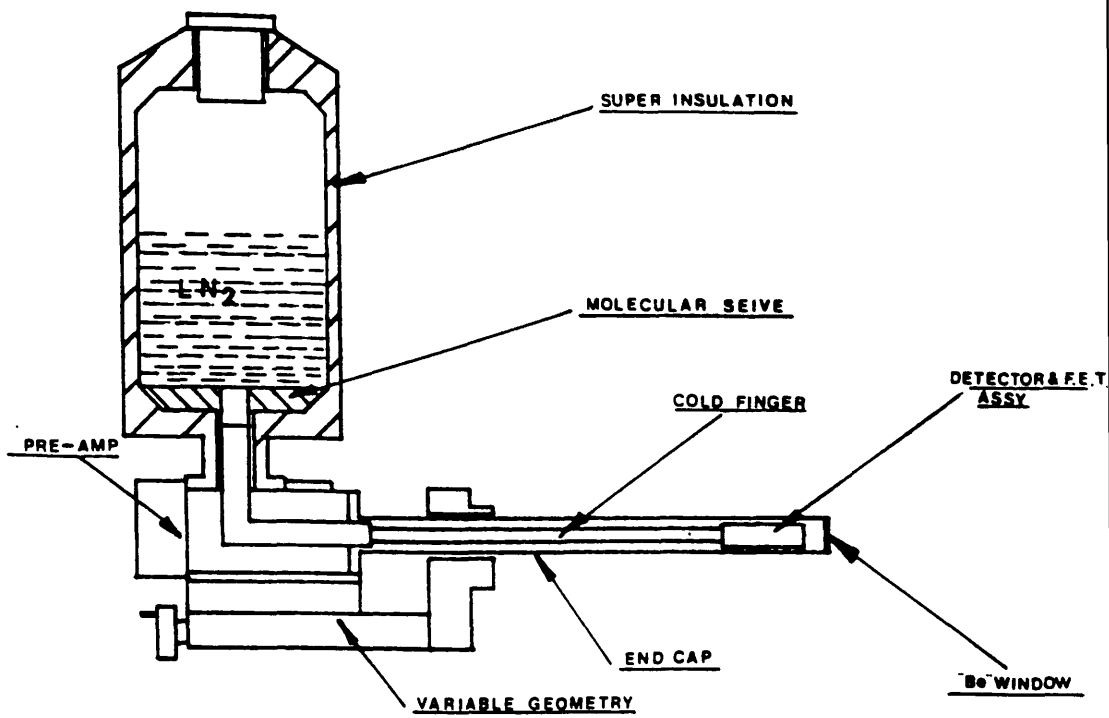


Fig. 3.2 (a) Schematic of a finished detector assembly.

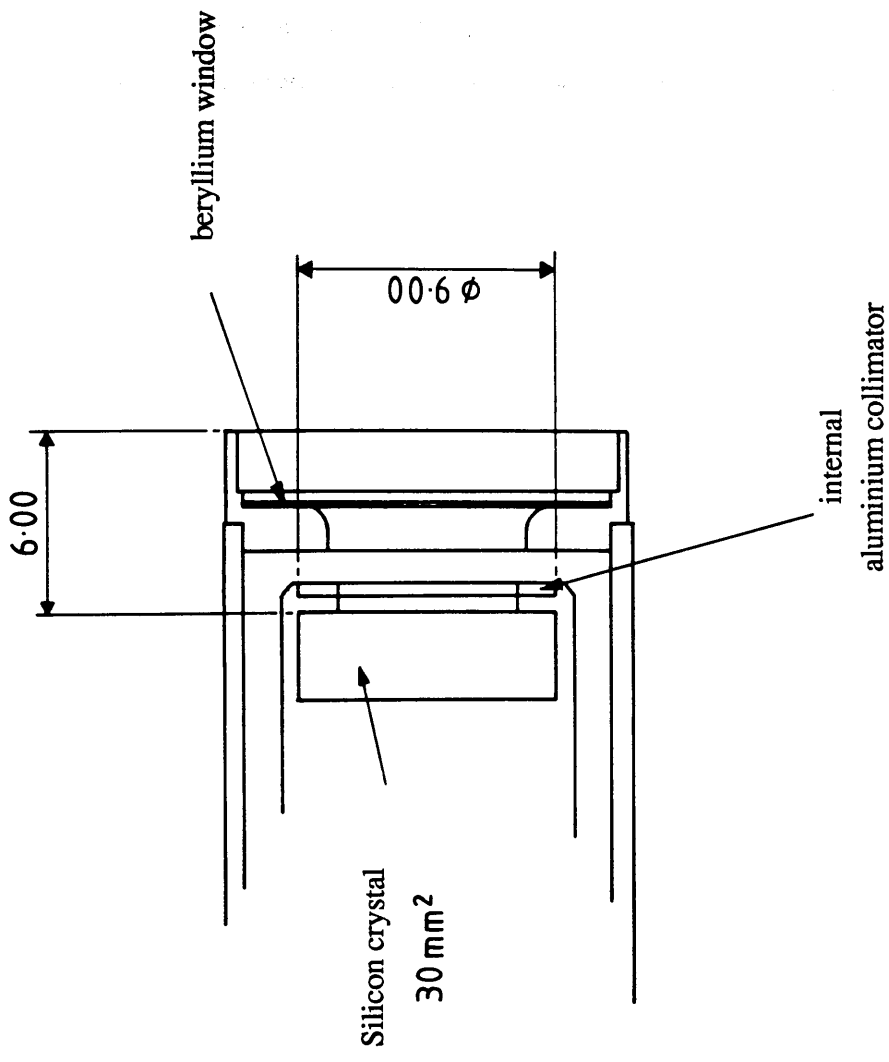


Fig. 3.2 (b) Close-up view of the front of the detector.

claim a new type of ultra thin window (Super Quantum) made from a boron and nitrogen polymer, this allows detection of the elements down to boron.

In addition to the UTW detectors are the windowless type detectors (Musket, 1981). These windowless detectors do not suffer from the same absorption problems as those detectors having a window, but pose their own set of particular problems which have to be offset against the benefits which they provide. Windowless detectors are discussed in more detail in section 3.9.

Entrance windows do however serve one useful purpose, they isolate the crystal from the environments in which they have to work. These environments may often contain molecules which can condense on the cold crystal. This can lead to the front surface becoming contaminated and additional absorption occurring. This can be a major problem with the windowless type detectors.

### 3.4 Detection process.

The operation of the detector relies upon the semiconductor crystal's ability to convert photon energy into measurable pulses of charge. As was mentioned in chapter 2, a photon can interact with an atom by any one of three different types of interaction. However, for the range of energies generally of interest in elemental analysis the photoelectric effect is the dominant type of photo-interaction. The detector operation will be explained by first assuming all the photons are absorbed by a photoelectric interaction, the other types of interaction will then be considered along with any differences which they may cause.

Incident photons are absorbed by the crystal somewhere between the front surface and a distance that can be predicted from the mass absorption coefficients. The absorption of these photons results in photoelectrons being created and silicon atoms being left in an excited state. These photoelectrons will have an energy characteristic of the difference between the photon and the binding energy of the particular electron shell of the silicon atom which was ionized (equation 2.11). The excited silicon atoms de-excite by either emitting a silicon x-ray or an Auger electron. If an x-ray is emitted, it

will be absorbed to create a second photoelectron. A situation arises where the initial photon has disappeared but has given rise to a number of Auger and photoelectrons which between them carry the energy of the initial photon. It is these energetic electrons which create the charge carriers within the crystal. The kinetic energy of the Auger and photoelectrons is dispersed as these electrons scatter inelastically throughout the crystal. This inelastic scattering process results in a series of electron-hole pairs being created as the scattered electrons receive sufficient energy to be promoted to the conduction band. The exact mechanism by which the carriers are created is complex and not yet fully understood. Shockley (1961) proposed an idea similar to the ionization of gases. Here, every electron-hole pair created can subsequently create additional pairs until all carriers have insufficient energy to further ionize any other atoms. Regardless of the exact mechanism the average number of electron-hole pairs created per photon can be approximated by the equation

$$N = hv/W \qquad 3.1$$

where  $N$  is the average number of carrier pairs, and  $W$  is the average energy required to create an electron-hole pair. Typical values for  $W$  appear to differ somewhat depending on the author, some of these being: 3.92 eV (Aitken, 1968); 3.8 eV (Fiori and Newbury, 1978); 3.58 eV (Fink, 1981).

Photons which Compton scatter within the detector are collected in a similar fashion to the photons which have undergone a photoelectric event. Here however, there are additional processes to be considered. After the initial Compton event, there exists a Compton scattered photon, a Compton electron and an excited atom. Any Compton scattered photons obviously have to undergo an additional interaction in order to be detected. This can be a photoelectric event or even a second Compton event. The excited atom will decay by the usual emission of an Auger electron or a characteristic photon. The Compton electron will scatter inelastically creating carrier pairs. In effect there are a variety of different possible routes available before the initial photon loses all its energy to the creation of electron-hole pairs.

The cross-section for the Compton effect increases with photon energy, as shown

in fig. 2.4. As the energy of the incident photons increases, a greater fraction of interactions will be via a Compton event. However, the overall probability of an interaction decreases. Thus there is a greater chance of this Compton scattered photon escaping the crystal without being detected. In this case the Compton electron is left to create charge carriers, hence the detected pulse is in effect that of a Compton electron. This idea is discussed in more detail in chapter 7.

It is important to realise that this entire process of converting a photon into a number of charge carriers occurs in an extremely short time. These carriers have a very short transit time in the crystal due to their high mobility in the electric field. This effectively means that the entire charge pulse arrives at the collection electrode over a period of time which is short by comparison to the time required for the pulse to be electronically measured. If this were not the case then the detector would be severely limited in the number of photons which it could safely detect without fear of the charge pulses arriving so close in time that they effectively overlap and give rise to coincidental results. Coincidental results give rise to what is known as "pile-up" (Statham, 1981). If two photons of energy  $E_p$  are detected simultaneously, this is equivalent to one photon of energy  $2E_p$  being measured, this giving rise to what is known as a "sum peak". In fact this idea is slightly more complicated since the pile up of two photons of energy  $E_p$  can ideally give rise to counts with any energy from  $E_p$  to  $2E_p$ , this depending on the exact arrival of the second photon. A situation can occur whereby a "pile-up continuum" (Statham and Nashashibi, 1988) is possible. Here, counts which should ideally contribute to the sum peak exist at all energies up to the sum peak energy and these are not easily corrected for. Pile-up of this kind has been known to corrupt the spectra from windowless detectors (Garratt-Reed, 1989). Here, the higher count rates of low energy photons (photons of energies less than 1.5 keV) can pile-up to give artifacts in the spectrum.

Fortunately pile-up was rarely a problem in this work since the count rates being used were usually far below the rates at which pile-up begins to become important.

### 3.5 Detector electronics.

The electronics which run the detector are very important since they have the ability to corrupt the spectra from what may otherwise be a good detector. The following section outlines the electronic processing involved for our Link detectors but the principles are fairly general to most manufacturers.

The charge arriving at the rear electrode of the crystal alters the potential at this point simultaneously altering the potential of the gate electrode of the FET. This FET being directly coupled to the crystal. The FET forms the first stage of a charge sensitive pre-amplifier (Statham, 1981). The output from this amplifier consists of a voltage ramp with steps which are characteristic of the detected photons energy. When this voltage ramp exceeds a certain level the accumulated charge is neutralised to stop the FET saturating.

A pulse processor is used to convert this voltage ramp into individual pulses which are then digitised so that they may be sent to a multichannel analyser for counting. The pulse processor operation is based upon that of Kandiah et al. (1975). This design uses different electronic circuits, or channels, to process the incoming signals. These channels are in parallel with respect to the incoming voltage signals. The first channel, often known as the recognition or slow discriminator, senses the arrival of an incoming pulse and triggers the logic to start a sequence of processing stages. The second channel, or the fast discriminator channel, is used to protect the processor from "pile-up" effects. Pile-up occurs when the incoming photon rate is too high for the pulse processor to separate the individual charge pulses efficiently. Therefore, any pulses which arrive in a time, shorter than the time interval to process the previous pulse, must be rejected since these pulses would lead to a pile-up effect. While a pulse is being processed no others can be counted and must therefore be rejected. The fast discriminator channel detects these closely timed pulses and resets the recognition channel ready for the next pulse. The third and fourth channels are a delay line and a limit discriminator; these need not be discussed.

For efficient operation it is essential that the fast and slow channels have a small noise current ever present. This is to prevent the loss of low energy signals due to the

level discriminator associated with these channels. A compromise is required whereby we neither have too much nor too little noise. This level is usually determined by the manufacturers for the particular processor. Electronic noise can be a problem with low energy pulses where the noise level can be comparable with the incoming signal. A low energy threshold discriminator is incorporated at the input stage; this can be set to reject low level signals, which may only be noise. However, this has been found to reject counts which are thought to be caused by the effects of ICC.

The pulse processor used throughout this project, the Link 2020, allows the user a choice of three signal processing times, these being 10, 20 and 40  $\mu$ s respectively. For a low input count rate a longer processing time gives the best representation of the pulse. This is due to the way in which the noise contribution associated with the pulse shaping electronics can be more effectively minimised.

The precise setting-up procedure for the pulse processor is discussed in appendix 5. Additional information concerning the pulse processor can be found in the paper by Statham, (1981) or from the Link Analytical pulse processor manual.

### 3.6 Detector resolution.

The resolution of the detector is very important since it ultimately determines the line width of the detected peaks. Line widths are important when there are closely spaced peaks or overlaps occur from L and M lines. This is particularly important for low energy photons where the energy differences are small. Any overlap of adjacent peaks means that additional processing is required to obtain the peak integrals. It is therefore essential that we have a good resolution in order that we can separate the respective peaks.

The resolution of a peak is defined as the full width at the half maximum height (FWHM) of the peak in question. The resolution of any particular detector is determined by two factors, the electronic noise contribution and the detector contribution. Electronic noise is an unfortunate feature which can only be minimised.

Noise arises from several different sources each of which are tied in with the way the pulses are generated, processed and measured. The electronic noise contribution has steadily been reduced over the last twenty years by incorporating newer technology and better components. Currently, the noise contributions for the detectors we use are somewhere in the region of 100 eV. An important source of noise is the FET. The charge which accumulates on the FET during normal operation, has to be neutralised periodically so that the FET will not saturate. There have been several different techniques used for charge neutralisation of the FET (Statham, 1981) and it is these techniques which give rise to much of the noise contribution from the FET. At present the best FET's use a form of optical restoration. Here the FET is reset by irradiation from a light emitting diode. Link Analytical have recently developed new type of FET, the PENTAFET. This new type of FET employs a non-optical charge restoration technique. Charge is neutralised by an injection of an opposite charge into the channel of the FET. This further reduces the noise associated with charge restoration.

Electronic noise contributions in semiconductor detectors is described by Dearnaley and Northrop (1966) and in the Link pulse processor users manual.

The detector contribution arises from the statistical nature of the detection process, this can roughly be described by a Gaussian distribution. The FWHM of this Gaussian distribution can be calculated from the two sources of noise by quadrature addition. Mathematically the resolution can be described by

$$R = \sqrt{(\text{Noise})^2 + (\text{Detector})^2}$$

or 
$$R(\text{FWHM}) = \sqrt{N^2 + 2.355^2 F W E_p} \quad \text{eV} \quad 3.2$$

where N is the noise contribution, F is the Fano factor, a correction factor to allow for the fact that the detection process does not exactly follow Poisson statistics for random events. Typical values for this are around 0.1 for silicon (Fink, 1981). W is the average energy required to create one electron-hole pair, and  $E_p$  is the photon energy.

The resolution of a particular detector is normally quoted as the FWHM of the

manganese  $K\alpha$  line from an  $^{55}\text{Fe}$  radioactive source (see appendix 3). Typical values for the resolution range from about 150 to 156 eV. This corresponds to a noise contribution of around 100 eV, assuming  $F$  to be 0.1 and  $W$  of 3.8 eV (Link Detector Information Manual). With the recent advent of the PENTAFET, Link have reduced the electronic noise contribution and claim a detector resolution no worse than 133 eV for their 10 mm<sup>2</sup> detectors.

The resolution of the detectors can also be improved if the crystals are fabricated from high purity germanium instead of silicon (Cox et al. 1988). This improvement in resolution comes from a lowering of the detector contribution. The detector contribution is lowered because the average energy to create an electron-hole pair is lower for germanium (2.96 eV, Restelli, 1968) than for silicon. This results in a greater number of carriers being created per photon hence an improvement in the signal to noise ratio. Resolutions of less than 130 eV have been reported for such detectors (Link Analytical).

Germanium also has a greater stopping power for photons than silicon. This has the effect of extending the high energy efficiency of such a detector.

### 3.7 Escape peaks.

Figure 3.3 shows a typical example of a spectrum obtained from an  $^{55}\text{Fe}$  radioactive source. This spectrum is displayed with a logarithmic vertical scale. This is simply to give a global overview of the entire spectrum. Most of the spectra referred to throughout this work are displayed in a similar fashion. The spectrum also shows peaks from aluminium and argon. These were caused by fluorescence of atmospheric argon and fluorescence of the edges of the internal aluminium collimator.

From fig. 3.3 the two manganese K photo-peaks are visible as are their respective escape peaks. Escape peaks result when an excited silicon atom emits a K photon and this photon escapes the crystal. The energy of the escape peaks are therefore 1.74 keV lower than the photo-peaks. Escape peaks are most significant for elements whose photons are absorbed near to the surface of the detector, i.e. x-rays which have a large

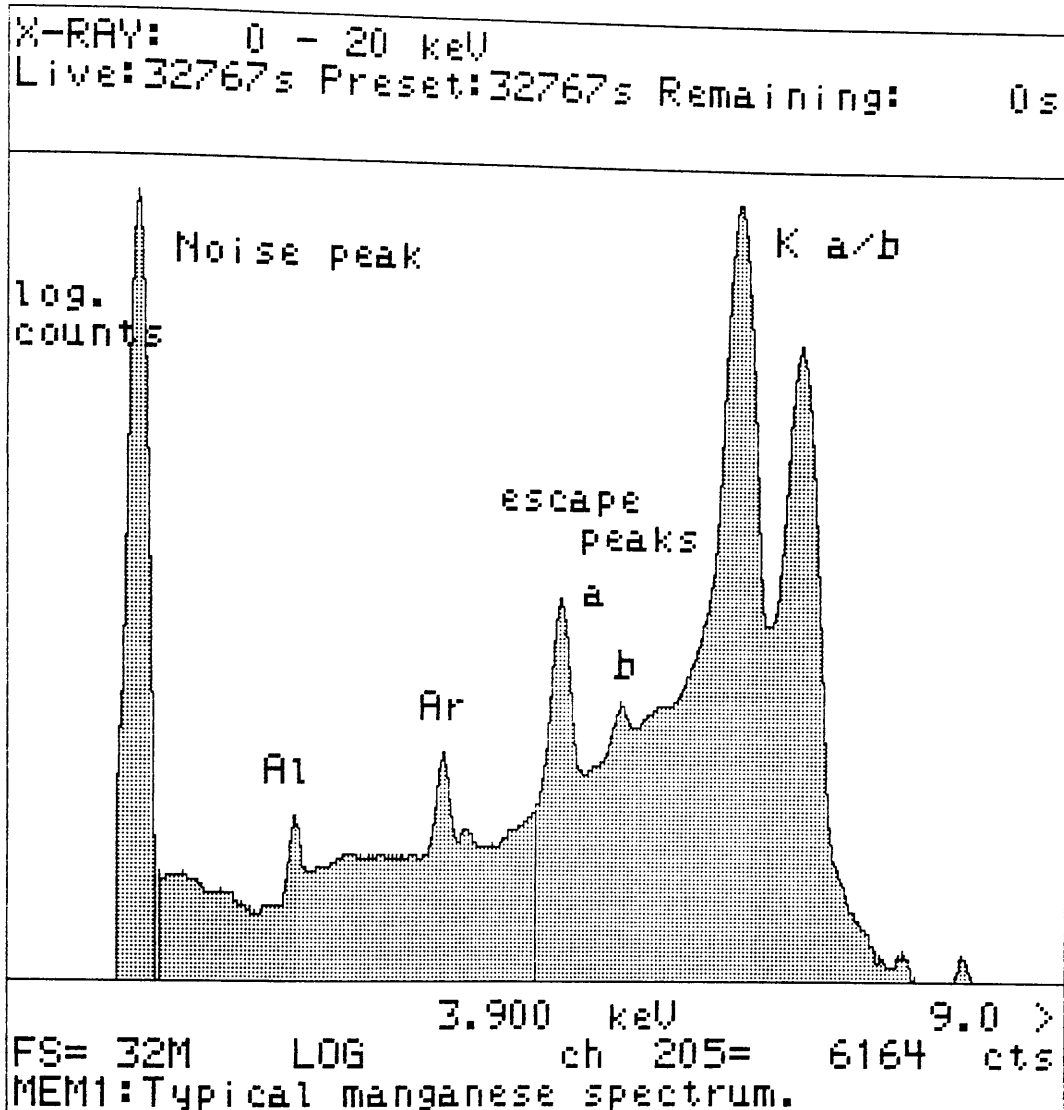


Fig. 3.3 Manganese spectrum, displayed in a logarithmic scale.

Figure 3.3 shows the X-ray spectrum of Manganese, displayed on a logarithmic scale. The spectrum shows several peaks, including a noise peak, Al, Ar, escape peaks (a and b), and the K a/b peak. The energy scale is in keV, and the y-axis is in log. counts. The spectrum is typical for Manganese.

mass absorption coefficient in silicon. Absorption near to the surface means that the silicon photons have a greater probability of escaping since they are created near to the surface. This idea has been studied by Reed and Ware (1972) where they make some theoretical predictions about the size of escape peaks expected for low Z elements.

In addition to the escape peaks, there are other fundamental effects occurring which also manifest themselves as the escape of radiation. For example, photons which are absorbed near the surface can result in electrons being able to escape. These electrons can either be the photo or Auger electrons, or indeed any of the electrons which gain energy during the energy dispersion process. This escape process can only occur over a finite range due to the short range of the electrons. One other mechanism, is that of the escape of bremsstrahlung. This bremsstrahlung being that created by the photoelectrons as they scatter within the crystal. This idea is covered in more detail in chapter 7.

### 3.8 Incomplete charge collection.

Inspection of figure 3.3 shows a background or tail on the low energy side of the characteristic manganese photo-peaks. This tail is caused by incomplete charge collection, ICC (Dearnaley and Northrop, 1966; Llacer et al. 1977) of the carriers. ICC was first studied in association with the development of semiconductor particle detectors and is thought to occur as a result of carriers being lost to the collection process by some form of trapping or recombination (Fink, 1981). Fiori and Newbury (1978) attribute part of the observed ICC to the escape of photons from the detector. These photons being generated as the photoelectrons scatter within the crystal.

Exact mechanisms to explain the nature of the ICC do not exist. However, several models do exist which propose mechanisms to explain why charge carriers may be lost, these include: Llacer et al. (1977), Shima et al. (1983), Joy (1985) and Heckel and Scholz (1987). These models all use the idea of a surface layer of crystal in which the collection efficiency of the carriers is reduced. Each model considers different ways in

which carriers can arrive at, or be created in, this inefficient layer. Each of the models can claim partial success in explaining some property of the ICC. However, no model is general enough to explain the detailed shape of the tail. An important point is the fact that all of these papers propose models for detectors which exhibit far more ICC than the new type Link detectors being used in this work.

Other published work quotes experimental data able to describe certain properties associated with the occurrence of the ICC (Craven et al. 1985, 1987, 1989; McHardy et al. 1989). This experimental evidence clearly shows that the detector crystal's surface must play a significant role in the effect. Photons which are absorbed nearest to the surface give rise to the greatest level of ICC in their spectrum. This is one fact which appears to be consistent with all detectors regardless of the manufacturer or the subsequent improvements to the design. Other experimental evidence indicates that the sides of the crystal play a significant role in the level of ICC observed (Fiori and Newbury, 1978; Craven et al. 1989).

During the last few years the detector manufacturers, Link Analytical, have developed a new process which resulted in an order of magnitude improvement in the level of ICC in their detectors. This process is thought to be a type of surface reprocessing (Nicholson, 1988). These detectors, known as the series E type detectors, were the ones used throughout this project.

The effects of ICC causes problems in various different ways. For example, counts which make up the low energy tail ideally belong in the main photo-peaks. This loss of counts constitutes a source of error when the area of a peak is being measured. If there are several closely spaced peaks in the spectrum there will be an overlap between the peaks and the ICC. Secondly, when a bremsstrahlung background is being fitted by theoretical modelling, some consideration has to be given to the level of ICC which "sits" on top of the bremsstrahlung (Statham, 1981, Adam, 1986). A correction of this kind is not easy to do.

### 3.9 Detector efficiency.

The detector efficiency is in effect a measure of the detectors ability to detect an x-ray. The low energy efficiency of the detector is limited by the beryllium window and the outer layers of the detector. Low energy photons suffer from absorption in these layers and may not reach the detector. A detector's low energy efficiency for the detection of photons of energy E can be calculated from

$$\epsilon(E) = \exp(-(\mu/\rho)_{\text{Be}} \cdot \rho \cdot t) \cdot \exp(-(\mu/\rho)_{\text{Au}} \cdot \rho \cdot t) \cdot \exp(-(\mu/\rho)_{\text{Si}} \cdot \rho \cdot t) \quad 3.3$$

where t is the thickness of the layer of material the x-rays have to pass through. This calculation is based upon a three layer model which is really only a good approximation at best. The thickness values for all three layers are subject to large errors. The beryllium window, for example, is nominally quoted as 8  $\mu\text{m}$ . However, Statham (1981) has shown that this value can vary by up to 30% and that pin holes can exist in the foil. The thickness of the evaporated gold layer is nominally quoted as 20 nm. Jaklevic and Goulding (1971) have indicated that the gold layer may exist as a series of islands, with large open areas existing. Jaklevic and Goulding conclude that the existence of these open areas may indeed be fortuitous for the detection of low energy x-rays. The fact that a windowless detector can detect photons from carbon and below can be interpreted as evidence for such open areas.

The thickness and the physical nature of the silicon layer, often called the dead layer (Statham, 1981) has been the subject of many investigations (Llacer et al. 1977, Elad et al. 1973, Dearnaley and Whitehead, 1961). Statham (1981), in a review paper, states that the dead layer is in fact a layer of silicon in which the charge collection is poor. Photons being absorbed in this region will give rise to counts which appear in the tail. The dead layer is therefore seen as a major source of the ICC. The idea of a totally passive zone of silicon on the surface has been considered by Reed and Ware (1972). The passive layer of silicon is thought to give rise to internal fluorescence of silicon, if the silicon photon travels into the active layer of crystal it will be detected and gives rise to a silicon peak. Reed and Ware quote a thickness of 0.1  $\mu\text{m}$  for this passive layer.

This was confirmed by Adam (1985) for the older generation of detectors.

The high energy efficiency is limited by the thickness of the detector (~3mm). At energies beyond 15 keV there is an increasing probability that the photons will pass through the detector, without being detected. The only way in which to extend the high energy efficiency of Si(Li) detectors is to increase the thickness of the crystal, this can be difficult due to problems associated with drifting of the lithium.

Figure 3.4 shows a low energy efficiency curve for a detector assuming a 8  $\mu\text{m}$  beryllium window, a uniform 20 nm layer of gold and with 0.1  $\mu\text{m}$  of silicon used to represent a dead layer. If the beryllium window is removed we can see that the efficiency is vastly improved, fig. 3.5. This is one reason why manufacturers have developed the windowless type of detectors (Musket, 1981).

Windowless detectors can ideally detect photons down to beryllium, at 110 eV, this being the claim of Link Analytical. These detectors obviously extend the number of elements which can be detected. Windowless detectors do however, pose certain problems which makes normal operation more difficult. Surface contamination of the crystal is one such problem. With the crystal being exposed so often, the chances of surface contamination are fairly high. The build up of ice in particular (Cohen, 1987) can be a major problem. This build up of surface layers effectively leads to an ever changing low energy efficiency. To minimise the effect of any such surface layer, the vacuum in which the detector operates should be maintained at better than  $10^{-7}$  Torr.

Link Analytical have recently developed a type of windowless detector which combats any build-up of surface layers. This can be done by warming the crystal to effectively boil off the adhering layers.

One additional problem which windowless detectors suffer from is that of the leakage current which can arise when such a detector is exposed to light, visible and I.R. In fact if enough light is incident upon the detector it can be caused to saturate. This therefore requires that the crystals be operated in a light tight environment. However, certain specimens are cathodoluminescent when irradiated by electrons, this too has to be taken into consideration.

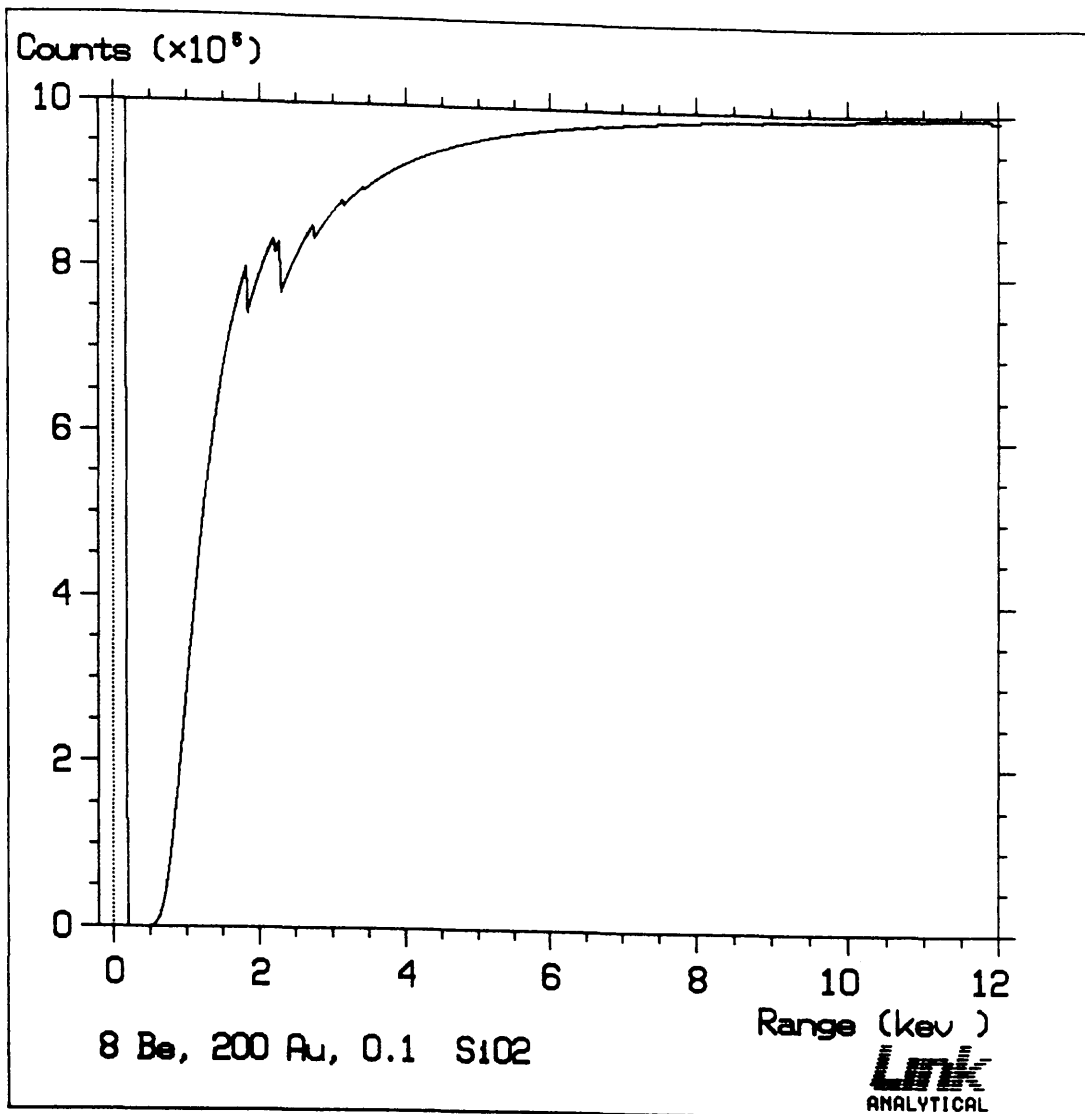


Fig. 3.4 Typical detector efficiency curve, assuming an 8  $\mu\text{m}$  beryllium window, 20nm gold layer and a 0.1 $\mu\text{m}$  silicon dead layer.

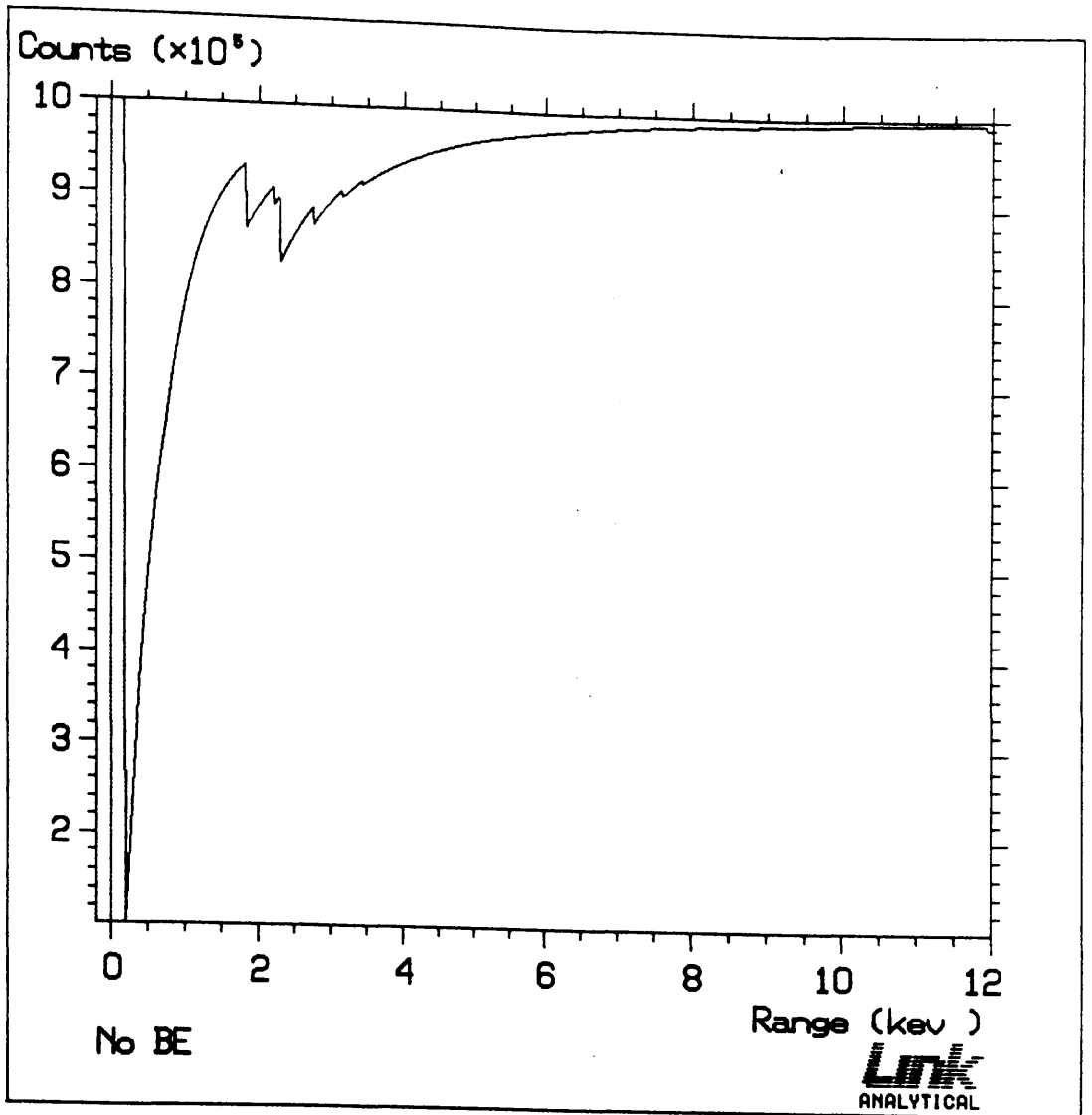


Fig. 3.5 Efficiency curve with no beryllium window.

### 3.10 The Link Analytical AN10000 Analyser .

The AN10000 Analyser is a complete microanalysis package manufactured by Link Analytical. This is essentially a small computer which drives the detector, pulse processor and various other hardware devices. The AN10000 is supplied with a package of programs which are used to acquire, display and manipulate x-ray spectra. These also allows some simple processing of the spectra. The AN10000 can also be obtained with a Fortran compiler which allows the user to write programs. These programs can be used to process any spectra acquired by the AN10000, or to simply do numerical calculations. Fortran programming on the AN10000 is described in appendix 2.

The AN10000 was used extensively throughout this work to acquire the various spectra. An older version of this x-ray analyser, the Link 860 mk.1 X-ray Analyser, was used occasionally. Although very similar to the AN10000, the 860 differs in that it uses an older and far inferior operating system. This makes any programming far more difficult, time consuming and limits the options available.

### 3.11 Summary.

This chapter has introduced the Si(Li) detector and has discussed in some detail the necessary details required throughout the remainder of this thesis. In the next chapter the usefulness of such a detector for the acquisition of electron generated x-ray spectra is investigated.

## CHAPTER FOUR

### Preliminary Investigation of Thin Film Spectra

#### 4.1 Introduction.

The aim of this preliminary investigation was to look at the bremsstrahlung backgrounds from thin specimens with the view to performing a theoretical background fit. Bremsstrahlung backgrounds for thin film specimens obtained from the VG HB5 had never been studied using the new Link series E type crystals. It was obviously very important to assess how these new crystals would behave. The theoretical backgrounds for these spectra were obtained using the MBH theory for bremsstrahlung production. These backgrounds were then corrected for absorption using the new Heinrich (1987) mass absorption coefficients. In this way an estimate for the accuracy of the theoretical backgrounds in the low energy region could be made. Modelling the low energy end in this way is very closely related to calculating the detector efficiency. Calculating the detector efficiency for a particular detector is very important since this characterises the detector; the information obtained about the detector parameters is useful in any subsequent work concerning the detector.

Section 4.2 explains how the detector efficiency is calculated for real situations and considers the difficulties which can arise. Section 4.3 describes the electron microscope and the techniques which were used to collect the x-ray spectra. The subsequent sections describe the results, how they were analysed, and the conclusions arrived at.

#### 4.2 Detector efficiency.

Calculating the detector efficiency was discussed in section 3.9. These ideas will

Equation 4.1 is not a general expression which can be used to represent all x-ray spectra. The final term  $I_{ICC}$ , makes this expression detector specific. ICC is found to vary from detector to detector hence invalidating eqn. 4.1 from being a general expression. The equation

$$I_D(E) = I(E).S(E).B(E).D(E)$$

is however a general expression which can be confidently used to express the detected contribution  $I_D(E)$ .

---

now be explained for the case of electron generated spectra with the difficulties which arise being discussed. For an ideal situation where bremsstrahlung is emitted with an intensity  $I(E)$ , the detected contribution  $I_D(E)$  can be represented by the expression

$$I_D(E) = I(E).S(E).B(E).D(E) \pm I_{ICC} \quad 4.1$$

where  $S(E)$  is the fraction of the intensity after self-absorption,  $B(E)$  is the fraction of the intensity transmitted by the beryllium window,  $D(E)$  is the fraction of the intensity reaching the crystal which is transmitted through the crystal's outer layers and  $I_{ICC}$  is the effect caused by ICC.

The self-absorption parameter  $S(E)$  can be a difficult parameter to establish. This is because the specimen thicknesses are rarely known accurately and the geometry of the specimens may differ from what we think they should be. For example, specimens are generally tilted at a specific angle towards the detector. It is generally assumed that the specimen is flat so that the tilt angle is constant over the entire area. If the specimen is bent in any way then this tilt angle may show considerable local variations. In addition the thickness of the film may not be uniform in all areas. These ideas are summarized in fig. 4.1.

It is important to establish the parameters  $B(E)$  and  $D(E)$  for any detector, these characterise the detector and are constant for all specimens of any thickness. The most accurate way of estimating these values is to use very thin films, 20 nm or less. Using thin specimens minimizes any specimen self-absorption, which simplifies matters somewhat since it effectively removes the parameter  $S(E)$  from equation 4.1. Ideally it is more accurate to use a variety of different thin films and film thicknesses to confirm the accuracy of the parameters chosen. Estimating the parameters  $B(E)$  and  $D(E)$  is done by accurately fitting a theoretical background to the low energy region of an electron generated spectrum. It is usual to scale the theoretical spectrum to the electron generated spectrum in a region between 6 and 12 keV. This being the region where the detector efficiency is approximately 1. Values chosen for the beryllium window thickness are then systematically varied until a reasonable fit has been achieved in the region below 3 keV. This beryllium window correction does not affect the high energy

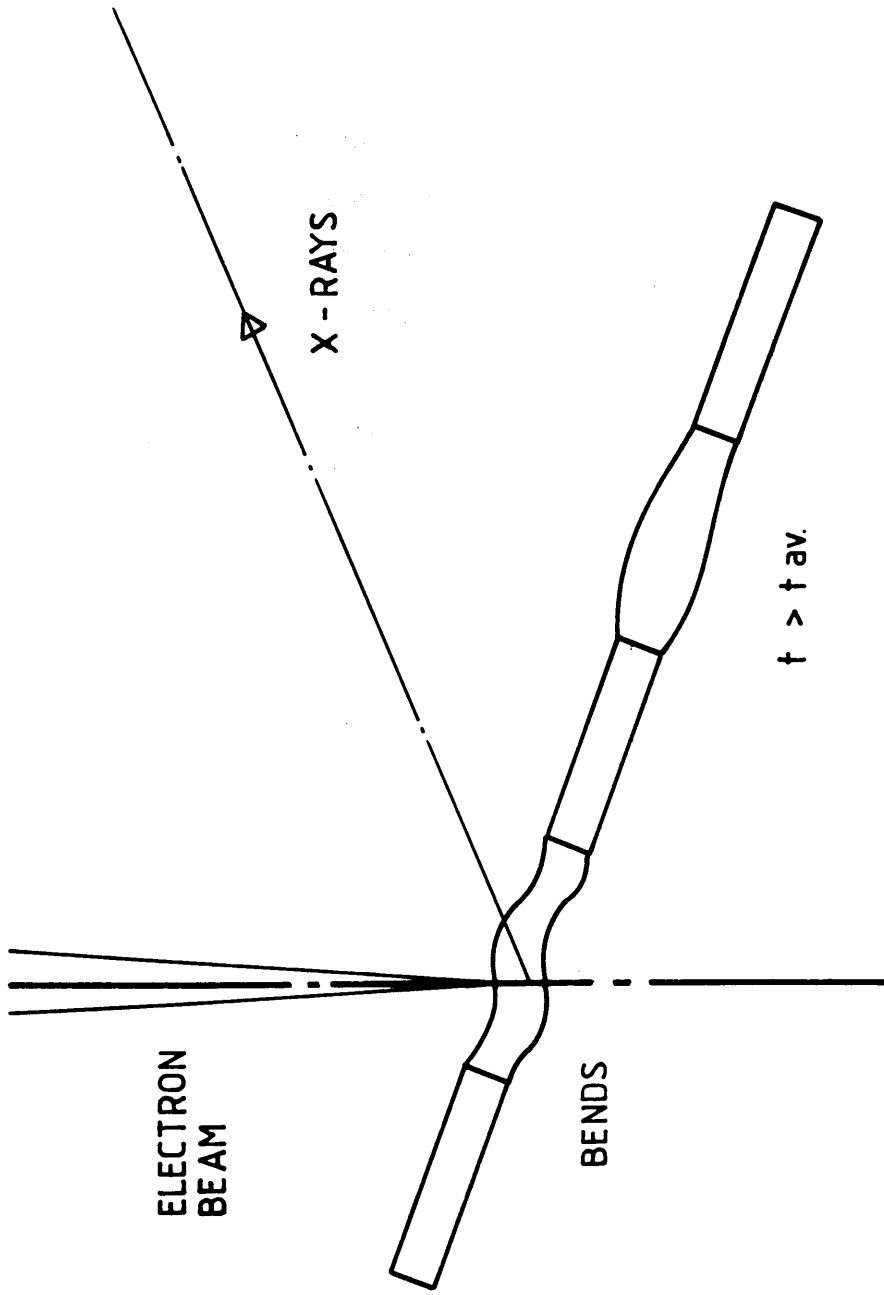


Fig. 4.1 Typical thin specimen showing bends and irregular thickness.

fit in any way. Finally, if required a correction for the gold layer and the silicon dead layer can be performed. This correction is not always found to be necessary however (Khan and Nicholson 1989). If this is the case this generally means that the fit achieved for the beryllium window has been over estimated slightly. This is not necessarily a problem since it implies that the multiplicative term  $D(E)$  from eqn. 4.1 has merely been considered as part of the term  $B(E)$ .

The final term in equation 4.1 is the contribution to the spectrum from the ICC. This is a complicated term which depends strongly upon the mass absorption coefficients for the photons being considered. The level of ICC in the spectrum serves to complicate the fitting process. The ICC can however be minimised by using a specimen whose characteristic x-rays have a low mass absorption coefficient in silicon (Adam, 1985). Craven et al. (1986) have shown that ICC is most serious when the majority of the photons are absorbed near to the detector's surface. Applying this idea to the bremsstrahlung, it is obvious that photons with energies at the silicon absorption edge and those just beyond, will on average, be absorbed nearest to the surface of the crystal. The net effect of this is to produce a large discontinuity in the bremsstrahlung spectrum at the silicon absorption edge. Figure 4.2 shows a bremsstrahlung spectrum modified by the effects of ICC for the older type of detectors (Craven et al. 1986). The new series E detectors which do not exhibit as much ICC, will display a similar step, only to a lesser extent.

#### 4.3 VG HB5 Scanning transmission electron microscope.

All the electron generated spectra in this work were collected on the VG HB5 scanning transmission electron microscope (STEM). Crozier (1985) has described this microscope in great detail. Adam (1985) was involved with the development of many of the analytical techniques which were used in the acquisition of the x-ray spectra. The necessary details which are important to this work shall now be outlined.

The HB5 STEM has many special design features which make it ideal for elemental microanalysis. The source of electrons is a field emission gun (FEG). This FEG is

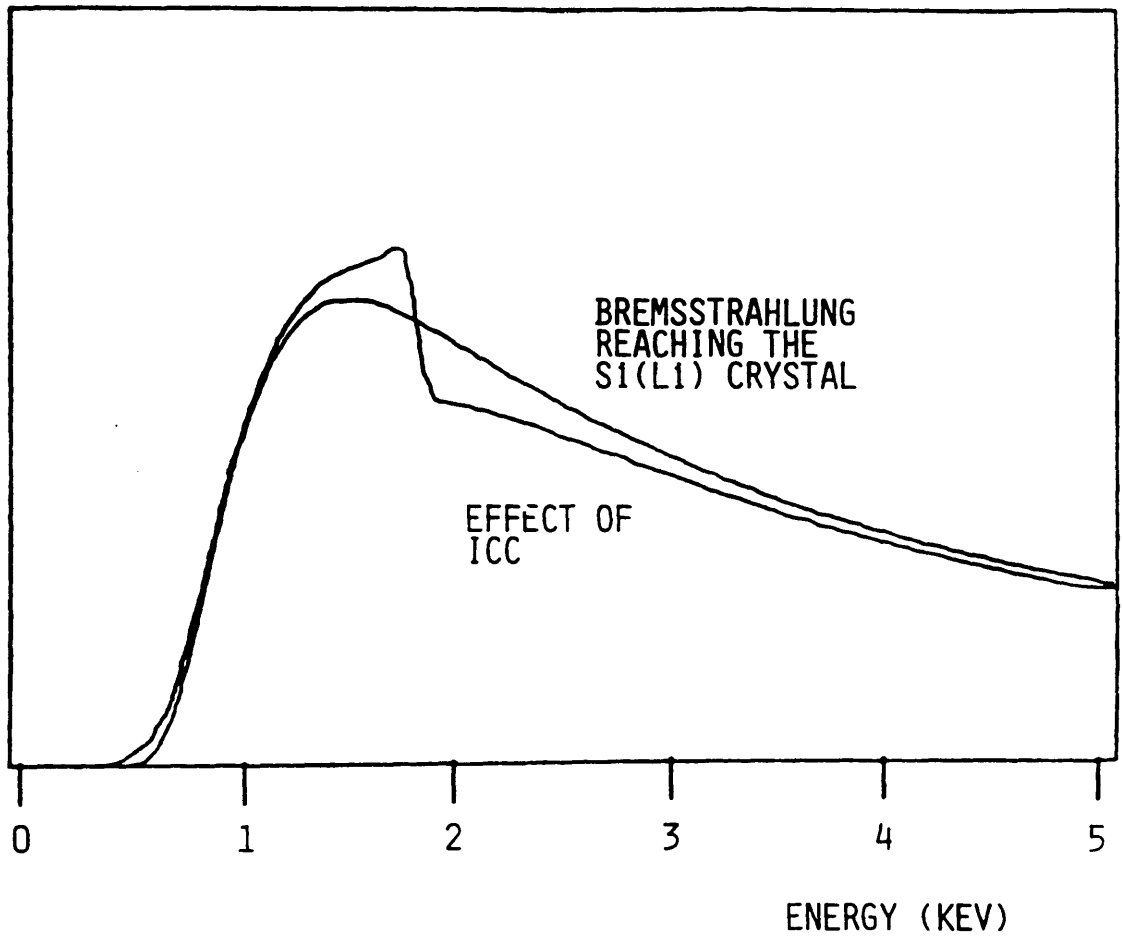


Fig. 4.2 ICC corrected MBH background, Craven et al. (1986).

designed to produce a very large brightness ( $\sim 5 \times 10^9$  A/cm<sup>2</sup>/sr) electron source. The image of the source is subsequently demagnified to form an electron probe upon the specimen. The size and current density of this probe is controlled by the configuration of various lenses and apertures. A high current is important since the number of x-rays produced is dependent upon the number of electrons incident upon the target.

In normal operation the microscope uses an accelerating voltage of 100 keV. However, this can be lowered to other values if a specific application necessitates this. The energy distribution of electrons emitted from the source has a FWHM of  $\sim 0.5$  eV. This enables beams with average electron energies of 100 keV to be treated as essentially monochromatic.

For x-ray acquisition two pre-specimen apertures are normally used. The first, a virtual objective aperture (VOA) serves as a probe defining aperture. Due to its close proximity to the electron gun this aperture serves as a means of effectively limiting the number of electrons which travel towards the specimen. The second aperture, the selected area diffraction aperture (SADA) lies in the plane of the beam cross over and serves as an effective spray aperture. This aperture is required to minimise any extraneous radiation generated by stray electrons which would only serve to complicate the spectrum.

The geometry of the specimen, electron beam and x-ray detector is very important in an electron microscope. The specimen-detector geometry effects the level of self-absorption, as it effectively defines the path length through which the x-rays must travel to be detected. Self-absorption corrections for thin films have been studied by many authors. It is by the Zaluzec (1979) model that self-absorption corrections were performed here. The detector-electron beam geometry determines the collection angle for the x-rays. The detector enters the microscope through a side port which is at 90° to the electron beam. The collection angle, with respect to the emergent electron beam, is set by a tantalum collimator which fits into the front of the detector. This collimator makes an angle of 10.5° to the detector axis. The angle of the emergent electron beam with respect to the detector is therefore set at  $\theta_0 = 100.5^\circ$ . The geometry of the detector, specimen and electron beam are shown in fig. 4.3.

In the HB5, the x-ray detector is conveniently situated at an angle ( $\theta_0$ )

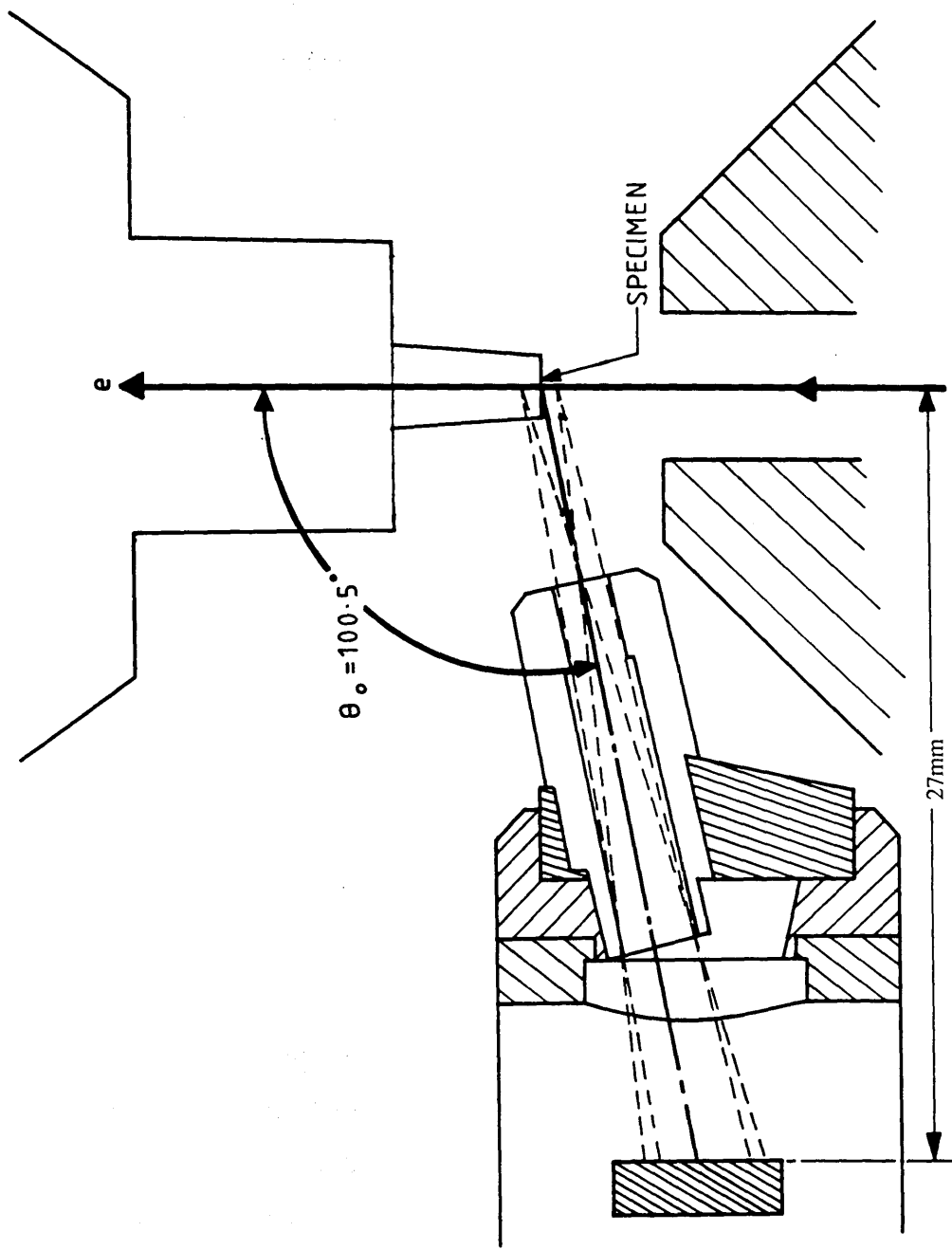


Fig. 4.3 Detector, specimen, electron beam geometry for the HB5 electron microscope. (see section 6.5)

which gives a relatively low intensity of bremsstrahlung radiation. This idea was mentioned in section 2.5 when the anisotropic nature of the generated bremsstrahlung was explained; this is described in more detail by Gray (1981).

The specimens were mounted upon titanium 50 mesh grids. These were held in a specially designed low background cartridge (Adam, 1985). The low background cartridges were designed to minimise the generation of any stray x-rays which might occur from scattering of electrons off the specimen onto any bulk material nearby. These cartridges consist of a main phosphor bronze body into which fits an aluminium insert. This insert is machined so that the specimen, which is held by a pair of titanium "fingers", is mounted at a fixed angle of  $20^\circ$  towards the detector; this is shown in fig. 4.4.

The acquisition of the x-ray spectra required no special techniques. Care is taken however to minimise the extraneous x-ray contribution from the titanium grid. This merely involved selecting an area of specimen in the centre of the grid to maximize the distance from the grid bars to the analysed area.

#### 4.4 Experimental techniques.

As previously stated, the aim of this investigation was to study the accuracy to which a theoretical background could be fitted in the region below 3 keV. In this region there exist two sets of important absorption edges. The silicon K absorption edge at 1.84 keV and those associated with the M shell for the gold layer, at 1.65, 2.12 and 2.2 keV. An edge at 1.84 keV can give useful information about any dead layer and the redistribution of counts caused by ICC. The thickness of the gold layer is normally difficult to establish (see section 3.9). If any gold edges can be seen in the bremsstrahlung these can be used to infer a value. This is not a particularly accurate method however. These edges referred to above, are in fact smoothed by the Gaussian nature of the detection process. This further complicates any fitting to these edges.

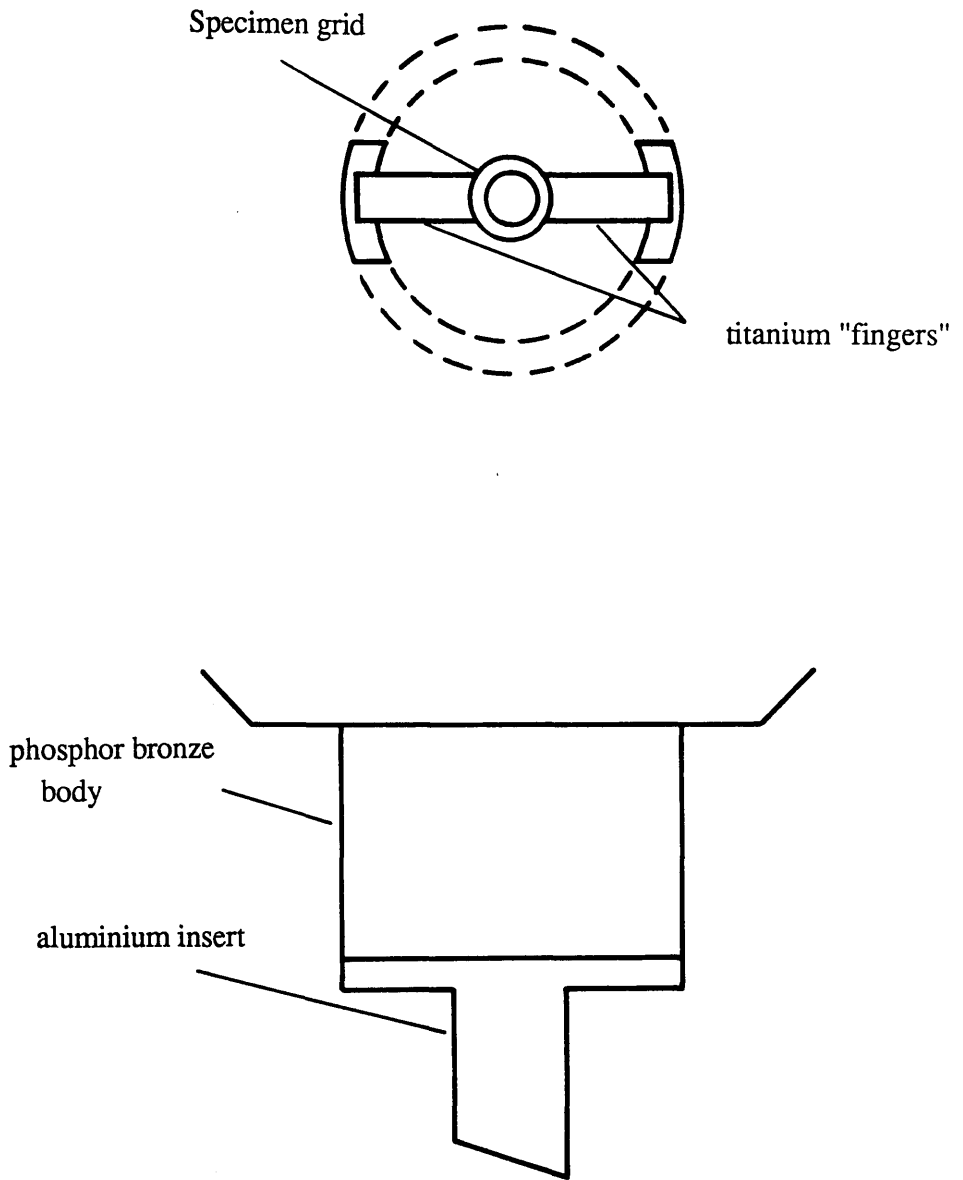


Fig. 4.4 Fixed tilt low background cartridge.

It is important not to mask any of the above effects with characteristic peaks. In choosing specimens, care had to be taken to ensure that there were no peaks in this region. The choice of specimens for background fitting was therefore fairly limited. The criteria which had to be met were:

(1) The spectra should give as few characteristic peaks as possible, as these only serve to complicate matters and add to the overall level of ICC in the spectrum.

(2) There should be no peaks in the region between 800 eV and 3 keV. This is the region over which the accuracy of the fit is to be tested.

(3) The specimens must be of a suitable thickness to be used in the microscope. They must be easily produced in a variety of known thicknesses, since the absorption corrections were to be tested as a function of film thickness.

(4) Specimens must be UHV compatible to be suitable for use in the HB5.

From the above list, (1) and (2) rules out elements with a detectable L line. This limits us to elements with  $Z < 28$ , (2) and (3) rule out elements sodium through argon. This left carbon, vanadium, chromium, manganese, iron and cobalt.

Carbon can be prepared very simply by evaporation in a vacuum evaporator. However, initial attempts at preparing and analysing such carbon specimens showed that high purity specimens were difficult to attain and the thickness of the films was not easily estimated. High purity films can be regarded as those which do not contain any stray elements with peaks in the regions of interest. In addition, any stray elements present should be at a concentration at least two orders of magnitude lower than the desired element so as not to add to the level of ICC already present. Chromium was found to be a much more suitable specimen to investigate. Chromium was prepared by R.F. sputtering with a thickness measured at  $30 \pm 5$  nm. The chromium specimens did contain one main impurity that being chlorine which was thought to have come from the rock salt substrate onto which the chromium was sputtered. Although undesirable, this impurity would not be a major problem. In addition, cobalt specimens were also produced by sputtering; these again were measured at approximately  $30 \pm 5$  nm. Sputtering was found to produce specimens of the highest purity and was therefore adopted as the only specimen preparation technique. Sputtering targets for iron,

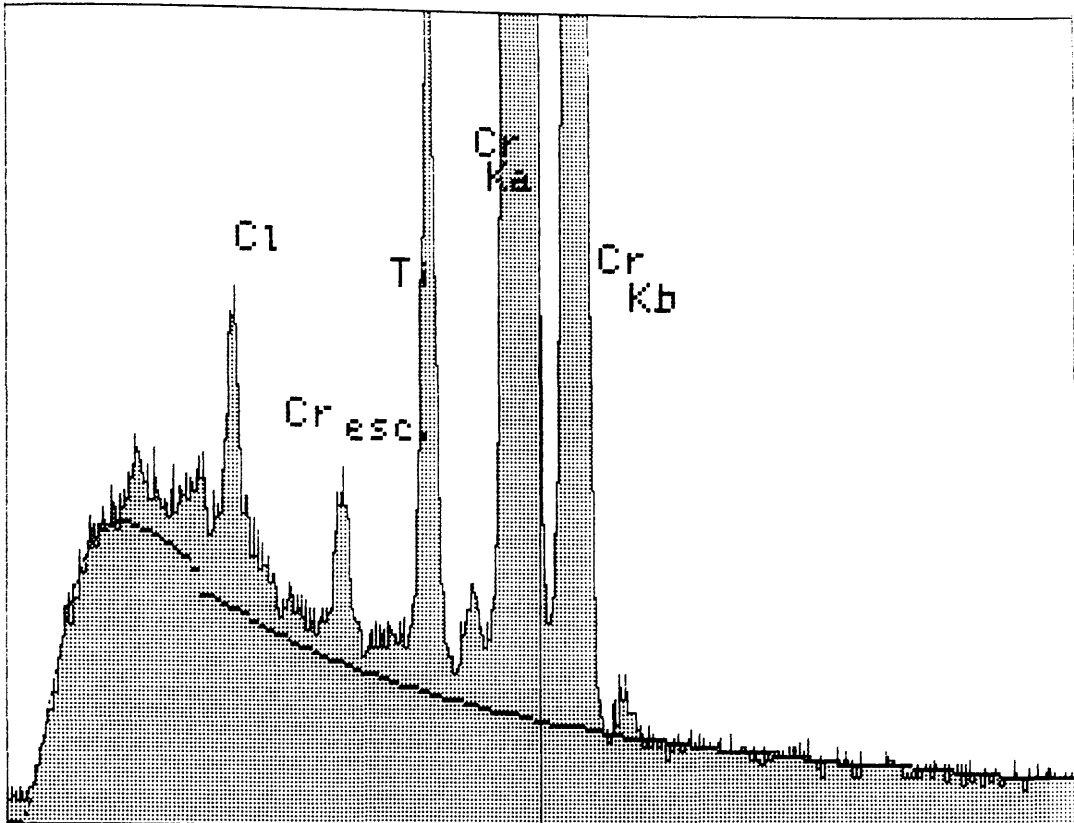
manganese and vanadium did not exist so it was not possible to produce specimens of these elements. Appendix 1 gives a full discussion of the various techniques used in specimen preparation and film thickness measurement.

#### 4.5 Results and analysis.

The first specimen analysed was a carbon film, the thickness of which was approximately 100 nm. A series of carbon spectra were taken from the HB5. The specimens were found to often contain regions where the impurity level was unacceptably high. Due to these problems with impurity levels and problems with thickness monitoring no subsequent carbon films were analysed. Chromium was the next element to be used. The chromium specimen was perhaps slightly too thick for an accurate detector efficiency to be calculated. Thicker specimens give rise to a greater degree of self-absorption; hence it is more difficult to estimate values for the required parameters. However, since this was only a preliminary study the specimen was considered to be quite suitable to test the accuracy of the fitting technique. The theoretical background for chromium was generated using software which had been developed within our group over the past 6 years. The package is based upon programs written by Drs. Adam and Nicholson. These had been recently updated and rewritten for the AN10000 by Mr. Khalid Khan, Dr. Nicholson and myself. A summary of these programs is given in appendix 2.

Figure 4.5 shows the chromium spectrum fitted with a background corrected for 9  $\mu\text{m}$  of beryllium and 20 nm of gold. The spectra have been scaled between 6-10 keV, a region where no peaks exist and the detector efficiency is approximately 1. The peaks, other than those from the chromium correspond to the titanium grid contribution and the small chlorine impurity. Figure 4.5 appears to indicate that the theoretical background has been modelled with too much absorption being allowed for in the region below the chromium escape peak at 3.6 keV, down to around 1.2 keV. However, below 1.2 keV the fit seems to be acceptable. Figure 4.6 is a background corrected for 6  $\mu\text{m}$  of beryllium, chosen since this would represent a lower limit for the window thickness

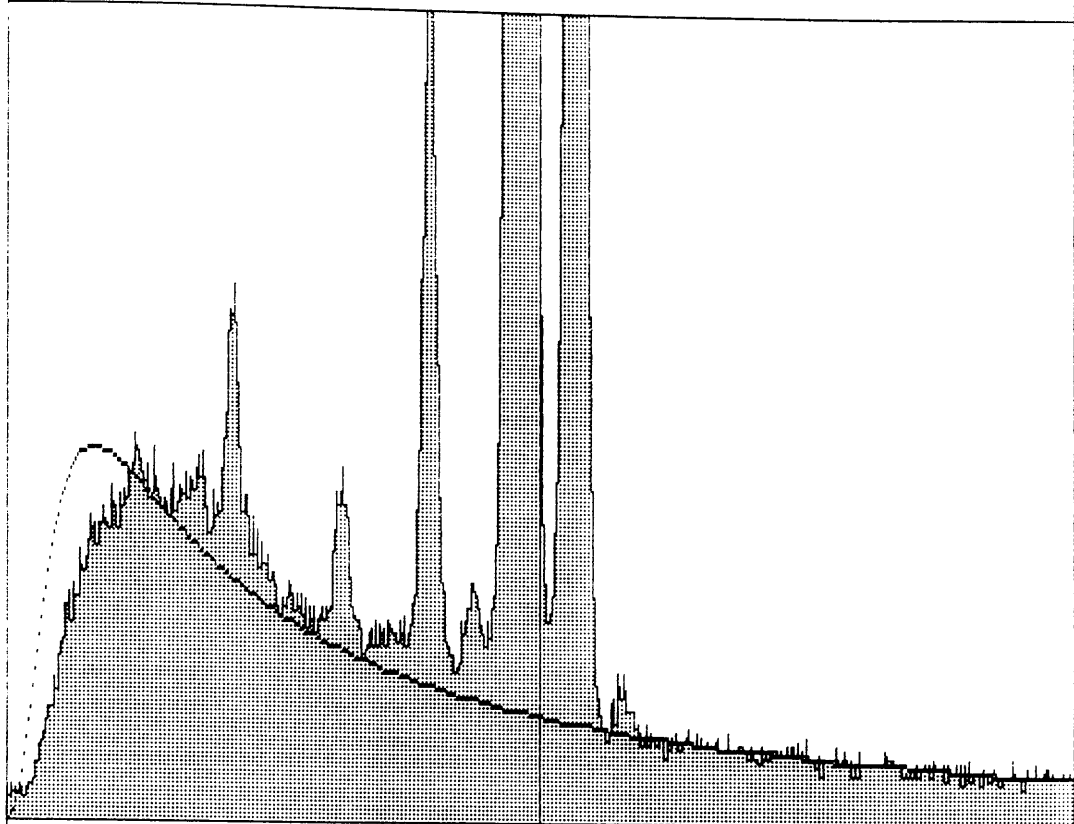
X-RAY: 0 - 20 keV  
Live: 100s Preset: 300s Remaining: 200s  
Real: 106s 6% Dead



< .5 5.600 keV 10.7 >  
FS= 1M ch 290= 1194 kcts  
MEM1:Cr /MEM2

Fig. 4.5 Chromium, MBH corrected for 9 $\mu$ m beryllium and 20nm gold.

X-RAY: 0 - 20 keV  
Live: 100s Preset: 300s Remaining: 200s  
Real: 106s 6% Dead



< .5 5.600 keV 10.7 >  
FS= 1M ch 290= 1194 kcts  
MEM1:Cr /MEM2

Fig. 4.6 Chromium with MBH corrected for 6 $\mu$ m of beryllium.

and hence the total absorption. This also appears to show too much absorption below 3.6 keV, but in this case there is now too little absorption below 1.4 keV. This fit is peculiar since a deliberate attempt at underestimating the absorption would be expected to give the type of fit seen below 1.4 keV, but should also give a similar type of fit around 3.6 keV.

Three other specimens were prepared and tested; these were cobalt, germanium and silicon. Silicon and germanium were used simply because they could be quickly produced on the sputterer, were of high purity and accurately known thicknesses. Figures 4.7 and 4.8 show what were regarded as the best fits that could be made for the cobalt and germanium specimens with the fitting parameters used being quoted. These just like chromium appear to give very poor fits in the low energy region. Again these have been scaled in the 6 to 12 keV region.

The silicon spectrum poses additional problems in that its characteristic peak is at a very low energy. This makes the fitting process very difficult in the very low energy region since the silicon peak sits upon the background at the place where the detector efficiency causes the bremsstrahlung intensity to roll-off. It is very difficult to estimate the level of ICC in the region below the silicon peak. Below the characteristic peak this ICC sits upon the detected bremsstrahlung. This makes fitting to the bremsstrahlung very difficult. Ideally a silicon spectrum would not be used in attempting to make a background fit until the detector parameters had been established for other specimens. Figure 4.9 shows an attempted fit for the silicon spectrum. This fit was made by fitting to the region just beyond the silicon K photo-peak. This fit does appear to be quite good in our region of interest; however, it is difficult to say how accurate this fit actually is.

When the background fit for chromium is subtracted off the real spectrum, fig. 4.10, the residual counts appear as a bump centered around 2.0 keV. This is similar to what Adam (1985) had found when he performed background subtractions for his ICC corrected spectra. This bump represents an increase in counts of up to 30% over the region of interest. It is interesting to notice that this bump exists in the region around the silicon absorption edge. This may indicate how the counts are redistributed by the





X-RAY: 0 - 20 keV  
Live: 600s Preset: 200s Remaining: 0s

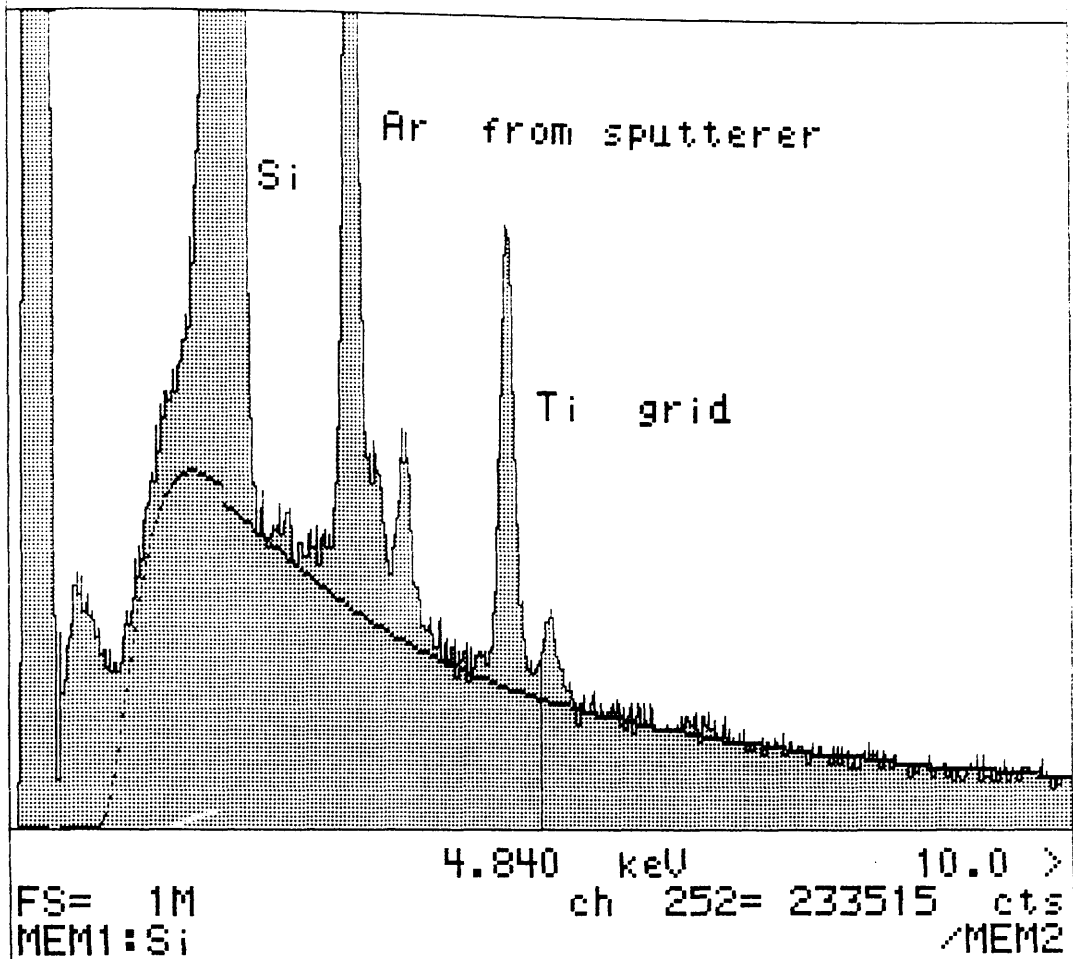


Fig. 4.9 Silicon with MBH corrected for 8 $\mu$ m beryllium, 20 nm gold and 25 nm self absorption.

X-RAY: 0 - 20 keV  
Live: 100s Preset: 300s Remaining: 200s  
Real: 106s 6% Dead

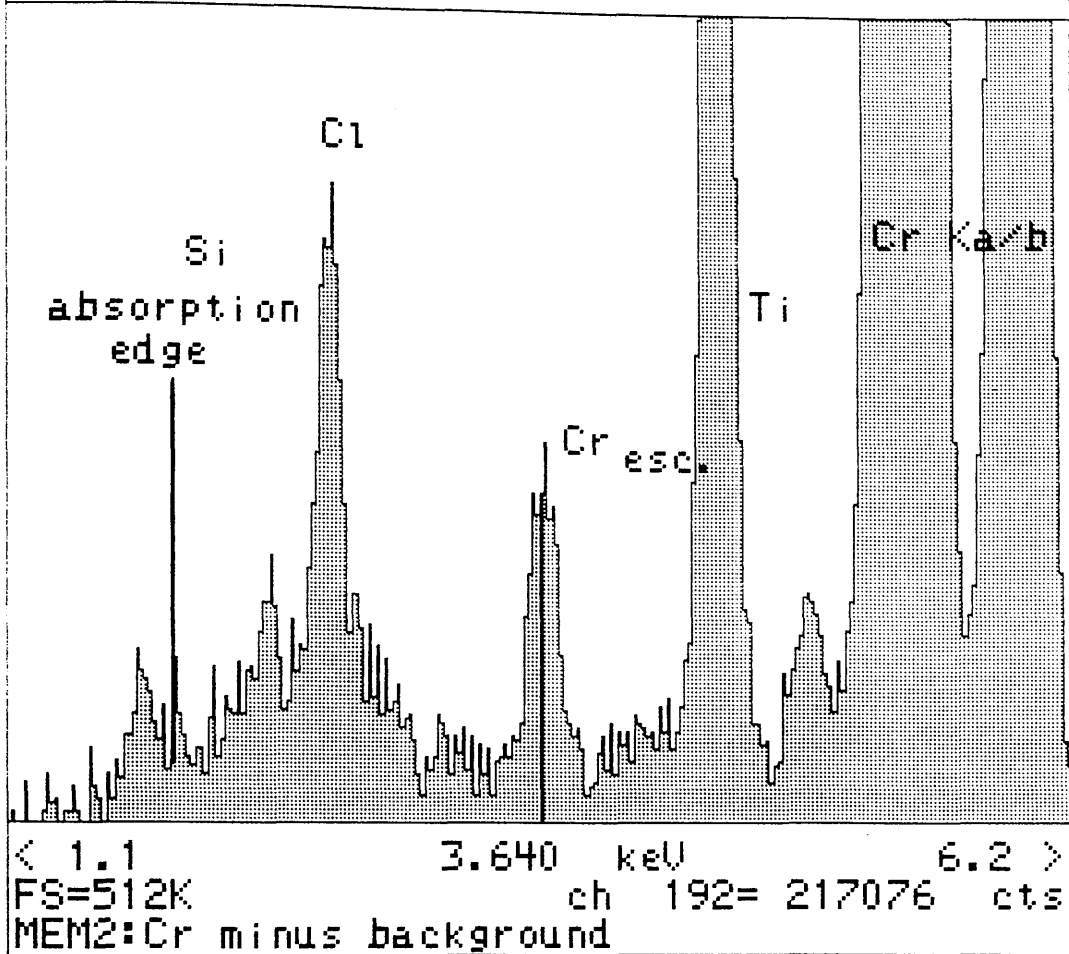


Fig. 4.10 Chromium spectrum with corrected MBH subtracted off.

effects of the ICC or may even suggest that errors in the mass absorption coefficients exist around the absorption edge.

The poor quality of background fits achieved for the various spectra appeared to indicate that there was something wrong with these spectra. The evidence for this was based upon the following conclusions:

(1) The attempts at modelling the background proved very difficult. Four different specimens did not appear to be suitable to estimate a window correction. This was unusual since previous work performed within our group had always shown that a window correction was straightforward and by itself gave a reasonable fit to the spectrum. Adam (1985) had used specimens of copper, iron and carbon. Paterson (1988) had used nickel, cobalt, germanium and silver. Both had achieved reasonable fits for these specimens. Adam had in fact used the older generation of Si(Li) detectors in his work.

(2) In the region just below the K photo-peaks the real spectrum always had more counts than the theoretical spectrum could predict. This was confirmed by using a low estimate of the total absorption, 6  $\mu\text{m}$  of beryllium. This still showed that the real spectrum had more counts in the 1 to 3 keV region.

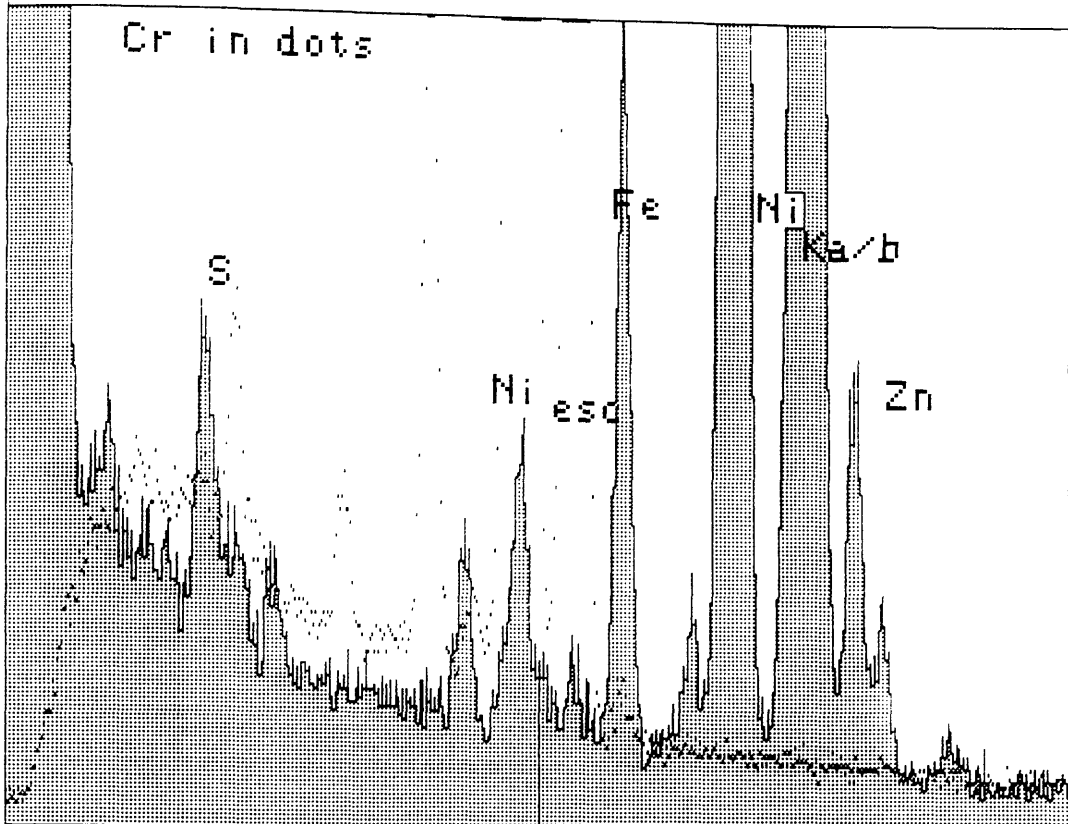
If it were to be assumed that the spectra did not truly represent a bremsstrahlung background, some reason for this had to be found. In chapter two the importance of the bremsstrahlung angle was explained. If somehow the detector collimator had become misaligned then the bremsstrahlung collection angle would have changed; hence the background shape would change. This idea can be tested by generating theoretical backgrounds for a range of bremsstrahlung angles. Using these backgrounds the absorption corrections can be performed as before. The relative differences caused by the detector being misaligned can then be checked. Theoretical backgrounds were generated for  $95^\circ$  and  $105^\circ$ , this representing a  $5^\circ$  angular displacement. This angular displacement would represent an upper limit to any possible detector displacement. If the detector is displaced so that the bremsstrahlung angle changes to  $95^\circ$  then the detected intensity will rise. If the theoretical bremsstrahlung intensities generated for  $95^\circ$  and  $100.5^\circ$  are scaled to the high energy end (energies greater than 8 keV) then the

average increase in the region 1 to 3 keV is 7%. This figure is well below the observed excess of counts which appear in the real spectrum.

A second method for checking the quality of the spectra was to compare them to spectra acquired under similar conditions. Dr J. Paterson had used an VG HB501 STEM at Harwell (Paterson, 1988). This microscope was similar to the Glasgow HB5, but was equipped with a Link windowless detector. This detector had the same bremsstrahlung acceptance angle as the HB5,  $100.5^\circ$ , and had a series E type crystal. One of the spectra taken by Paterson was from a nickel oxide thin film. This spectrum could be compared to the cobalt and chromium spectra acquired in Glasgow. Ideally the shape of the bremsstrahlung background from these three elements should be similar due to the approximate  $Z^2$  dependence of the bremsstrahlung. The main difference between the three spectra would be due to the nickel oxide spectrum, having been acquired on a windowless detector, therefore having a far greater number of counts at the low energy end of the spectrum. The specimen thicknesses were approximately the same in all cases, less than 50 nm. This is important to minimise any self-absorption which would lower the intensity at low energies. Figure 4.11 shows a comparison of the chromium and nickel oxide spectra after having been scaled between 8 and 12 keV, the region where both detectors would have an efficiency of about 1. It is quite apparent that the chromium spectrum has far more counts in the region between 1.6 and 5 keV. Figure 4.12 shows the nickel oxide and cobalt spectra scaled in the same way. Again the Glasgow spectrum has more counts than the nickel. The average difference in the counts between the two in this region represents an increase of approximately 50%. A more careful inspection of fig.'s 4.11 and 4.12 shows that this apparent excess in detected counts only occurs below the characteristic K photo-peaks on the Glasgow spectra. This may therefore indicate that these excess counts are an ICC phenomena.

By subtracting the nickel oxide spectrum from the chromium and cobalt spectra (scaled at high energy) it is possible to effectively remove the bremsstrahlung background. From ICC considerations (Craven et al. 1987), it can be inferred from the respective mass absorption coefficients that a nickel oxide spectrum would have less ICC than a chromium spectrum (providing the different detectors did not vary too significantly). Therefore such a subtraction should ideally leave a small residual of

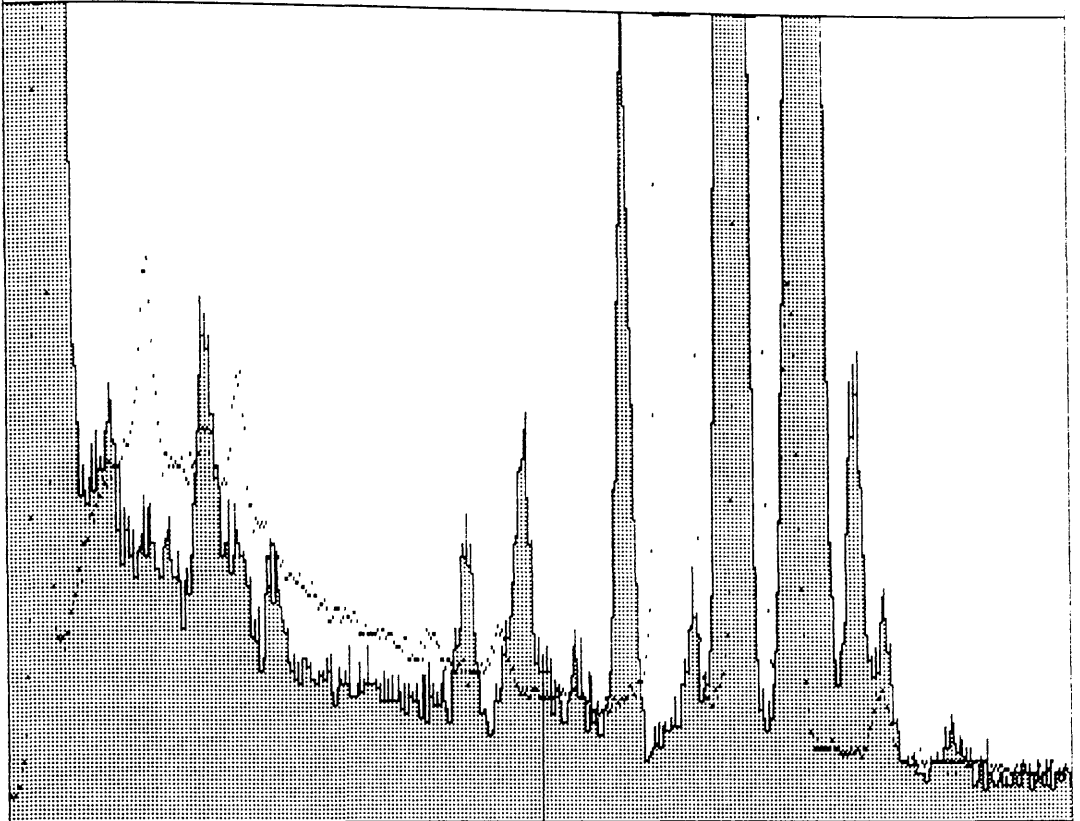
X-RAY: 0 - 20 eV  
Live: 61s Preset: 600s Remaining: 539s  
Real: 70s 13% Dead



< .5 5.600 eV 10.7 >  
FS= 1M ch 290= 225225 cts  
MEM2: Ni and Cr comparison /MEM1

Fig. 4.11 Comparison of the chromium and nickel oxide spectra, acquired with different series E Si(Li) detectors.

X-RAY: 0 - 20 eV  
Live: 61s Preset: 600s Remaining: 539s  
Real: 70s 13% Dead



< .5 5.600 eV 10.7 >  
FS= 1M ch 290= 225225 cts  
MEM2: Ni and Co comparison. /MEM1

Fig. 4.12 Comparison between the cobalt (dot memory) and nickel oxide spectra.

† It is not possible to fluoresce chromium K x-rays efficiently using the  $^{55}\text{Fe}$  source. Thus the closest element available is vanadium which will have slightly more ICC than chromium. If the difference between the Glasgow chromium and Harwell nickel oxide spectra gives considerably more counts than observed in a suitably scaled fluoresced vanadium spectrum, then additional ICC is occurring.

---

chromium ICC. The nickel oxide spectrum should also have slightly less ICC than the cobalt spectrum, therefore such a subtraction should once again leave a small residual of ICC. When the nickel oxide spectrum was subtracted from the chromium there was a large level of excess ICC counts remaining. To get an estimate of this additional ICC the chromium minus nickel oxide "difference spectrum" was compared to a fluoresced spectrum of vanadium. Vanadium is the adjacent element to chromium on the low Z side. The ICC contribution for vanadium should be greater than that for chromium. Figure 4.13 shows the chromium - nickel oxide difference compared to the fluoresced spectrum of vanadium, this being shown in a log. scale. These spectra have been scaled to their  $K\alpha$  peaks and shifted energy wise to coincide. Here it can be seen that considerably more counts exist in the difference spectrum than in the vanadium. The regions where no counts exist are regions where the nickel oxide spectrum had more counts than the chromium spectrum, generally impurity peaks. The "difference" spectrum does in fact show a level of ICC similar to that observed on the old pre-series E type detectors. This must be evidence that the new detectors are not behaving as expected. Subtracting the nickel oxide from the cobalt spectrum shows a similar effect.

#### 4.6 Conclusions.

The findings of this chapter have shown that the spectra obtained from the HB5 using our new type of detector, were not of a sufficiently high quality to perform background fitting satisfactorily. A range of elements were tried each giving the same poor fit.

Examination of the spectra appears to indicate that they do not accurately represent a bremsstrahlung background in the way that they should. All spectra obtained contained excess counts in the region below their characteristic K photo-peaks. This suggests that these excess counts are ICC. This level of ICC is far greater than would be found if the same detector was irradiated by a fluorescence source when outside the microscope. The level of ICC present in the electron generated spectra was in fact higher than that found for electron generated spectra acquired with the older generation of detectors. It

X-RAY: 0 - 20 keV  
Live: 100s Preset: 300s Remaining: 200s  
Real: 106s 6% Dead

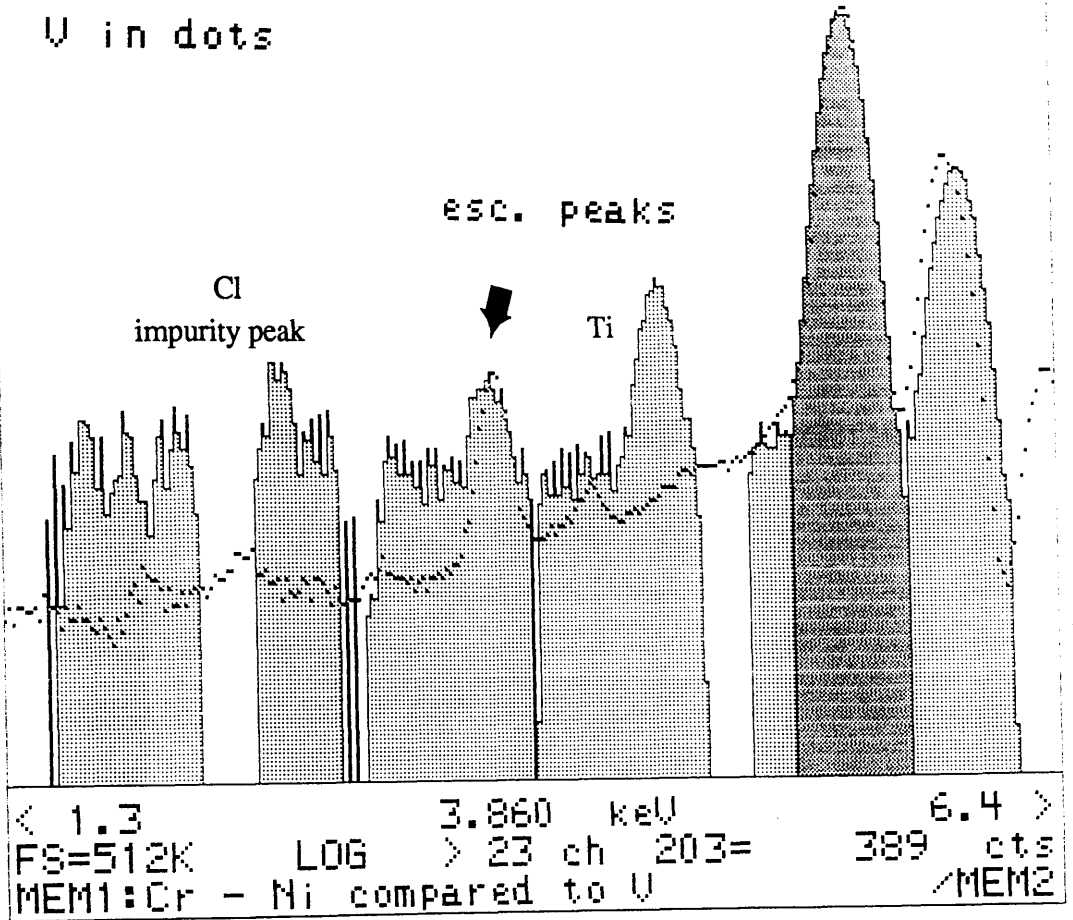


Fig. 4.13 Chromium - nickel oxide difference compared to fluoresced vanadium.

must therefore be assumed that the detector is no longer behaving in the expected manner. As a starting hypothesis it has to be assumed that the detector performance is being affected by the microscope in some subtle manner. The next chapter will explore this idea in more detail.

... during a period of ... which was ...  
... by the ... microscope ...  
... Si(L $\alpha$ ) detectors were used ...  
... IEM IEM ...  
... IEM detector ...  
... IEM detector ...  
... IEM and ...  
... analysis ...  
... comparison ...

### Differences between Si(L $\alpha$ ) x-ray detectors

... the spectra from ...  
... manufactured by ...  
... detectors which ...  
... detectors ...  
... have had different ...  
... and ...

## CHAPTER FIVE

### Considerations of the Effect of the Electron Microscope Environment on Detector Performance

#### 5.1 Introduction.

This chapter details a series of experiments which were designed as an initial investigation into studying the effects the microscope environment has on the detector performance. Three different Si(Li) detectors were used in this study. The first detector had been in use on a JEOL JEM 100C TEM/STEM for approximately one year (this will be referred to as the JEM detector). The second detector was the one used on the HB5 (referred to as the HB5 detector). The third was a detector which had been used on a Hitachi 300 keV TEM and had experiments performed upon it by the manufacturers (Link Analytical) as part of a collaboration. In addition one further detector was used for comparison purposes. This was a new detector which had never been used on a microscope.

#### 5.2 Differences between Si(Li) x-ray detectors.

In this section the spectra from three different Si(Li) detectors are compared. These detectors were all manufactured by Link Analytical. The purpose of doing this is to show the various differences which exist between the detectors. Ideally the performance of these detectors should be exactly the same. Each of the detectors studied in this project have had different histories and it was uncertain what effect this would have on the experiments, results and the conclusions being drawn. The main problem in this study was the fact that two of the detectors had been used on electron microscopes for long periods (over a year) and it was not known what effect, if any,

this may have had upon these detectors. Therefore, by comparing to a detector whose history is accurately known, it should be possible to gain information about the other detectors. The simplest way of doing this was to compare the two "microscope detectors" with a new detector which had not been used on a microscope. The various detectors were studied quite simply by comparing the manganese spectra obtained from a radioactive  $^{55}\text{Fe}$  source. The detectors were all highly collimated by external collimators; this was to expose only the central region of the crystal. The detectors used were:

- (1) The detector commonly used upon the JEM 100C. This was around three years old and had been used very frequently upon this microscope.
- (2) The detector used on the HB5. This was approximately two years old and had been used extensively upon the HB5 during this time.
- (3) A new windowless detector which had not been used upon any microscope.

Figures 5.1 through 5.3 show a manganese spectrum for each of these detectors, these are displayed in a logarithmic mode to give a global overview. Many common features can be seen throughout the spectra; the escape peaks, an aluminium peak from the detectors internal collimator and a peak from fluoresced atmospheric argon. Subtle differences between the detectors can only be seen when the spectra are compared directly. Figure 5.4 shows such a comparison between the JEM and the windowless detector. Here, apart from the stray contamination peaks there is no obvious difference between the two until the very low energy region where the spectra appear to terminate differently. This can be explained by the fact that they had been acquired using different pulse processors. The difference between the JEM and the HB5 detector is far more obvious however. Here the difference can be seen as a large excess of counts in the region very near to the photo-peaks for the JEM detector, see fig. 5.5. When Gaussian peaks are fitted to the manganese K peaks, then subtracted off to leave the tail regions alone, the difference between the two tails is found to be approximately 14%. Figure 5.4 did not show such a difference between the JEM and windowless detector. This perhaps indicates that the large difference between the JEM and HB5 detectors is not necessarily damage caused by use on the microscope, since the new windowless

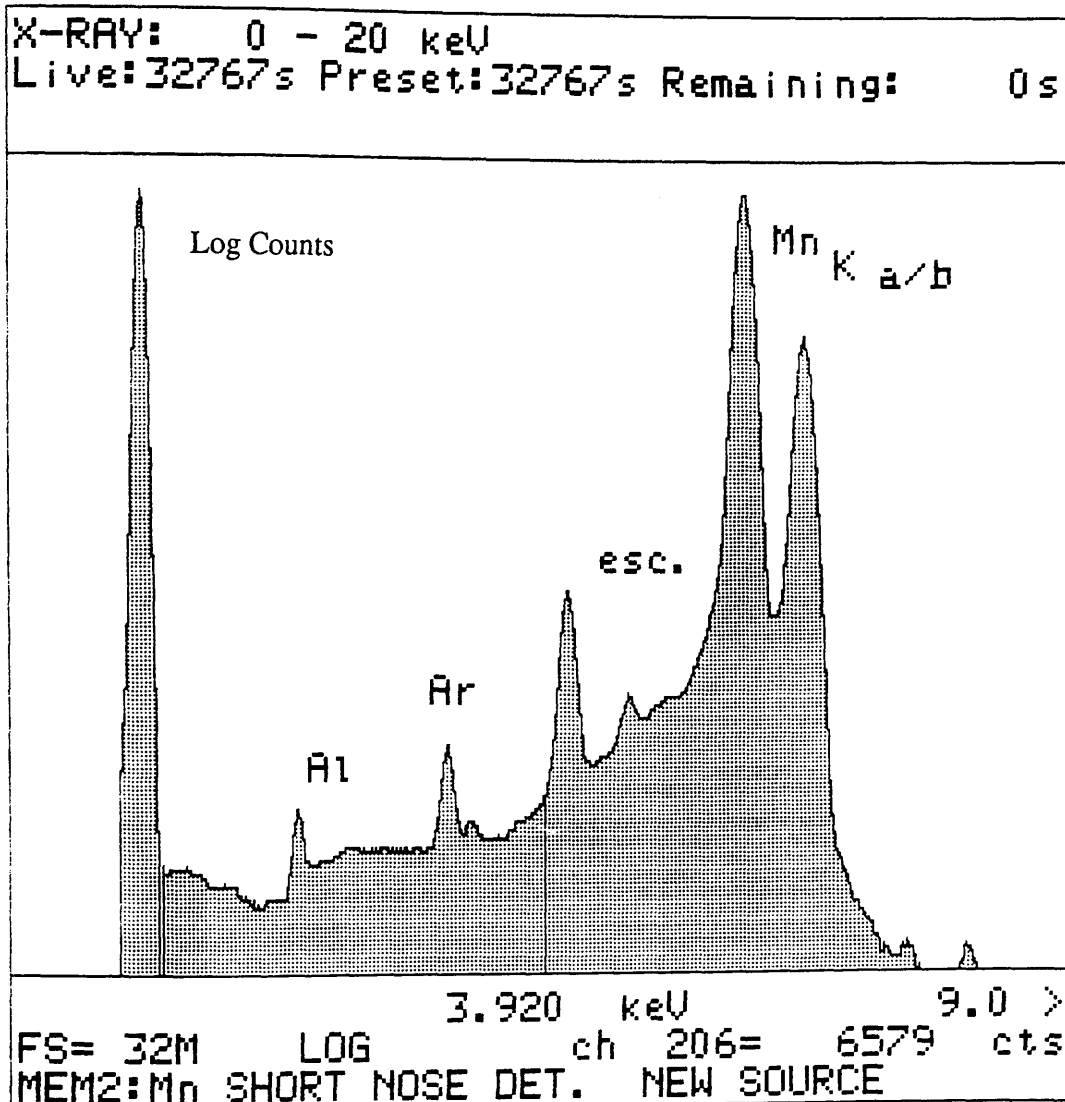
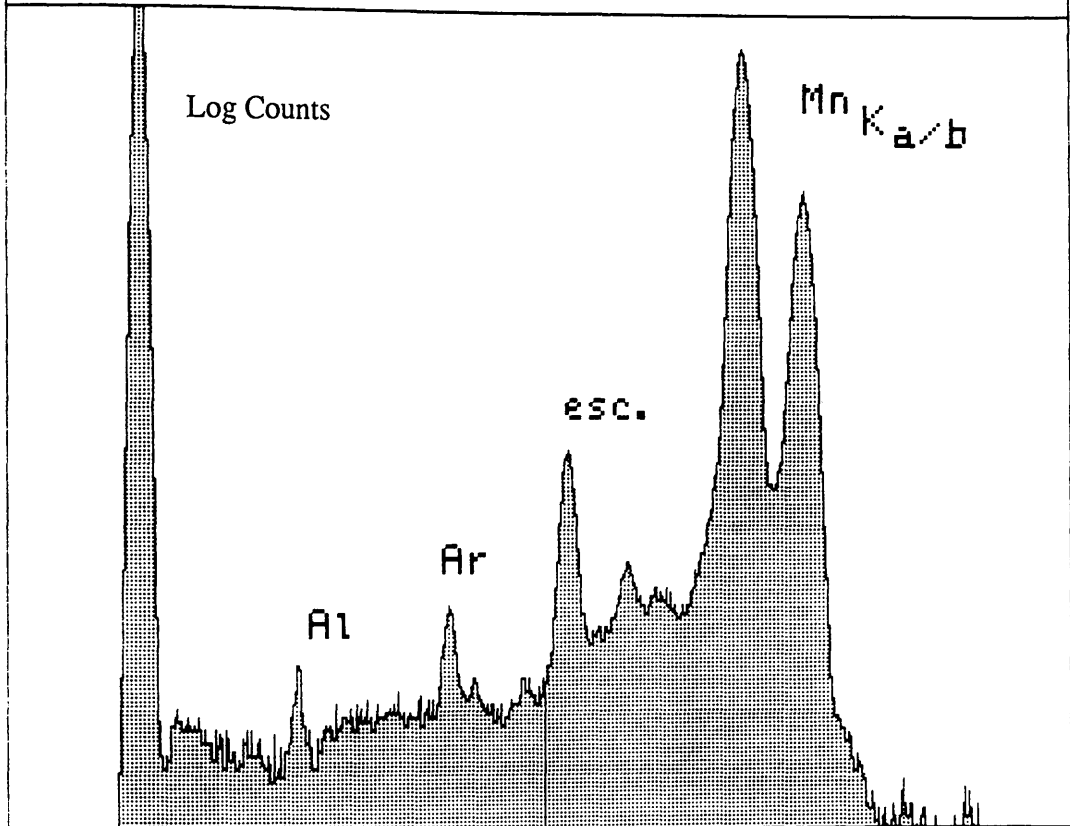


Fig. 5.1 JEM detector.

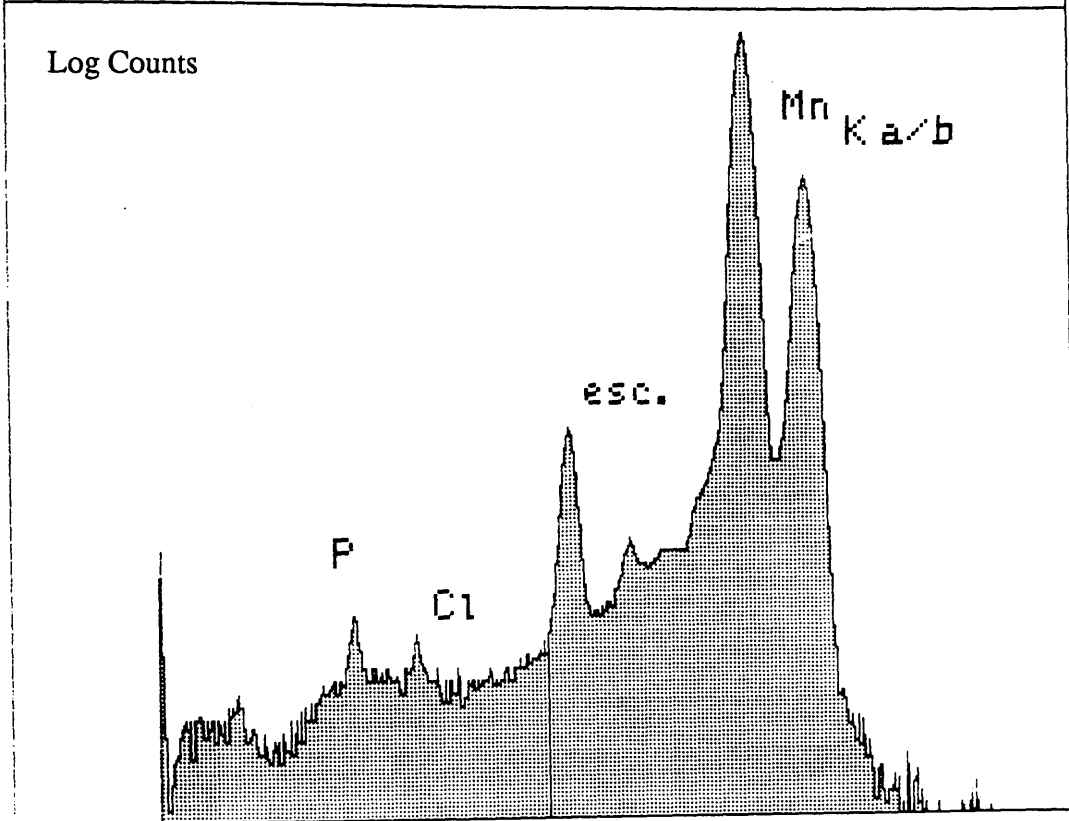
X-RAY: 0 - 20 keV  
Live: 10000s Preset: 10000s Remaining: 0s



FS= 32M LOG 3.920 keV 9.0 >  
MEM2: HB5 Detector. ch 206= 4089 cts

Fig. 5.2 HB5 detector.

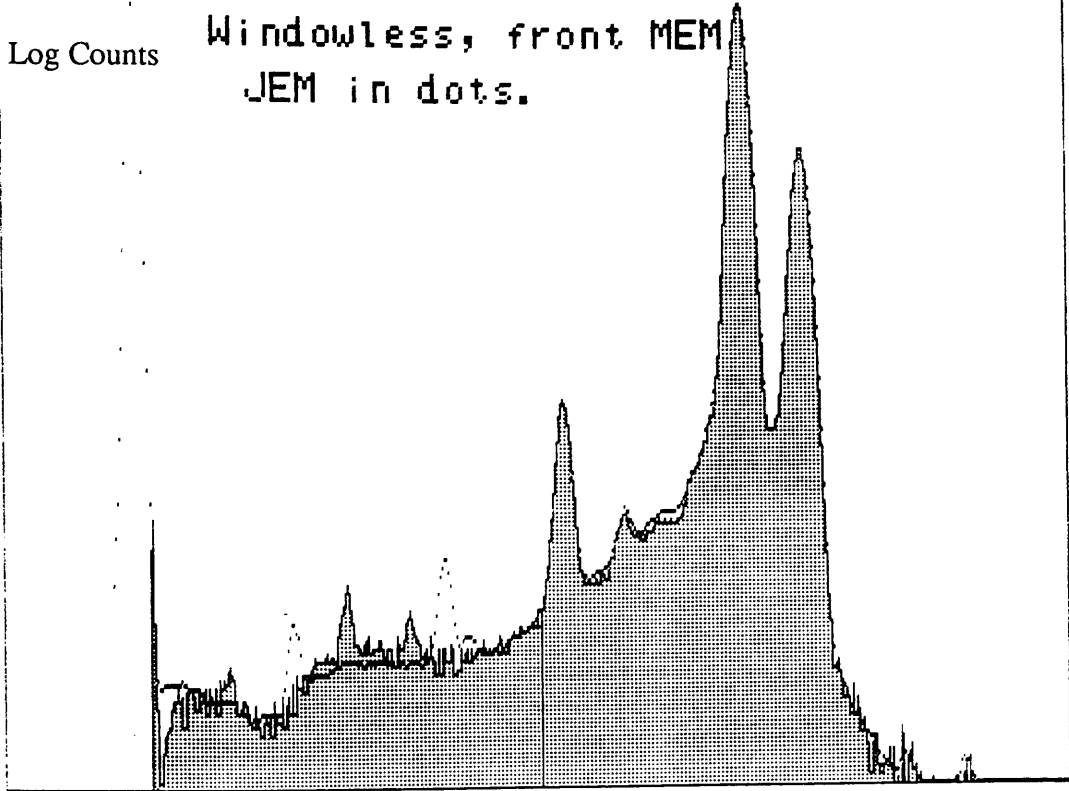
X-RAY: 0 - 20 keV  
Live: 10000s Preset: 10000s Remaining: 0s



3.920 keV 9.0 >  
FS= 32M LOG ch 206= 6927 cts  
MEM1: Windowless detector.

Fig. 5.3 Windowless detector.

X-RAY: 0 - 20 keV  
Live:10000s Preset:10000s Remaining: 0s



3.920 keV 9.0 >  
FS= 32M LOG ch 206= 6584 cts  
MEM1:Windowless and JEM /MEM2

Fig. 5.4 Comparison of the JEM and windowless detector.

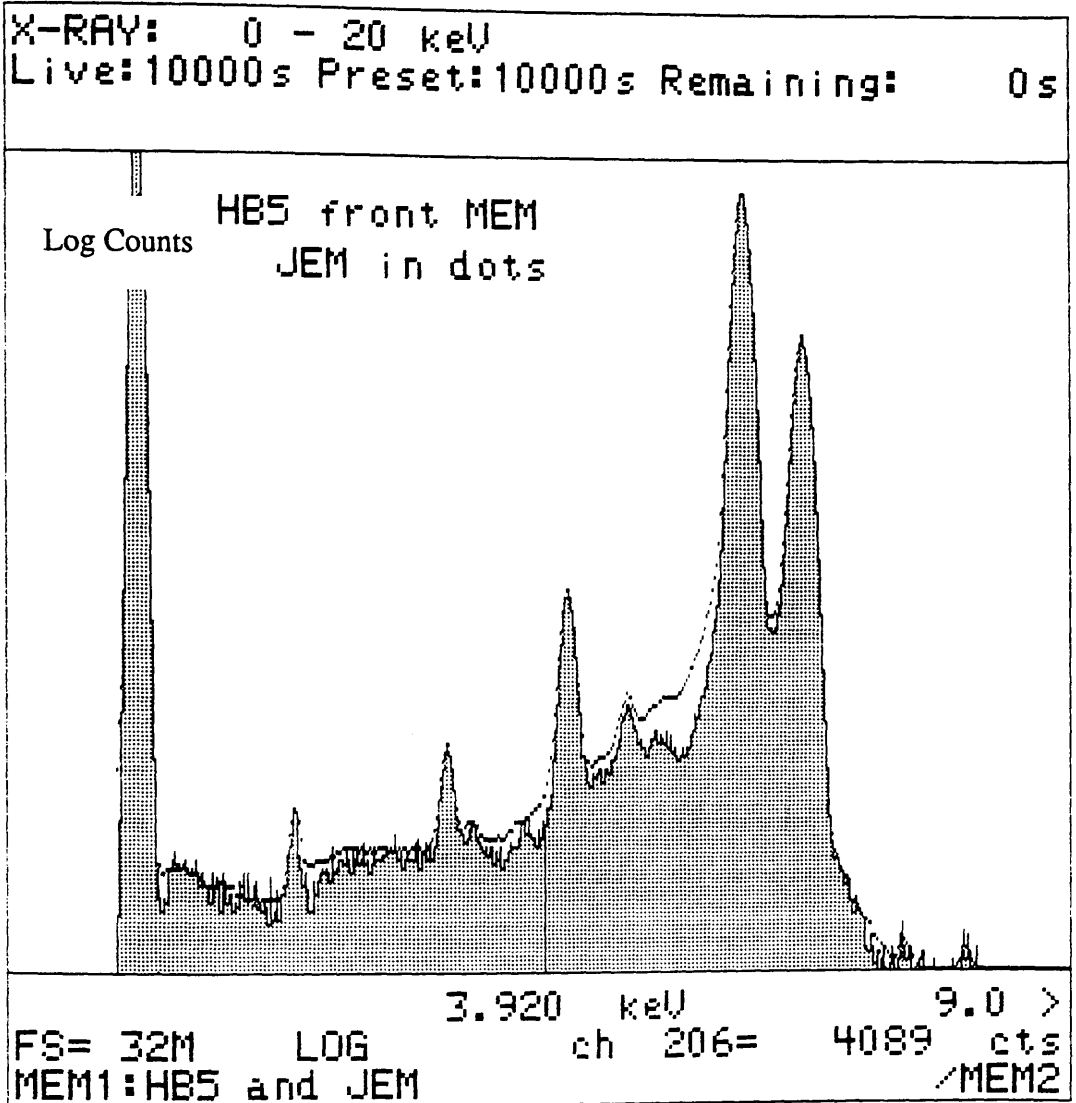


Fig. 5.5 Comparison of the JEM and HB5 detector's.

detector, which had not been used on a microscope, had approximately the same shape of ICC tail in the region close to the photo-peaks. Tolerances in detector manufacture may allow for such differences to exist in the ICC tail. However, this was an extremely small sample on which to base a firm conclusion.

At present there is no established method in describing differences between the ICC tails for different detectors. Manufacturers, such as Link Analytical quote a figure of merit by comparing the average background at 1.0 keV to the peak height at 5.9 keV in a manganese spectrum.

### 5.3 Microscope environment.

When a Si(Li) detector is being used on an electron microscope the detector is situated very close to the specimen. The crystal in the detector in use on the HB5 is approximately 2.5 cm from the specimen when fully wound in. When in such close proximity to the specimen, the crystal/FET is immersed in the strong magnetic field of the objective lens. For the HB5, this field can be as high as 0.3 Tesla at the detector. Under normal operation the detector is continually being subjected to large doses of radiation. X-rays of an energy up to 100 keV are incident upon the detector at all times when the microscope is in use and with the detector fully wound into the operating position. The actual dose of radiation which hits the detector is controlled by many factors, for example, the number of electrons incident upon the specimen, the type of specimen and the solid angle subtended at the detector.

As the electrons probe the specimen many will be backscattered. These electrons do not usually arrive at the detector because of the confining effect of the objective lens field. However, in the low magnification mode the objective lens is off or very weakly excited and electrons can hit the detector. In addition, detectors with high take-off angles are beginning to be used more frequently and these do not offer the same degree of protection to the detector from electrons since the confining effect of the objective lens field is not as effective. The term "normal use" within the confines of our research group often infers that the objective lens field is off; certain low magnification

applications necessitate this. This therefore allows scattered electrons to hit the detector even when wound back away from the specimen. Electrons incident upon the detector are known to cause short term perturbations in detector performance (Fiori and Newbury, 1978; Lowe, 1988). The effects of electron irradiation are therefore very important for Si(Li) detectors being used on electron microscopes. The electrons can have a kinetic energy of up to 100 keV for the microscopes used in our group. However, microscopes with accelerating voltages of up to 400 keV are becoming more common. The main differences between electron and photon irradiation is that the electrons can transfer more momentum in a collision with an atom than photons can. Electrons also give rise to bremsstrahlung in this collision process so electron irradiation is a combination of electron and photon irradiation since most of the electrons energy will be converted to bremsstrahlung during the collision with the beryllium window. Using very high energy electrons increases the probability of an electron passing through the beryllium window. In silicon, the energy below which an electron cannot transfer sufficient energy to displace a silicon atom from its atomic site is around 250 keV (Dearnaley and Northrop, 1966<sup>2</sup>). This implies that the electrons in a 100 keV electron microscope cannot cause displacement damage. However damage, which must therefore be caused by some other mechanism, is found for irradiation with 100 keV electrons; this is discussed in chapter 6.

#### 5.4 The effect of a magnetic field.

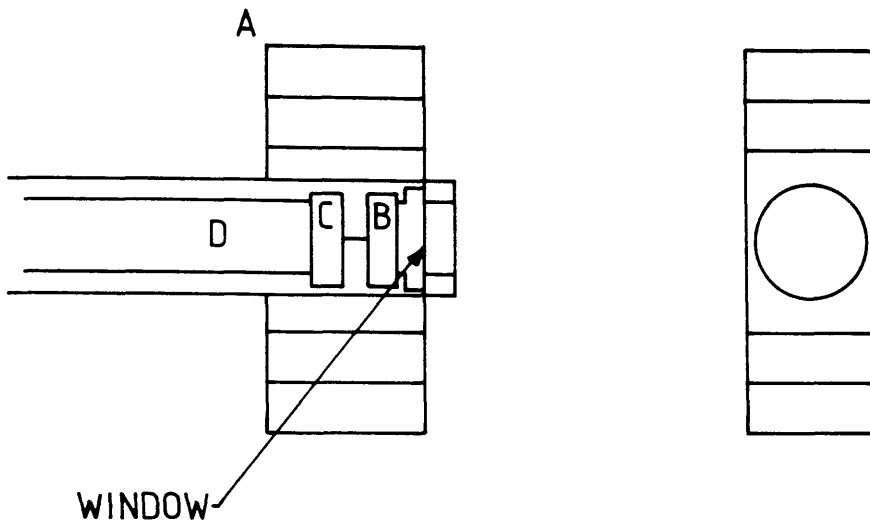
The idea behind these experiments was to study any changes to the ICC present in a manganese spectrum when the magnetic field was applied. Any effects which the magnetic field causes would be seen as a deterioration in either the photo-peak resolution and/or the level of ICC present in the spectrum.

The first set of experiments involved subjecting the detector to a magnetic field of comparable strength to that in the microscope. The first detector studied was the detector currently in use on the JEM 100C. The magnetic field was supplied by a set of SmCo<sub>5</sub> permanent magnets approximately 2.2 cm x 1.4 cm. The magnets were

separated by 1.8 cm by mounting them on a mild steel yoke. The field was localised to approximately this area and was measured (using a Hall probe) at 0.22 Tesla in the central region between the poles. No external collimator was used on the detector during this experiment.

A manganese spectrum was first taken without any magnetic field being applied. (this is usual procedure to check that the detector is operating properly). The first experiment was a check to see whether the magnetic field had any effect upon the spectra. When this was confirmed more accurate measurements were taken. These involved moving the magnets laterally along the detector tube in 1 cm steps. This was to indicate whether the field strength and the position at which the field was applied were important. The magnets were then placed at the position along the tube where the worst ICC was observed, this being directly above the crystal. Initially the magnets were set perpendicular to the tube, see fig. 5.6. Spectra were then taken with the field in eight azimuthal directions around the crystal. The magnets were removed and another manganese spectrum was taken. This was similar to the previous case without the magnets. To check for reproducibility the entire set of azimuths were repeated. The results were found to be totally reproducible.

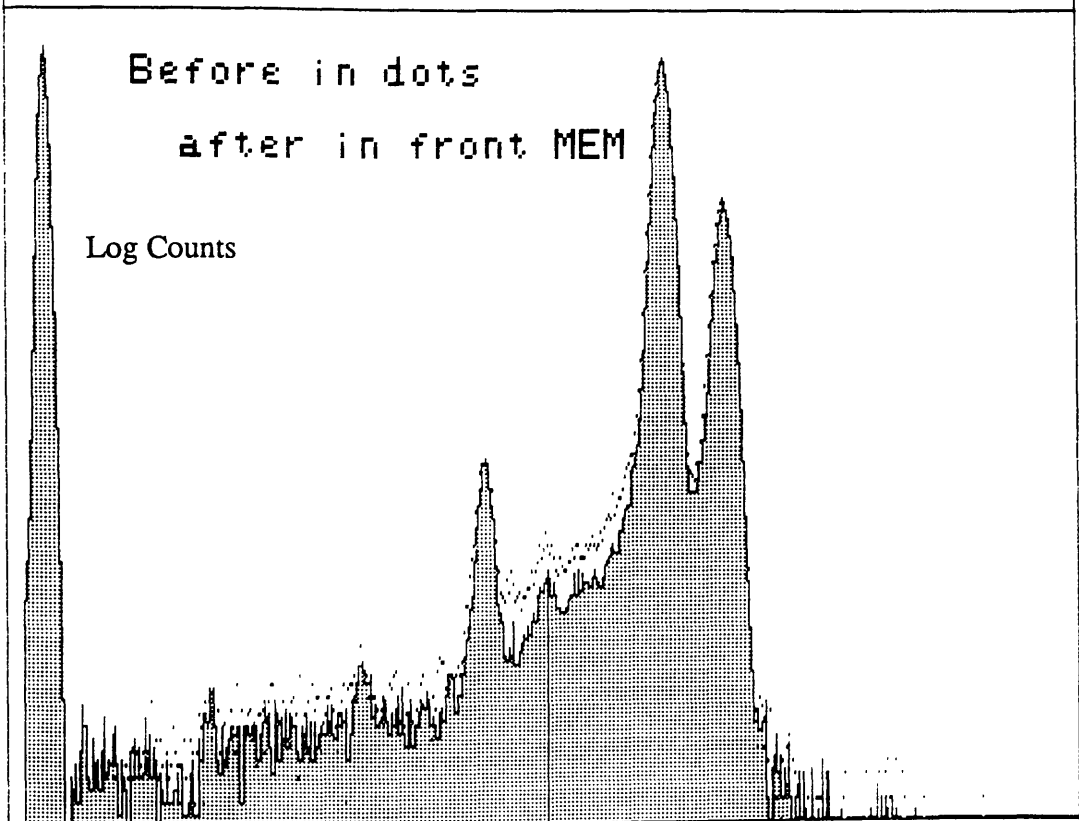
After the experiments described above were performed the bias was removed from the detector and it was allowed to warm to room temperature and left for approximately 24 hours. The detector was then re-cooled and the bias was applied. The performance of the detector was re-measured, with and without the magnets. After being warmed to room temperature the performance of the detector without the magnets was found to have improved slightly. This spectrum was used as a "bench-mark" with which to compare the other spectra. More importantly, after the warm-up the effects caused by the magnetic field had totally disappeared. Figure 5.7 shows the spectra before and after warm-up with no magnetic field applied. Figure 5.8 shows the difference between these two spectra. In both cases the spectra were normalised to the same gross number of counts ( $4 \times 10^6$ ). From fig. 5.8, the main difference between the two spectra can be seen as residual counts between the photo-peak and the escape peak. Below the escape peak the spectra show no differences other than some contamination peaks (probably caused by traces of specimens used in previous experiments with the radioactive



- A - MAGNET
- B - Si Li CRYSTAL
- C - FET
- D - COPPER COLD FINGER

Fig. 5.6 Experimental set-up for the magnetic field experiments.

X-RAY: 0 - 20 keV  
Live: 1200s Preset: 1200s Remaining: 0s  
Real: 1544s 22% Dead



4.760 keV 9.9 >  
FS=256K LOG ch 248= 129 cts  
MEM2: Before / after warm-up. /MEM1

Fig. 5.7 Comparison of the spectra from JEM detector before and after warm-up.

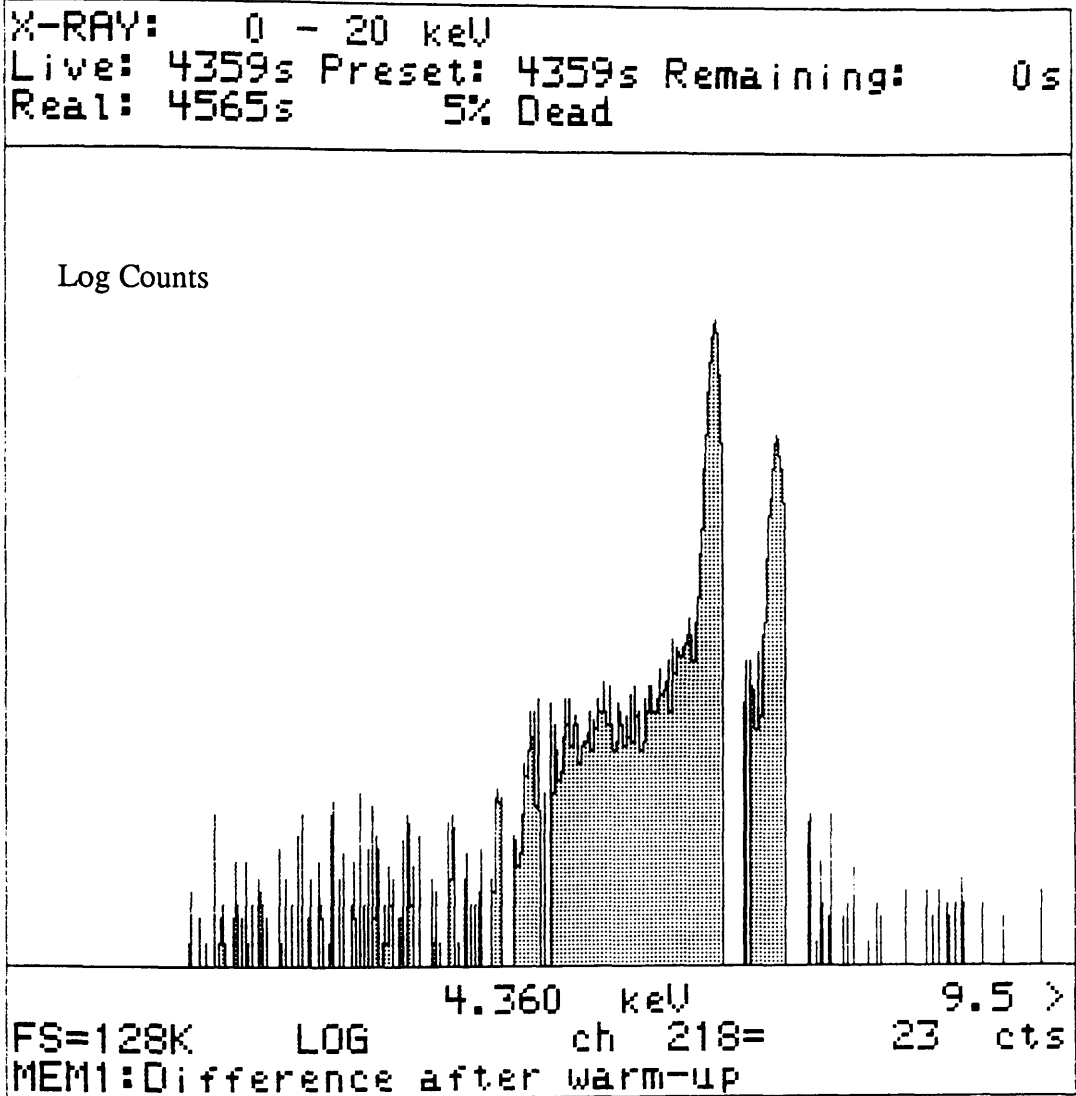


Fig. 5.8 Difference between the spectra shown in fig. 5.7.

source). Since these residual counts appear below the photo-peaks it appears they must be associated with an increase in ICC and hence a deterioration in detector performance. Figure 5.9 shows the changes as the magnet was moved along the snout. As the magnet was drawn away from the detector (negative directions) the effect caused by the magnet decreases. Going in the opposite direction firstly seems to increase the effect then it drops off as before. The reason for this increase is due to the magnet now being directly above the crystal. Figure 5.10 shows the changes for the different azimuths. The magnets can be seen to cause large changes in the ICC background at certain azimuthal angles whereas other azimuthal angles, those diagonally opposite, appear to cause little or no effect. The detector performance with the magnets at 225° is very similar to that without the magnet. In fact this azimuth actually improves the detector performance when it is compared to the spectrum acquired without the magnets and before the warm up.

The effects caused by the magnetic field are thought to be related to the deflection which the carriers undergo in the field (c.f. the Hall effect). The magnetic field causes the charge carriers to drift at an angle to the detector axis. Therefore it is possible for carriers to drift into peripheral regions of the crystal not otherwise accessible by a well collimated beam of x-rays. These peripheral regions may contain more defects and hence add to the overall level of ICC. The variation of the change in ICC around the crystal must therefore indicate the distribution of these defects.

Consideration of the forces acting on the electrons shows that the angle of deflection of the drift direction of the carriers is given by

$$\begin{aligned}
 \phi &= \tan^{-1}(F_B/F_E) \\
 &= \tan^{-1}(evB/eE) \\
 &= \tan^{-1}(\mu_C B) \qquad 5.1
 \end{aligned}$$

where  $\mu_C$  is the carrier mobility. For typical electron mobilities in silicon at 77K an

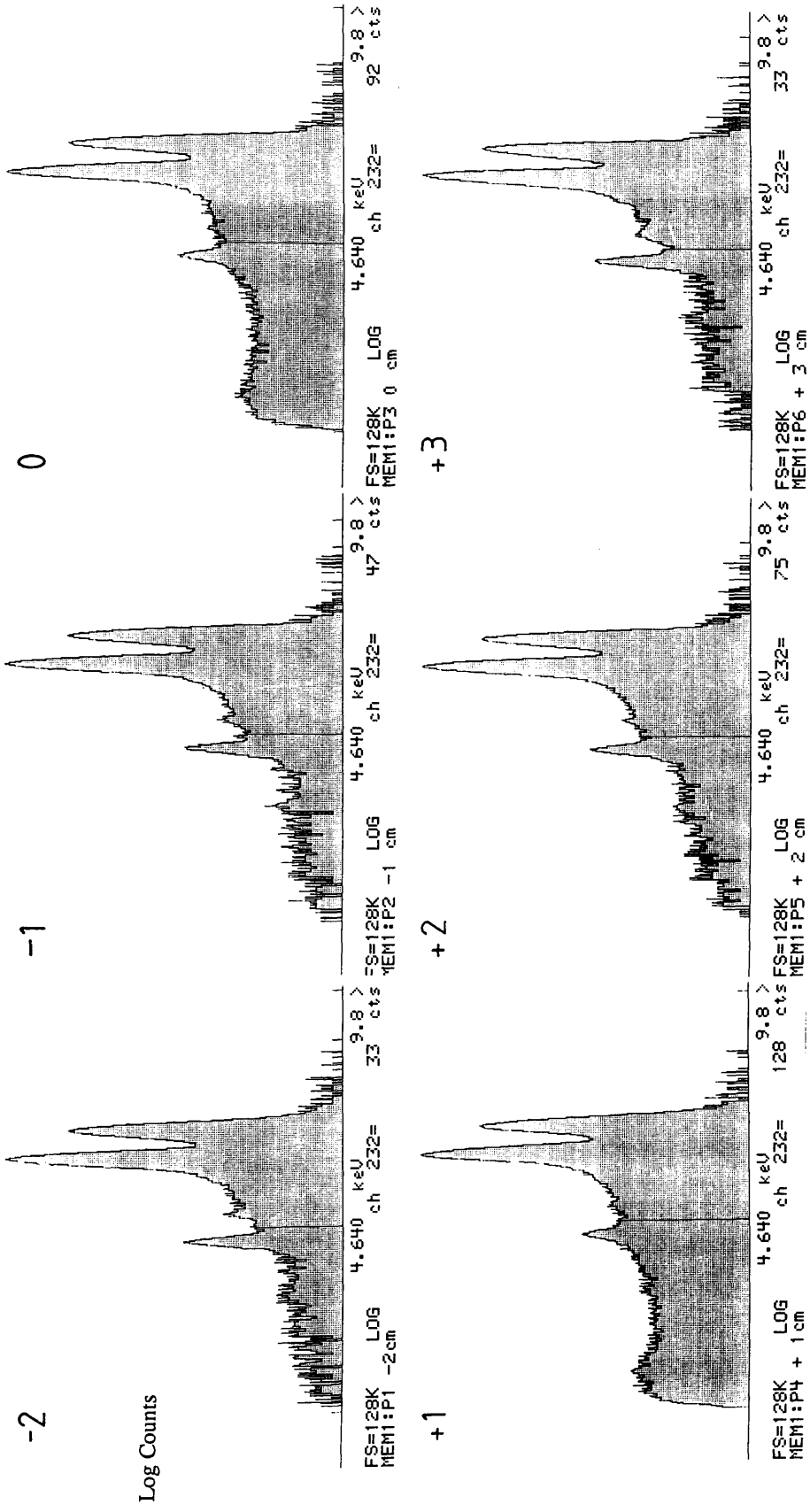


Fig. 5.9 Spectra taken at different positions along the detector tube.

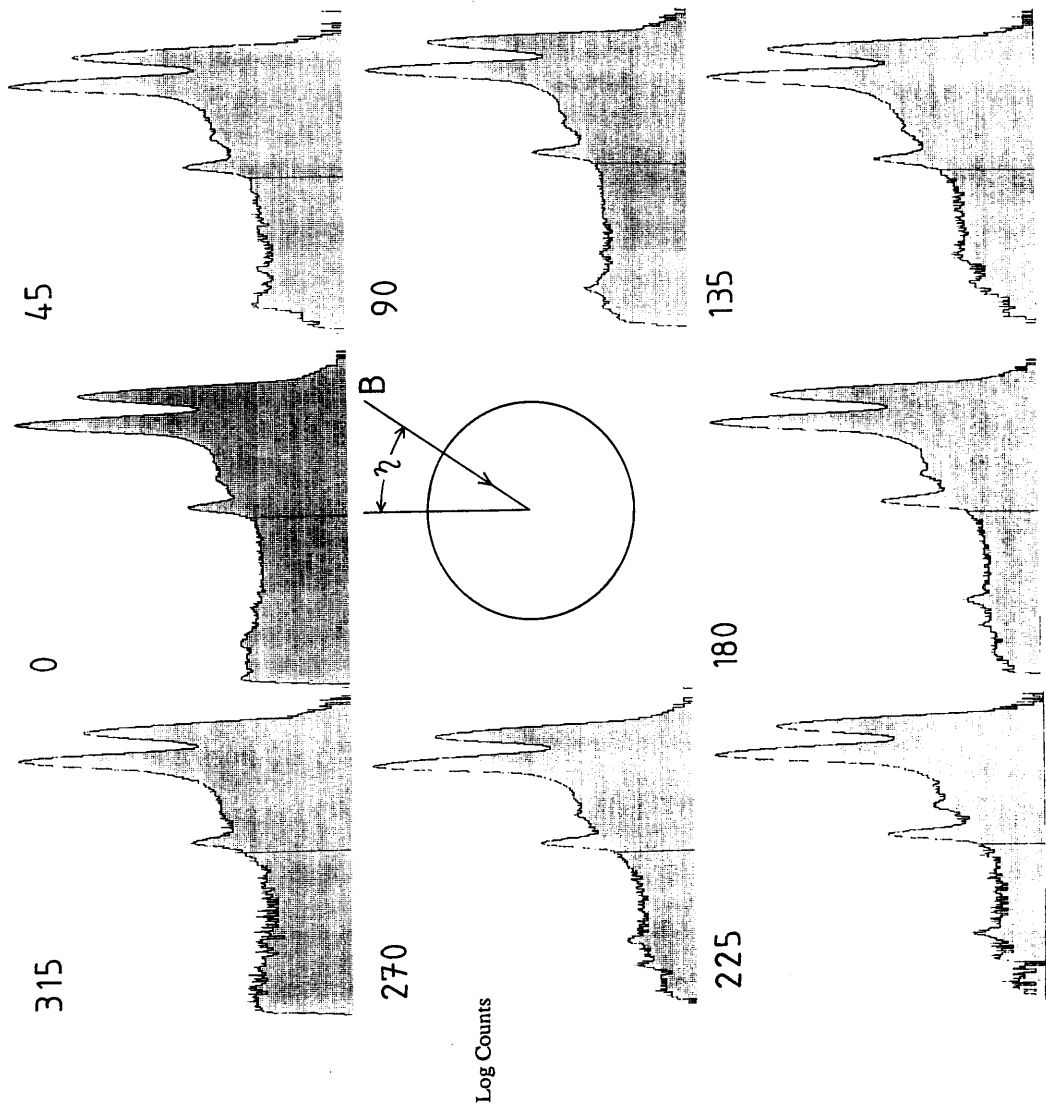


Fig. 5.10 Spectra taken at different azimuthal directions around the crystal.

order of magnitude estimate suggests a tilt of around  $20^\circ$ . Strictly speaking it should be the free electron conductivity tensors which are considered (Long, 1988) not simply the forces upon the electrons. However the same result is found for the more rigorous treatment.

Figure 5.11 shows a schematic of a section of the detector. The electric and magnetic field directions are shown as are the carrier deflections. An important point is that the electrons and holes both get deflected in the same lateral direction. This can be derived by considering the Lorentz force on charge carriers of opposite charge and with opposite velocities.

It would be reasonable to expect that if the x-ray source was tilted with respect to the detector then the peripheral regions of the crystal could be explored directly. Figure 5.12 shows the results for the source tilted at  $30^\circ$  to the detector axis. The diagram is arranged so that the tilt angle is in the same direction into which the magnetic field would deflect the carriers. The similar changes in ICC appear to confirm that it is peripheral defects that cause the effect. The reason for this is thought to be due to carriers being created under the internal aluminium collimator. It is in this region that the side traps probably exist.

Manganese x-rays have a very short absorption length in silicon, approximately  $30\mu\text{m}$ . Thus the lateral distance probed by x-rays from the tilted source is very small. For this reason the effects seen in fig. 5.12 must be caused by a different volume of crystal to those with the magnetic field applied. When a magnetic field is applied the carriers will suffer a deflection proportional to the drift length to the collection electrodes. The holes which are created near to the surface will therefore be deflected far less than the electrons. The electrons which have to travel almost the entire length of the crystal ( $\sim 3\text{mm}$ ) will therefore be deflected through large distances. An order of magnitude estimate for the electron deflection gives lateral displacements up to approximately 1.1 mm. It therefore seems reasonable to attribute the increase in ICC to these electrons being deflected into regions of the crystal where the trap density is high. If it is carriers being generated near to the periphery that leads to these "edge" effects then if the x-rays are highly collimated to the centre of the crystal very few x-rays will

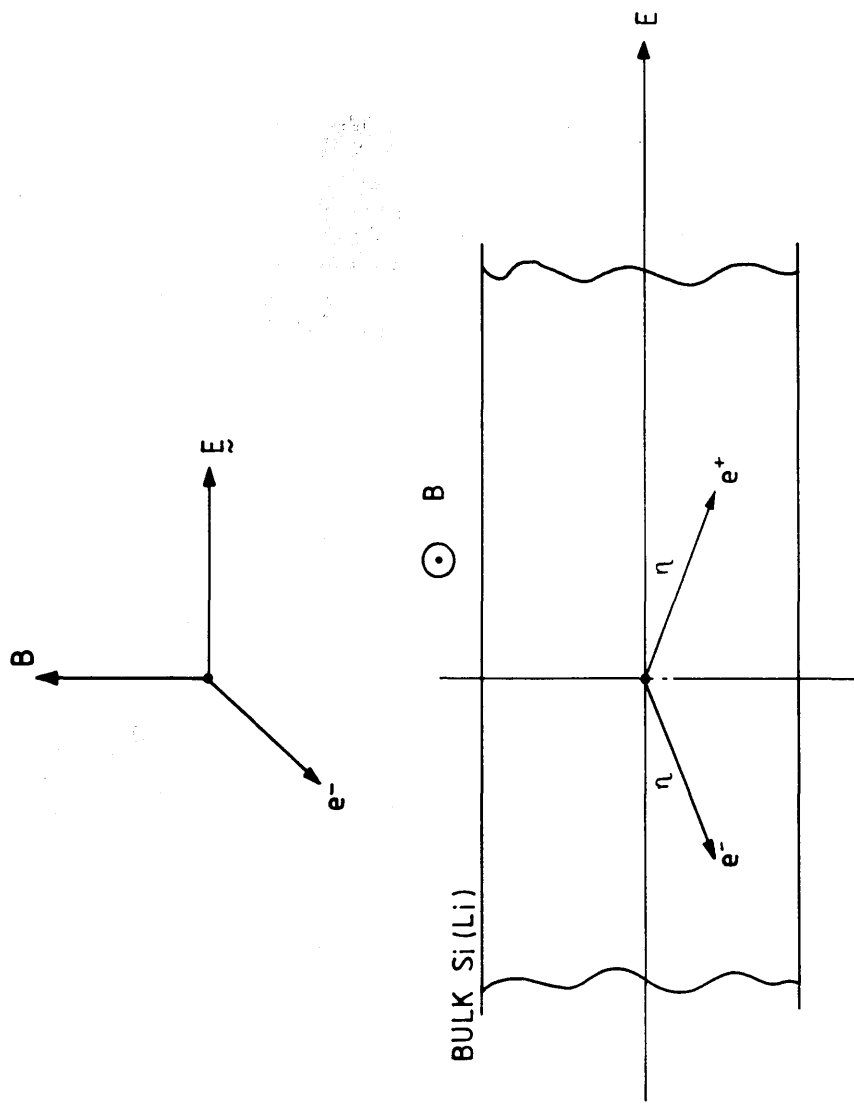


Fig. 5.11 Schematic showing the deflection of the carriers under the influence of an external magnetic field.

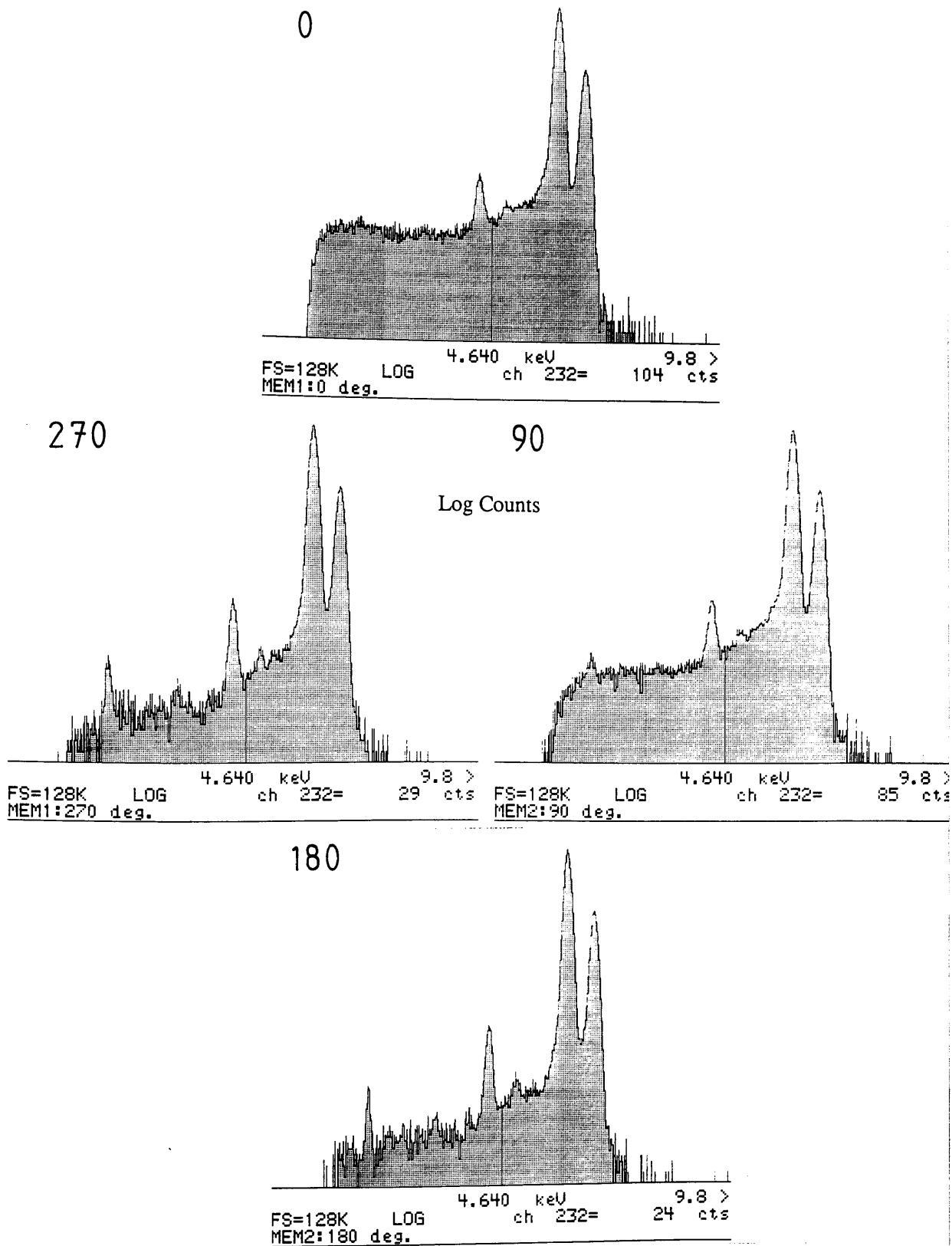


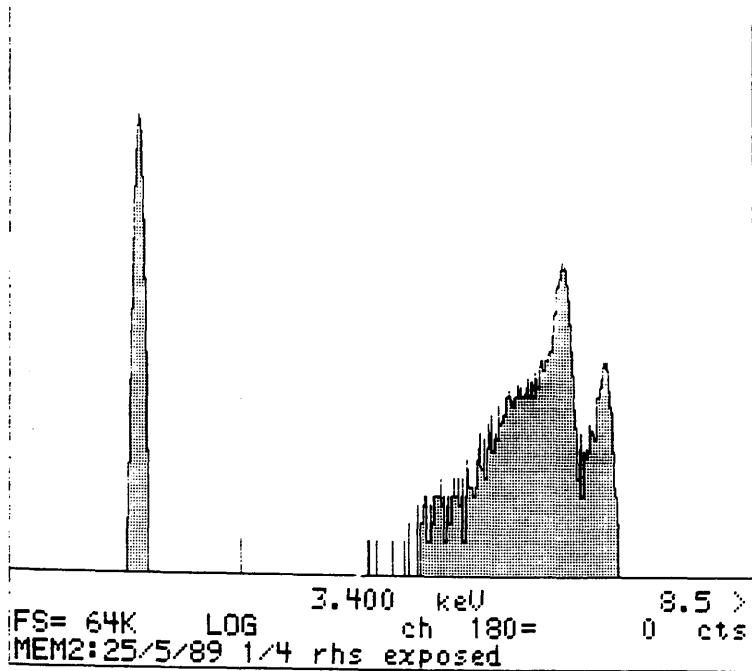
Fig. 5.12 Spectra showing the effect of tilting the source at  $30^\circ$  to the detector.

reach these regions and the magnetic field should make no difference. A lead sheet with a 0.5 mm hole was used to collimate the x-rays. This was first positioned so that the x-rays would hit the centre of the crystal, it was subsequently moved around so the crystal surface could be mapped for bad regions. The results showed that for the majority of the crystal's surface no difference could be seen. However, there was one region of crystal where the collection efficiency was never 100%. This was located at the top right half of the crystal looking into the detector. The spectra gradually reverted to the "well collimated case" as the lead shield was moved towards the centre of the crystal. Figure 5.13 shows the results for the two worst regions. This effect was found to disappear when the magnets were removed thus indicating that the bad region of crystal must exist under the aluminium collimator.

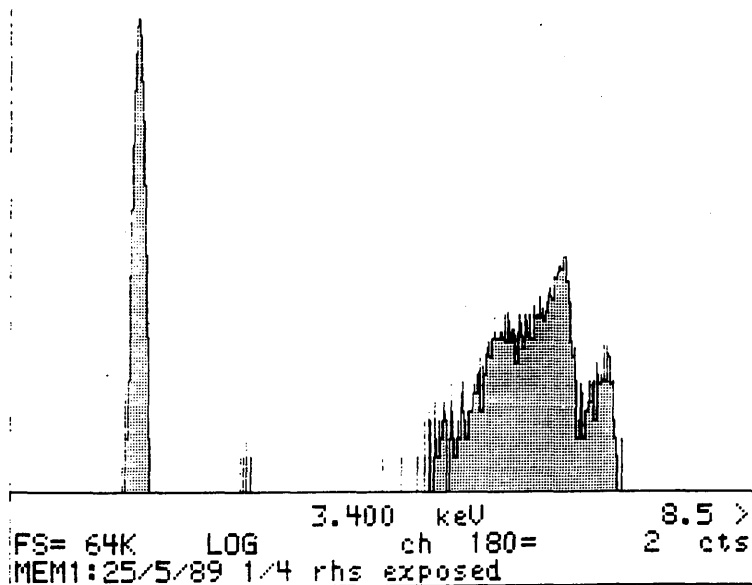
Finally, the bad region of crystal shown in fig. 5.13 was re-examined approximately 6 months later. This study revealed that this region had continued to deteriorate. Figure 5.14 shows a manganese spectrum for this region with the magnetic field in the 0° azimuth. The ICC can now be seen to be flat across the entire spectrum until peaking at the very low energy region. The reason why the crystal should deteriorate as such is not yet established.

### 5.5 Effect of irradiation on detector performance.

It was suspected that the irradiation the detector receives on the microscope during normal operation was the cause of the increase in the ICC levels. To test this hypothesis the detector was re-installed on the JEM 100C and both detector and microscope were used extensively for one week. The detector was then tested as before. The increase in ICC was again apparent for certain field directions, these directions corresponding to the directions previously found before the detector had been warmed to room temperature. In fig. 5.15 this effect is shown, here the spectra have had the bench-mark spectrum subtracted off to show the increase more clearly. To test this further the detector was re-installed on the JEM 100C and was used for two more months to acquire x-rays only. Figure 5.16 shows that the ICC has indeed continued to increase



Log Counts

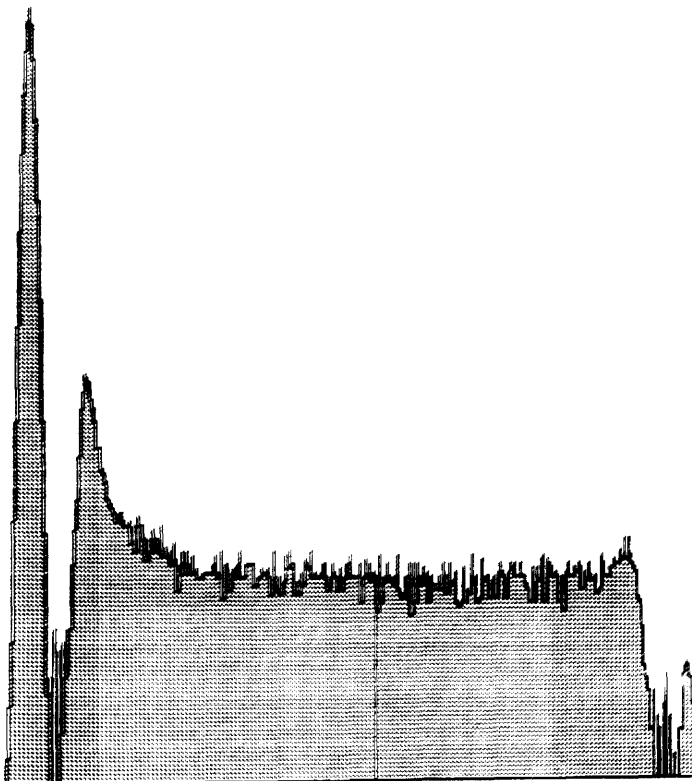


5.13 Spectra taken for the two worst regions of crystal.

Note, these are not difference spectra like some of those shown before.

X-RAY: 0 - 20 keV  
Live: 2540s Preset:25000s Remaining:22460s  
Real: 2825s 10% Dead

Log Counts



3.400 keV 8.5 >  
FS=128K LOG ch 180= 33 cts  
MEM1:20/1/90 JEM 0 DEG. EXT. RHS VIS.

Fig. 5.14 Spectrum taken for same region as those shown in fig. 5.13, taken 6 months later.

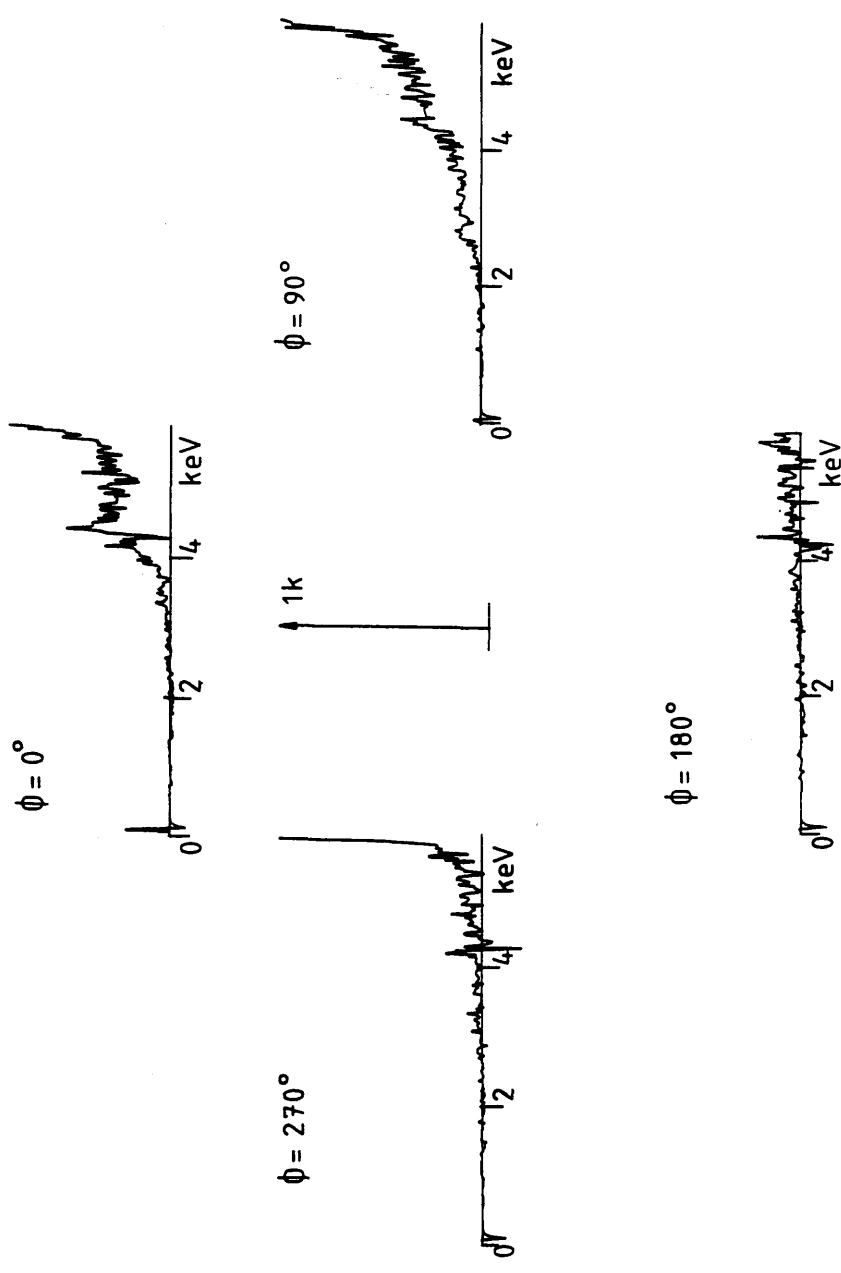


Fig. 5.15 Spectra taken after 1 weeks use upon the JEM.

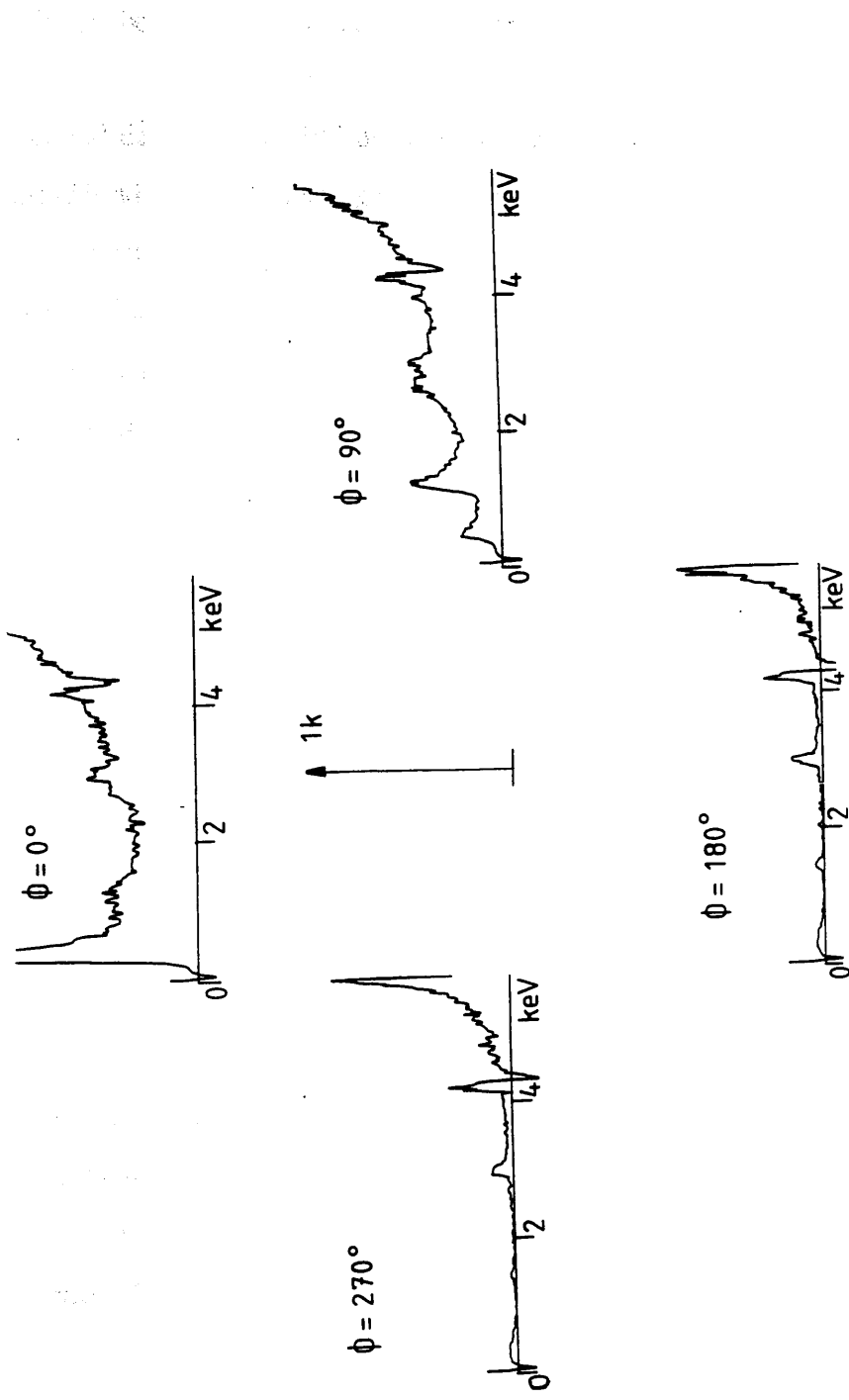


Fig.5.16 Spectra taken after 2 months further use upon JEM.

with the additional time of use on the microscope. In fact for the 0 and 90° directions the increase in ICC is worse than was found before warm-up.

### 5.6 On the bench performance of the HB5 detector.

A second detector, the HB5 detector, was also investigated, firstly by normal manganese irradiation with the magnetic field applied and then with the source tilted at 30° to the detector axis. No changes to the spectra could be observed for the case with the magnetic field being applied. When the source was tilted at 30° to the detector there was, however, some degradation which varied with azimuthal angle. This detector unfortunately developed a vacuum leak across the beryllium window and this limited the study. On return from the manufacturer the detector was tested with the magnetic field applied. The detector did not show any increase of ICC in these tests. These "as delivered" test spectra were kept for future reference and were used as comparison spectra for subsequent experiments, described in chapter 6.

It is important to emphasise that these experiments were actually performed before the spectra described in chapter 4 were acquired.

### 5.7 Detector irradiation by electrons.

The third detector studied in this series of experiments was a detector which had been previously used upon a Hitachi 300 keV TEM. As part of a research collaboration with Link Analytical, Dr. B. Lowe made available the results of a series of irradiation experiments that he had carried out. In these experiments the detector was irradiated with electrons from a 1 milli-Curie <sup>90</sup>Sr radioactive source. This <sup>90</sup>Sr source emits β's with energies up to 2 MeV plus a background of high energy bremsstrahlung. The detector was irradiated for approximately 4 hours with no bias being applied to the crystal. When the detector was tested with a manganese source the effect found was similar to that found on our detectors; there was an increase in ICC between the escape

peak and the photo-peaks. However in this case the extra ICC was considerably worse than had been found in our experiments. Figure 5.17 shows an example of a spectrum taken after 200 minutes irradiation with the  $^{90}\text{Sr}$  source. When a magnetic field was applied the ICC was found to increase in certain azimuthal directions. This again was similar to what we had found. Unfortunately no spectra exist for the effects caused by the magnetic field. Finally this detector was warmed to room temperature. Again after the detector was re-cooled and the bias applied, the aforementioned effects had disappeared.

## 5.8 Discussion and conclusions.

Although by no means general for all detectors, these experiments have shown that the three detectors that we have studied can be affected by irradiation. Whether this was electrons or photons is not yet established. In addition, the magnetic field associated with the objective lens can potentially affect the spectra since magnetic fields have been shown to be capable of deflecting carriers into poorer regions of the crystal, at the sides. This can cause a substantial increase in the ICC depending on the orientation of any poor regions of crystal with respect to the magnetic field.

It is thought that the high energy irradiation that the detector receives gradually degrades the detector performance. This degradation may be by the creation of traps within the crystal. Many of these traps must be situated in regions at the periphery. This can be deduced from the way the ICC increases in certain regions when a deflecting magnetic force is applied. Any traps in the centre of the crystal may be uniformly distributed but the high electric fields in this region do not allow these traps to capture carriers since the drift velocity is very large. For traps at the periphery of the crystal, the electric field is much lower (Lowe, 1989) and the reduced drift velocity in this region may lead to the traps being able to capture more carriers. In any case it has been shown that careful collimation of the crystal will remove any of the effects caused by the magnetic field.

The subsequent chapters will develop the ideas discussed in this chapter in more

Log Counts

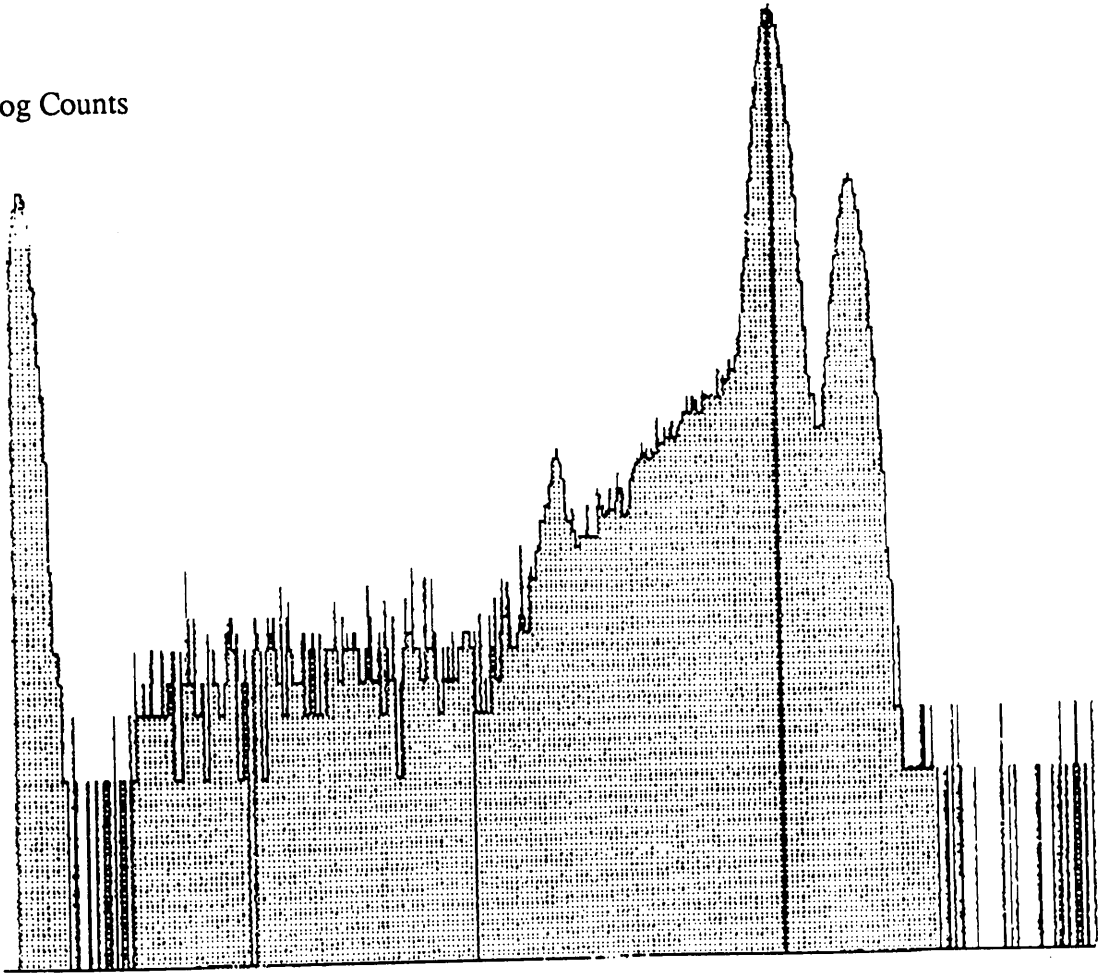


Fig. 5.17 Spectrum taken after 200 minutes irradiation with  $^{90}\text{Sr}$ . B. G. Lowe, Link Analytical.

detail. Chapter 6 further develops the idea of damage through irradiation by studying the effects that high energy photons have on the detectors.

## CHAPTER SIX

### Effect of High Energy Photons upon Detector Performance.

#### 6.1 Introduction

Chapter 5 discussed results which showed that the JEM detector suffered irradiation damage whilst in use on the JEM 100C electron microscope. This damage was unlikely to have been caused by backscattered electrons due to the confining effects of the microscopes objective lens. This chapter extends this investigation of irradiation damage by studying the effects of irradiation by high energy photons. The "after irradiation" performance of the HB5 detector was of particular importance, since it was the aim of this project was to investigate possible reasons why this detector should behave differently on the HB5. An extensive study was performed with both the JEM and HB5 detectors. Ideally both detectors should have been subjected to the same set of experimental tests. This would indicate whether both series E crystals behave the same after high energy irradiation. However, it was soon very apparent from the results that these two detectors were behaving very differently and this altered the experiments slightly. The JEM detector was studied first; again this was due to difficulties in obtaining the HB5 detector. This investigation showed that high energy irradiation had the opposite effect to that which we were looking for. The irradiation actually improved the JEM detector's performance. The performance of the HB5 detector was compared under similar experimental conditions. Here, the irradiation was seen to effect the detector in a way which could be used to explain why we obtained such poor electron generated spectra. This assumption was later proved to be correct when a separate investigation discovered the actual reason for the poor electron generated spectra. A third detector was obtained to continue the investigation. Unfortunately the beryllium window was broken before this study could be completed. Some results from this detector were obtained and these are briefly described since they show different

properties to the JEM and HB5 detectors.

## 6.2 The effect of high energy photons on the JEM detector.

In the microscope, bremsstrahlung photons of energies up to 100 keV are possible. Photons of these energies are very penetrating and the majority pass straight through the detector without any interaction. Those which do interact can be absorbed at any point within the entire crystal; all areas are therefore subjected to the very high energy photoelectrons which are produced. Sources of high energy photons which can be used with relative safety in the laboratory are fairly limited. The source used for these experiments was a 0.1  $\mu\text{C}$  americium ( $^{241}\text{Am}$ ) "variable x-ray source". This americium isotope emits alpha particles and gamma rays and is a source of several different x-rays. The alpha particles are absorbed in the stainless steel housing which the source is encased in, only the higher energy photons can escape. The principal emission is a 59.5 keV gamma ray photon, this constitutes approximately 36% of the output flux from the source. These gamma ray's are used to fluoresce secondary targets, it was the characteristic photons from these targets which were used in this investigation. For a full description of this source see appendix 3.

After the experiments described in chapter 5 were completed, the JEM detector had been replaced and used as normal on the JEM 100C. The following experiments took place approximately 6 months later.

After removal from the microscope, the detector was tested to check its performance at that particular time. This would indicate whether the previous six months use on the microscope had affected the detector in any obvious way. These tests simply involved taking a series of manganese spectra with and without an external collimator in place. The magnets were then used to test whether damage existed in the side regions of the crystal. These spectra were compared to reference spectra known to best represent this particular detector. The spectrum which was shown in fig. 5.1 is one of the reference

spectra. This spectrum was taken with an external collimator being used.

The results from these tests showed that those spectra taken with the collimator in place did not show any observable differences from the reference spectrum. Removing the collimator resulted in more counts being seen in the region close to the  $K\alpha$  photo-peak. This is a common occurrence for all Si(Li) detectors and is due to irradiation of the peripheral regions of the crystal. No obvious damage could be seen with the magnetic field applied, this having been done with and without the collimator in place. This result was thought of as being rather strange. This detector had previously been found to exhibit damage after use on the microscope (see section 5.5). It now seemed as though this effect had disappeared. The reason for this was eventually established and is explained later in this section.

The first experiment involved irradiating the detector with high energy photons. Terbium x-rays were used for the irradiation since these were the highest energy x-rays which could be obtained from the americium source. The fluoresced terbium x-ray spectrum is composed of three terbium K shell x-rays, with energies ranging from the 43.7 keV ( $K\alpha_2$ ) to 51 keV ( $K\beta_1$ ). The main constituent x-ray is the  $K\alpha_1$  at 44 keV. The spectrum also contains a small level of Rayleigh scattered gamma rays at 59.5 keV and some Compton back-scattered gamma rays with a mean energy of 48 keV. The x-ray spectrum from the terbium target is shown in fig. A3.6 (appendix 3). The detector was initially irradiated for several hours and no external collimator was used in order to maximize the count rate, this being approximately 950 counts per second. After the irradiation, the performance of the detector was retested with the  $^{55}\text{Fe}$  source and the magnets using the method described above. With the external collimator in place no difference could be seen in any of the manganese spectra. This was found to be the case whether the magnetic field was in place or not. Removing the collimator resulted in an increase in the number of counts close to the  $K\alpha$  photo-peak. This increase was approximately 3% greater (in terms of counts in the tail region alone) than the previous spectrum taken without the collimator. Spectra taken with the magnetic field applied,

but without the collimator, showed that the ICC had increased in a similar way to that found in chapter 5; see section 5.4. Figure 6.1 shows the spectra for the various azimuthal directions around the crystal. These can be compared with fig. 5.11 which shows that the same azimuthal directions are contributing to the ICC increase. This is perhaps not surprising being the same detector.

This increase in the ICC appeared at first sight to have been caused by the irradiation from the terbium x-rays. The fact that it could only be observed with the magnetic field applied and without an external collimator, meant that it must be an effect associated with the sides of the crystal. The subsequent experiments were to show that these conclusions were not totally correct.

The afore mentioned tests using the manganese x-rays were repeated in order to see whether the ICC had decayed in any way. The magnetic field was set for the  $0^\circ$  azimuth, a direction where the ICC was substantially different from the reference spectrum. This time however, the ICC appeared to be worse than in the previous case for this azimuth. This spectrum was taken approximately 130 minutes later than the first, during which time the detector had been used to collect the other spectra shown in fig. 6.1. To test this time variation more thoroughly the detector was left for a period of around 15 hours with manganese spectra being continually acquired for the  $0^\circ$  azimuth. The AN10000 was programmed to acquire a spectrum for 30 minutes, save it, then reset to acquire a new spectrum for the same time. This series of spectra showed that instead of a decay process, the ICC steadily got worse with time. Figure 6.2 shows a selection of these spectra with the relative time differences given, these times are with respect to the very first spectrum acquired in the  $0^\circ$  position. These effects were found to disappear when the detector was highly collimated or when the magnetic field was removed.

Information made available by the manufacturers (Lowe, 1988), had lead us to believe that this damage may disappear if the crystal was left unbiased for a short time. The bias was removed from the detector and it was left unbiased for 1 hour. The bias was re-applied and the detector was allowed to settle for 30 minutes (the recommended procedure after applying bias) after which the performance was again tested. The damage effects described above were all found to have disappeared. Without having

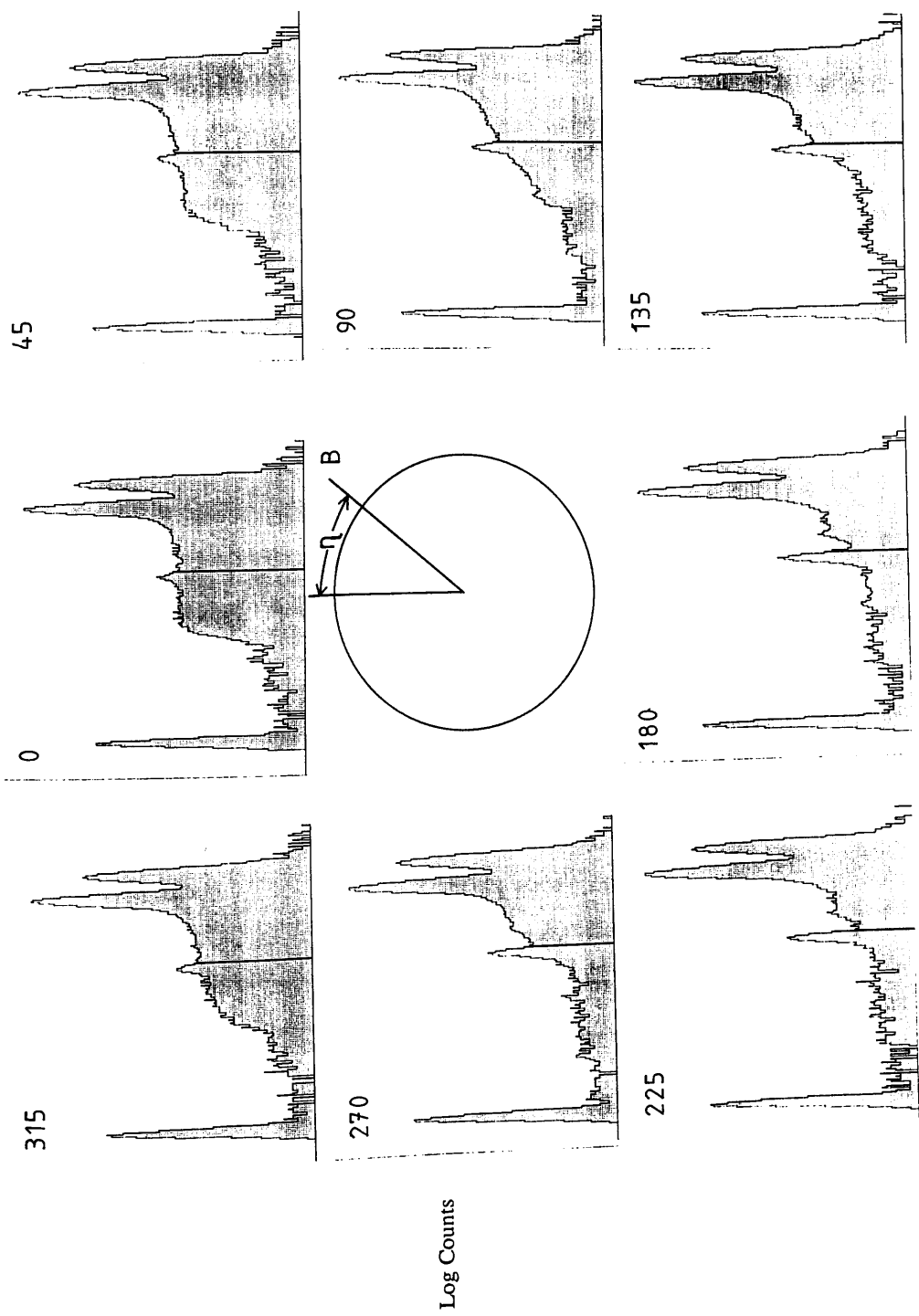


Fig. 6.1 Damage for the various azimuthal directions in the JEM detector.

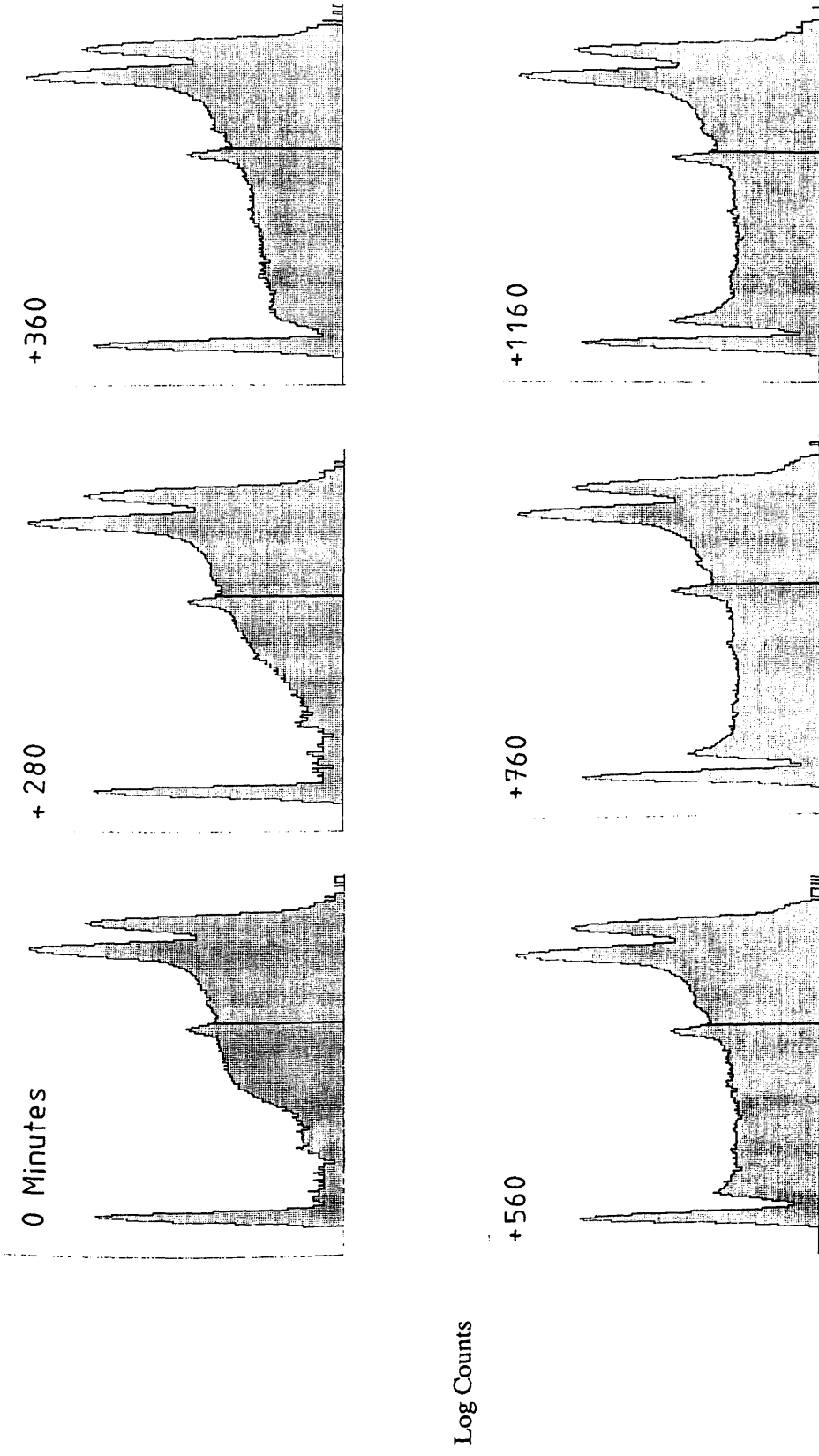


Fig. 6.2 Damage increasing as a function of time for 0° azimuth.

received any irradiation from the high energy source, the detector was studied by continual irradiation from manganese x-rays for a period of approximately 2 days. This also revealed that the ICC increased with time in a similar fashion to that which had been observed previously. Figure 6.3 shows a sequence of these spectra with the relative time differences given. These times are given with respect to time at which the bias had been re-applied. The bias was removed once more and the effects were again found to have disappeared. The next experiment tested whether the ICC would increase when the detector was left biased but with no photons incident upon it. This showed that after an equivalent period of time to the previous experiments (~40 hours), the level of ICC exhibited by the detector was the same.

These experiments have shown that this detector's performance deteriorates as a function of the time over which the bias had been applied. A magnetic field was the only requirement needed to show this effect. However, when highly collimated, the detector's performance was not seen to be affected in any way. Removing the bias for a short time also temporarily improved the performance. These results again show that it is in the side regions of the crystal that the damage manifests itself. Although this damage can severely affect the spectra, collimation to the centre of the crystal totally removes the effect.

It was eventually realised that these time dependent effects were being masked by secondary effects caused by the high energy source. A more detailed study of the effects caused by the terbium x-rays showed that it actually improved the detector performance by decreasing the level of ICC. If the detector is left for the ICC to build up to its maximum level, then irradiated with terbium x-rays, the detector performance improves to an extent which depends upon the duration of the irradiation. Figure 6.4 shows this effect in more detail. The spectra shown in this figure are manganese test spectra taken after irradiation by terbium x-rays for irradiation times of 0, 30, 60, 90, 120, and 1500 minutes. These spectra were taken with the magnetic field being set for the 0° azimuth. The irradiation can be seen to improve the performance. However, a limit is eventually reached beyond which no further improvement is achieved.

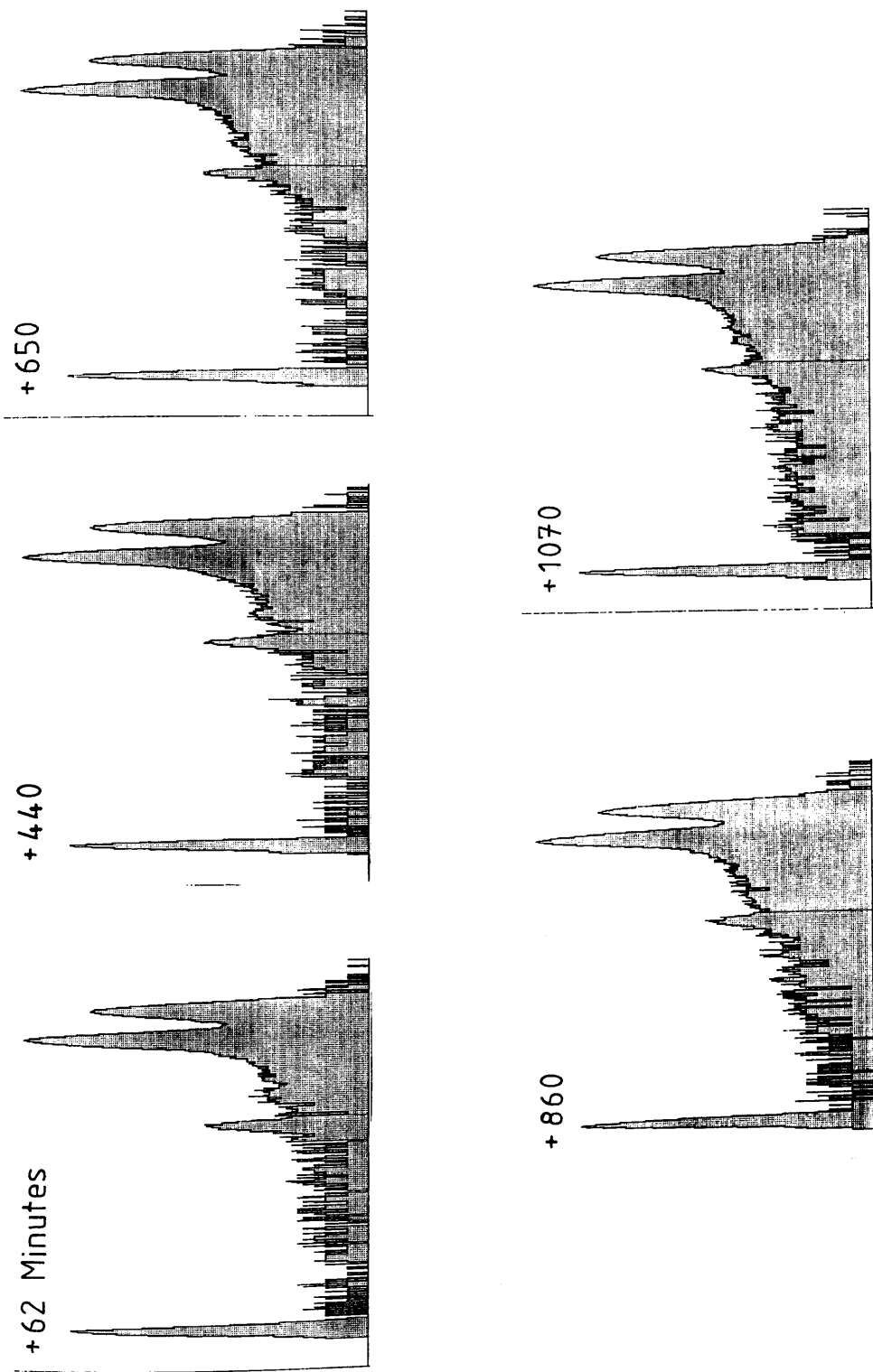


Fig. 6.3 Increase in ICC as a function of time for manganese irradiation only.

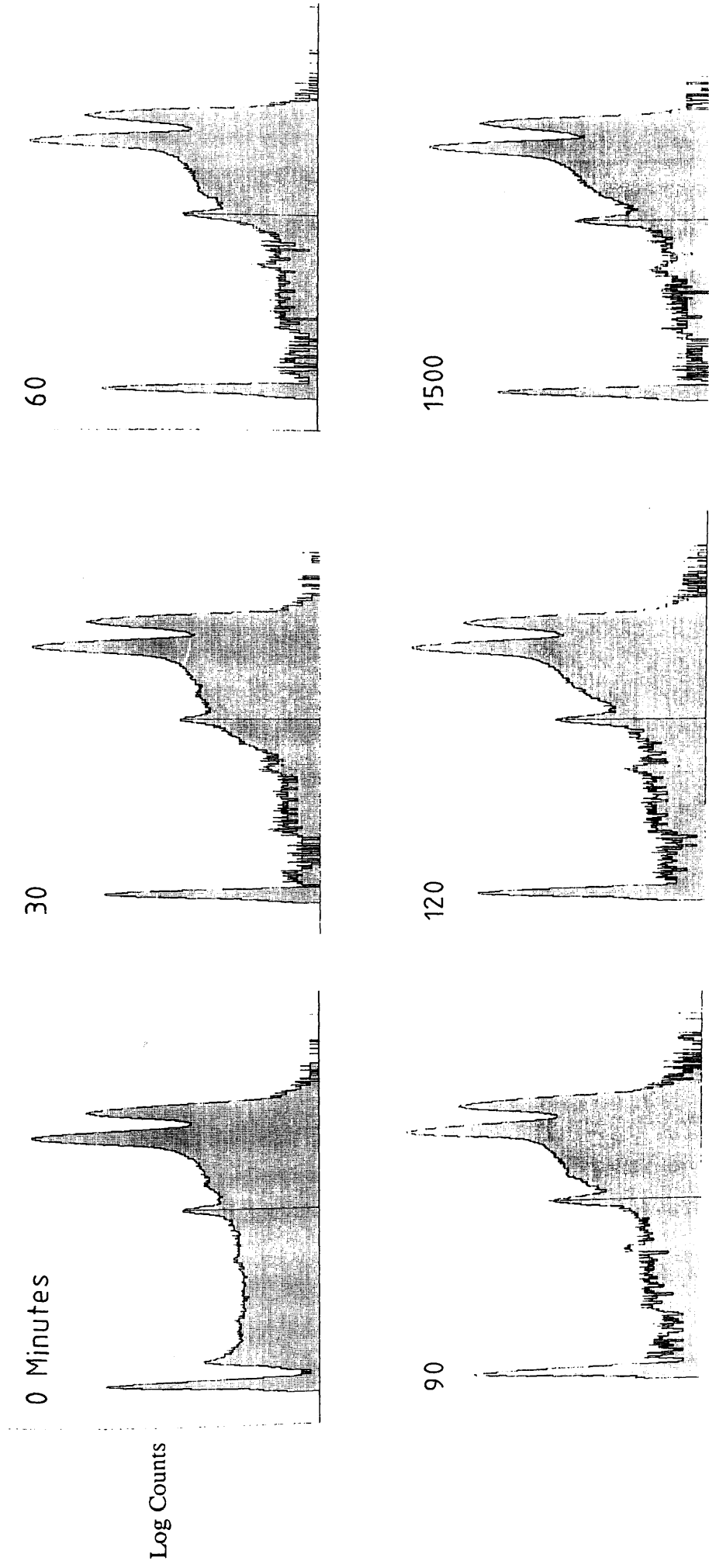


Fig. 6.4 Improvement of damage after terbium irradiations of 0, 30, 60, 90, 120 and 1500 minutes.

To analyse the ICC growth process, a reference spectrum (acquired without a collimator) was subtracted from each of the spectra acquired during the time sequence showing the ICC growth. It was then possible to study the growth of the ICC for this detector directly. Figure 6.5 shows a graph of the ICC, expressed as a percentage of the total number of counts in the reference spectrum, plotted against time. The ICC can be seen to remain constant for a short time (~300 minutes) before steadily increasing until arriving at a situation where it has apparently saturated. The region where the ICC increases can be seen to be similar to the situation for a capacitor charging from zero to a maximum voltage. A simple model can be set-up for this region. The increase in the level of ICC can be hypothesised to be caused by an increase in the number of traps or trap density  $N_{DAM}$ . This number of traps increasing with time. This increased level of traps must be added to a constant level of traps always present; these which give rise to the normal level of ICC seen in a spectrum,  $N_{NOR}$ . Therefore,  $N_t$  the number of traps at time  $t$ , can be approximated by the equation

$$N_t = N_{NOR} + N_{DAM}(1 - \exp(-(t-t_0)/\tau_G)) \quad 6.1$$

where  $\tau_G$  represents a constant which characterises the rate of growth of the number of traps and  $t_0$  is the time interval before this growth begins.

To study this in more detail, the detector was once more "reset" by removing the bias and the time dependent effects were studied for a far longer period of time. The results showed the same effect as that seen before, see fig. 6.6. This longer time of study (4 days) allowed an extrapolation to be performed so that an estimate for  $N_{DAM}$  could be obtained (ideally when  $t = \infty$ ). From the value of  $N_{DAM}$  (1.88% +/- 0.06%) it is possible to establish the value for  $\tau_G$ , the growth constant for this detector. If we let  $N = N_t - N_{NOR}$ , then substitute this into 6.1, then by simple algebraic manipulation

$$N = N_{DAM}(1 - \exp(-(t-t_0)/\tau_G))$$

$$1 - N/N_{DAM} = \exp(-(t-t_0)/\tau_G)$$

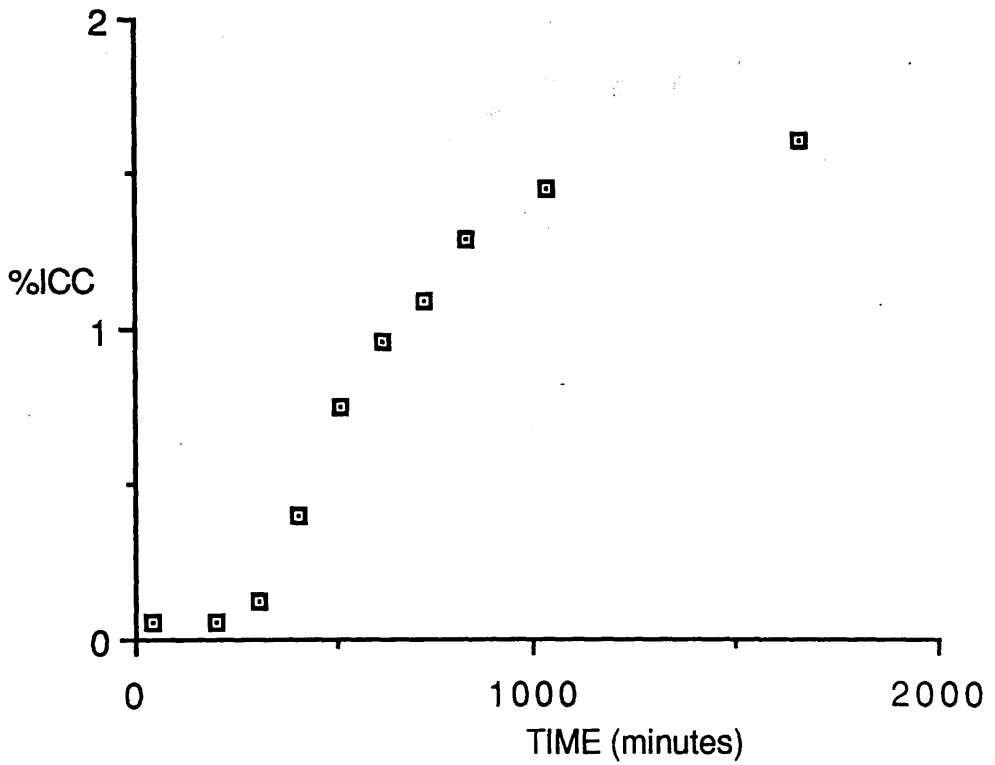


Fig. 6.5 Graph showing the increase of ICC with time for JEM detector.

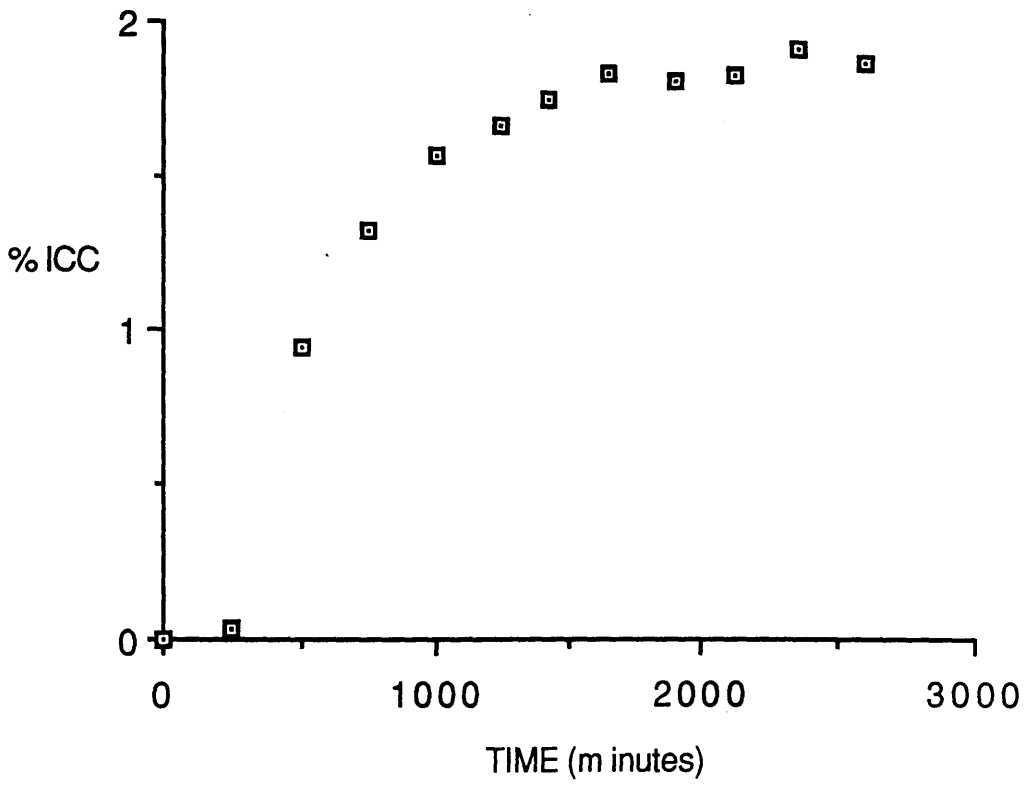


Fig. 6.6 Graph showing the growth of ICC with time, repeated for a longer time.

$$\ln (1 - N/N_{DAM}) = -(t-t_0)/\tau_G \quad 6.2$$

hence a graph of  $\ln (1 - N/N_{DAM})$  against  $t-t_0$  should give a straight line graph with gradient equal to  $-1/\tau_G$ , this graph is shown in fig. 6.7. The fact that this graph does not follow a perfectly straight line is an indication that the proposed equation of 6.1 does not represent the ICC growth process exactly.

A more careful analysis of the spectra shown in fig. 6.3 shows that the ICC in the region between the escape peak and the photo-peak (4.1 to 5.89 keV) grows at a faster rate than the ICC in the low energy end (200 eV to 1.6 keV). After a time of around 900 minutes the ICC in the high energy region appears to stay constant whilst the ICC in the low energy end suddenly grows, this is illustrated in fig. 6.8 where the additional ICC in the high and low energy ends has been plotted as a function of time. The additional ICC appears to grow in a way which gives the appearance of the ICC "travelling" down towards the low energy end. This can be seen in fig. 6.9 where a sequence of spectra are shown in which the low energy end grows whilst the remainder stays constant. This must indicate that a proportionately higher percentage of the carriers are being trapped each time. This must be caused by an increase in the number of traps.

It is difficult to interpret this effect. The fact that two different regions grow independently of one another, may indicate that two different effects are occurring.

The reason that no damage was observed after the detector was removed from the microscope can now be seen to be due to the fact that the bias had been removed. In addition, this detector has changed in some way which has caused the observed damage to grow as a function of the applied bias time. This effect must have occurred during the previous 6 months when the detector was on the microscope. The spectra shown in fig. 6.1 can now be explained by the time which the detector had biased applied and were not caused by the irradiation with the terbium x-rays. The terbium irradiation would in fact have kept the level of ICC at a lower level than would have otherwise

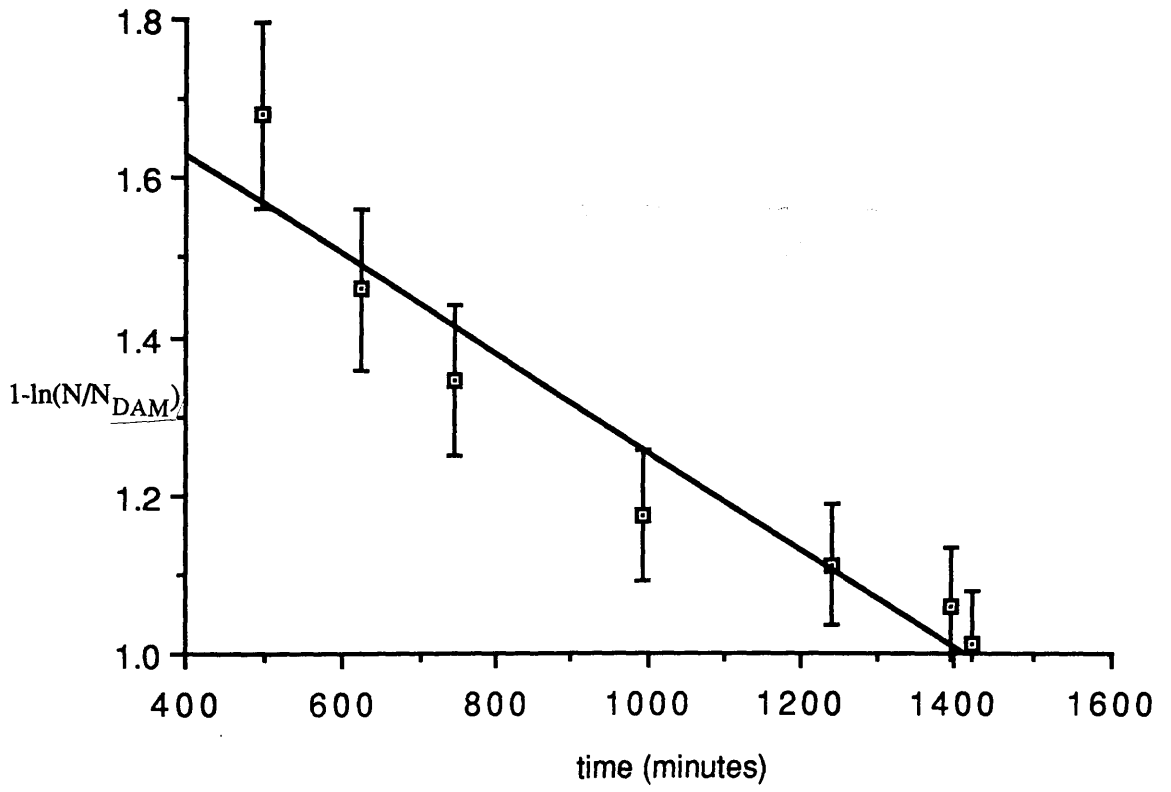


Fig. 6.7 Graph showing the  $\ln (1-N/N_{DAM})$  against time.

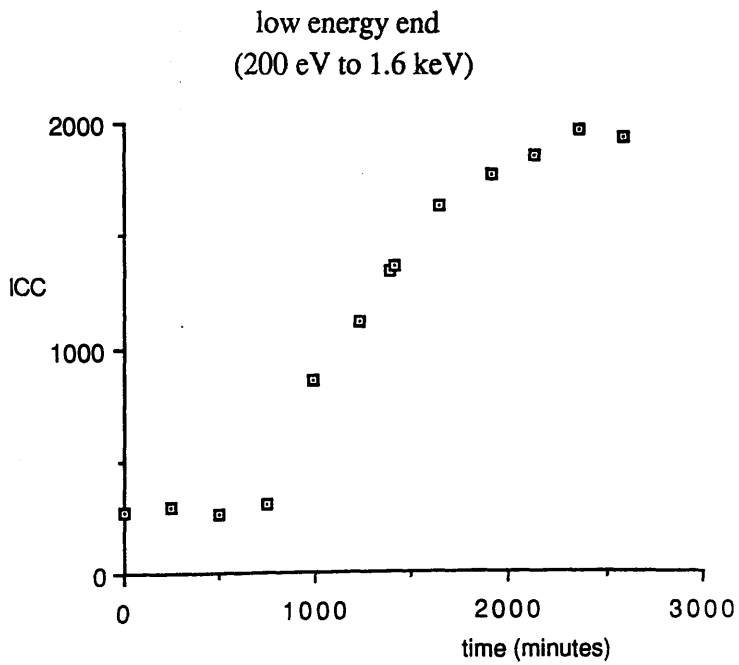
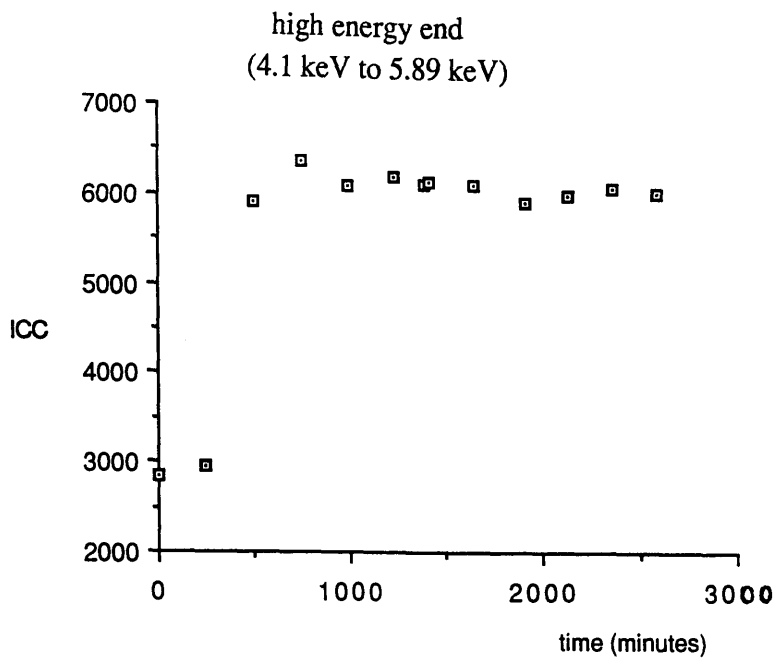
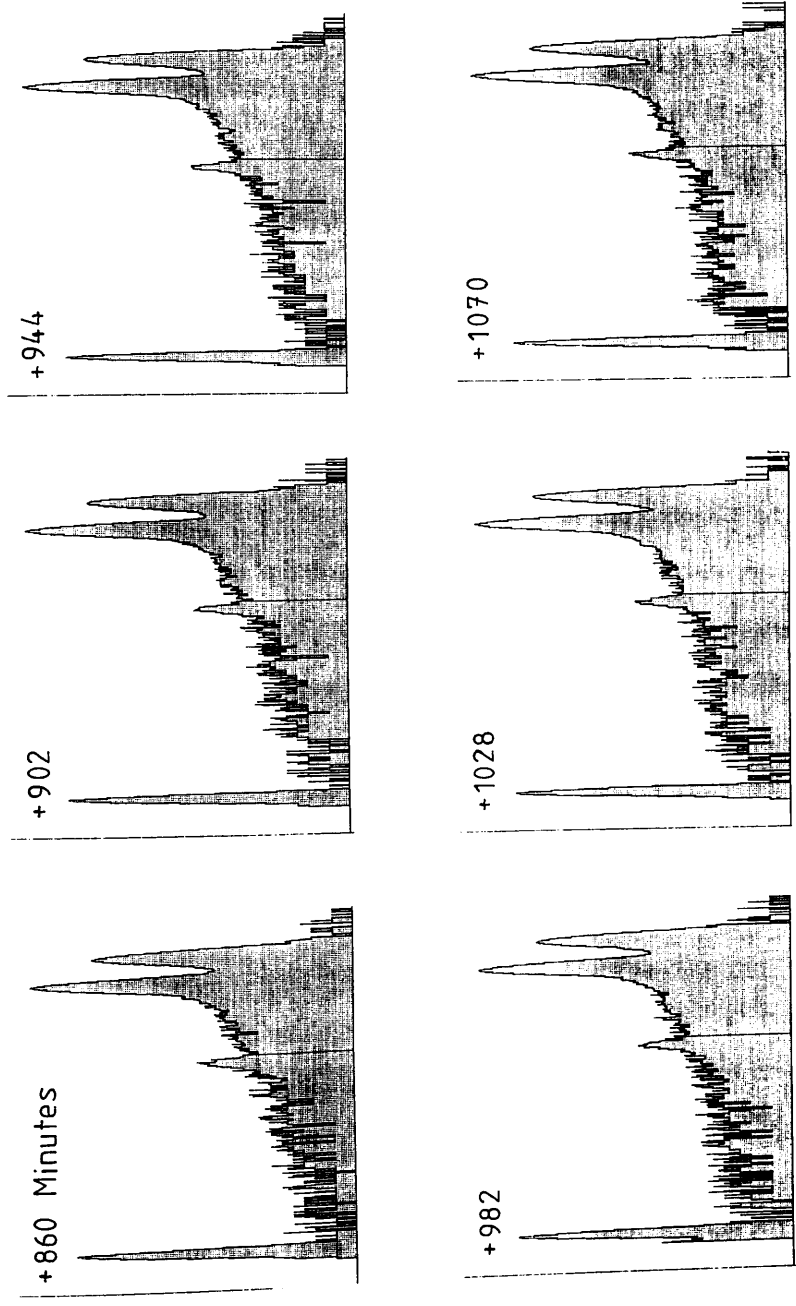


Fig. 6.8 Graph showing the way in which the high and low energy portions of the ICC tail develop with time.



Log Counts

Fig. 6.9 Series of spectra showing the ICC in the low energy region growing with time.

been seen. A possible explanation for this effect could be that the charge carriers, which can be created throughout the entire crystal by the terbium x-rays, temporarily fill trapping sites. These trapped carriers gradually de-excite and in doing so they allow more of the deflected carriers to be trapped. The majority of these traps must exist at the sides of the crystal since the magnetic field is required to produce any effects. Removing the bias must also have the effect of swamping all such traps with carriers.

### 6.3 Investigation of the HB5 detector.

The experiments performed upon the JEM detector had shown that the electron microscope can indeed affect the detector and that other effects can be caused by irradiation with high energy photons. It was therefore very important to extend this investigation to the HB5 detector since this was the detector which we were really interested in. Several months had passed since the electron generated spectra were taken, during this time the detector had been used on the HB5 as normal.

The first experiments tested the initial state of the detector. These were performed using the manganese source and the magnets as described in the previous section. The spectra which were obtained from this detector after the refurbishment of its window (see section 5.6) were used as reference spectra. The spectrum that is shown in fig. 5.2 was the spectrum used for any comparison purposes. The initial tests using the manganese source, with and without a magnetic field, did not show that any deterioration in the performance of this detector had taken place. Removing the external collimator resulted in an increase in the ICC close to the photo-peaks. This was no different to that seen in a reference spectrum taken under similar conditions. No magnetic field was required to produce this effect.

The experiments performed with the JEM detector had shown that the ICC increased as the bias time increased. To check this the detector was left for 4 days after which its performance was tested in the usual way. No difference was seen in any of the spectra taken. This result immediately indicated a major difference between the two detectors.

The hypothesis to which we were working, was simply that the microscope environment somehow affects the detector in a manner which lowers the collection efficiency of the carriers; hence causing an increase in the observed ICC. To test this idea the detector was irradiated with terbium photons and its performance was re-tested. This time we decided to initially leave on the external detector collimator throughout the entire set of experiments. This was slightly different to the experiments performed with the JEM detector, but would be more in keeping with the way the spectra were acquired on the microscope. The reason for doing this, was that the collimator had been in place throughout the acquisition of the electron generated spectra. This meant that the collimator does not prevent damage occurring. In addition, the JEM detector had also been seen to be damaged in the JEM 100C. This occurred when it too had a collimator in place. If no effects were seen with this approach then the collimator could simply be removed and the experiment repeated as was done for the JEM detector.

The detector was irradiated with terbium x-rays for 18 hours at an average count rate of 275 counts per second. This was the highest count rate that could be obtained with the detector collimator in place. The choice of 18 hours irradiation was made since it represented an equivalent number of photons incident upon this detector. After this irradiation the detector performance was immediately re-tested with the manganese source in the usual way. With no magnet field being applied a slight excess of counts could be seen in the region between the escape peak and the photo-peaks. Figure 6.10 shows the spectra before and after the terbium irradiation. This was similar to that seen in section 5.4 during the experiments with the detector on the microscope. When the magnetic field was applied a large increase in ICC could be seen, again this was similar to that seen in section 5.4. Figure 6.11 shows the spectra for eight azimuthal directions around the crystal. Once again this shows that in certain directions there is a large increase in the level of ICC, whereas in other directions, there is almost no difference. The effects caused by the high energy photons appear to only affect some areas of the crystal, this is similar to what had been found for the JEM detector. The fact that these effects can only be seen with the application of a magnetic field indicates that the damage caused only exists at the sides of the crystal.

X-RAY: 0 - 40 keV  
Live: 1368s Preset: 32000s Remaining: 30732s  
Real: 1486s 8% Dead

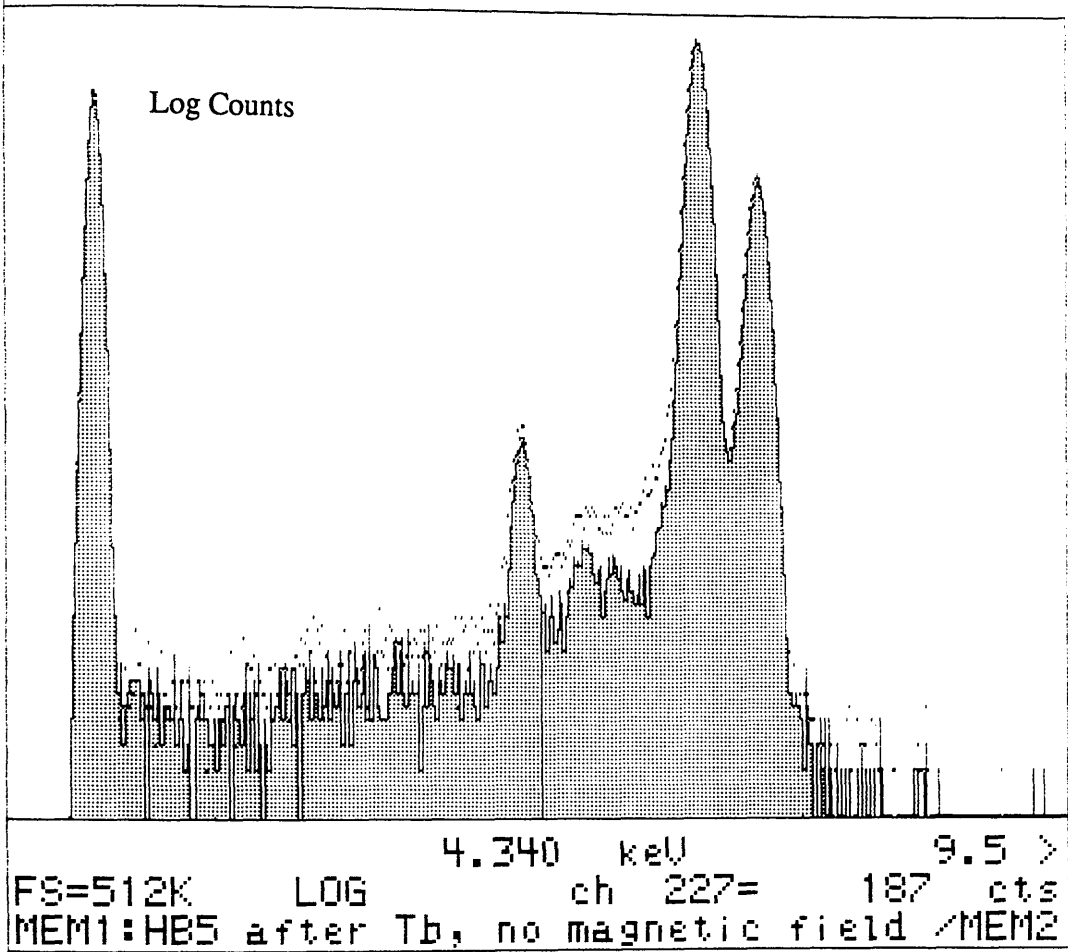


Fig. 6.10 HB5 detector before and after (in dot memory) irradiation with terbium x-rays.

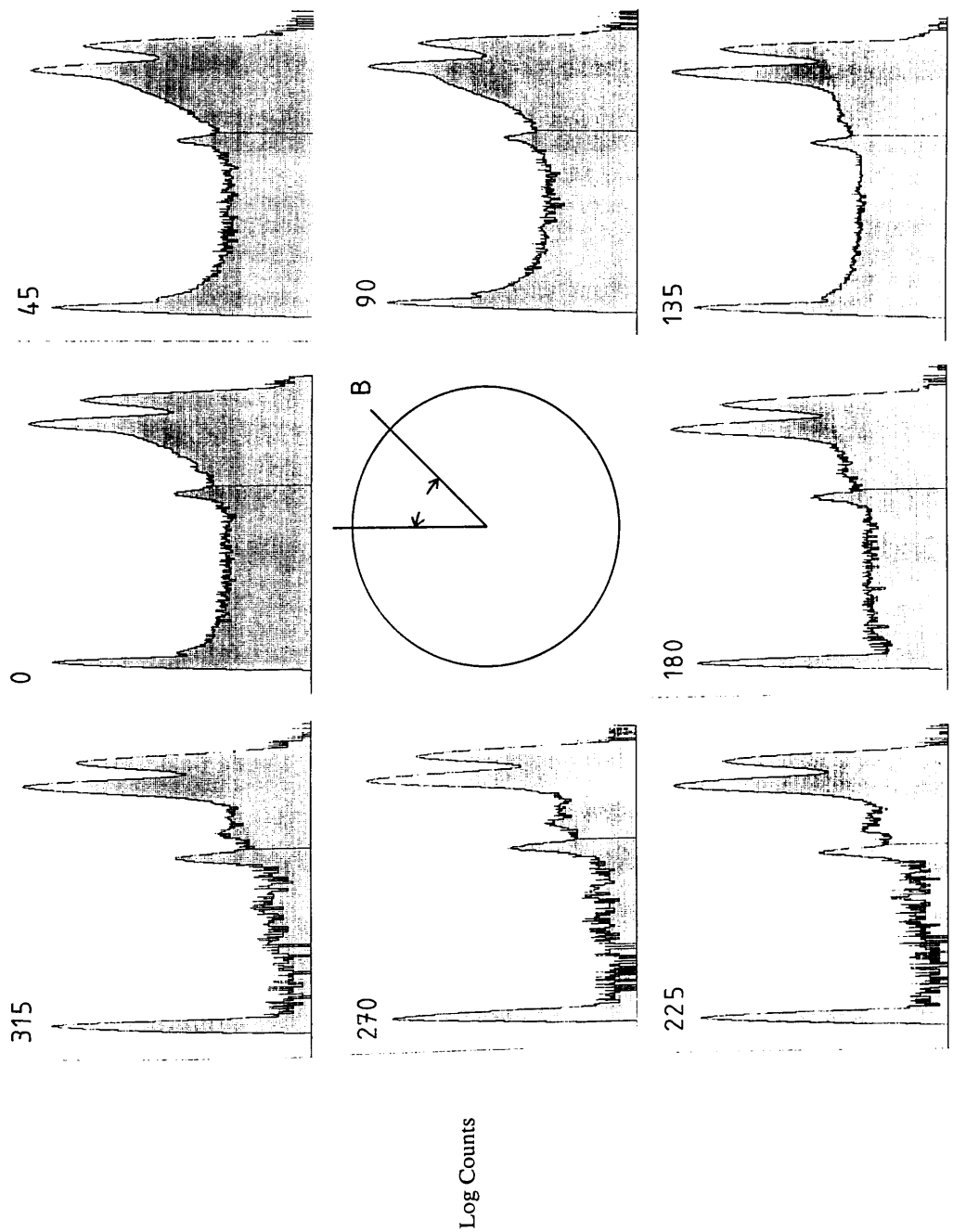


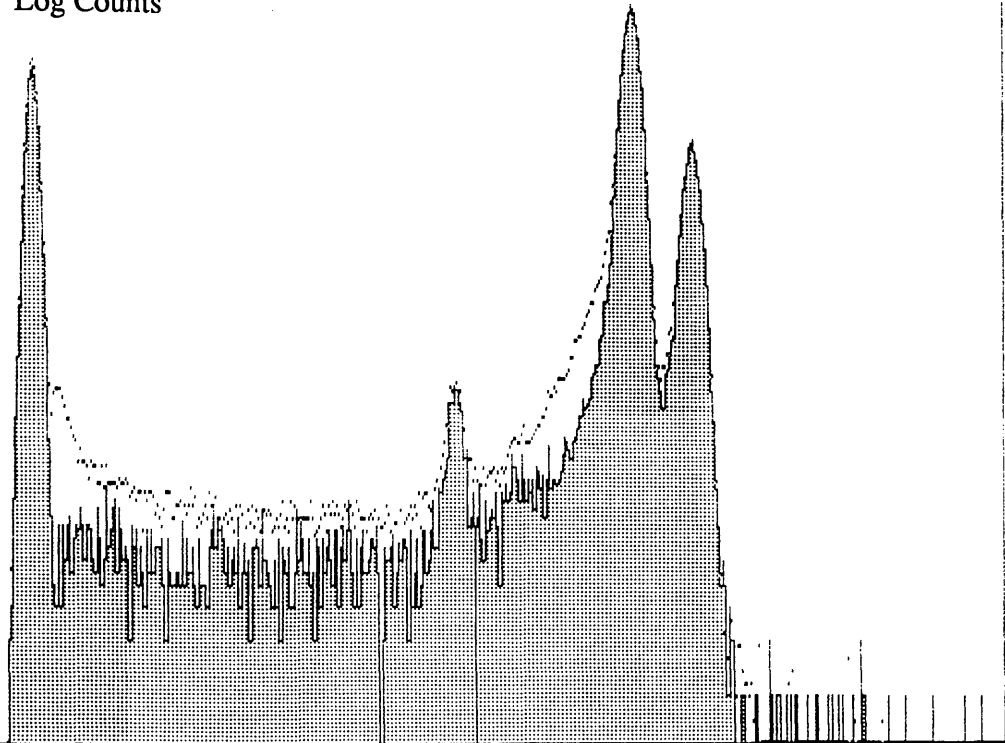
Fig. 6.11 Damage regions for the various azimuthal directions for the HB5 detector.

The test experiments were repeated to study what affect time had on the enhanced ICC. This time the ICC was found to decay slowly. Figure 6.12 shows this effect, here two spectra for the 0° azimuthal are given. These two spectra were acquired 5 hours apart under the same conditions. During this 5 hour period the detector had been used to acquire the spectra for the various other azimuths and had been left for around 2 hours doing nothing. The AN10000 was programmed to acquire a series of spectra, each spectrum being acquired for a 30 minute period then saved. In this way the detector was monitored over the next 48 hours to establish how long the decay lasted. This was found to be approximately 26 hours. Before the decay could be studied in any detail the detector had to be irradiated once more to bring back the damage. At this stage there were no results to indicate any relationship between the time of irradiation and the extent of damage. This was an experiment planned for a later date. To keep the experiments consistent, the irradiation time was made the same as for the first case, 18 hours. After the irradiation the detector was tested with the manganese source and the magnets to check the reproducibility of the irradiation process. Figure 6.13 shows a comparison between the respective test spectra for the 0° azimuth after the irradiations. It is obvious that the extent of the damage was not the same in each case. The reason for this is thought to be due to a slight misalignment of the terbium source resulting in a slightly different region of crystal being irradiated. The level of damage exhibited was still suitable for the decay experiment to be performed. This decay experiment involved a continual irradiation of the detector with the manganese source with the magnets at the 0° position. The AN10000 was programmed to save a spectrum every 30 minutes. Figure 6.14 shows 6 spectra at a regular interval over the decay sequence, the relative time differences are given with respect to the end of the high energy irradiation.

To analyse this decay, each of the spectra showing the effects of the enhanced ICC had the test spectrum for the "as new" detector (fig. 5.2) stripped off. The difference, expressed as a percentage of the number of counts in the "as new" spectrum, was plotted against time. This graph appeared to show an exponential decay and so was replotted this time taking the natural logarithm of the ICC, fig. 6.15. This straight line graph indicates that the total number of counts attributed to the enhanced ICC, decays exponentially with time, to a constant level, this being the ICC normally associated with

X-RAY: 0 - 20 keV  
Live: 300s Preset: 300s Remaining: 0s  
Real: 328s 9% Dead

Log Counts

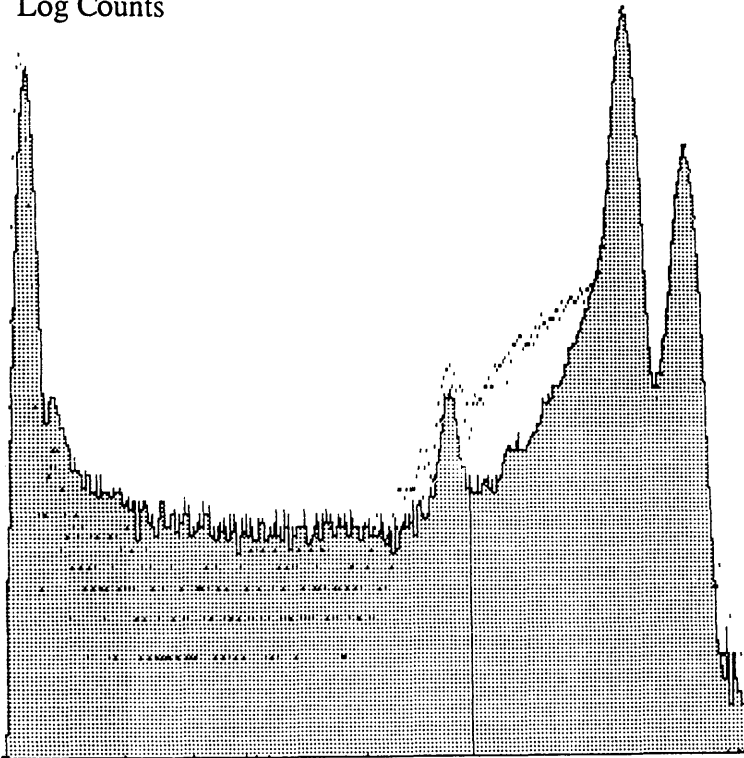


2.070 keV 4.6 >  
FS=128K LOG ch 227= 45 cts  
MEM1:Decay of damage, 5 hours apart /MEM2

Fig. 6.12 Decay of the damage for the 0° azimuth.

X-RAY: 0 - 40 keV  
Live: 1531s Preset: 32000s Remaining: 30469s  
Real: 1672s 8% Dead

Log Counts



4.340 keV 9.5 >  
FS=128K LOG < 1 ch 227= 100 cts  
MEM1: Comparison of damage effect /MEM2

Fig. 6.13 Comparison of the  $0^\circ$  azimuth after two different terbium irradiations. Dot memory represents the second irradiation.

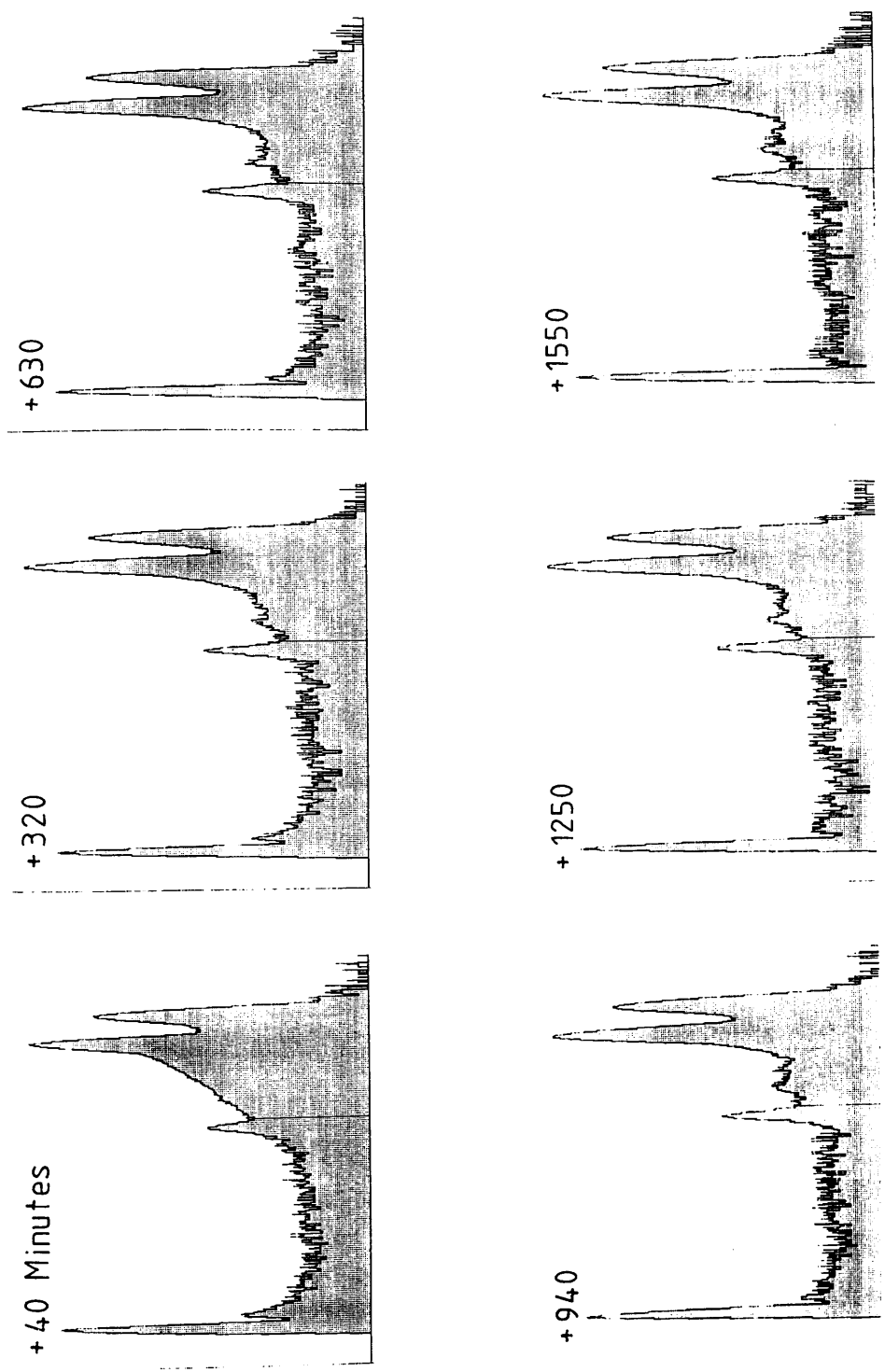


Fig. 6.14 Six spectra for  $0^\circ$  azimuth showing the decay of the damage.

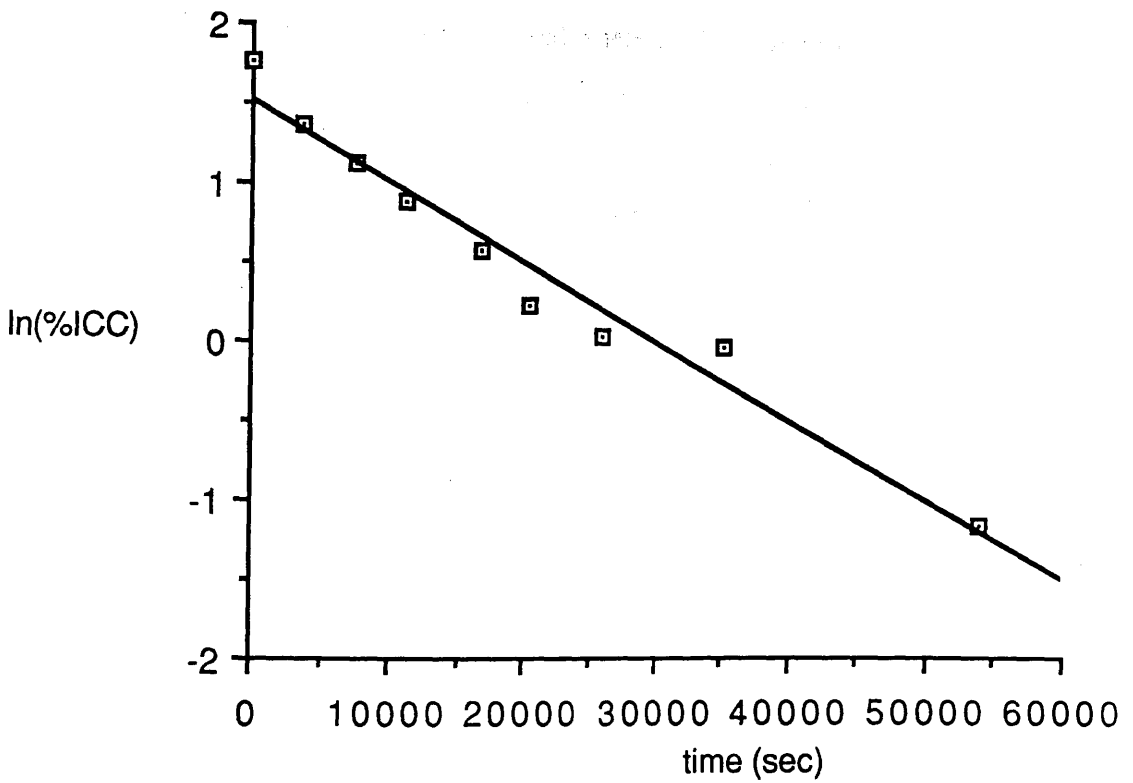


Fig. 6.15 Graph showing the variation of the ICC with time for the HB5 detector.

the detector.

Since the exact trapping mechanisms which give rise to the shape of the ICC tail are not fully understood, it is difficult to infer what the decay of the ICC actually means. It is not necessarily correct to infer that the number of traps are also decaying exponentially with time. However, it is convenient to postulate that this is the case. The real difficulty in interpretation arises since different regions of the tail correspond to vastly different numbers of carriers being lost to the collection process. For example, for a count to appear in the region very close to the  $K\alpha$  photo-peak, only requires approximately 10% of the charge carriers to be lost. However, in the central region, we need approximately 50% of the carriers to be lost before a count can appear here.

A simple model can be proposed where the ICC is attributed to the existence of a number of traps. These traps give rise to the shape of the tail by some complex trapping mechanism, the exact mechanism need not be considered at this stage. The total ICC after the terbium irradiation,  $ICC_t$ , can be considered as being composed from two contributions,  $ICC_{NOR}$ , the normal level of ICC for the detector and  $ICC_{DAM}$ , the additional ICC caused by the high energy irradiation. If these ICC contributions are caused by two different trapping densities,  $N_{NOR}$  and  $N_{DAM}$  then the decay of the number of traps at a given time  $N_t$ , can be approximated by the equation

$$N_t = N_{NOR} + N_{DAM}^0 \exp(-t/\tau) \quad 6.3$$

where  $\tau$  is the decay constant for the traps created by the high energy photons. At large values for  $t$ ,  $N_{DAM}$  tends to zero and the total number of traps or trap density equals  $N_{NOR}$ , which is the level normally seen for the detector. From the graph shown in fig. 6.15,  $\tau$  has a value of  $(17.5 \pm 0.2) \times 10^3$  minutes.

Nothing so far has been said about the nature of the traps or trap density. Experimental data from fluoresced targets (Craven et al. 1987) indicated that the ICC is found to be strongly dependent upon the surface of the crystal (see section 3.8). This may be interpreted as evidence of a high trap density at the surface which decreases as the depth from the surface increases. These surface traps must contribute mainly to the  $ICC_{NOR}$  since the enhanced level  $ICC_{DAM}$  must be caused by side traps accessed by the

deflecting force from the magnetic field. These must differ from the surface traps since the ICC caused by these traps is never seen to decay in any way. This simple model has assumed that  $N_{\text{NOR}}$  and  $N_{\text{DAM}}$  are in some way different, a possibility consistent with the experimental evidence. However, it is possible that  $N_{\text{NOR}}$  is the result of a more dynamic type of trapping mechanism. Here traps are continually being created and filled to give the net effect of a constant trapping density. This possibility must be allowed for.

#### 6.4 Detector damage as a function of radiation dose.

The previous section discussed how damage could be induced by a long term irradiation with terbium x-rays. The next set of experiments investigated this damage process by gradually building up the terbium dose and monitoring the damage between each step. The irradiation was built-up in steps of 1 hour. The average count rate in this time was around 275 counts per second. The results indicated that a series of short irradiations did not produce the same effect as one long irradiation covering the same total time. For example, the first experiment involved 8 irradiations each of one hour duration, with a manganese test spectrum taken after each. After this period of time damage was only just noticeable in the region close to the photo-peaks, see fig. 6.16. As the duration of each irradiation was subsequently increased the damage became more apparent. Figure 6.17 shows the results for irradiations of 4, 8, 12 and 18 hours, with the times referring to one continuous irradiation.

In a similar approach to studying the decay, these damage spectra had the "as new" spectrum subtracted off. It was hoped this would show some kind of relationship between the time of irradiation and the level of ICC present. Unfortunately no such relationship could be found.

During this investigation we established that removing the bias (for a short time) caused any damage effects from the high energy irradiation to disappear. This result had already been seen with the JEM detector.

X-RAY: 0 - 40 keV  
Live: 1368s Preset: 32000s Remaining: 30732s  
Real: 1486s 8% Dead

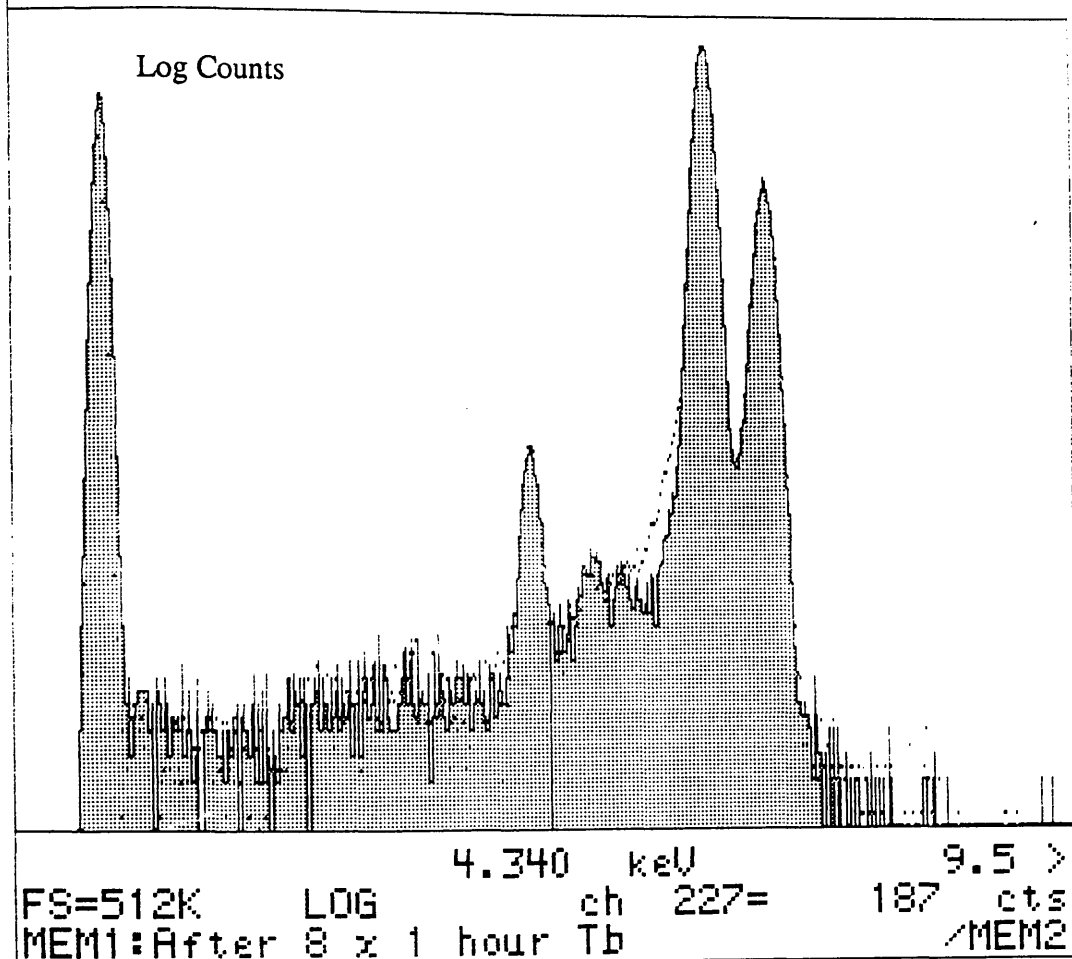


Fig. 6.16 Damage after 8 irradiations of 1 hour with terbium x-rays (in dot memory) compared to normal spectrum.

Log Counts

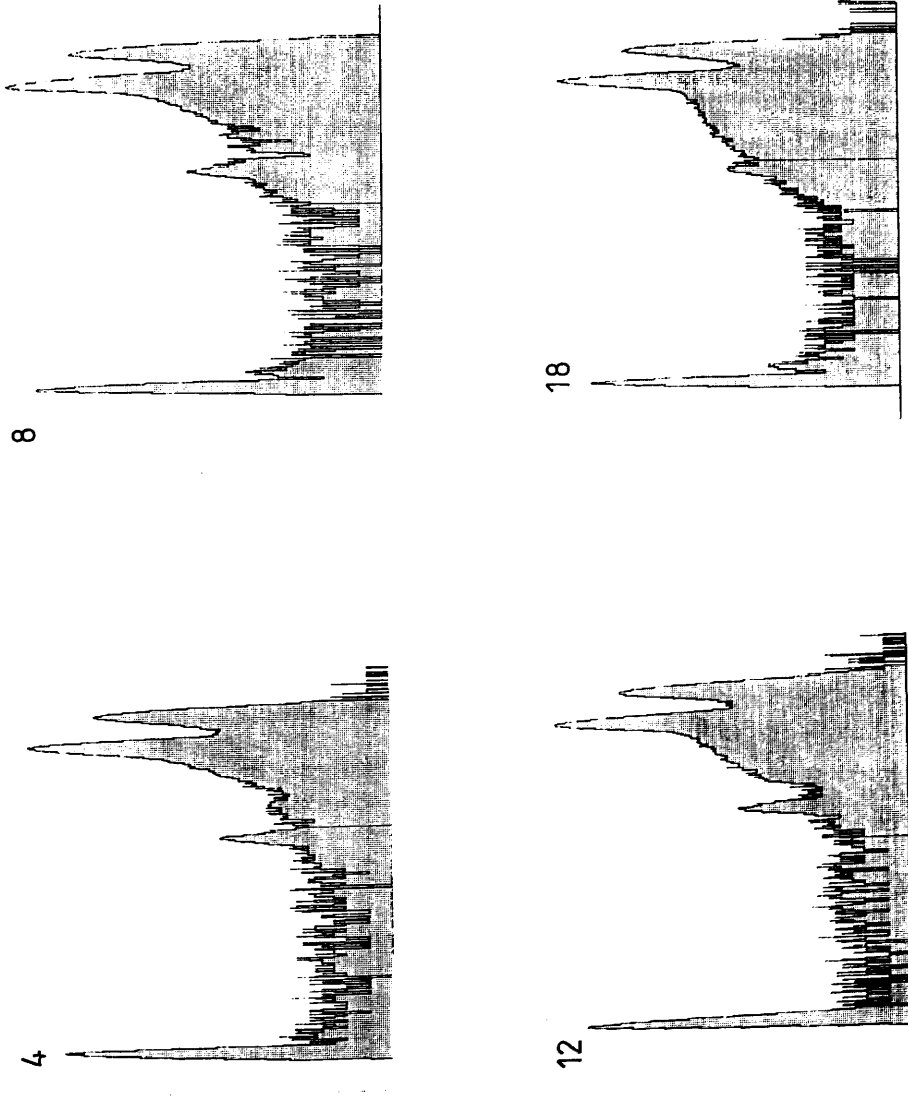


Fig. 6.17 Damage after irradiations of 4, 8, 12 and 18 hours.

## 6.5 Field direction in the HB5 objective lens.

The "bench" experiments on the HB5 detector had shown that for certain orientations of the applied magnetic field the ICC would be far worse than for other directions. The orientation of the magnetic vector for enhanced ICC in the HB5 detector corresponded to the azimuthal angles between  $270^\circ$  and  $135^\circ$ , going in a clock-wise direction, see fig. 6.18. It was obviously very important to establish the orientation of the magnetic field for the HB5's objective lens. This would indicate whether the objective lens field would force carriers into the poor regions of crystal or would force them into a region which gave no additional ICC.

In the HB5, at the position of the detector, the objective lens magnetic field is orientated by  $22^\circ$  away from the microscope's axis, fig. 6.19. When measured using a Hall probe, this field was found to point in the direction normally associated with the magnets being in the  $180^\circ$  azimuth. This result was very strange since, for the HB5 detector, the  $180^\circ$  azimuth was a direction normally associated with no increase in the level of ICC. This result appears to contradict all the effects found up till now. Neither the HB5 nor JEM detector could be shown to exhibit anywhere near the degree of damage required to explain the results from chapter 4 without aid of the magnetic field. Possible reasons to explain this are not easily obtained. Considering the results found for this detector, it could be assumed that the energies of the photons used to create the damage were insufficient to create the level or type of damage encountered in the microscope. A second reason, which was eliminated by experiment, was the fact that the magnetic field being used was only 0.22 T whereas the field in the objective lens was around 0.3 T. It was reasonable to imagine that the lower field strength might not be able to deflect the carriers in to the very worst region of the crystal particularly in the azimuthal direction corresponding to the field in the objective lens ( $180^\circ$ ). A second magnet of field strength 0.3 T was obtained to verify whether this was the case. The HB5 detector was once more irradiated by terbium x-rays to bring back the damage, after which the different azimuths were once again investigated. The level of damage was found to be no different than that which had been found before.

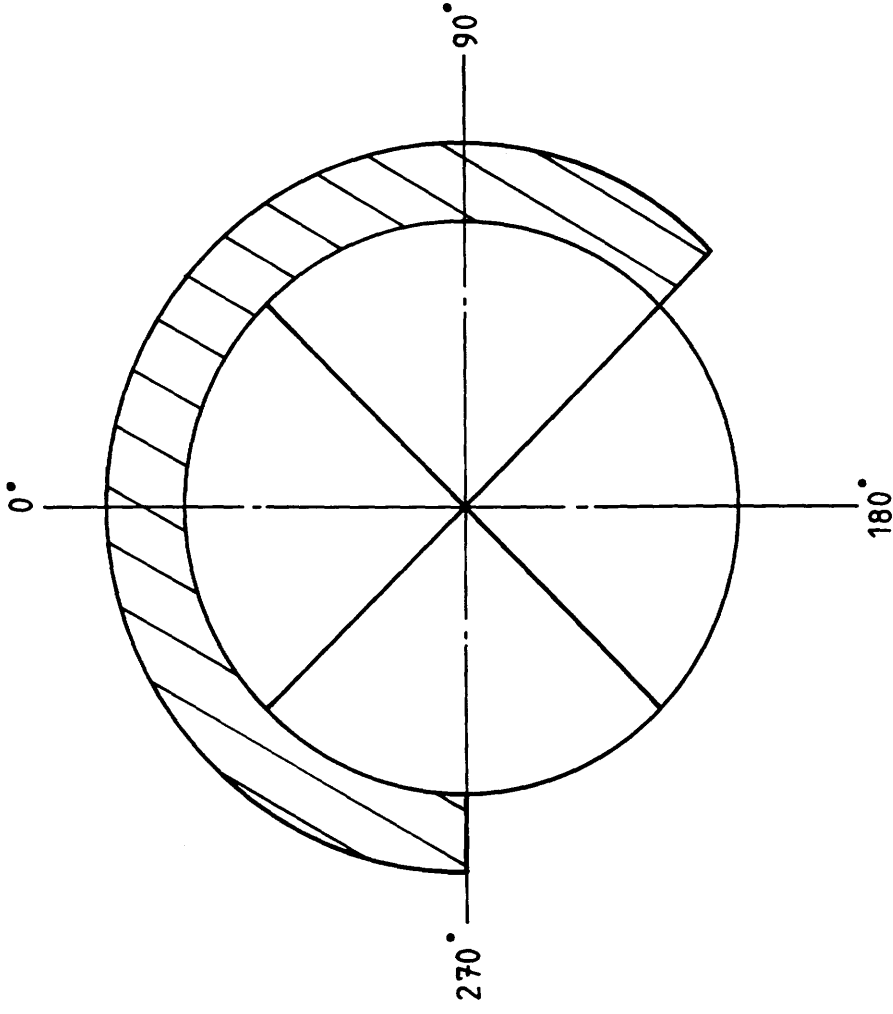


Fig. 6.18 Diagram showing what is regarded as the poor region of the HB5 detector, as looking into the detector.

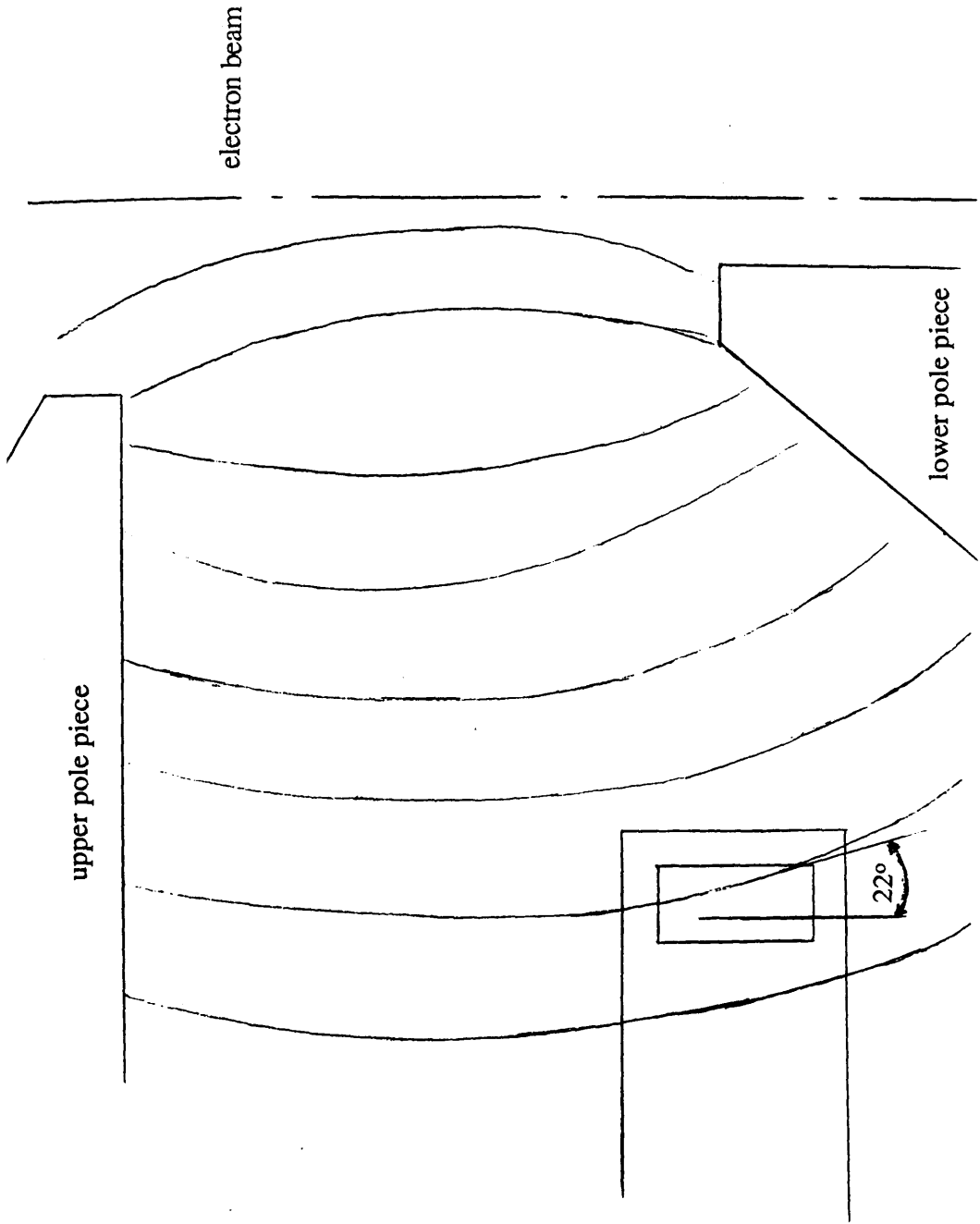


Fig.6.19 Diagram showing the orientation of the objective lens magnetic field lines with respect to the detector crystal.

The actual reason for the poor quality of electron generated spectra was eventually realised during work to establish a means of accurately aligning the detector on the HB5 (Craven and Nicholson, 1990). Up until this time it had been assumed that the detector/specimen geometry was that depicted by fig. 4.3. However, it was found that the detector crystal was in fact closer to the front of the detector assembly than the original drawing had indicated. This was due to the HB5 detector being slightly different in design to the previous detector used on the microscope. The crystal was in fact 1.7 mm closer to the collimator. This meant that the central region of the crystal had not been used to collect the x-rays as it should. It was the top of the crystal, near to the internal collimator which was being irradiated. Normally the collimation is such that a central region of approximately 15 mm<sup>2</sup> is irradiated. The actual detector alignment had meant that approximately 5 mm<sup>2</sup> was being irradiated; this being at the top of the crystal. This misalignment had allowed the peripheral regions of the crystal to be irradiated. This was why the spectra had all contained excess ICC.

The experiments carried out in this chapter had actually indicated this without us realising this at the time. The fact that damage could still be seen with an external collimator being used during the irradiations, meant that side regions were still being irradiated. During the acquisition of the electron generated spectra, these side regions would have been irradiated with both characteristic and bremsstrahlung photons. The bremsstrahlung would have affected the crystal in a similar way to the terbium x-rays. The characteristic photons incident on the same region of crystal would have been affected in a similar way to the manganese photons used in the bench tests. Therefore, all of the spectra contained excess ICC on their characteristic peaks, this was what we observed in chapter 4.

## 6.6 Possible mechanisms to explain the damage effects.

The previous sections have described several interesting phenomena found to be occurring with the 2 different Si(Li) x-ray detectors which were studied. The following sections look at these observations in more detail and hopefully suggest some plausible

reasons for these effects. It is not the aim of these sections to derive any fundamental underlying theory to explain these damage effects/mechanisms but through applying existing theories possible reasons for these effects may be inferred.

### 6.7 Radiation damage in silicon.

One obvious point to begin with is to consider the effect that the high energy electrons and photons have upon the silicon crystal. These electrons could either be those which are created within the crystal by the absorption of high energy photons or in special cases those which are scattered off the specimen and pass through the beryllium window to strike the crystal.

Silicon detectors are being very commonly used in the detection of particles and photons, consequently there is much available literature describing damage effects in these detectors. Most of these studies have been made for the effects of high energy irradiation where different effects are possible i.e. displacement damage or even nuclear reactions. There are alarmingly few results for the energies being considered in this work and even less information exists on damage within Si(Li) type detectors. From the available data, it appears that structural damage (displacement damage) cannot occur in bulk silicon with electrons of energies less than 200 keV (Guye and Jarron, 1987), Dearnaley and Northrop (1966<sup>2</sup>) quote 250 keV. However, electrons of energies less than 200 keV can induce defects at interfaces, for example, at the SiO<sub>2</sub>-Si interface and these defects can trap holes. This is consistent with the claims of other authors, Lowe (1989) for example.

Magorrian and Allinson (1988) have studied the effect of low energy photon damage in silicon charge coupled devices (CCD's). Although primarily designed as a study of MOS devices there are certain similarities which make this work applicable to Si(Li) detectors. In this paper, they discuss how the fracturing of chemical bonds in the vicinity of the SiO<sub>2</sub>-Si interface can lead to a formation of interface states. The formation of these interfacial states are claimed to be caused by the migration of "non-bridging oxygen defects". These arise due to the rupture of an oxygen-silicon bond.

These non-bridging oxygen defects are mobile and are responsible for a subsequent lattice rearrangement. A Si(Li) crystal has quite a considerable surface area for its size, which is not helped by the groove cut in the back surface. This means that there is a large surface area of SiO<sub>2</sub>-Si interfaces. Any of this area can be irradiated by the high energy bremsstrahlung, so it is conceivable that surface states can be created over the entire crystal surface. The magnetic field can deflect carriers into these side regions; hence the increase in the observed ICC.

### 6.8 The effect of the electric field.

The electric field which exists within the crystal is essential so that the carriers may be swept to their respective collection electrodes (and in a very short time). Field lines for an applied bias of 400 V have been shown in fig. 3.1 (b). At the sides of the crystal the field strength drops off sharply and this is thought to be one reason for carriers being lost (Goulding, 1977). The reason for these weak peripheral fields are thought to be caused by the lithium drifting profile and irregularities at the edge surfaces which can lead to hole trapping (Lowe, 1989). The effect of the oxide layer has been known to be important from studies of MOS technology. Trapping of carriers in the oxide layer can lead to high leakage currents or even self counting (Chevalier, 1988). This oxide layer can cause hole trapping which can then lead to a screening effect at the front surface contact and hence a reduction of the electric field in the bulk (Lowe, 1989). Exact values for this effect are not given.

A result which might be an example of such an effect was found with the HB5 detector. After a long irradiation of 30 hours with the terbium source (no external collimator fitted) the manganese test spectra all contained a stray peak centred at 5.46 keV, this has the appearance of a chromium K $\alpha$  peak, (see fig. 6.20). However, this could not be stray chromium x-rays since no changes in the apparatus or experimental procedure had taken place which could introduce such x-rays. This must therefore be a manifestation of a space charge effect in the crystal which leads to gross peak distortion. This effect must be caused by defects at the sides of the crystal since

X-RAY: 0 - 40 keV  
Live: 5999s Preset: 32000s Remaining: 26001s  
Real: 12888s 53% Dead

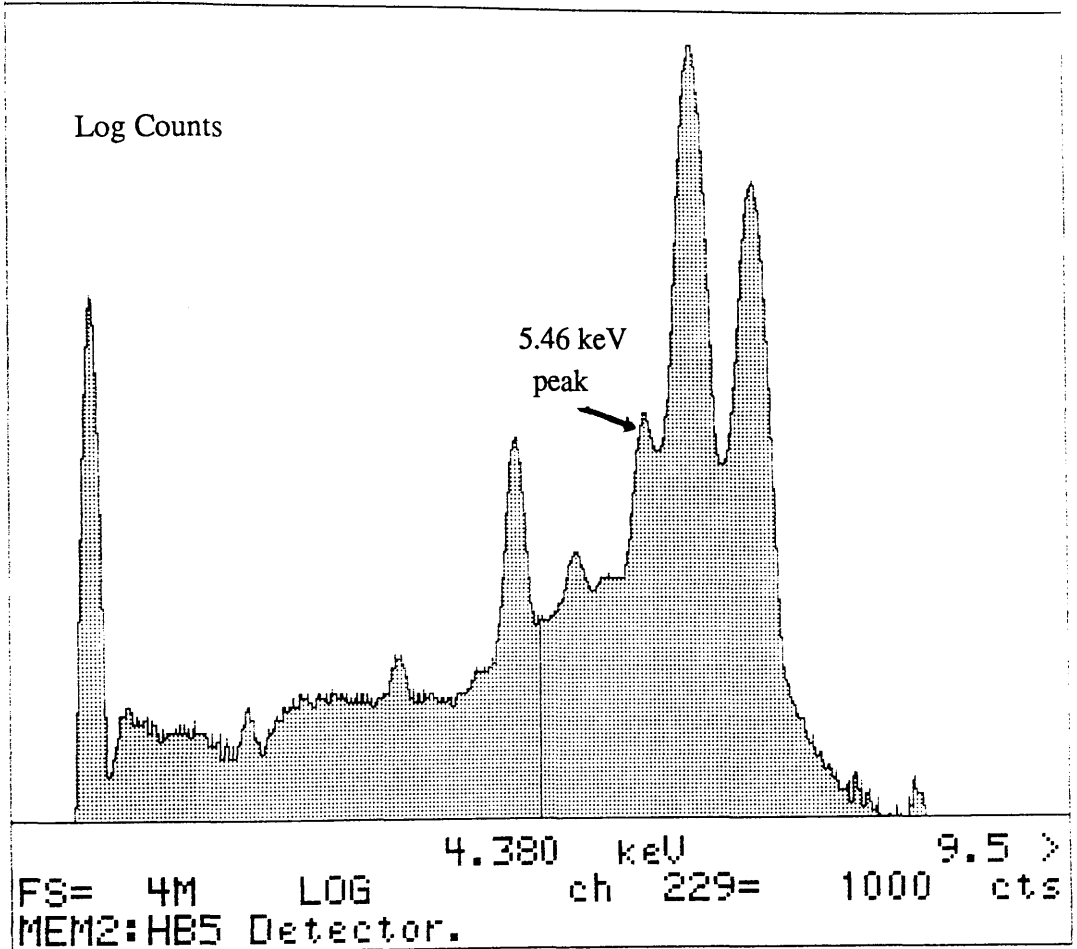


Fig. 6.20 Spectrum for manganese showing the "peak-like" artifact at 5.46 keV.

collimation of the detector totally removes the stray peak. With the magnetic field applied the stray peak disappeared for the 0, 90 and 270° azimuthals; however at 180° it was just worse.

Electrons which move to the edges can be "lost" giving rise to spurious low energy peaks or tails. Consequently electrons reaching the back electrode via the edges (slow charge) give rise to an increased background (Lowe, 1989). The reason for these slow charges may be due to the variations in the carriers mobility as they move into regions where the electric field is lower. The dependence of mobility on field strength has been studied by Alberigi Quaranta et al. (1968) where they have shown that the drift velocity for electrons and holes is field dependent, for silicon at 77K.

From the results found earlier in this chapter, some of the ideas mentioned above can be seen to be applicable. The magnetic field has been shown to deflect carriers by up to 1mm and hence into the edge regions. Here they may be trapped either temporarily or may even recombine, hence the increase in the observed ICC. However, section 5.4 showed that in certain directions within the crystal, the ICC did not increase but could in fact be decreased. This must surely indicate that the edges are not necessarily bad around the entire crystal circumference, but that good areas do exist. Therefore there should be no reason why the entire crystal circumference could not be manufactured as such. It may indeed be a step in the fabrication process that is leading to these poor regions at the edges. If crystals are to have larger active areas then it is important for the manufacturers to improve their manufacturing techniques.

Low energy tails have been observed in section 6.2. These tails were seen to grow as the time for which bias was applied. These may indeed be due to "slow charge" and must be due to an edge effect since they are not seen without the deflecting field of the magnets. The reason for the growth of this low energy peak with time may be due to surface charging at the sides and hence an increase in the slow charge. Lowe (1989) talks a little on this idea but gives no details.

## 6.9 Study of the photon damage on a new detector.

A new detector was obtained on which damage type experiments were to have been performed. Unfortunately this detector had its beryllium window broken before these experiments were performed. However, some experiments were performed with this detector which did show some interesting results. These experiments were not designed to be compared directly with those performed for the JEM and HB5 detectors, but were similar enough for some comparisons to be drawn.

This detector was first characterised with the manganese source and the magnets in the usual way. This was primarily to check the performance and secondly, to provide a set of spectra with which a comparison could be made after irradiation. The spectra from this detector were slightly different from those from the JEM and HB5 detectors. Spectra acquired without an external collimator had a greater amount of ICC than is usually associated with the series E type crystals. With collimation the overall shape was similar to that found for the series E type detectors, but with a resolution of around 152 eV, which is about 3 eV better than the JEM or HB5 detectors. Without an external collimator there was a change in level of the ICC across the entire tail region. This was different to the other detectors which only exhibit differences in the region close to the photo-peaks for spectra which are acquired with no external collimator. Figure 6.21 shows spectra for this detector with and without external collimation. The tail region shows where the spectra differ most. No difference was seen in any of the spectra when a magnetic field was applied. In addition, this detector's performance did not change as the bias time increased.

As part of a separate investigation, this detector was used to collect spectra from all the targets available from the high energy variable x-ray source. It was during these experiments that an important discovery was made. The various fluoresced spectra from the americium source were collected beginning with the highest energy photons and subsequently decreasing the photon energy. There was no particular reason for doing this in this order. The detector was irradiated with terbium for approximately 12 hours followed by barium, silver and molybdenum for approximately similar times.

X-RAY: 0 - 40 keV  
Live: 8888s Preset: 32767s Remaining: 23879s  
Real: 10460s 15% Dead

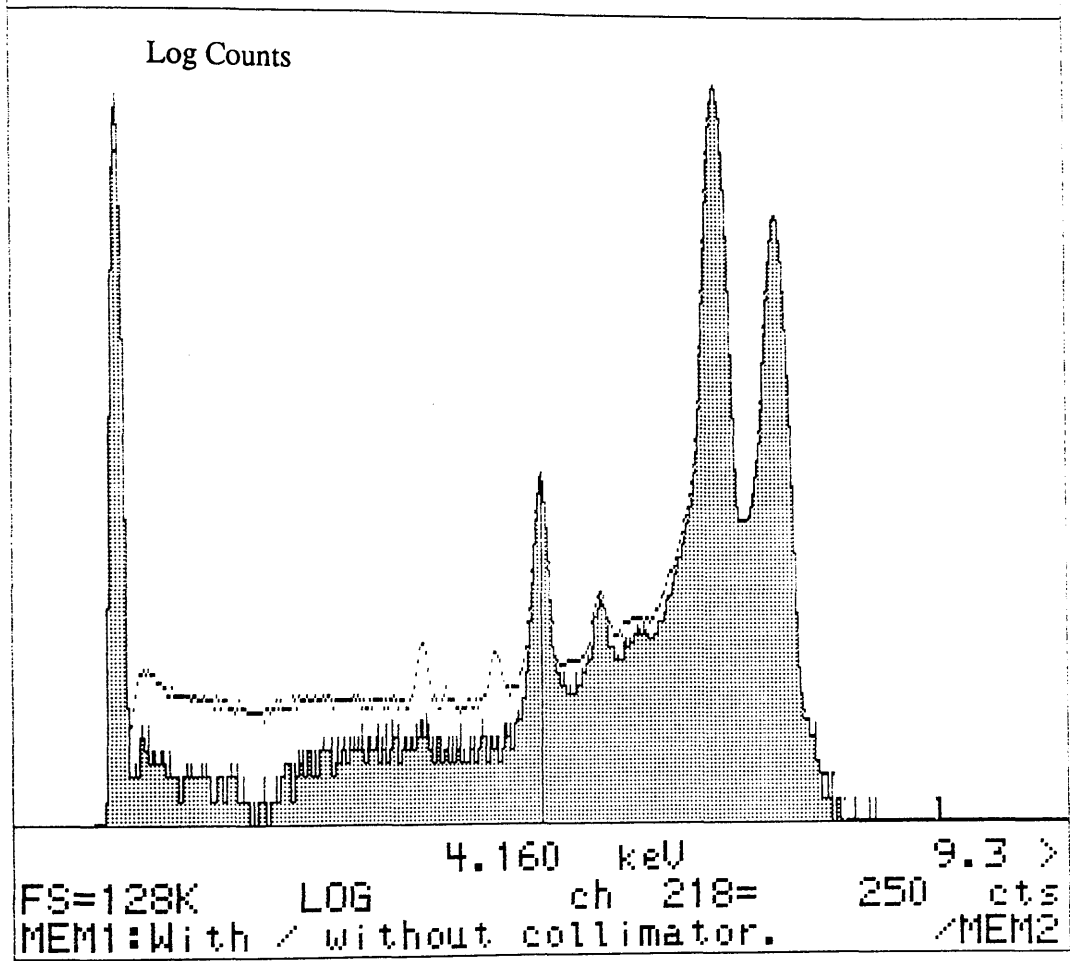


Fig. 6.21 Irradiation damage detector, showing spectra with and without (dot memory) an external collimator being used.

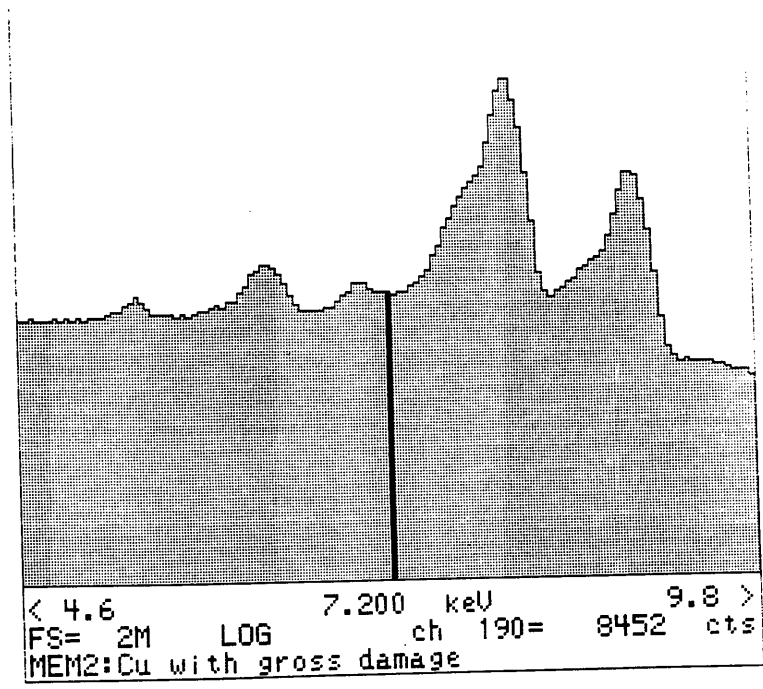
When the rubidium and copper targets were used the characteristic peaks for these x-rays were found to contain a broadening on the low energy side of the photo-peaks, see fig. 6.22. The important fact here, is that the magnets were not present to create this effect. A spectrum of manganese was taken to check that this effect was not being caused by the high energy Compton scattered gamma rays present in the copper and rubidium signal. This too exhibited the same broadening on the low energy side of the photo-peaks. This is shown in fig. 6.23. The bias was removed from this detector and it was left for around 1 hour after which the bias was re-applied and a manganese spectrum taken. The damage effect was found to have totally disappeared. This was similar to what was found for the other detectors. The detector was left for several days periodically being tested with the manganese source to see whether the damage had returned. No increase in ICC was found over this time.

These results apparently indicated that this detector would exhibit photon induced damage without the aid of the magnetic field, i.e. the bad region of crystal was not necessarily obscured by the internal aluminium collimator. Unfortunately this detector had its beryllium window broken before any further tests could be performed upon it.

## 6.10 Conclusions.

This chapter has described several different types of physical phenomena found to occur when Si(Li) detectors, which should ideally behave the same, have been irradiated with high energy photons. The results show that certain properties of the behaviour are particular to each specific detector.

The JEM detector behaved in a very unexpected manner. Damage, probably due to the formation of traps, was found to increase as a function of the time in which the detector had bias applied. Irradiation with high energy photons partially cured this damage. It appears although irradiation with the high energy photons swamp the crystal with carriers, these carriers then fill the traps so that the manganese test spectra appear as normal. During the course of time the traps de-excite and the level of ICC steadily



Log Counts

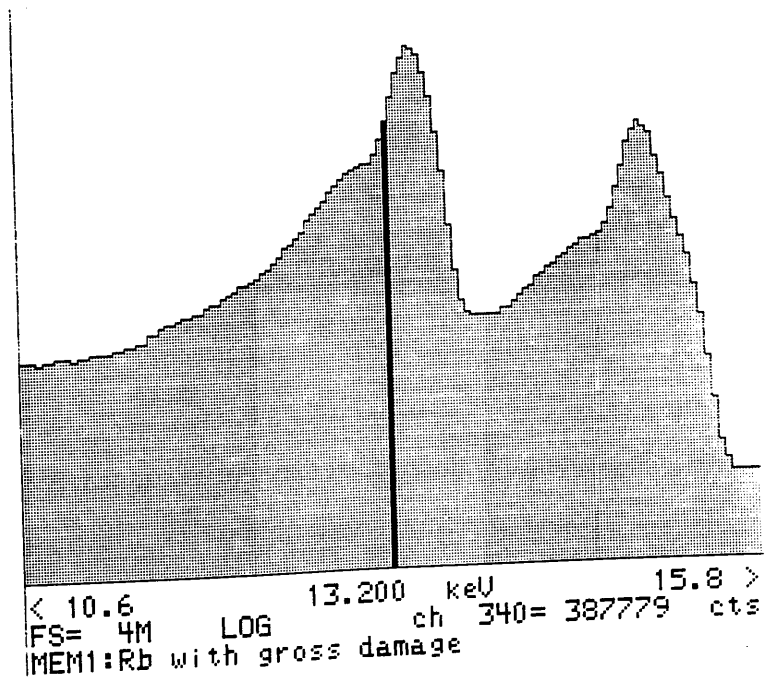
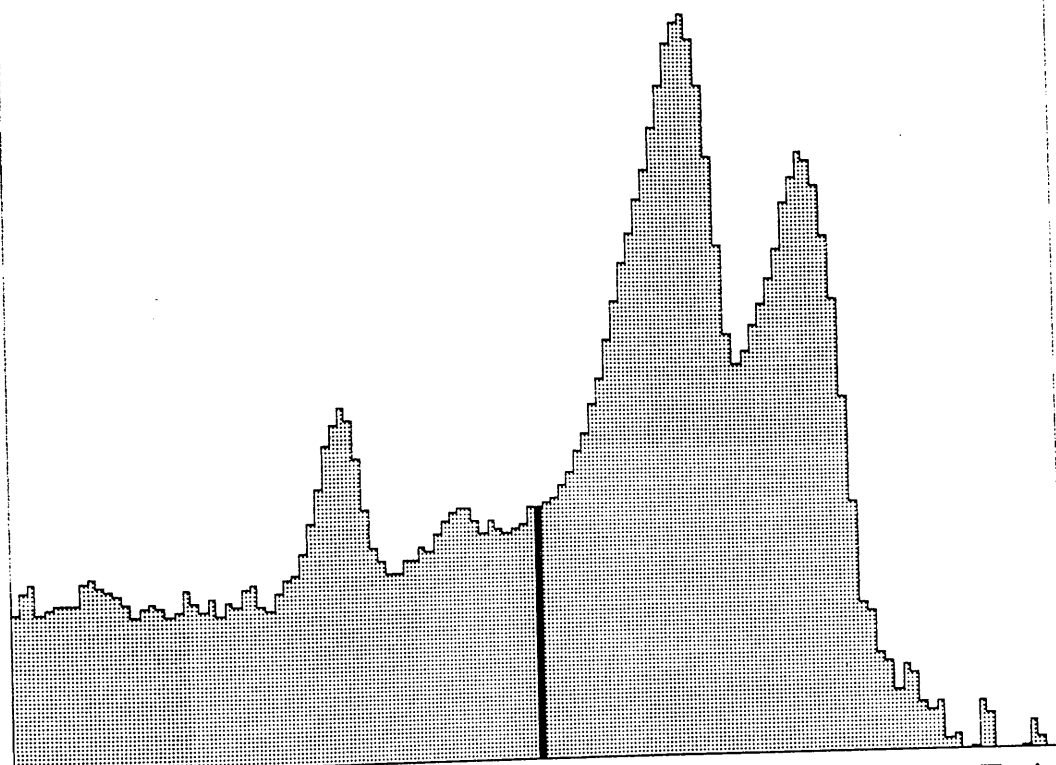


Fig. 6.22 Copper and rubidium spectra showing damage effects near to the K photo-peaks.

X-RAY: 0 - 80 keV  
Live: 243s Preset: 30000s Remaining: 29757s  
Real: 561s 57% Dead



< 2.6 5.160 keV 7.7 >  
FS=512K LOG ch 139= 272 cts  
MEM2: High energy damage effect

Fig. 6.23 A manganese spectrum for the same detector showing the same effect as seen in fig. 6.22.

increases. These traps must exist at the sides of the crystal (where the electric field is lower) since the damage effects could only be seen with a magnetic field being applied. Something which was not established, was the point at which this detector started behaving in such a manner. But from the limited data available, it must have been during the 6 month period that the detector had been used on the JEM 100C. This was after the experiments described in chapter 5 and before those described in chapter 6. The fact that the ICC grows with time can easily be overlooked, since normal bench tests with a manganese source do not require long term acquisitions. The fact that the damage disappears when the bias is removed (i.e. when removing from the microscope) does not help this.

Evidence does exist which shows that the peripheral regions of this detector were deteriorating with time. This can be deduced from the results stated in section 5.4. Here a region of the crystal, known to contain a high trap density, was studied 6 months after being first tested. The quality of spectra obtained from this region had deteriorated quite considerably in this time.

The HB5 detector was found to exhibit additional ICC after a long term irradiation with terbium x-rays. These x-rays only supply up to 60% of the total energy encountered in a 100 keV electron microscope. However, x-rays of this energy have been shown to be capable of affecting the sides of the crystal. Irradiating these side regions appears to create traps. The number of traps appears to be dependent on the region of crystal irradiated. When the carriers are deflected by an external magnetic field these traps lead to a gross increase in the level of ICC.

When considering the ICC over the entire tail region, the damage was seen to decay in an approximately exponential fashion; however, this may only be fortuitous, since the exact nature of the process which gives rise to the ICC is not well enough understood at this point to infer the significance of this result. It is also possible that the damage caused by the high energy photons is not truly reversible and in effect the crystal is under a continual deterioration. The fact that the irradiations did not give the same effect each time may be evidence for this. The final irradiation experiment which gave rise to the extraneous peak centred at 5.46 keV (fig. 6.20) may also partially back-

up this claim. Similarly there was evidence from the JEM detector that the damage effects exhibited by this detector were also slowly getting worse.

The experiment to establish the field direction in the objective lens gave a result which appeared to contradict all that had been found in the experiments involving the magnetic field. If the magnetic field vector had been in a direction which corresponded to an increase in the ICC, it would have been easy to come to the wrong conclusion that this effect, coupled with the effects of the high energy photons, was the cause for the poor fitting spectra. In looking for possible reasons to explain why this lens field could not be the cause of the additional ICC, it was eventually established that it was simply detector misalignment which was causing the poor quality of spectra. This was unfortunate but can easily occur due to the extremely high tolerances required in component design and detector alignment. Looking optimistically however, this misalignment did give rise to the discovery of the interesting phenomena associated with the detectors. This information may otherwise have gone unnoticed for some time.

The strangest effect observed in this chapter was the fact that the JEM detector's performance deteriorated with time whilst the HB5 detector's performance remained constant. In addition to this the JEM detector's performance improved with high energy irradiation whilst the HB5 detector's performance deteriorated. Each detector appeared to show properties opposite to that displayed by the other. This indicates how totally different two series E detectors can behave, each of which can be made to operate correctly if collimated suitably. This is perhaps the most important find in this project.

The third detector, which only had a limited study performed upon it, exhibited yet another manifestation of detector damage. This detector did not require a magnetic field for it to exhibit the effect of the photon damage. This detector also differed in the level of ICC present when irradiated without an external collimator. Under such circumstances it is usual for a slight increase in the number of counts close to the  $K\alpha$  photo-peak. This did not happen for this detector. The additional ICC was distributed across the region of the tail from the escape peak down to the cut-off.

This chapter has shown that there are many strange effects possible with the Si(Li)

detectors when the peripheral regions of the crystals get irradiated by high energy photons. Fortunately the detectors still behave in the desired manner when collimated to the central region of the crystal. The detectors studied here were all examples of the 30 mm<sup>2</sup> variety. However, far larger crystals are available and it is possible that these damage effects could be more serious for these crystals. This may limit the area being used and would minimise any benefits from having a larger crystal to begin with.

## CHAPTER SEVEN

### Factors Contributing to the Low Energy Tail.

#### 7.1 Introduction.

This chapter discusses some of the mechanisms known to contribute to the low energy tail associated with the Gaussian photo-peaks. Conventionally this tail has often rather casually been referred to as being caused by the effects of ICC. However, certain contributions to the tail can be attributed to other effects, some fundamental, which should not be confused with the ICC. The origin of these additional contributions can be attributed to processes occurring both in the detector and the various sources of x-rays used in studying these tails.

If it were possible to obtain a perfectly monochromatic source of x-rays, then the spectrum associated with such a source would contain a low energy tail caused only by the effects of ICC. This ICC can be attributed to trapping of carriers at the surface, bulk or sides of the crystal, or to the escape of radiation from within the detector. All of these lower the total number of carrier pairs collected hence redistribute counts outside the Gaussian photo-peaks. These "detector effects" are a combination of both fundamental and technological effects. The escape of radiation from the detector is an example of a fundamental effect. This radiation which escapes the detector can be the bremsstrahlung radiation created as the charge carriers scatter within the bulk silicon or the silicon photons which escape giving rise to the characteristic escape peaks. The technological effects include the various imperfections associated with the silicon crystals which can lead to trapping or recombination of the carriers. These technological effects can in theory be minimised as the manufacturing processes improve.

In general the x-ray sources used are not monochromatic. For example, the  $^{55}\text{Fe}$  source used extensively throughout this work, gives rise to both  $\text{K}\alpha$  and  $\text{K}\beta$

manganese x-rays. In addition, there are fundamental effects occurring within this source which give rise to additional sources of extraneous radiation. These effects include those from Compton scattering of the x-rays as they escape the  $^{55}\text{Fe}$  source and from the escape of secondary bremsstrahlung radiation. Compton scattering has the effect of broadening the energy distribution of the x-rays emitted from the source. This has the effect of further complicating the detailed shape of the tail. The bremsstrahlung radiation results from photo and Auger electrons emitting radiation as they scatter within the  $^{55}\text{Fe}$  source. These electrons are those created as manganese x-rays are absorbed by iron L shell electrons in the  $^{55}\text{Fe}$  and by the Auger electrons created in preference to a manganese x-ray. Bremsstrahlung is also found when bulk targets are fluoresced by the  $^{55}\text{Fe}$  source. Again this bremsstrahlung is that created by photo and Auger electrons scattering within the fluorescence targets. Here, the bremsstrahlung energy distribution depends upon the binding energies of the particular electrons in the target being fluoresced. Other minor effects which occur include; the effect of the high energy bremsstrahlung emitted by the radioactive source (see appendix 3) and that of cosmic radiation. Both of these effects give rise to a small number of counts in the spectrum.

It is very important to have some idea of the magnitudes of the effects occurring in the detectors and x-ray sources. This knowledge is important to detector manufacturers since this allows them to establish how much of the tail is actually due to defects, surface or otherwise; these the manufacturers can always strive to eliminate. The information concerning the x-ray sources is important as it determines the usefulness of any particular source in the study of the ICC. This chapter looks at some of these effects and discusses their significance. Source effects are considered first; these being the Compton effect and the effects from the escape of bremsstrahlung. Bremsstrahlung escaping from the detector is then considered and some experimental means of estimating its magnitude are described. Finally a short section is included which looks at a possible means of parameterising the shape of the tail region; this closely follows previous work performed on this idea.

## 7.2 The effect of Compton scattering in the source.

The effects of Compton scattering are best illustrated by fig. 7.1 and 7.2. Here manganese photons backscattered off wax and iron targets are shown. These spectra contain photons which have been either Compton or Rayleigh scattered off the respective targets. Any fluoresced x-rays from the wax or iron targets (carbon K and iron L's) are not detected since they are of too low an energy to pass through the beryllium window. The photo-peaks on the wax spectra are seen to be grossly distorted. Since Rayleigh scattered photons suffer no energy loss, this distortion must represent the effects of the Compton scattered photons. The spectrum from the iron target shows stray impurity tin L lines and an additional artifact just below the  $K\alpha$  photo-peak. This effect is caused by bremsstrahlung escaping from the target.

Compton scattering has the effect of broadening the energy distribution of the incident radiation. This results in the ideally monoenergetic  $K\alpha/\beta$  photons now extending over a range of energies. Manganese x-rays emitted from an  $^{55}\text{Fe}$  source can Compton scatter from the iron L, M and N shell electrons. The M and N shell electrons have small binding energies and a free electron approach will suffice. However the energy difference between a manganese  $K\alpha$  x-rays ( $E_p = 5.898$  keV) and the L shell binding energy is not sufficiently large to totally justify the free electron approach (iron L's have a binding energy of approximately 750 eV). The electrons binding energy has the effect of further broadening the energy distribution. The half-width for the energy broadening is given by

$$\Delta E = \pm 2.(T.E_B)^{1/2} \quad 7.1$$

Evans (1958), where T is the maximum loss in energy after a Compton event (free electron) and  $E_B$  is the binding energy of the particular shell being considered.

In the signal from the  $^{55}\text{Fe}$  source, only a very small fraction of the x-rays have been Compton scattered. The majority of those travelling towards the surface of the source escape without interaction and only a small fraction of those travelling into the source are Compton scattered so that they escape. However, when the manganese x-

X-RAY: 0 - 20 keV  
Live: 25639s Preset: 25639s Remaining: 0s  
Real: 27924s 8% Dead

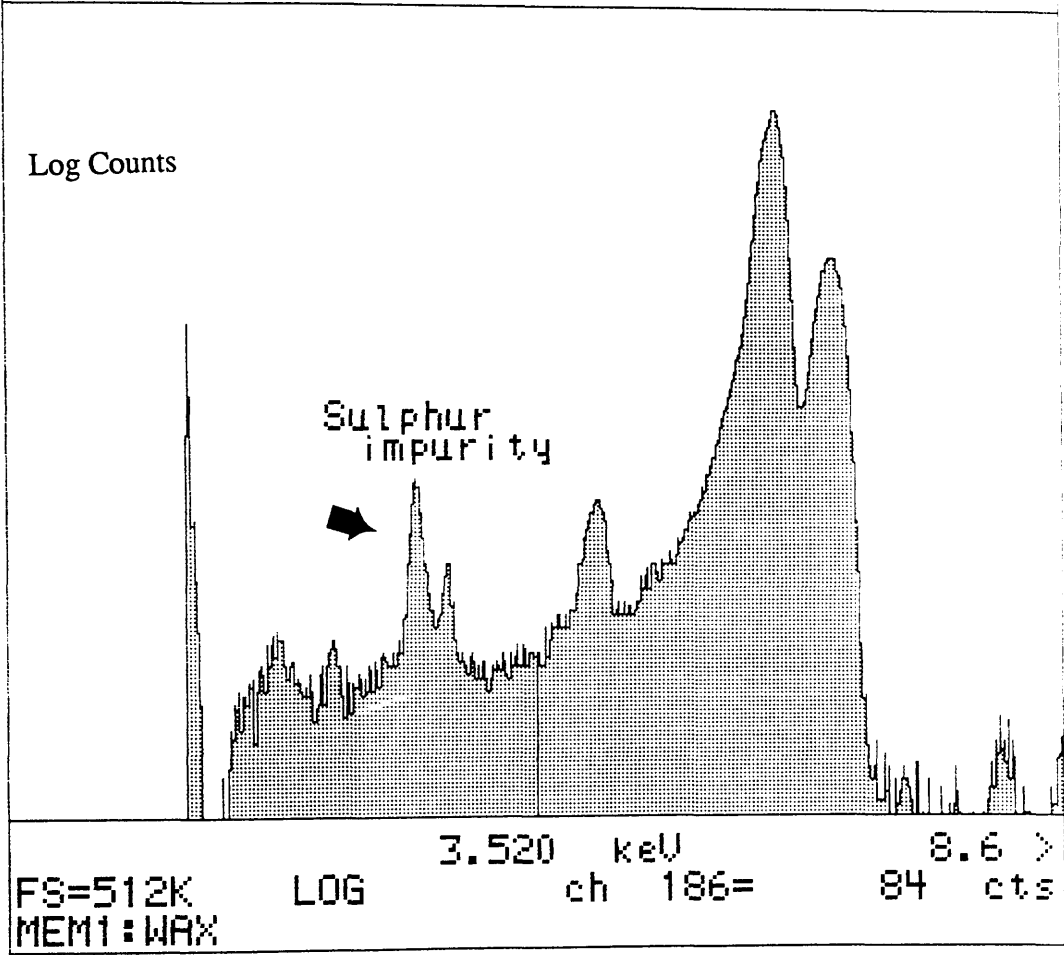


Fig. 7.1 Manganese spectrum backscattered off a wax target.

X-RAY: 0 - 20 keV  
Live: 20233s Preset: 20233s Remaining: 0s  
Real: 24395s 17% Dead

Log Counts

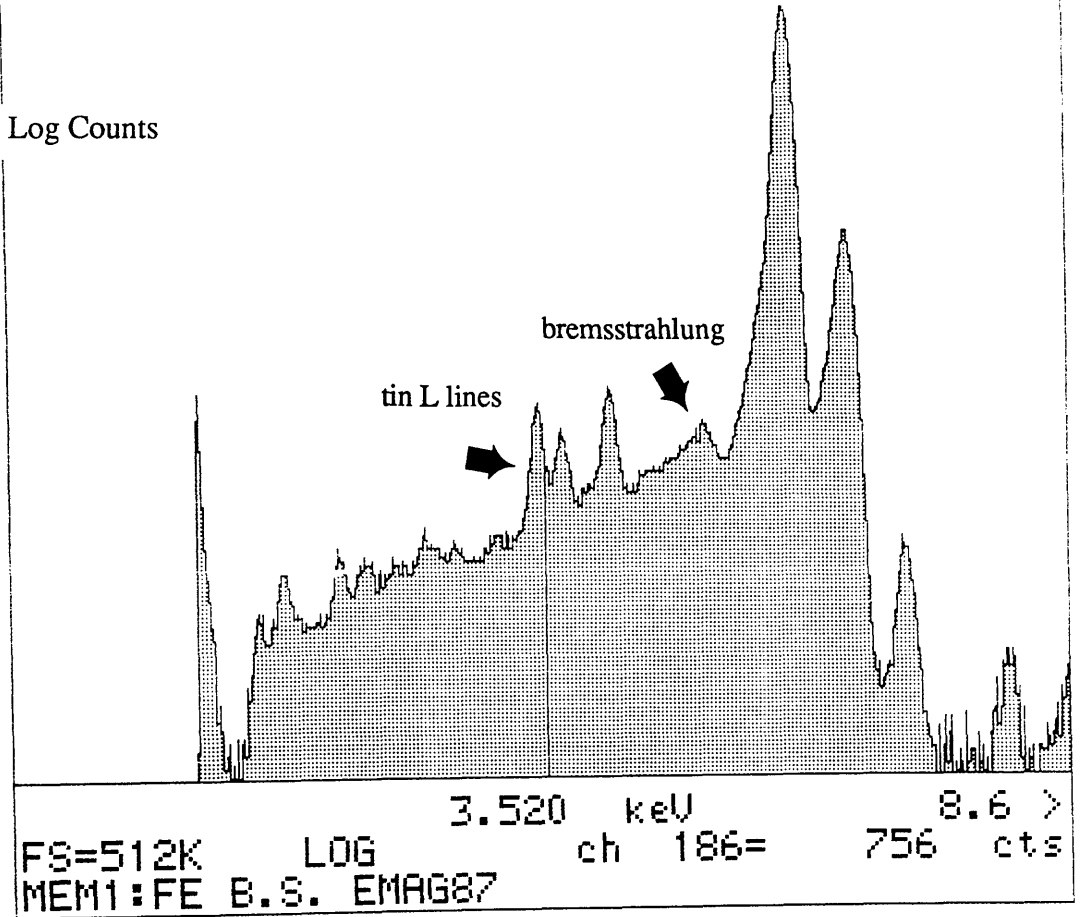


Fig. 7.2 Manganese spectrum backscattered off an iron target.

rays are incident on a target in a source with the geometry of fig. A3.9, only those undergoing either Rayleigh or Compton scattering reach the detector so that the effect of broadening is more obvious as shown in fig. 7.1 and 7.2. However, the majority of the characteristic x-rays fluoresced in the target contain only a small fraction which have undergone Compton scattering like the manganese x-rays from the source itself. Eqn. 7.1 means that the energy spread from the Compton scattering can be much larger than that for a free electron interaction, thus Compton scattering may contribute significantly to the tail. Methods of estimating the magnitude of the Compton contribution in the characteristic signal are considered below.

---

An approximate method can be used to estimate the level of the Compton intensity in the manganese photons emitted from the source. In a manganese spectrum, the photo-peaks only contain a small fraction of Compton scattered photons. The photo-peaks contain a "direct" contribution (i.e. photons directly emitted without any energy broadening) and a very small "backscattered" contribution (photons having been scattered in the source before escaping). In a backscattered spectrum however, the manganese photo-peaks are caused by the backscattering of manganese photons. The magnitude of this effect is approximately equal to the backscattered contribution in the direct source (actually depends on Z of scattering material).

To estimate the backscattered contribution we must calculate the source brightness B. Source brightness B, is defined from the equation which governs the photon rate R, this being

$$B = R / A_S \cdot \Omega_{\text{DET}} \quad 7.2$$

where  $A_S$  is the area of the source and  $\Omega_{\text{DET}}$  is the solid angle subtended at the detector. The brightness of the manganese source is made-up from two contributions,

these being;  $B_D$ , the brightness of the direct source of unscattered manganese x-rays and  $B_{BS}$ , the brightness of the backscattered source of x-rays. The brightness of the backscattered source contains only one term, the backscattered contribution  $B_{BS}$ . The ratio of the brightnesses of the two x-ray sources can be approximated to

$$\begin{aligned} & (B_D + B_{BS}) / B_{BS} \\ & \sim B_D / B_{BS} \qquad 7.3 \end{aligned}$$

Therefore, by calculating the ratio of the brightness of the direct  $^{55}\text{Fe}$  source and that of the source backscattered off iron, it is possible to get an estimate of the ratio of the direct photons to the backscattered photons. This method assumes that the amount of backscattering in the  $^{55}\text{Fe}$  source is the same as the level of scattering occurring within the iron target. This is a justifiable assumption for targets of equal Z. The major difficulty in actually performing this calculation is to estimate the integrated product of the source area and detector solid angle for the two source configurations. The configuration of the collimation and the actual shape of the sources makes this difficult. Figure A3.8 (appendix 3) shows a diagram of the  $^{55}\text{Fe}$  source holder in the actual experimental set-up used during the experiments. Figure A3.9 shows the experimental arrangement for the source being used to fluoresce a secondary target (backscatter case). From these diagrams the solid angle/area products were approximated to: 0.1 sr.mm<sup>2</sup> for the direct case and 0.67 sr.mm<sup>2</sup> for the backscattered case. The experimentally measured photon rates were: 1500 c/s (+/- 6%) for the direct case and 23 c/s (+/- 8%) for the backscattered case (backscattering off iron). These correspond to brightnesses of

14,500 photons/ sr mm<sup>2</sup> for the direct case  
and 34 photons/ sr mm<sup>2</sup> for the backscattered case

these give a brightness ratio of 420:1 (+/- 10%).

The experimental ratio of the brightnesses can then be used to get an estimate for the Compton intensity present in the "direct" manganese spectrum. A manganese spectrum backscattered from iron contains approximately the same proportions of Rayleigh and Compton scattered photons as the backscattered contribution present in the  $^{55}\text{Fe}$  source. Therefore by scaling a manganese spectrum to a spectrum backscattered from iron we are assuming an equal number of photons. If the "iron" spectrum is then divided by the brightness ratio we have essentially the number of backscattered events present in the direct signal. If we then compare the backscattered and direct spectra over the region thought to contain the Compton contribution i.e. the region containing the "tailing" seen on the photo-peaks, we find that the backscattered spectrum contains approximately 0.6% of the number of counts present in the direct spectrum. This very low value indicates that the Compton contribution does not affect the spectrum in any observable way.

If the theoretical cross-sections for the photoelectric effect and for the total scattering (Compton + Rayleigh) are considered (Storm and Israel, 1970) these being:

$$\tau = 7510$$

$$\sigma_C = 5.5$$

$$\sigma_R = 192$$

barns/atom respectively, then the ratio of the photo cross-section to that for the total scattering is

$$38 : 1$$

This theoretical ratio is approximately one order of magnitude less than the brightness

ratio obtained from the experimental data. The exact reason for this is unclear.

Finally, in this section the effects of Compton scattering of high energy photons within the detector will be briefly discussed.

Compton scattering of high energy photons within Si(Li) detectors has been studied by Craven et al. (1989). This work considers the effects of Compton scattering of the high energy bremsstrahlung present during the acquisition of electron generated spectra. Compton scattering of high energy photons within the detector gives rise to a low energy Compton contribution. This Compton contribution is caused by the detection of the Compton electron; the original Compton scattered photon having escaped the detector. The probability of the Compton scattered photon escaping the detector increases as the energy of the photons increases. This is because the photoelectric cross-section steadily decreases as the photon energies increase. Therefore, the low energy tails associated with the detection of high energy characteristic photons have an additional contribution, that from the Compton electron. Figure 7.3 shows the low energy end of a fluoresced rubidium spectrum. The Compton contribution can be clearly seen. For photon energies less than 10 keV this Compton contribution is undetectable due to the low energies involved. Energies of 10 keV or greater are outwith the realm of energies being considered within this chapter and are not considered any further.

### 7.3 Bremsstrahlung from the x-ray sources.

The sources of x-rays used to study the ICC tails are not monochromatic as we would ideally wish. Compton scattering has already been mentioned as one particular mechanism which broadens the energy distribution. A second and potentially more serious perturbation from the ideal is that of the escape of bremsstrahlung radiation from the x-ray sources. This source of radiation is potentially more serious since it gives rise to a broad energy distribution which depends upon the initial energies of the



electrons. This bremsstrahlung radiation is that produced by the electrons existing within the fluoresced targets when incident photons are absorbed. The existence of bremsstrahlung originating from the specimen has been mentioned by Goulding and Jaklevic (1977) and experimentally observed by Craven et. al. (1987) in a fluoresced vanadium spectrum. Here, the vanadium spectrum was found to contain additional counts below the  $K\alpha$  photo-peak. The energy at which these counts appeared, began at an energy equivalent to that of the L shell binding energy below the  $K\alpha$  photo-peak. These counts covered an energy range of approximately 1.5 keV (after which the bremsstrahlung is indistinguishable from the tail). The occurrence of these counts appears to indicate that fluoresced vanadium K photons can be self absorbed by vanadium L shell electrons, thus creating photoelectrons which can generate bremsstrahlung as they scatter within the vanadium target. It is important to remember that vanadium has a K shell fluorescence yield of  $\sim 0.2$  (Dyson, 1973<sup>3</sup>). This means that 80% of the time an Auger electron will be emitted in preference to a vanadium K shell x-ray. The energies of these Auger electrons are virtually identical to the energies of the photoelectrons produced by vanadium L shell electrons capturing K shell vanadium x-rays. These Auger electrons increase the number of electrons available to create the bremsstrahlung.

The manganese photons used to fluoresce a particular target also provide an additional source of photoelectrons. The energy distribution of these photoelectrons will be related to the energy difference between the manganese photons and the binding energy of the fluoresced target. These photoelectrons can also give rise to a source of bremsstrahlung. A similar effect will also occur within the  $^{55}\text{Fe}$  source. Here, the iron L shell electrons can absorb escaping manganese photons to create a source of photoelectrons. In addition, manganese Auger electrons will provide an extra source of electrons which can produce bremsstrahlung radiation.

This extraneous radiation can be eliminated by incorporating an appropriate absorber between the specimen and the detector. However it is not feasible to remove all of the bremsstrahlung in this way. The energy difference between the upper limit of the bremsstrahlung and that of the  $K\alpha$  photo-peak is quite small, hence an absorber which would remove all the bremsstrahlung would remove virtually all the  $K\alpha$  photo-

peak in the process.

Figure 7.4 shows two fluoresced vanadium spectra. Both spectra were acquired under the same conditions, only in one the detector was covered by 25  $\mu\text{m}$  of aluminium. This thickness of aluminium absorbs 45% of vanadium  $K\alpha$  x-rays and 61% of the bremsstrahlung at 4.2 keV. The intensity change although small can still be seen. Estimating the magnitude of the bremsstrahlung contained in either spectrum is difficult but an approximate method based upon experiment can be performed.

If these vanadium spectra are scaled together correctly then subtracted, the difference between the two represents the radiation absorbed in the aluminium,  $I_a$ . A knowledge of this absorbed radiation can be used to estimate the initial intensity of radiation present,  $I_0$ . Using Beer's Law,  $I_0$  can be estimated from  $I_a$  using

$$I_0 = I_a / (1 - \exp(-(\mu/\rho)_E \cdot \rho \cdot t)) \quad 7.4$$

where  $(\mu/\rho)_E$  is the mass absorption coefficient of the bremsstrahlung radiation at energy E. The intensity absorbed is known as a number of counts,  $N_a$ , this being obtained from the subtraction of the two spectra. The initial intensity  $I_0$ , expressed as a number of counts,  $N_0$ , can then be obtained by the following argument

$$I_a = I_0 - I_t \quad 7.5$$

where  $I_t$  is the transmitted intensity

or 
$$N_a = N_0 - N_t$$

and 
$$I_a/I_t = N_a/N_t$$

$$N_t = N_a \cdot I_t/I_a$$

therefore 
$$N_0 = N_a + N_a \cdot I_t/I_a \quad 7.6$$

Before the above analysis can be performed, the effect that the absorber has on the

X-RAY: 0 - 20 keV  
Live: 11100s Preset: 11100s Remaining: 0s  
Real: 12054s 8% Dead

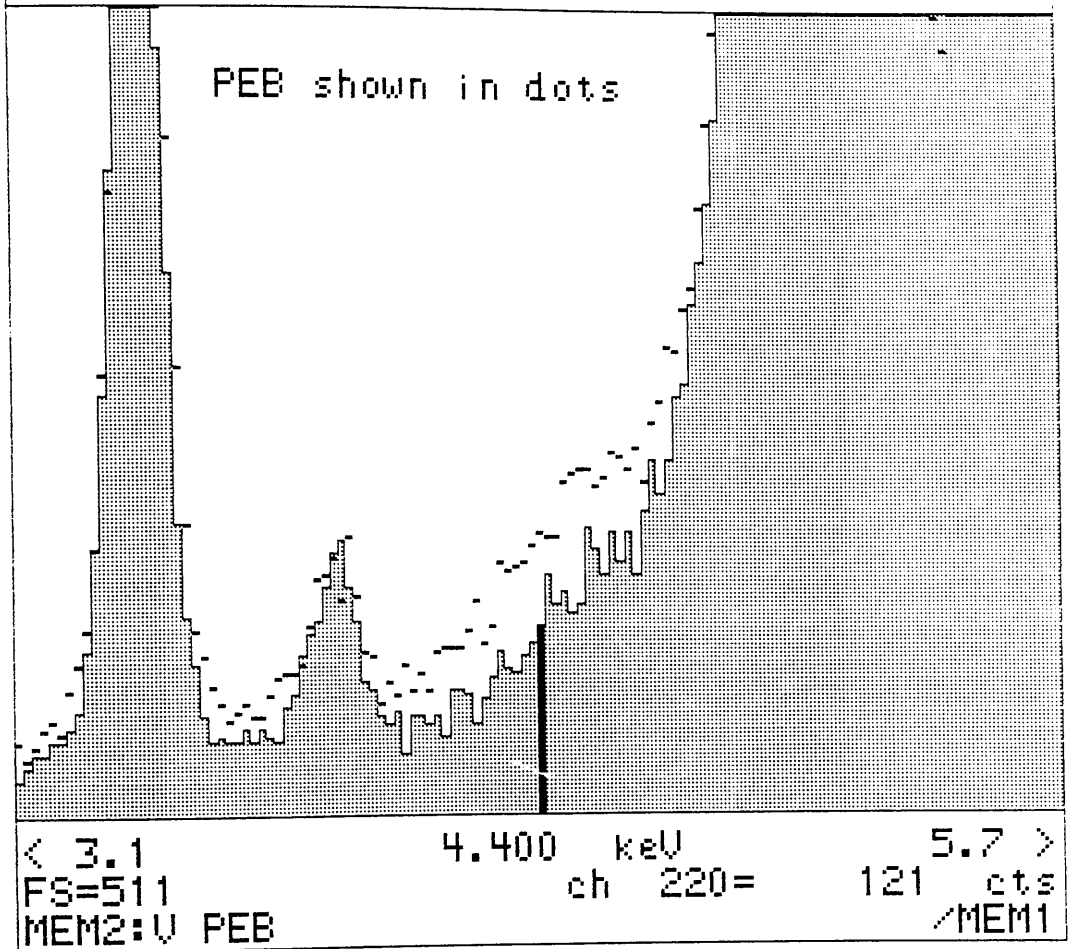


Fig. 7.4 Fluoresced vanadium spectra, one acquired with 25 $\mu$ m of aluminium to absorb the bremsstrahlung, the other (dot memory) acquired with no absorber.

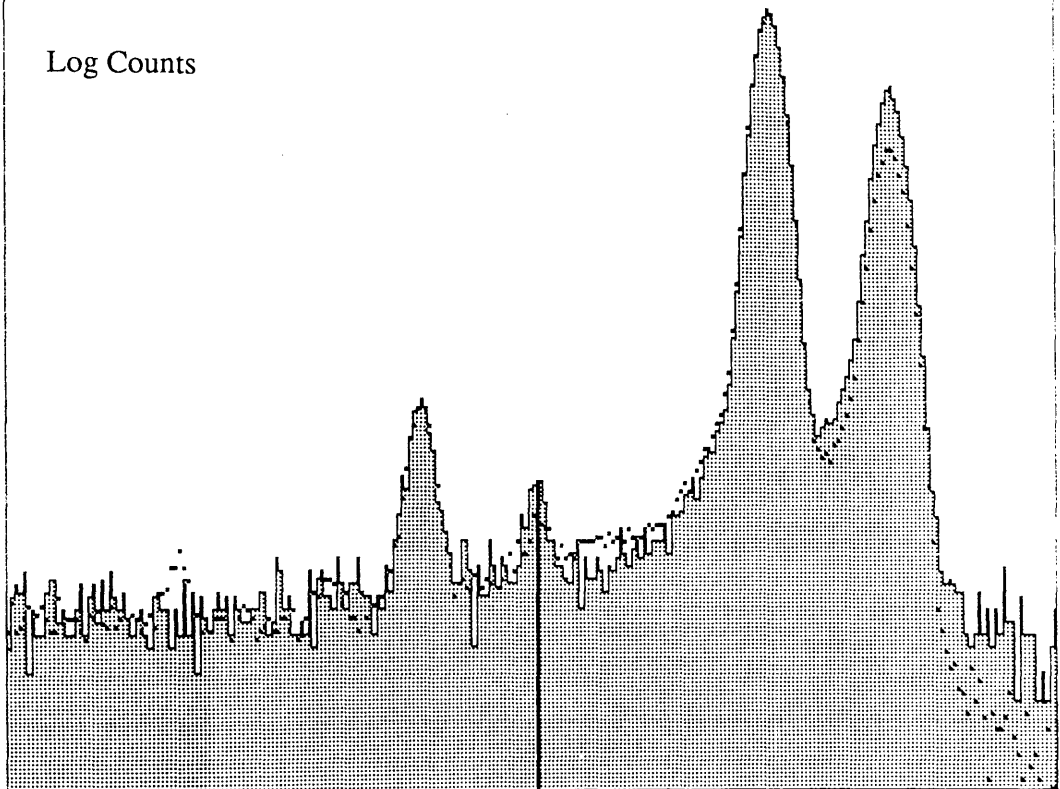
rest of the spectrum had to be established. The aluminium absorber will attenuate the  $K\alpha$  photons more efficiently than the  $K\beta$ 's and this could potentially change the underlying shape of the ICC. If this occurs, then the "difference" between the two vanadium spectra would not truly represent the absorbed radiation. It is therefore important to establish the effect that any particular thickness of absorber has upon the ICC shape in the region of interest.

A simple experiment was performed whereby the absorber thickness was progressively doubled to study if this had any effect on the manganese spectra. The thickness of aluminium was 12.5  $\mu\text{m}$  to begin with. This experiment showed that, providing the absorber was not too thick i.e.  $<100 \mu\text{m}$ , then the resulting spectra would not differ by an amount liable to cause any significant error. Figure 7.5 shows a comparison of two manganese spectra, one acquired with 100  $\mu\text{m}$  of aluminium absorber the other with no absorber. These spectra have been scaled to the integral of the  $K\alpha$  peaks. The spectrum acquired with the aluminium absorber shows slightly less counts in the region beneath the  $K\beta$  escape peak, this being caused by the loss of bremsstrahlung originating from the manganese source (this amounts to approximately 2.5% of the number of counts in the tail region). The increase in the  $K\beta$  signal does not appear to effect the ICC in any obvious way. Hence the only real difference to the tail region is due to the increased  $K\beta$  escape peak signal.

The two vanadium spectra (shown in fig. 7.4) were scaled to a central portion of the  $K\alpha$  photo-peak then subtracted. The residual counts were then corrected for the effects of absorption in the aluminium. Figure 7.6 shows the bremsstrahlung intensity before the absorption correction. Traces of the two escape peaks can still be seen. The trace from the  $K\alpha$  escape peak is due to a slight miscalibration between the spectra. The trace from the  $K\beta$  escape peak is caused by the enhanced  $K\beta$  escape peak signal. The intensity distribution shown in fig. 7.6 was then corrected for the absorption effects. An extrapolation had to be performed to estimate the number of counts below the escape peaks. Figure 7.7 shows the bremsstrahlung intensity distribution before and after (in dot memory) the absorption correction. The corrected intensity was established as being  $0.3 \pm 0.05 \%$  of the entire vanadium spectrum, or  $8.3 \pm 1.4 \%$  of the tail region. This value indicates that the fluorescence source is adding a significant number

X-RAY: 0 - 20 keV  
Live: 15574s Preset: 32767s Remaining: 17193s  
Real: 17250s 10% Dead

Log Counts



< 2.2 4.740 keV 7.3 >  
FS=256K LOG ch 247= 316 cts  
MEM2:8 & 0 Al scaled to Ka /MEM1

Fig. 7.5 Manganese spectra, one acquired with 100 $\mu$ m of aluminium to absorb the bremsstrahlung, the other (dot memory) acquired with no absorber.

X-RAY: 0 - 20 keV  
Live: 32000s Preset: 32000s Remaining: 0s  
Real: 39303s

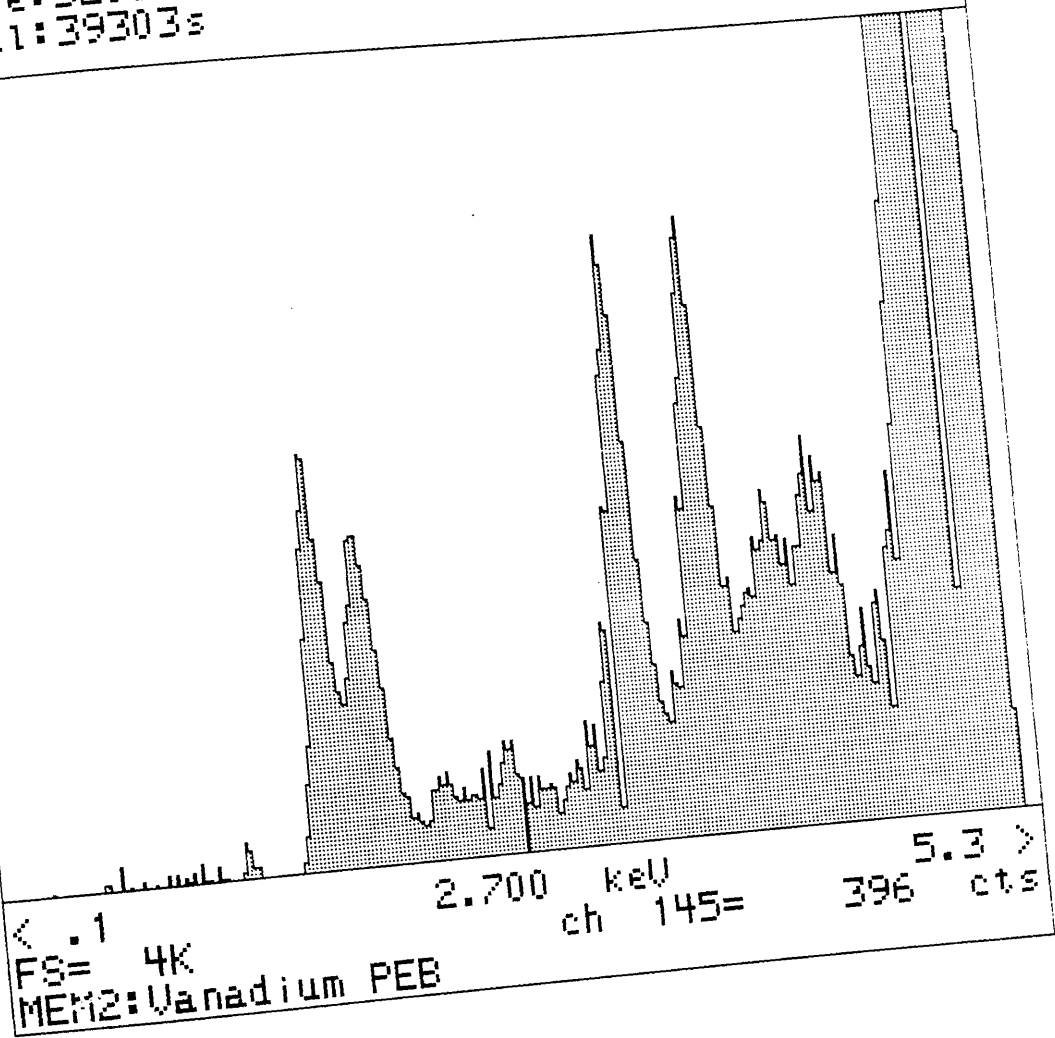


Fig. 7.6 Residual counts left after the vanadium spectra were subtracted.

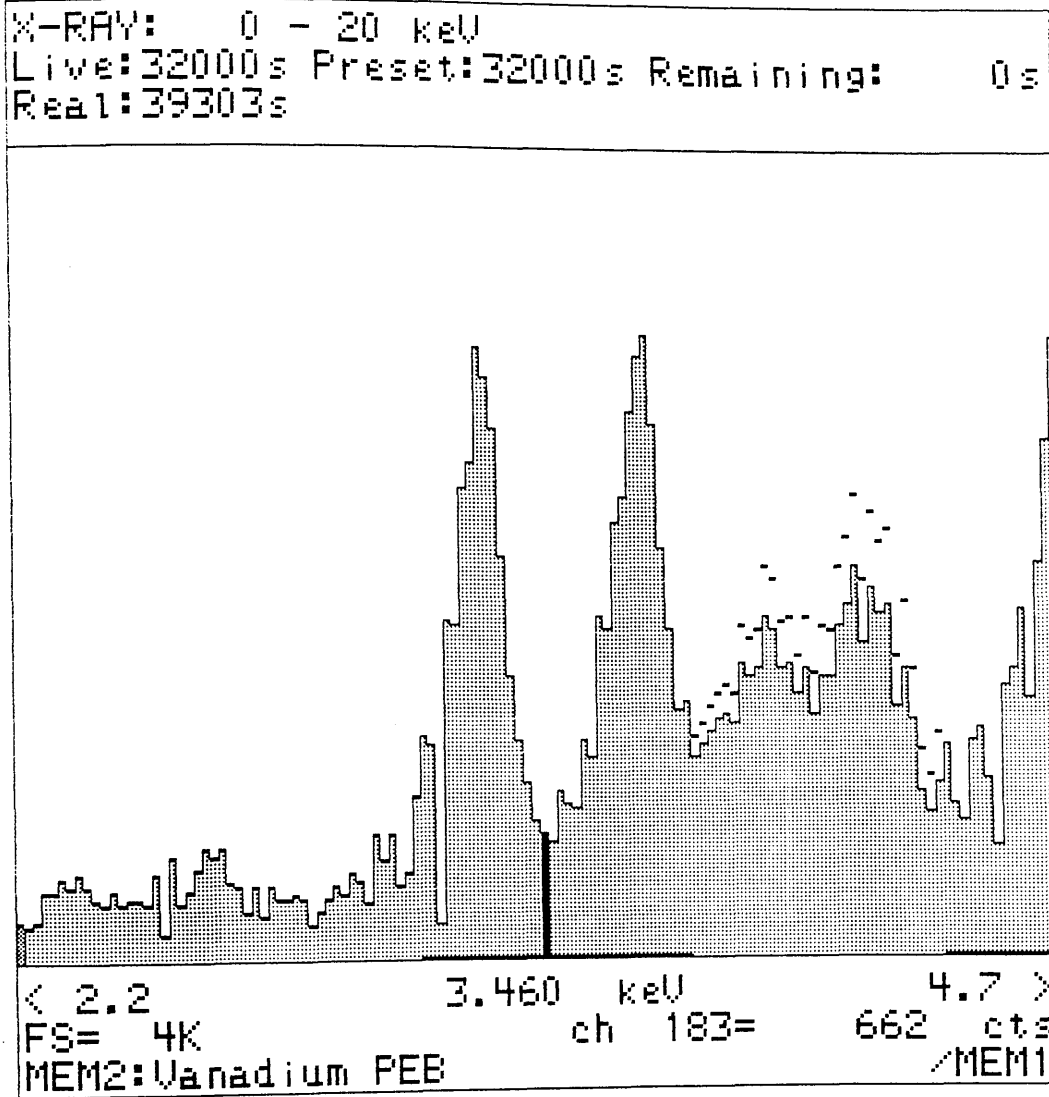


Fig. 7.7 Corrected vanadium bremsstrahlung intensity distribution, before and after (in dot memory) the absorption correction.

of counts to the ICC tail. In addition, these counts are localised to a region very close to the photo-peaks this results in a significant perturbation to the "true" ICC tail in this region.

The amount of bremsstrahlung originating from any target must be related to the mass absorption coefficient of the fluorescing manganese photon in the target material. Manganese photons absorbed close to the surface of the target create photo and Auger electrons close to the surface; hence increase the chances of the bremsstrahlung escaping. This would indicate that targets such as vanadium, titanium and scandium would contain the largest fraction of this extraneous radiation.

#### 7.4 The effect of bremsstrahlung escaping the detector.

Bremsstrahlung can also escape from the detector as it does in the fluoresced x-ray sources. Any radiation which escapes from the detector carries away energy which would otherwise be used to create electron-hole pairs and consequently this effect gives rise to counts in the tail. Since this is a fundamental effect it contributes to the ICC associated with the particular photon being detected. Bremsstrahlung escaping the detector can be included in the definition of ICC since it is a fundamental effect and cannot be eliminated by improving the detector. The magnitude of this effect is very important to establish since in an ideal detector, one with no crystal imperfections, the ICC tail would be composed only from this particular component.

Each particular species of x-ray detected gives rise to bremsstrahlung of a different energy distribution. For example, manganese  $K\alpha$  photons of energy 5.898 keV create photoelectrons in the detector of energy 4.058 keV. These photoelectrons can give rise to bremsstrahlung photons of energy up to 4.058 keV. In addition to the photoelectrons are the silicon Auger electrons, these too can give rise to bremsstrahlung radiation as they scatter through the crystal. However, the energy distribution of the silicon "Auger electron bremsstrahlung" is lower and hence more likely to be absorbed before escaping.

Any such radiation escaping from the detector would give rise to a "tailing" effect.

...theoretical model for the bulk bremsstrahlung would have been better represented using Kramers expression (eqn. 2.3) rather than the MBH theory.

### References

...References

† Strictly speaking the theoretical model for the bulk bremsstrahlung would have been better represented using Kramers expression (eqn. 2.3) rather than the MBH theory.

The nature of this tailing would depend on the energy distribution of the radiation which escapes. The tail region of a manganese spectrum contains a feature at an energy around 2.0 keV which could in theory be caused by the escape of bremsstrahlung radiation. Figure 7.8 shows this feature which can be seen as a gradual roll-off in intensity below 2.0 keV. This gradual roll-off in intensity can be thought of as the upper limit to the energy which escapes the detector when photoelectrons of an initial energy of 4.058 keV emit bremsstrahlung. The energy of the photon escaping the detector has to be subtracted away from the energy which otherwise makes up the Gaussian photo-peak. Hence, a 4.058 keV photoelectron creating a 4.058 keV bremsstrahlung photon would give rise to a count at  $\sim 1.84$  keV in the tail (remembering the Gaussian convolution). It is obviously very important to obtain an estimate for the intensity of bremsstrahlung escaping the detector in order to establish whether the roll-off seen in the manganese spectrum is caused by the escape of bremsstrahlung or some other effect.

The intensity distribution for such bremsstrahlung photons is very difficult to calculate because of the manner in which the electrons scatter in the bulk silicon. For example, the photoelectrons can create a bremsstrahlung photon at any stage during the process in which they scatter inelastically dispersing their energy. The problem actually involves multiple scattering of electrons in a bulk solid covering a range of possible energies. The depth at which the initial photoelectron is created is important since this effects the amount of radiation which can escape. It should be possible to get some information on the nature of the escaping radiation by assuming only the electrons of maximum energy are creating the bremsstrahlung. By calculating the appropriate absorption that these photons undergo on their escape from the crystal, the bremsstrahlung intensity distribution can be suitably modified. The bremsstrahlung distribution can be obtained from the MBH theory as a first approximation. Calculating the absorption undergone by the bremsstrahlung intensity can be performed using the model proposed by Reed and Ware (1972) for calculating the intensity of the escape peak. The Reed and Ware model considers what fraction of the silicon photons created within the detector that can escape. The detector is assumed to be infinitely deep and wide, which is perfectly justifiable for low energy photons. From this starting point

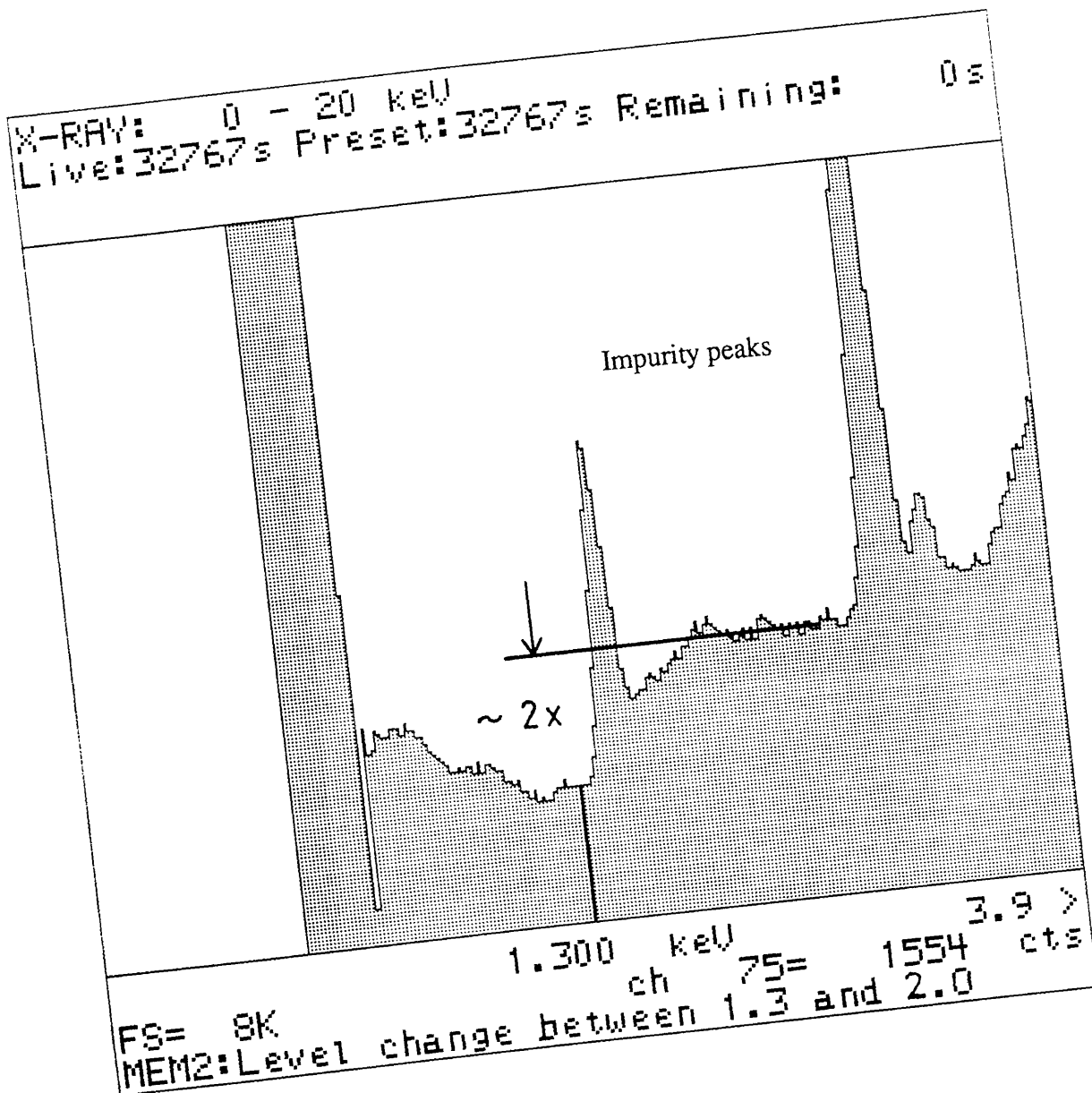


Fig. 7.8 Gradual intensity "roll-off" seen in the manganese spectrum below 2.0 keV. A level change of ~2 is seen.

Reed and Ware have shown that  $\epsilon$ , the fraction of the emitted silicon K radiation that escapes from the detector is given by

$$\epsilon = 0.5(1 - (\mu/\rho)_{Si} / (\mu/\rho)_i \cdot \ln(1 + (\mu/\rho)_i / (\mu/\rho)_{Si})) \quad 7.7$$

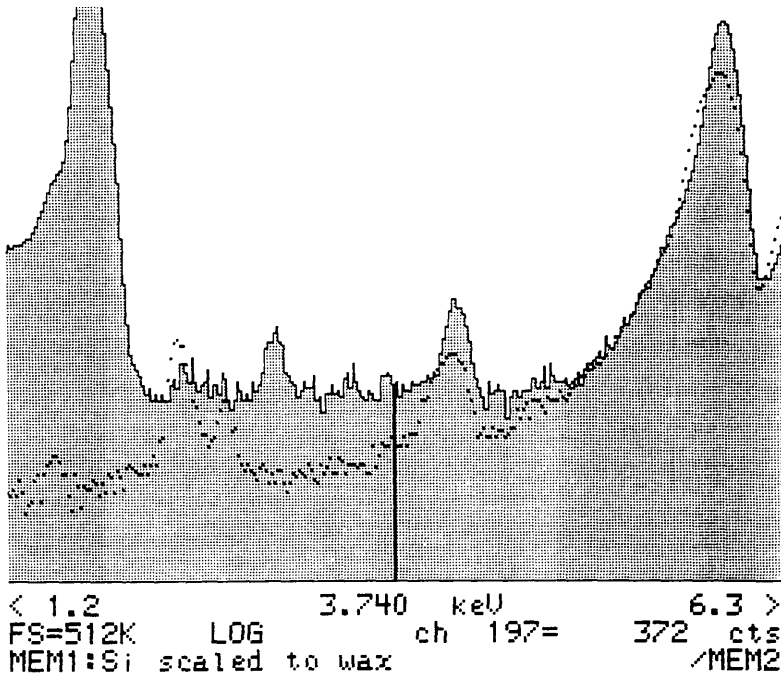
where  $(\mu/\rho)_{Si}$  is the mass absorption coefficient of the silicon photons in silicon and  $(\mu/\rho)_i$  is the mass absorption coefficient of the incident photon. This expression can be simply modified to consider the bremsstrahlung. This merely involves replacing  $(\mu/\rho)_{Si}$  by  $(\mu/\rho)_p$  the mass absorption coefficient of the escaping bremsstrahlung. The major difficulty with this idea is the fact that the efficiency of the bremsstrahlung production is difficult to estimate. Hence the above method can only provide a shape function and this is only an approximation to the actual shape. If accurate efficiency calculations could be made then the photoelectron's energy could be divided into suitable portions and a bremsstrahlung intensity distribution derived for each. These could then be summed and finally corrected for absorption. A Monte Carlo type simulation could be used for such a problem but an experimental approach is much simpler.

There are two convenient experimental methods for studying the bremsstrahlung intensity escaping the detector. The first method involves fluorescing bulk silicon with manganese photons. The spectra obtained from such an irradiation is equivalent to the radiation which escapes the detector under a similar irradiation. The second method involves irradiating bulk silicon with low energy electrons. Any bremsstrahlung radiation which escapes the silicon on irradiation with electrons is equivalent to the radiation contribution from the photoelectrons generated during the detection process.

The information revealed by these experiment would allow an estimate to be made to determine whether the level of bremsstrahlung escaping the detector would allow the magnitude of the roll-off seen in the manganese spectra. These experiments, the physical basis for performing them and their results are now described.

When bulk silicon is fluoresced by manganese photons the spectrum consists of all the radiation which escapes the silicon, this being fluoresced silicon photons,

backscattered manganese photons and any bremsstrahlung that may escape; see fig. 7.9 (a). As was mentioned earlier, a 4.058 keV photoelectron is produced for every manganese  $K\alpha$  photon absorbed by a silicon K shell electron. Therefore any bremsstrahlung escaping the silicon manifests itself as a change in the background level from 4.058 keV down towards 0 eV. Strictly speaking there will be additional contributions from the absorption of  $K\beta$  photons by K shell electrons and from the absorption of both  $K\alpha$  and  $K\beta$  x-rays by L shell electrons. However, these extra contributions will be of a far lower intensity than any bremsstrahlung from the  $K\alpha$  photons (purely on the basis of the relative intensities of the particular photons). In the region between the silicon and manganese photo-peaks the background consists of the ICC from the backscattered manganese x-rays plus any additional bremsstrahlung. Therefore, by carefully removing the manganese contribution the bremsstrahlung should be seen. In a fluoresced silicon spectrum the backscattered manganese photo-peaks contain a far higher proportion of Compton scattered photons than in a normal manganese spectrum. This results in the manganese photo-peaks being broadened somewhat and gives problems when trying to perform an accurate subtraction. Two different manganese spectra were used to perform this background subtraction. The first was the spectrum obtained from the backscattering of manganese photons off wax. The second was a normal manganese spectrum. Using these two spectra for the subtraction process gives an upper and lower limit for the energy broadening actually seen for the backscattered peaks seen in the silicon spectrum since the amount of Compton scattered photons in a backscattered spectrum varies approximately linearly with Z (more with low Z targets). Fluoresced silicon spectra were acquired over a period of days to obtain high statistical accuracy. In subtracting the manganese contribution, the spectra were scaled to the integral of the  $K\alpha$  photo-peak. This is equivalent to scaling to equal numbers of incident  $K\alpha$  photons and should result in an equal proportion of ICC in each spectrum. After removing the manganese contributions residual counts were seen in both silicon spectra. These should be caused by the effects of bremsstrahlung escaping the silicon. Figures 7.9 (a) and (b) shows the silicon spectrum before and after the subtraction of the manganese contributions. The counts which remain after this subtraction are at a very low level and suffer from poor



Log Counts

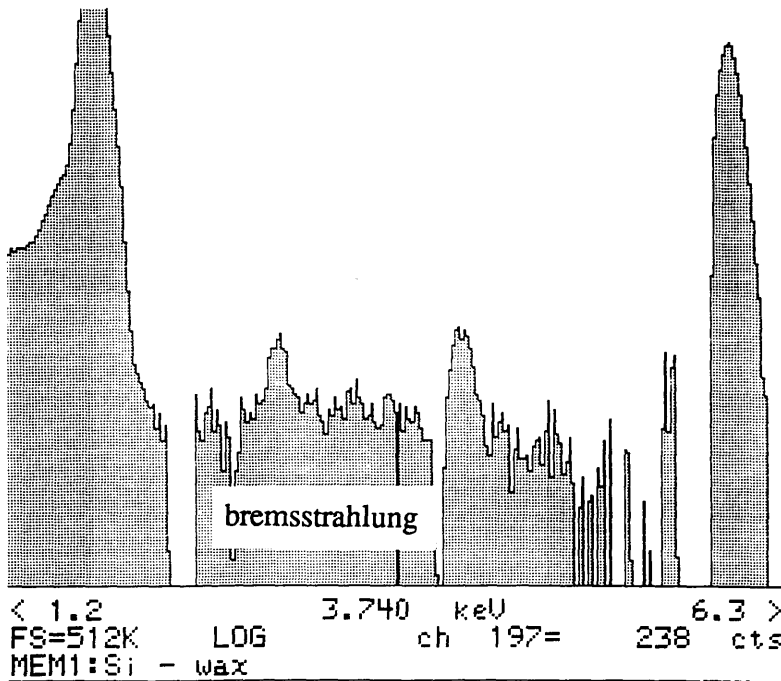
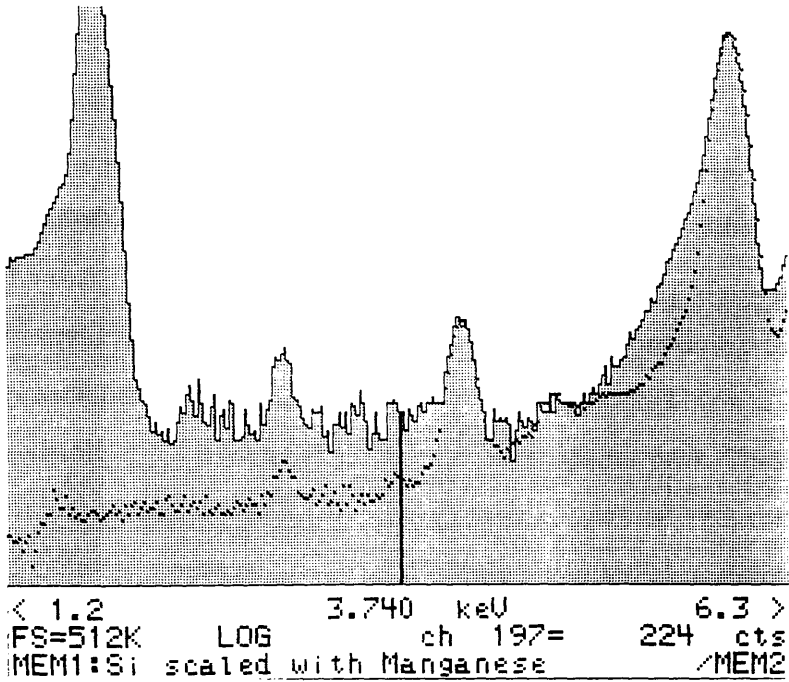


Fig. 7.9 (a) Fluoresced silicon spectrum before and after the subtraction of the manganese contribution (dot memory; manganese backscattered off wax).



Log Counts

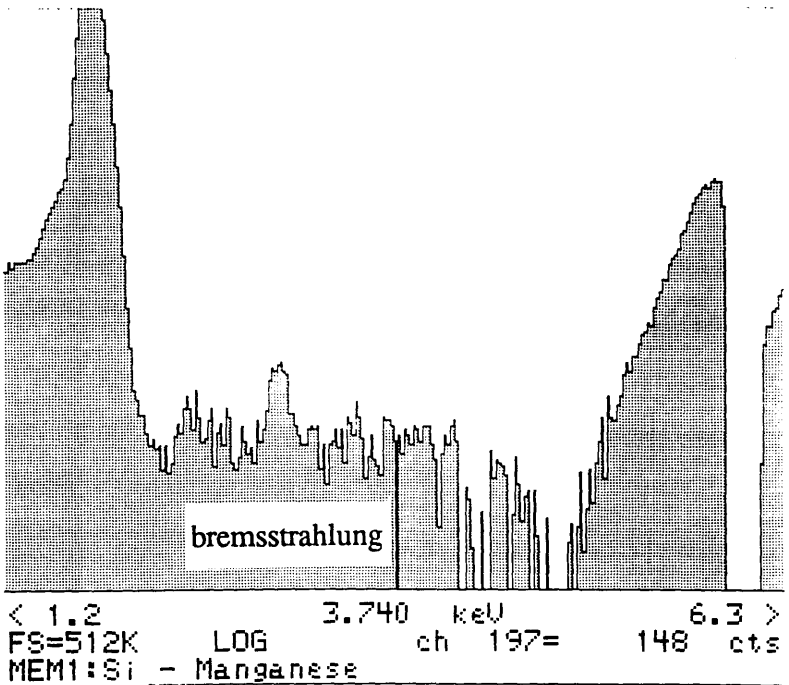


Fig. 7.9 (b) Fluoresced silicon spectrum before and after the subtraction of the manganese contribution (dot memory; normal manganese spectrum).

statistical accuracy. The spectrum terminates at 4.1 keV due to an over subtraction of the escape peak contribution.

The bremsstrahlung contribution for the two different subtractions were divided by the total number of counts in the silicon photo-peak. This indicated that the first silicon spectrum (the one from which the "wax" spectrum had been subtracted) contained 0.15% bremsstrahlung and the second silicon spectrum (containing the manganese subtraction) contained 0.2% bremsstrahlung. These values were obtained by integrating those counts visible to the right hand side of the silicon photo-peak. These values have a large error associated with them purely on the basis of the subtraction. A conservative estimate would suggest that this value may vary by up to +/-20%. This must indicate that manganese photons incident upon the detector give rise to very little bremsstrahlung escaping the crystal, this is probably due to the large depth distribution of the absorbed manganese photons (~30  $\mu\text{m}$ ).

Geometrically this target, source, detector arrangement should in fact give rise to more bremsstrahlung than for the case of manganese photons incident upon the detector. This can be seen from the diagram in fig. A3.9 (appendix 3). As indicated in the diagram, the manganese photons are incident upon the silicon target over a wide range of angles. This effectively means that the depth distribution for the creation of photoelectrons is less than it would be for a normal incidence situation. This geometrical factor increases the probability of the bremsstrahlung escaping the target. Hence any bremsstrahlung escaping the detector would be at an even lower level than that quoted above.

This information on the bremsstrahlung escaping the silicon can now be used to establish whether this effect affects the tail of the manganese spectrum.

If the tail on the manganese spectrum is indeed caused by the effects of bremsstrahlung escaping the detector, then ideally, the ratio of the number of counts in the silicon escape peak, to the number of counts in the tail of the manganese spectrum, should be the same/similar as a similar ratio taken with the two fluoresced spectra (after the manganese subtraction) described earlier. The silicon escape peak in the manganese

spectrum is equivalent to the silicon photo-peak in the fluoresced spectrum (i.e. the escape of silicon K photons). For practical reasons this was actually done by setting an "energy window" over a small region of the bremsstrahlung tail then dividing the number of counts in this window by the number of counts in the silicon photo-peak. This "energy window" eliminates problems with any "zero's" in the bremsstrahlung tail due to over subtraction of the manganese ICC. A similar energy window was set in the manganese spectrum and this window was subsequently divided by the number of counts in the silicon escape peak. The manganese spectrum had also to be corrected to allow for the shape of the tail under the region thought to be caused by bremsstrahlung escaping. It was difficult to infer what this underlying shape would be, so to keep matters simple to begin with a constant level was subtracted off the entire spectrum. This constant level was chosen as the number of counts in the channel containing the least counts (1.14 keV). If this technique was found to give the kind of answer that we were looking for, then more thought could be given to infer the exact shape below the bremsstrahlung (probably some kind of gradual exponential decrease from the photo-peak down to 0 eV).

Using the spectra shown in fig. 7.9(a) and (b), a window was chosen between 3.4 and 3.8 keV, the mid-point being 1.86 keV higher in energy than the silicon photo-peak. The number of counts in this region were integrated. Since this fluoresced spectrum represents energy escaping the detector crystal, a similar window has to be set in the manganese spectrum 1.86 keV "lower" than the escape peak. The manganese spectrum having also been corrected to allow for the step at 2.0 keV. This window integral along with that from the escape peak were taken. The ratios obtained were found to be:

silicon spectrum minus wax: 0.00031 (+/- 20%)

silicon spectrum minus manganese: 0.00034 (+/- 20%)

manganese spectrum: 0.08 (+/- 3%)

The ratios for the two fluoresced spectra are very similar; however, the equivalent ratio from the manganese spectrum is approximately two orders of magnitude higher.

This difference is far too large to be explained by any error in the subtraction of the underlying shape of the tail and hence must indicate that the tail on the manganese spectrum is caused by ICC originating from the various trapping effects. If this is indeed the case, then this suggests that this tail could in theory be minimised to virtually insignificant levels by subsequent detector improvements.

A second means of experimentally estimating the intensity distribution of the bremsstrahlung escaping the detector can be obtained by irradiating a piece of bulk silicon with low energy electrons. This can be done on a scanning electron microscope where the bremsstrahlung intensity distribution can be studied as a function of electron energy. Ideally the energy of the incident electrons should be the same as the photoelectrons created within the detector crystal as a particular photon is absorbed. The electrons incident upon the silicon can interact with the atoms in several different ways, one being the emission of bremsstrahlung. This bremsstrahlung can be considered as being emitted into a solid angle of  $4\pi$ , which is justifiable due to the random scattering of the electrons. The detected bremsstrahlung spectrum is equivalent to the bremsstrahlung distribution created as photoelectrons scatter inside the detector crystal. However, this intensity distribution must be considered as having been created in a surface layer  $dx$ . Irradiation by electrons therefore allows far more radiation to escape since the interactions take place much nearer the surface of the silicon. The bremsstrahlung distribution must therefore be corrected for the absorption effects which occur as the bremsstrahlung escapes the crystal from a depth consistent with absorption of manganese photons. This absorption correction is necessary since the range of electrons in silicon is far less than the range of the photons required to create photoelectrons of that energy. (The depth distribution of the electrons in the bulk silicon can be calculated from Fitting's equation (1974)). The absorption correction was performed using the method of Reed and Ware (1972); see eqn. 7.7. In addition to the creation of the bremsstrahlung some of the incident electrons ionize the silicon atoms, in doing so they generate Auger electrons and silicon K and L shell x-rays. Any silicon x-rays which are created in this way are equivalent to those created by photoelectrons as they scatter within the detector. The intensity of silicon x-rays created by the electron

irradiation is far lower than the intensity created when the silicon target is irradiated by photons. For each photon absorbed within the silicon target an atom is excited. This excited atom must de-excite and in doing so creates a source of Auger electrons and silicon x-rays.

The number of electrons incident upon the target is approximately equal to the number of photoelectrons produced by K shell photo-absorption in silicon (neglecting backscatter). Hence, we also know the number of silicon K ionizations. If the number of electrons incident upon the target is known (obtained from the beam current), then the number of silicon K shell x-rays created by photo-absorption can be approximated. The number of electrons is simply multiplied by the K shell fluorescence yield for silicon ( $\sim 0.043$ , Dyson, 1973<sup>3</sup>) to obtain the number of silicon K shell x-rays produced. The number of photons must subsequently be corrected for the effects of absorption as the silicon x-rays escape the target. The number of x-rays can subsequently be corrected to consider only those which are collected, this requires the solid angle subtended at the detector. Once the correction for the silicon intensity has been made, we can again use the ratio of the silicon peak to the background as a comparison to the manganese spectrum.

An experiment based on the above method was performed to test the accuracy of the ratio's obtained earlier. Due to certain difficulties with the equipment the accuracy of this experiment was limited. However, it is sufficient to provide an order of magnitude estimate for the value we require. A bulk silicon target was irradiated with 6 keV electrons in a scanning electron microscope. The energy of these electrons was slightly higher than the energy of the photoelectrons which would be created as manganese photons were absorbed in silicon; however results about to be described show that this was not serious enough to justify repeating the experiment. The beam current was measured at approximately  $0.3 \pm 0.1$  nA. The solid angle subtended at the detector  $\Omega_{\text{DET}}$ , was calculated as being  $6.2 \times 10^{-5}$  st. rad. The acquisition time  $t$ , was 1200 s. The number of photons which would have been collected is therefore

$$N_x = (I/e) \cdot t \cdot (\Omega_{\text{DET}}/4\pi) \cdot \omega_K \quad 7.8$$

$$= (0.3 \times 10^{-9} / 1.6 \times 10^{-19}) \times 1200 \times 6.2 \times 10^{-5} \times 0.043$$

$$= \sim 6 \times 10^6 (+/- 30\%)$$

The Reed and Ware model predicts that 9% of the silicon photons created by 7.84 keV photons will escape the silicon target (7.84 keV = 6 keV for the incident electron + 1.84 keV for the silicon binding energy). This therefore means that a total of 540,000 (+/-30%) silicon K photons should have been produced. The experimental bremsstrahlung intensity was corrected for absorption as the photons escape the silicon. This was done using the Reed and Ware (eqn. 7.7) with the mass absorption coefficient for a 7.84 keV photon used to estimate the depth distribution of the incident radiation. Figure 7.10 shows the experimental bremsstrahlung intensity before and after the absorption correction.

A 400 eV "window" was set in the bremsstrahlung background centered at an energy 1.86 keV higher than the silicon photo-peak. The ratio of the number of counts in this "window" to that of the "true" silicon photo-peak (detected silicon + theoretical estimate) was calculated, this being 0.00027 (+/- 7%). This value can be seen to compare very favourably with the values found for the fluoresced silicon target (0.00031 and 0.00034). This therefore gives a second verification that the level of bremsstrahlung escaping the detector has an insignificant effect on the tail of the manganese spectrum.

Goulding and Jaklevic (1977) have studied mechanisms which can give rise to the low energy tails. In this work they considered bremsstrahlung escaping from the detector and from the source. They derive a qualitative model for the probability of the emission of photons of energies ranging from  $E_p$  to  $E_p/n$ , this takes the form

$$P_T = 2.5 \times 10^{-6} Z E_x (\ln(n) + (1/n) - 1) \quad 7.9$$

where  $E_x$  is the energy of the photoelectron, in keV's. Using this expression to calculate the probability of bremsstrahlung escaping from silicon (over an

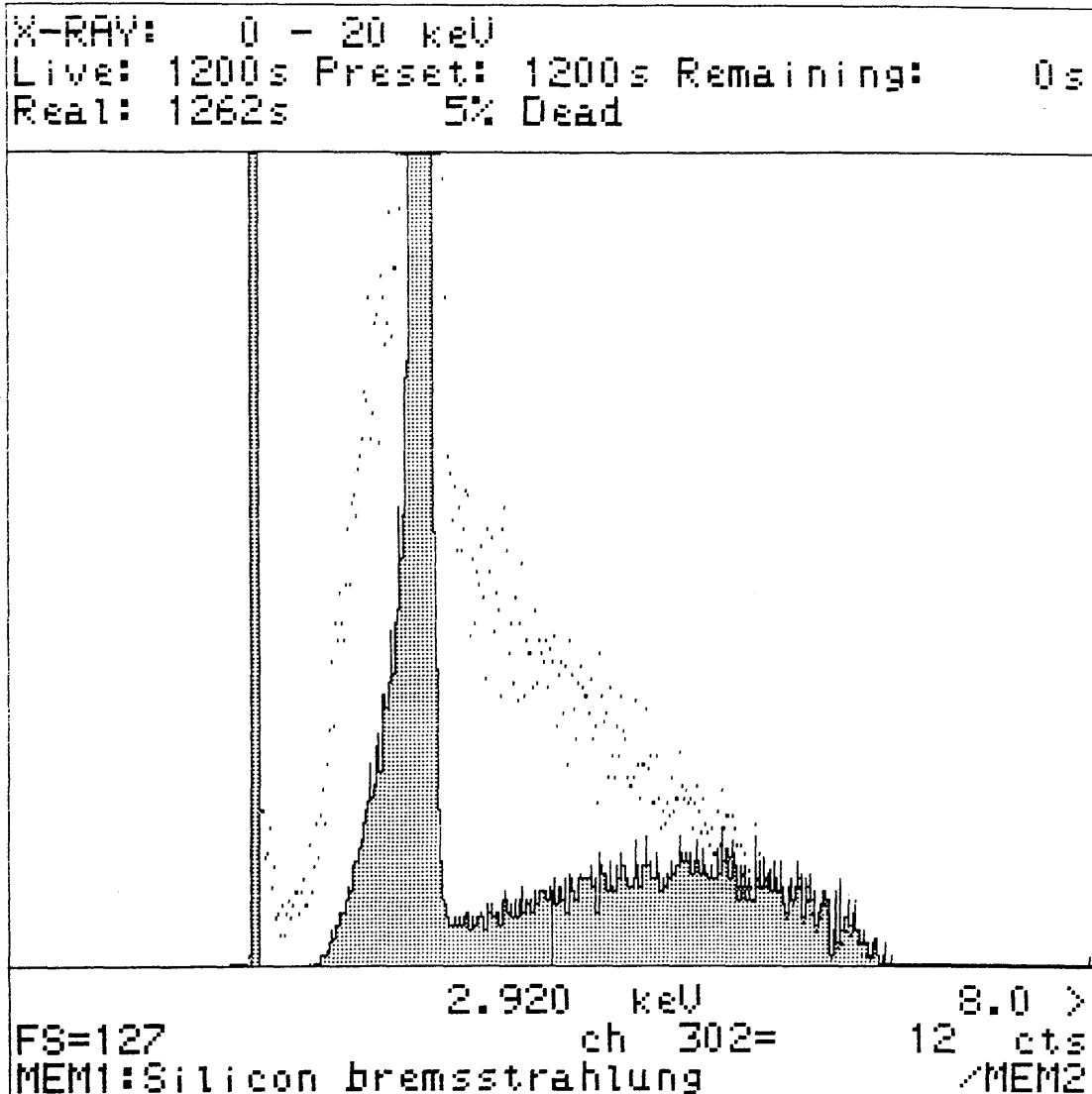


Fig. 7.10 Experimental bremsstrahlung intensity before (dot memory) and after correction for absorption in silicon.

energy range of 2 to 4 keV, where  $n = 2$ ) for incident manganese photons, gives a probability of  $\sim 2.8 \times 10^{-5}$ . This value is the probability of getting a count in a channel over the energy range 2 to 4 keV, per count in the photo-peak. This indicates that for a silicon photo-peak containing  $16.5 \times 10^6$  counts, the bremsstrahlung contribution in the tail should be

$$16.5 \times 10^6 \times 2.8 \times 10^{-5}$$

$$\sim 460 \text{ counts}$$

whereas the observed tail contains  $\sim 3000$  counts over an equivalent energy region.

Our experimental results have given two independent estimates for the bremsstrahlung contribution which give close agreement. This therefore appears to indicate that the analytical expression of Goulding and Jaklevic underestimates the level of bremsstrahlung.

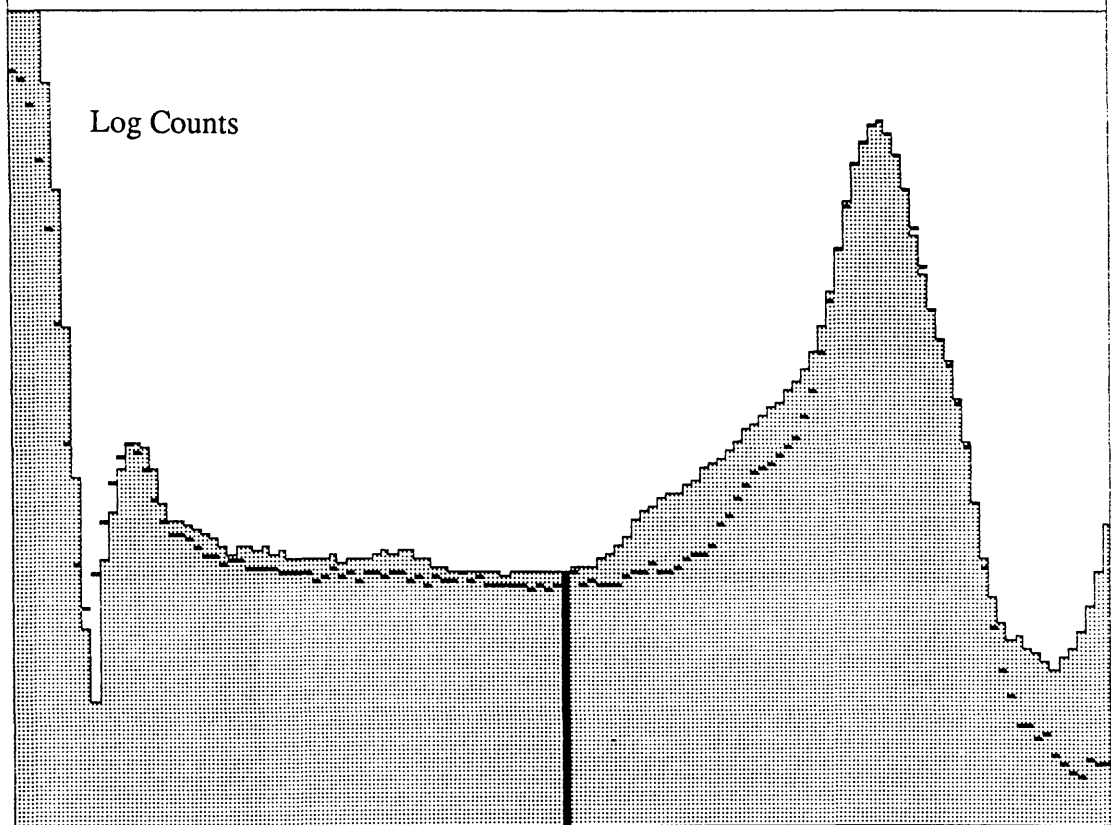
#### 7.5 Considerations for a model to describe the ICC in the ICC tail.

Ideally it would be desirable to have an analytical expression to describe the shape of the ICC which also allows for the other effects which contribute to the tail. At present, the nature of the trapping processes which give rise to the tail are not known with enough accuracy to allow such a model. Several authors have however proposed qualitative models which can describe the particular shape of the tail obtained as a function of the incident photon energy. Using fluoresced spectra from the older type Link detectors, Craven et al. (1985) have very successfully parameterised the exact shape of these spectra as a function of their photon energy and mass absorption coefficient in silicon. This model does not consider or require any of the detailed mechanisms which may be occurring in the detector in order to arrive at the final mathematical expression. Campbell et al. (1985) have developed a fitting technique for

the spectra from Si(Li) detectors using the HYPERMET function (Phillips and Marlowe, 1976). In this work they also consider some of the processes likely to give rise to the observed shapes. Using a similar mathematical approach to that of Campbell et al., Inagaki et al. (1987) have developed a detector response function capable of describing the exact shape of the tail. In this work they also propose a simple explanatory model whereby the escape of photo or Auger electrons, from the bulk, into a silicon dead layer gives rise to the ICC. This "dead layer model" does manage to predict a similar shape for the spectra in the region close to the photo-peaks, but cannot predict the correct shape of the tail at lower energies. A careful study of the spectra given in this paper shows that the detectors being used were of a poorer quality, in terms of the ICC tail, than the Link series E detectors being used in this work. This is an important factor which must be allowed for in any expression to describe the tail, i.e. it must be detector dependent. Figure 7.11 shows examples of two phosphorus spectra taken with the HB5 and JEM detectors, these clearly show that a large difference exists between these two detectors. This difference has already been illustrated in fig.'s 5.1 to 5.5 for manganese spectra. However, the surface effect, which is obviously very different for these two detectors, can be seen more clearly with phosphorus x-rays which probe the surface of the detectors more directly. The only real difference between the two spectra can be seen close to the photo-peak. Here we can see that there is far more ICC for the JEM detector. It is correct to say that this difference is ICC since the level of the fundamental effects would be approximately the same for both detectors. It is also interesting to note that the difference which exists between these two detectors manifests itself as ICC extending down to approximately  $E_p/2$ . This means that the additional traps can only trap up to 50% of the carriers from any charge pulse.

Previous work carried out within our research group had provided a set of fluoresced spectra covering most elements from magnesium to vanadium. When observed in a logarithmic mode all of the fluoresced spectra can be seen to have regions which are approximately linear; fig. 7.12 shows this for a titanium spectrum. These linear regions would therefore represent an exponential decay when observed in a linear energy scale and could be fitted by an exponential function. The exponential decay

X-RAY: 0 - 40 keV  
Live: 32767s Preset: 32767s Remaining: 0s



< .0 1.280 keV 2.6 >  
FS= 2M LOG < 1 ch 74= 1132 cts  
MEM2: Phosphorus JEM & HB5 /MEM1

Fig. 7.11 Phosphorus spectra from JEM and HB5 (dot memory) detectors.

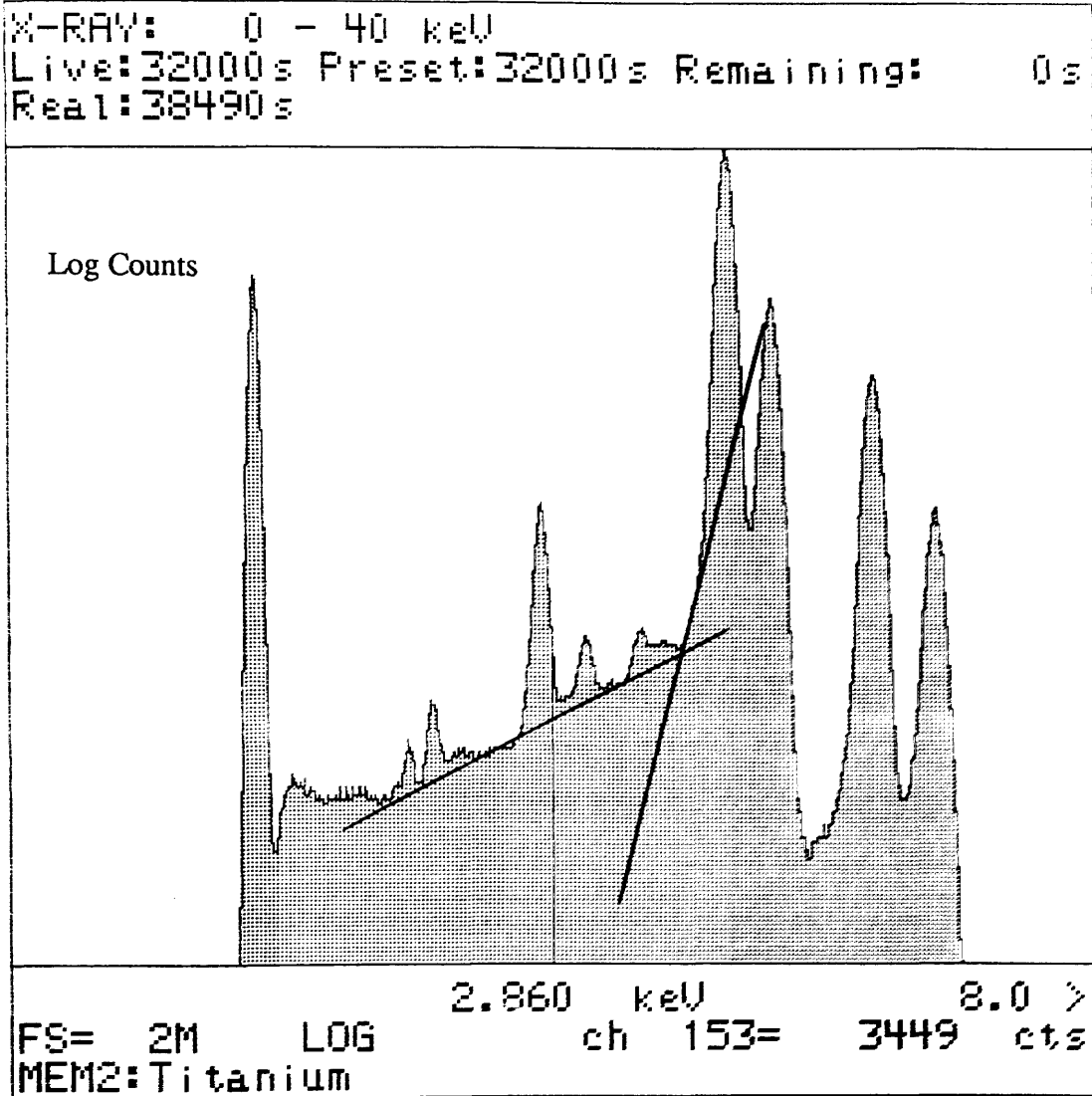


Fig. 7.12 Titanium spectrum in logarithmic mode showing the apparent linear regions.

constant can be derived from the gradient of the linear regions. These exponential regions were similar to that found by Adam (1985) for the fluoresced spectra taken with the older detectors.

Since the spectra from the new detectors had similarities to those from the older detectors it was decided to use the same method of analysis as Adam had done for the older detectors. The various fluoresced spectra had their tails divided into regions normalised to represent equal fractions of photon energy. The ICC in these areas, expressed as a percentage of the total ICC in the spectrum, was graphed against the mass absorption coefficient of the photon in silicon. This is shown in fig. 7.13 for two such cases, those for the ICC at energies  $E_p/2$  and  $3E_p/4$ . These graphs along with others taken over other energy regions, show that the ICC tail varies linearly with the mass absorption coefficient over a range of energies. Below energies of approximately 600 eV a different type of relationship appeared to exist. The graph representing the half energy case shows that some points lie above the line. These points are from silicon and aluminium which have a low photon energy and are just beginning to show the effects that occur below 600 eV.

This relationship between ICC and the mass absorption coefficients was similar to that found by Craven et al. (1985, 1987). This work of Craven et al. had shown that a graph of the percentage ICC in a fluoresced target plotted against the mass absorption coefficient, of that target's photons in silicon, gave a straight line graph with a non-zero intercept on the y-axis, see fig. 7.14. The reason for this non zero intercept was not understood, but may have been caused by the poor fitting of Gaussians to the photo-peaks. Over a certain energy range, the new detectors display similar relationship between the ICC and the mass absorption coefficient. This may be an indication that it is possible to fit the fluoresced spectra from the series E detectors with an analytical expression similar to that found by Craven et al. (1985). The expression found by Craven et al. parameterises the tail as a function of the photon energy and the mass absorption coefficient of the photon in silicon. This parameterisation considers the tail being made up from three terms each of which dominates a particular region of the spectra. The final expression obtained takes the form

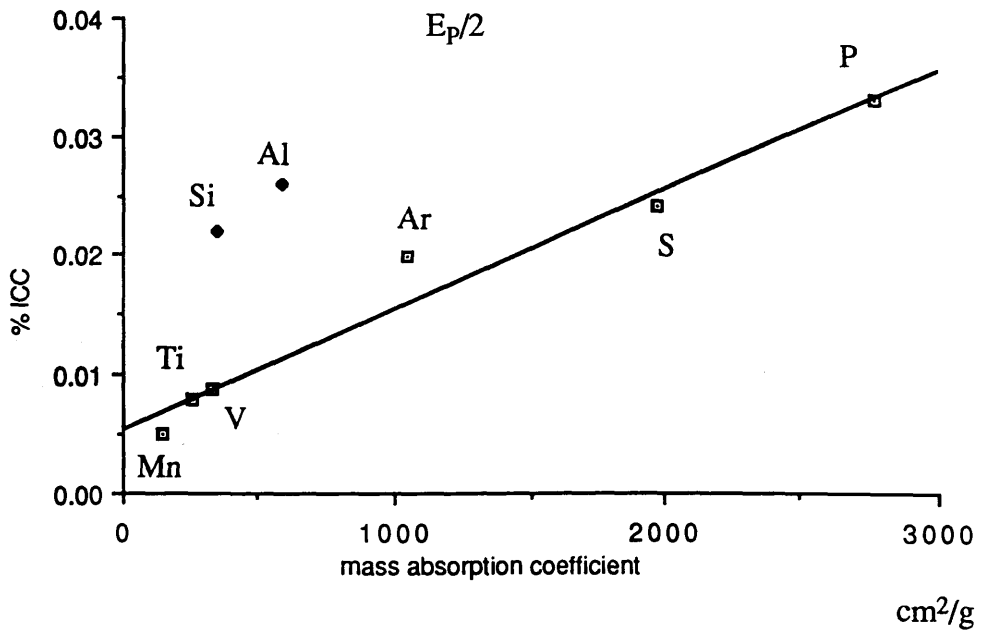
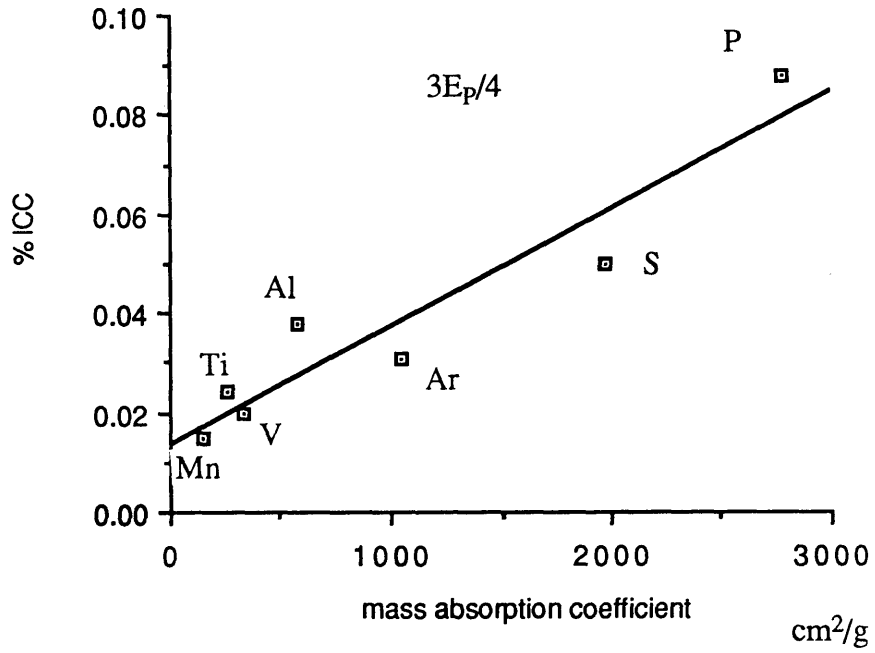


Fig. 7.13 Graphs showing the linear relationship between the ICC tail (at  $3E_p/4$  and  $E_p/2$ ) and the mass absorption coefficients.

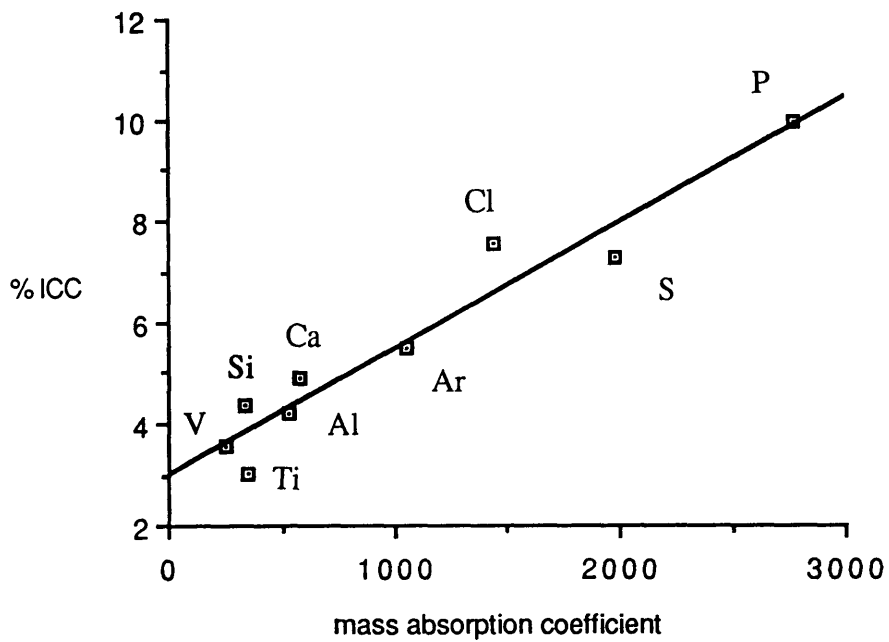


Fig. 7.14 Graph showing the linear relationship between the total ICC in the tail region and the mass absorption coefficients (Craven et al. 1987).

$$I_{ICC}/I_T = A(\mu/E_p)\exp(\alpha E/E_p) + B(\mu/E_p)\exp(\beta E/E_p) + C/E(1-\gamma E/E_p).H(E) \quad 7.10$$

where  $I_{ICC}$  is the intensity of ICC at a particular spectrum energy,  $I_T$  is the total intensity in the spectrum,  $\mu$  is the mass absorption coefficient of the photon in silicon,  $E$  is the energy in the spectrum,  $E_p$  is the photon energy,  $\alpha$ ,  $\beta$ ,  $\gamma$  and  $C$  are constants and  $H(E) = 1$  for  $E < E_p/\gamma$ , and 0 for all other values. The terms  $A(\mu/E_p)$  and  $B(\mu/E_p)$  are polynomials in  $\mu/E_p$ .

A short investigation indicated that the first term in eqn. 7.10 could be used to fit an exponential to the region below the photo-peak in each of the fluoresced spectra. However, no systematic variation could be found to explain the variations in the particular values of the exponentials used. The second term in eqn. 7.10 could be used with limited success. The spectra from those elements with photon energies greater than 3 keV (argon and those with greater  $Z$ ) show a second region over which a second exponential could be fitted. However, the spectra from the other elements (chlorine and elements with lower  $Z$ ) did not show this exponential region. These elements show an approximately constant region which extends across the spectrum. The third term in eqn. 7.10 did not fit the data.

## 7.6 Investigation of the low energy region of the tail.

The previous section has shown that the very low energy region of the ICC tail appeared to behave in a different manner from the rest of the tail. Possible reasons for this were investigated and are now described. For the remainder of this section the region below 1.2 keV will be referred to as the "low energy end".

When compared directly, a certain similarity in shape can be seen for each of the fluoresced spectra in the region around 1.0 keV. Each of the spectra appeared to have a minimum at  $\sim 1.14$  keV. This is shown in fig. 7.15 for four different combinations of the spectra. There is no obvious reason why the different fluoresced spectra should each have this common feature. Below this region the spectra all appear to "peak" before the electronic "roll-off", inherent to the Link pulse processors (see appendix 4),

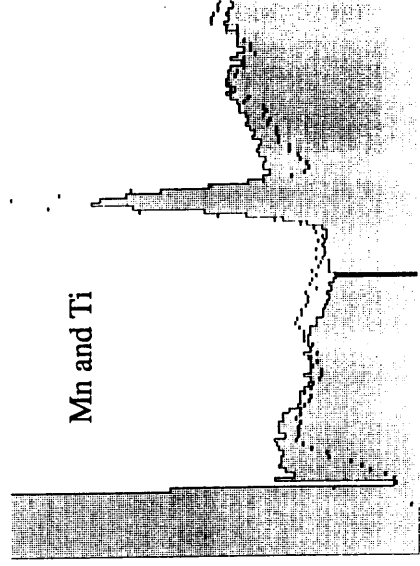
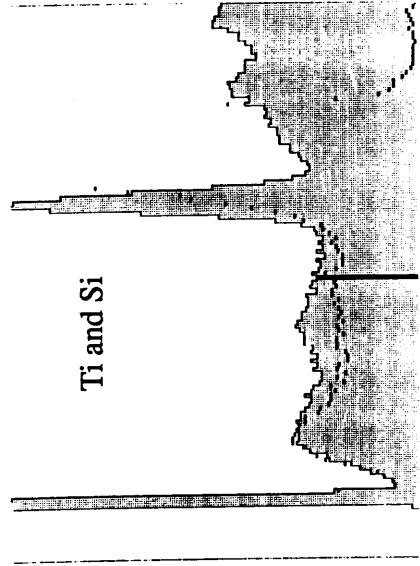
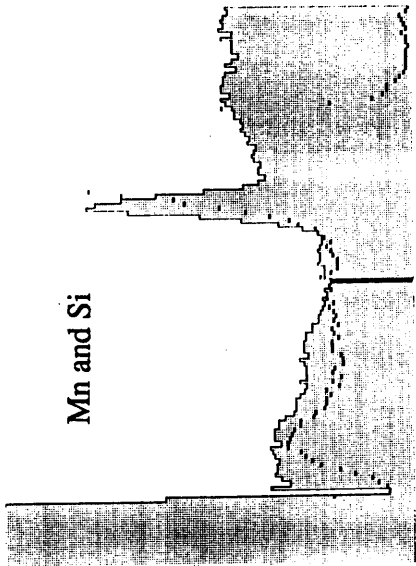
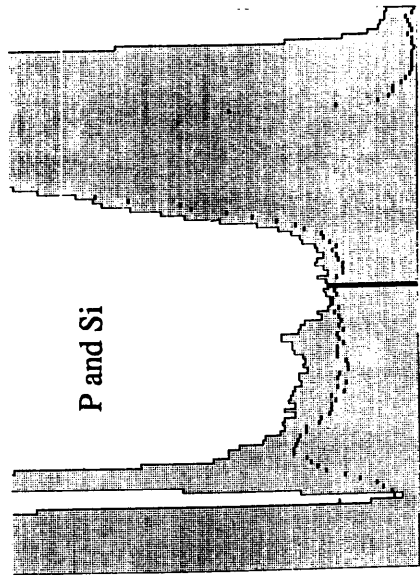


Fig. 7.15 Spectra showing the similarity in the tail regions at 1.14 keV.

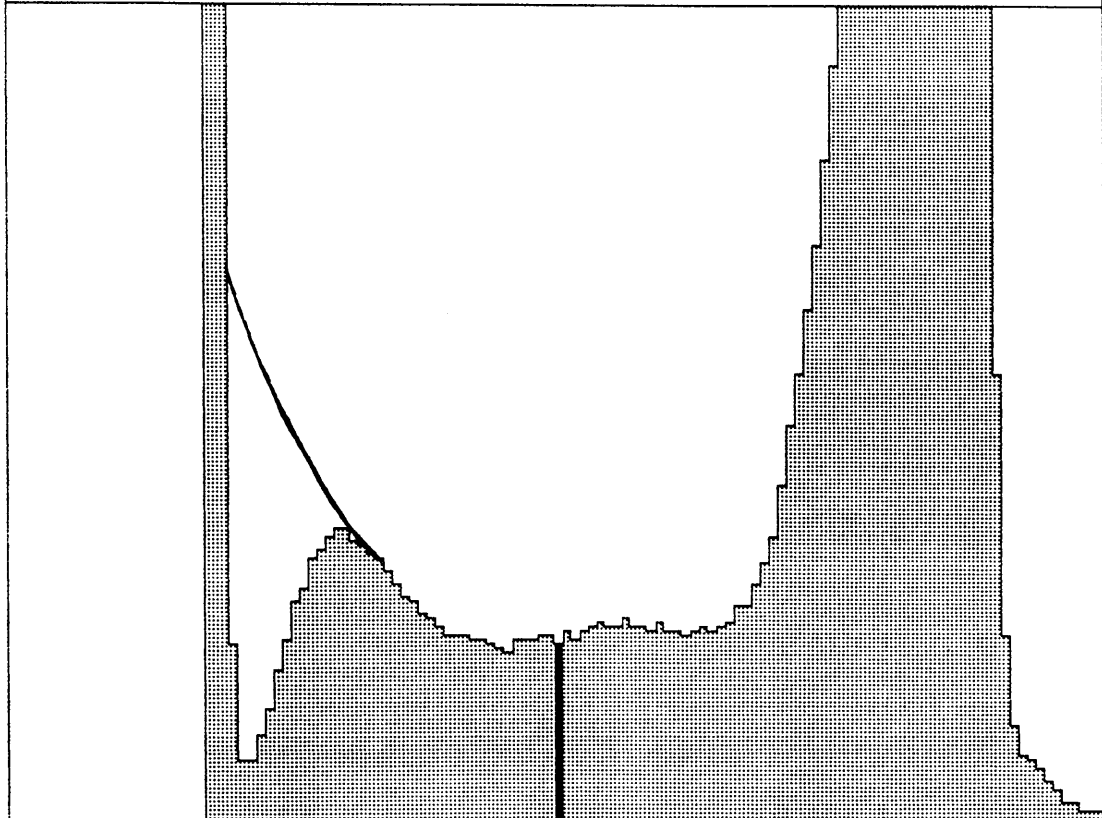
reduces the displayed counts. This changes the "true" low energy shape to give what appears as a "peak". This region may otherwise continue to rise until the spectrum merges into the noise peak. This idea is illustrated in fig. 7.16.

During any analysis, it is a usual practice to scale the spectra to the same gross numbers of counts, this assumes an equal number of photons make up the spectra. When this was done with the different fluoresced spectra, the number of counts in the low energy ends were seen to differ quite considerably. Figure 7.17 shows the difference between the spectra from aluminium/silicon and silicon/titanium. Initially this was quite confusing. No systematic relationship could be found which would describe the differences in the number of low energy counts between the various spectra. A variety of different parameters were investigated as a means of explaining these observed differences. This initially involved varying different combinations of the photon energy and the mass absorption coefficients i.e. the parameters which change most markedly between the respective spectra.

The effect of the high energy bremsstrahlung present in the  $^{55}\text{Fe}$  source (see appendix 3) had to be considered as a possibility. Those spectra acquired for longer acquisition times would contain more of this radiation. The high energy background from the  $^{55}\text{Fe}$  source can be obtained by using an absorber (aluminium) to absorb all manganese photons whilst aiming the source directly at the detector. This background can then be scaled to a particular spectrum either by scaling to the time of acquisition or by scaling to the number of counts in a window set at a high energy where the background can be seen. Results obtained after such a scaling process indicated that the high energy background did not effect the low energy region since it never adds more than 5% of the observed counts.

The only parameter which appeared to represent the experimental data in any way was the acquisition time of the spectra. When the various spectra were normalised to the same acquisition time, they all, with the exception of aluminium, appeared to contain a similar number of counts in the low energy end. This similarity inferred that the low energy ends had approximately equal acquisition rates for all the fluoresced targets except aluminium. This idea is quite surprising when the average output rates from the different targets are considered. These values being:

X-RAY: 0 - 40 keV  
Live: 32767s Preset: 32767s Remaining: 0s  
Real: 35554s



FS= 16K MEM1:  
.920 keV 2.2 >  
ch 56= 3678 cts

Fig. 7.16 Proposal for the shape of the low energy end of spectrum without the effects of the electronic roll-off.

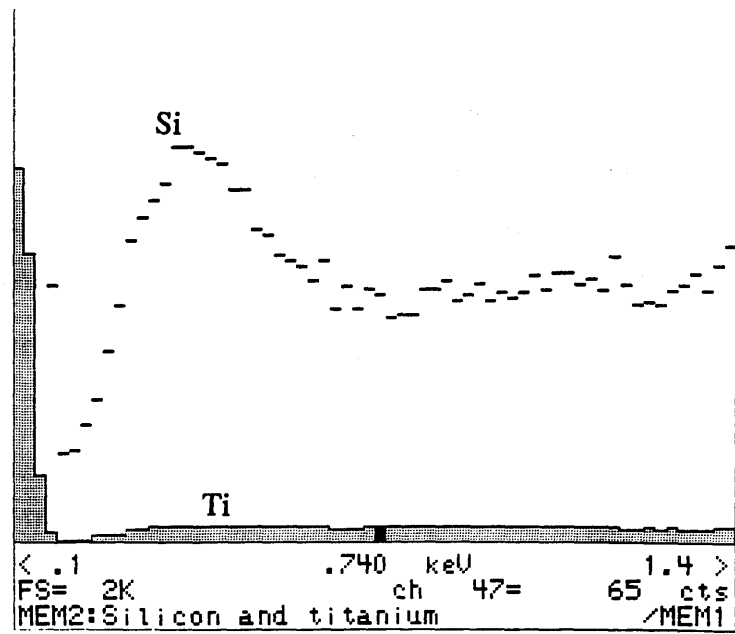
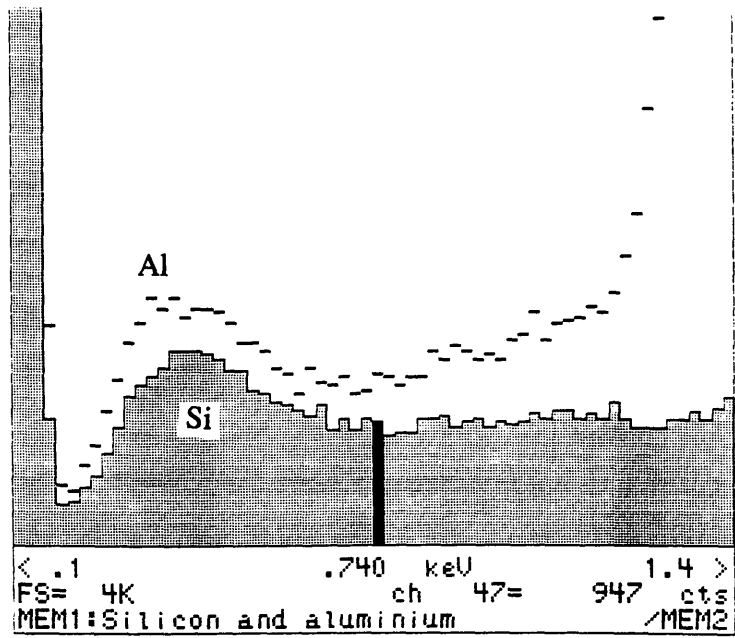


Fig. 7.17 Difference in the magnitudes of the low energy ends of spectra scaled to the same gross integral.

silicon, 28 c/s : phosphorus, 73 c/s : titanium, 435 c/s : manganese, 1250 c/s

with aluminium having an acquisition rate of 13 c/s. This meant that the acquisition rates for the low energy ends were approximately constant irrespective of the count rate. Scaling to acquisition time also scales the level of high energy bremsstrahlung present in each spectrum.

The manufacturers were consulted about this apparent low energy anomaly. They suggested that it may be the effects of low energy pile-up. When the photon energy is very low, pile-up effects are possible since the fast channel cannot always distinguish between the low energy counts and the noise counts (Link Analytical, 1989). Therefore, pile-up between noise counts and low energy counts becomes possible. This is worse for x-rays with a large mass absorption coefficient in silicon, since these x-rays will give rise to a greater number of low energy ICC counts to pile-up with the noise. To investigate the effect of noise on the spectrum an experiment was performed whereby the count rate from the manganese source was decreased by systematically doubling the source to detector distance so that the ratio of the electronic noise to the number of incident photons increased. Figure 7.18 shows this effect for two manganese spectra, one acquired at around 2000 counts per second the other around 20 counts per second, with the noise contribution set at approximately 100 c/s. It appears as though the spectrum acquired at the low count rate has more counts in the low energy end. This was initially thought of as being caused by the effects of the low energy pile-up. However, if the high energy background is subtracted from this spectrum we find that there is now no difference. It is still possible that those spectra which have a larger ICC contribution may give a pile-up effect. These spectra have a proportionately higher number of counts going into the low energy channels. So the chances of a "noise + ICC" pile-up count is increased. This is difficult to test for using the fluoresced targets. However, this may be seen in the phosphorus spectrum where the escape peak could possibly pile-up with the noise contribution to give a sum contribution at higher energies than the escape peak. In the phosphorus spectrum the

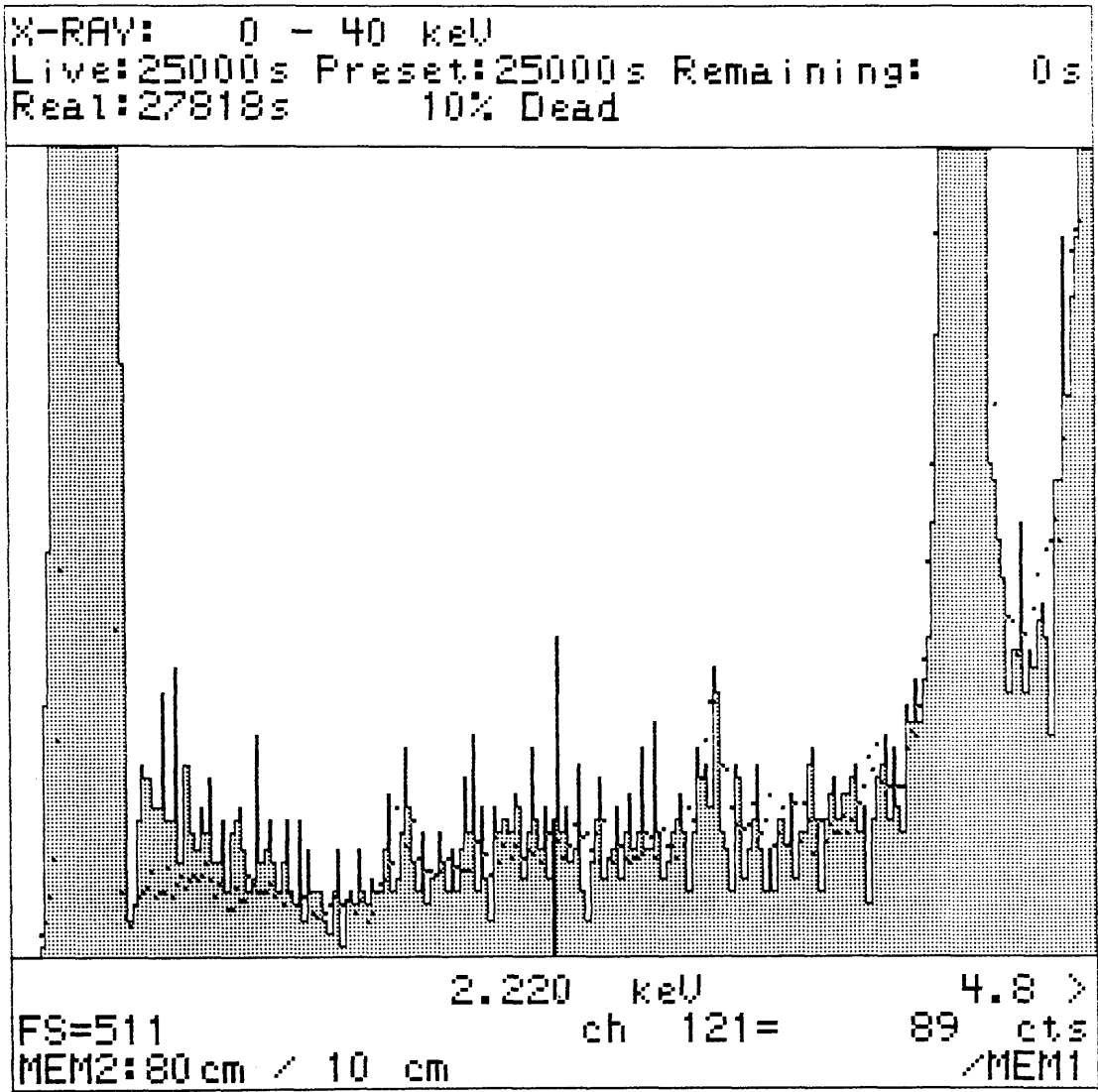


Fig. 7.18 Comparison of manganese spectra acquired at 20 c/s and 2000 c/s (dot memory).

region beyond the escape peak is seen to differ slightly from the other spectra, see fig. 7.11. This idea of low energy pile-up can be seen to be very analogous to the idea of continuum pile-up (Statham and Nashashibi, 1988) mentioned in section 3.4.

### 7.7 Real spectrum artifacts contributing to the tail.

The previous sections have considered some of the mechanisms which give rise to the complex shape of the tail region. This section proposes a simpler means of explaining the complex shape.

During an investigation into possible parameterisations for the tail region, one particular model seemed to be quite plausible if the tail was considered to be made up of two exponentially decaying regions both of which "sit upon" a constant background level. There did not appear to be any plausible reason why such a constant level should exist. However some of the fluoresced spectra can be seen to show a linear region below two exponential regions. Results from the JEM detector have shown that such a constant level is possible when gross damage effects are manifested, (see section 5.4). With this idea in mind, a simple model was set up whereby a constant level was fitted to each of the fluoresced targets. These were fitted over an energy range from 200 eV up to the photon energy. The areas of these linear regions were integrated and the percentage of the spectrum which they represented was established. This percentage was then plotted against the mass absorption coefficient for the target in silicon, see fig. 7.19. This graph shows that all but three elements lie upon a good straight line fit. The reason why the three other points do not fit is not clear, but these were all acquired at very low count rates and it is perhaps possible that this may have something to do with this effect.

Further consideration of the spectra shown in section 5.4 may lead one to the conclusion that a "real" spectrum is built-up from several different spectral artifacts each associated with a particular trapping mechanism. The trapping mechanisms may be caused by defects in the crystals, these being distributed throughout the crystal. The actual shape of the spectrum will then depend on how many of each particular type of

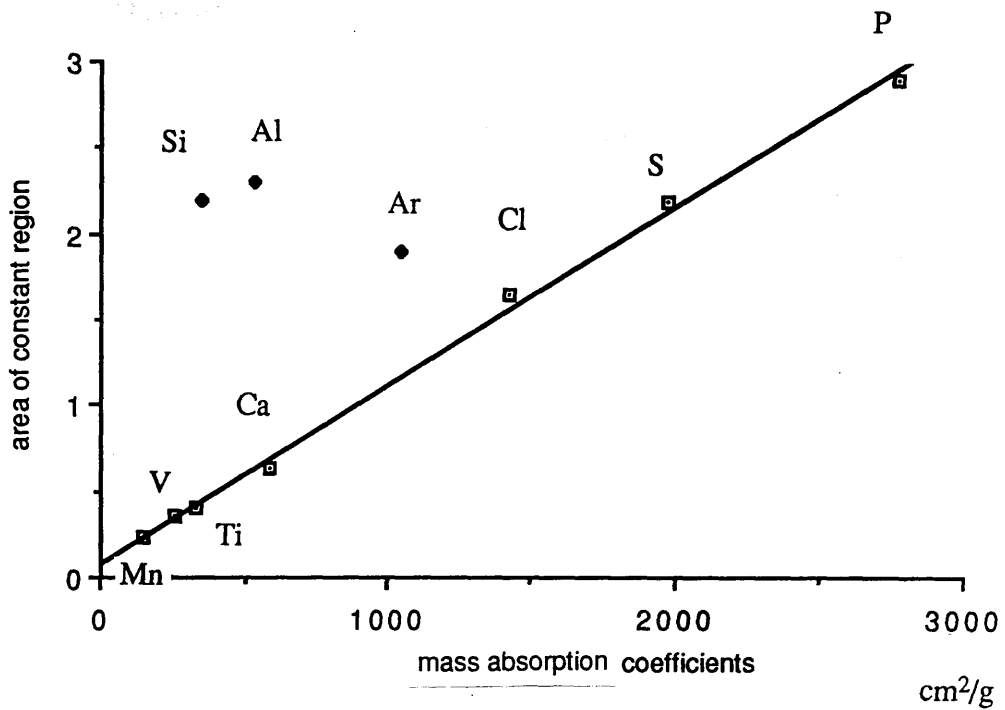


Fig. 7.19 Graph showing the linear relationship between the constant area under the spectrum and the mass absorption coefficients.

defect which is activated by irradiation. The side regions have been shown to contain more defects liable to cause severe ICC. If the crystal becomes damaged in any way, then the contribution from any particular mechanism may become grossly exaggerated, hence changing the overall shape.

## 7.8 Discussion and conclusions.

This chapter has shown that there are a number of measurable events occurring in the detectors and in the x-ray sources which give rise to extraneous counts in the spectra. However, for the spectra studied, these events were generally at a very low level by comparison to the ICC caused by the detector imperfections already present.

The most significant effect found to be occurring was the escape of bremsstrahlung radiation from the x-ray sources. This bremsstrahlung was that created by the photo and Auger electrons scattering within the fluoresced targets. For the vanadium spectrum studied, this contribution was in the order of 10% of the total number of counts in the tail region. Intuitively it could be assumed that this source of bremsstrahlung would decrease for those targets having a large average depth distribution for fluorescing manganese x-rays (at low photon energies at least). This was not tested however. The  $^{55}\text{Fe}$  source was found to contribute a small amount of bremsstrahlung to the spectrum, this being approximately 2.5% of total counts in the tail region.

Photons which Compton scatter as they escape the x-ray sources were shown to add an almost insignificant number of counts to the low energy fluoresced spectra. Tailing seen on the low energy side of the photo-peaks must therefore have been caused by trapping effects.

The level of bremsstrahlung escaping the detector was established for incident manganese x-rays. This level of radiation loss does not effect the spectrum in any way. The level of this radiation was approximately two orders of magnitude below the ICC already present in the tail. It is possible that photons with a lower average absorption depth would give rise to more of this type of bremsstrahlung. However, these photons

are generally low energy and give rise to low energy photoelectrons. The bremsstrahlung generated by these low energy photoelectrons has difficulty in escaping even the thinnest of surface layers. Two different experimental techniques were used to estimate the level of bremsstrahlung escaping the detector. Both these techniques gave a similar result. Although relying upon certain approximations, these experiments were thought to be quite accurate.

It may be concluded that that the  $^{55}\text{Fe}$  radioactive source, used commonly to characterise detectors, can be used safely in the study of ICC since the additional processes which occur with this particular source are at an insignificantly low level. From a manufacturing point of view, the levels of ICC would have to be decreased dramatically ( $\sim 2$  orders of magnitude in most regions) before any of these minor effects play any significant role. However, bremsstrahlung originating from the x-ray sources appears to be a problem. This problem will increase in significance as the detector manufacturers continually improve the detectors and lower the level of ICC in the tails.

An attempt at modelling the ICC indicated that the spectra from the new series E detectors were very similar to the spectra obtained from the older detectors. The ICC being seen to obey a similar linear relationship with mass absorption coefficients at all energies down to approximately 1 keV. Over the region where this linearity existed the qualitative model proposed by Craven et al. (1986) for the older detectors could be used to model the ICC. This was not tested to any great degree of accuracy however. This investigation also indicated that the very low energy region of the spectra (energies less than 1 keV) did not obey the same linear relationship with the mass absorption coefficient as was seen for the rest of the tail. This region was investigated separately to try to explain why it should differ from the rest of the tail. This investigation showed that the low energy region was very similar (i.e. it appears to "fill-up" at equal rates) for all fluoresced spectra, irrespective of their input count rates. This may be no more than a coincidence but could possibly be some kind of detector effect common to all spectra acquired with a particular detector.

## CHAPTER EIGHT

### Conclusions and Future Work.

#### 8.1 Introduction.

This final chapter summarizes the results and conclusions presented throughout this thesis. The results are first compared with the initial aims of the project and then discussed in terms of their significance. The final section makes some suggestions for further work which could clarify the unanswered problems which have arisen due to the findings presented in this thesis.

#### 8.2 General conclusions to this project.

Throughout this project many different phenomena were found for the various detectors being studied. However, the nature of these particular problems did not lend themselves easily to any kind of analytical solutions. Indeed, many of the conclusions are very qualitative and occasionally even speculative. This has arisen partially due to a lack of any similar published work from other sources. In particular the lack of published data originating from the numerous detector manufacturers. This information is often regarded as commercially sensitive. This can perhaps lead to a certain amount of "re-inventing of the wheel" but unfortunately this could not be helped.

As far as the original aims of this work were concerned we did manage to establish the reason for the poor quality of electron generated spectra obtained from the HB5 with the new series E detector. The actual reason was quite simply due to a misalignment of the detector collimator with respect to the detector crystal. This was due to an alteration in the design of the HB5 detector. This alteration had positioned the crystal 1.7 mm closer to the beryllium window than in the previous design. This meant

that the original collimator was collimating x-rays to the top region of the crystal. This alteration had gone unnoticed for several months. It was this misalignment which leads to the excess ICC seen in all of the electron generated spectra. The excess ICC originated from carriers being created in a region of crystal which we subsequently proved to have a poor collection efficiency. Various "bench test" experiments performed with different detectors had actually indicated this misalignment problem. However, it was not until these tests were completed and the results considered in some detail that this was realised. By this time the misalignment problem had been established by Craven and Nicholson (1990) during tests to check the alignment procedure.

Experiments were performed which investigated the effects of the microscope environment on the detector's performance. These experiments gave results which were very similar to those obtained with the detector in operation on the HB5 (with the misaligned collimator). In these experiments the charge carriers were deflected to the sides of the crystal by the influence of an external magnetic field. This magnetic field was supposed to represent the field always present in the objective lens when in operation. Certain regions of the crystal (around their periphery) were found to have a very poor carrier collection efficiency, this being manifested by a large increase in the ICC. Whilst the HB5 detector was in use on the microscope the poor collimation had actually been allowing x-rays to reach one of these poor regions, hence causing an increase in the normal levels of ICC. Both the HB5 and JEM detector's crystal's were found to have these poor regions around their periphery. These regions could only be accessed by a poorly collimated beam of x-rays or by the effects of an external magnetic field. Collimation of the x-rays down to a small central region (diameter ~ 4mm) removed this effect even with the external magnetic field being applied.

The poor regions of crystal had characteristics which could be associated with a high trap density (deduced from the poor carrier collection efficiency in these regions). These regions were found to be affected by irradiation from high energy photons. However, the effects caused by these high energy irradiations were not the same for the HB5 detector as the effects found for the JEM detector. With the HB5 detector, long term irradiation of the side regions with terbium x-rays (~ 18 hours) appeared to create

a number of traps which could subsequently be used to trap carriers being used to explore these regions. These traps were found to decay exponentially with time when the detector was not being used. If the bias was removed these traps disappeared totally in a short period of time. When the JEM detector was irradiated with terbium x-rays, no such traps were created, more surprising however; existing traps were found to gradually disappear. This appeared to indicate that different properties exist within the side regions of these two detectors. No further information regarding this effect was discovered.

The JEM detector was also found to have suffered some damage effects which were caused when this detector was in "normal" use on the JEM 100C electron microscope. These effects (an increase in the number of traps at the periphery of the crystal) were seen to increase the longer the detector spent on the microscope. A second study performed with this detector, approximately 6 months later, found that these effects had disappeared but a more serious problem had replaced it. As the time the detector had bias applied increased, the level of ICC increased, until eventually reaching saturation. This effect was only seen when the carriers were deflected into the side regions by the application of an external magnetic field. This effect could also be partially removed when the detector was irradiated with terbium x-rays. Again collimation of the x-rays to a small central region removed this effect.

One quite important point is the fact that the magnetic field from the HB5's objective lens did not deflect carriers into a poor region of this particular crystal. If the lens field had been reversed (as it could be without any changes to the microscope's operation) then additional ICC would have been observed if the carriers could reach the poor region. The fact that the bottom region of the HB5 detectors crystal was not damaged could be due to the fact that the misaligned collimator severely limited the number of x-rays arriving in this region.

Two additional detectors were studied, only to a far lesser extent. One detector was irradiated with high energy electrons and the other detector was irradiated with high energy terbium photons. The results obtained from these detectors indicated that they also suffered from the same type of damage manifestations (excess ICC on their

manganese test spectra) as the JEM and HB5 detectors. For both detectors the damage effects were found to have disappeared when the bias was removed. No further useful data was obtained from these detectors with which to make any further comparisons to the JEM and HB5 detectors.

A study of the fundamental processes which give rise to the low energy tail was undertaken. These processes occur both in the detector and in the sources of x-rays. The "detector effects" include those of the escape of bremsstrahlung radiation and trapping of carriers by crystal defects. The "source effects" include those of Compton scattering of the escaping x-rays and the escape of bremsstrahlung radiation. Detector effects such as the escape of bremsstrahlung were shown to be at a very low level and therefore would not add any significant number of counts to the tail. ICC is still the main factor contributing to the tailing of the photo-peaks. However, the fluorescence sources can contain secondary bremsstrahlung radiation and this can add a significant number of counts to the tails in the region just below the photo-peaks, this being ~ 8% of the total number of counts in the tail of a vanadium spectrum. These counts are also localised to the region just below the photo-peaks. If the levels of ICC in the tail region were drastically improved this would lead to the necessity for better x-ray sources which do not contain any extraneous bremsstrahlung.

### 8.3 Future Work.

It is hoped that this work has gone some way towards simplifying aspects of the physics involved during the operation of the energy dispersive Si(Li) x-ray detectors. Some problems still remain unanswered. There are two main areas which need investigating:

(1) An investigation still needs to be performed to study the accuracy to which the low energy end of electron generated spectra can be fitted using the MBH theory. This is required to verify whether the MBH theory is suitable in describing the low energy end of the spectra as the work of Chapman et al. (1983) and Adam (1985) suggest it

should. Work performed recently within our group (Khan, 1990) has suggested that the series E type crystals give spectra of suitably high quality to allow accurate background fits to be made. If this is true, then it is important to establish the accuracy of the technique and the range of specimen thicknesses to which it applies.

(2) The study concerning the fundamental processes which give rise to the low energy tail has indicated that virtually all the counts in the tail region are those from the effects of ICC. This leads to two different areas for investigation. The first is a fundamental study of the exact trapping mechanisms which give rise to the shape of the tail actually seen. This could perhaps be done using Monte Carlo techniques. The second course of study would be concerned with further improvement of the detectors, particularly the sides and surfaces. This may be helped by any information made available on the exact mechanisms behind the ICC process. It is still thought that the surface (and potentially the sides) of the crystal is dominant in the generation of any ICC.

Finally, from the way in which the JEM detector appeared to deteriorate during this project it is important to study if various detectors have an apparent "life-time" after which they will be unsuitable for certain applications.

## APPENDIX ONE

### Specimen preparation.

#### A1.1 Thin film specimens.

Thin film specimens can be produced by several different methods, evaporation, ion beam thinning and sputtering are just three examples of the techniques available. All methods have one thing in common, they have to be performed under high vacuum preferably ultra high vacuum (UHV). The reasons for this are: (1) to stop the specimens oxidising in air during the evaporation; (2) to minimise impurities in the specimens and (3) to minimise the atomic collisions between the molecules being given off during evaporation and the residual gas molecules in the evaporation chamber, this affects the uniformity of the film thickness.

Evaporation by resistive heating is a commonly used technique and was the first method tried. Impurities are the most troublesome aspect of this type of specimen preparation; previous specimens prepared within our group have usually always contained a small concentration of silicon and often sulphur. To minimise the concentration of any impurities, an existing vacuum evaporator was specially modified. The main modification was the incorporation of a polyphenol ether type of diffusion pump oil (Satorr 5). Silicon impurities had been a major problem with specimens prepared in the past and it was thought that this originated from the silicon based diffusion pump oil. A nitrogen cold trap was fitted above the diffusion pump, this was used to minimise any back streaming of oil vapour from the diffusion pump. All plastic coated wires removed from within the bell-jar since these can give off chlorine when heated. The substances to be evaporated, usually metals or semi-metals, were held in an alumina crucible. The crucible was heated resistively by passing a large current through a series circuit containing the crucible. Currents of up to 15 amps were usually required. The current was slowly built-up to allow the crucible and specimen to out-gas

and come to thermal equilibrium. During the evaporation the metal vapour is given off isotropically and coats all surfaces which it comes in contact with. This can be a problem since the evaporator bell-jar soon becomes opaque. This effect was minimised by collimating the evaporation source.

Thickness calibration was achieved by monitoring the evaporation with a quartz piezoelectric crystal oscillator. The piezoelectric crystal oscillates at a frequency which is mass controlled. As the mass of evaporant builds up on the crystal surface the natural frequency of oscillation slowly decreases, over a limited range this frequency drop is linearly proportional to the mass of the crystal. Calibration of the crystal is achieved by evaporating simultaneously onto the crystal oscillator and a glass calibration slide. The frequency drop for the evaporation being noted. The thickness of the metal evaporated onto the glass slide is then established by optical interferometry. This was repeated for a range of values, in this way a graph of frequency drop verses thickness can be obtained. In future evaporations, the desired thickness was obtained by "dropping" the required frequency to within the limits of accuracy attainable. The accuracy of this technique is very limited. This was due to the large uncertainties in the thickness values from the interferometer. These could be very large indeed when measuring very thin films. This large uncertainty was partially due to the condition of the instrument. In addition, the crystal oscillator was periodically found to be insensitive. Different frequency readings could be obtained after a particular evaporation depending on how long after the evaporation the reading was taken. This was thought to be due to local heating of the crystal. Overall it was estimated that the uncertainty on a 50 nm film maybe as much as +/- 20 nm. Thinner films could even be up to 100% over or under estimated.

Specimens were prepared by evaporating onto a rock salt substrate. The time for the evaporation depending on the rate at which the metal evaporates. This basically had to be judged by experience. The thin films were then "floated off" the rock salt into a jar of distilled water. The films were left for around an hour so that any rock salt crystals on the film surface would dissolve in the water, rock salt being very soluble in water.

The films were then "picked off" the water onto a microscope specimen grid mesh and left to dry.

Specimens prepared in this way were always found to contain a small percentage of silicon. It was difficult to say where this originated since there should ideally be no silicon in the evaporator. It was for this reason that a second method of specimen preparation was tried.

Sputtering is a process whereby atoms are dislodged from their atomic sites by bombardment from secondary ions in the form of a plasma. Sputtering is commonly used in the semiconductor industry to prepare thin films and metallic coatings. The sputtering unit which exists within our group should ideally be "cleaner" than the vacuum evaporators. The base pressure of the sputterer was around  $10^{-8}$  torr which was two orders of magnitude lower than the evaporators. The sputterer uses a method of cleaning the target material, known as pre-sputter. During the pre-sputter the target has its first few surface layers removed by sputtering. This is to clean away any oxide which will have developed. During this pre-sputter the substrate is shielded from the sputtered material, which coats all surfaces within the sputterer. The beauty of this method is that the substrate and target material are kept under vacuum throughout. The pre-sputter serves as a means of purging the vacuum with vapour of the sputtered material. The walls and all the internal metal-work are coated with the target material, this helps eliminate any impurities which may exist. After this pre-sputter the substrate can be revealed and the process repeated to coat the rocksalt substrate with the desired thickness of material.

The gas used to perform the sputtering is usually argon. The sputtering gas has to have a large enough atomic mass so as to be able to impart enough momentum to the target atoms to knock them out of their atomic sites. For the low Z materials which were sputtered argon was suitable. During the sputtering process, the sputtered vapour and the sputtering gas brings the chamber pressure up to around  $10^{-4}$  torr. This however, allows argon atoms to become trapped in the specimens as they are deposited.

Thickness calibration on the sputterer was achieved using a glass calibration slide, followed by thickness measurement using the interferometer. Nordiko, the manufacturers of the sputterer provide a calibration chart from which an approximate guide for the sputtering time can be obtained. Using the sputterer, specimens of chromium, silicon, germanium and cobalt were produced.

#### A1.2 Fluorescence specimens.

The specimens which were used in the fluorescence experiments were single element when ever possible. The manganese x-rays emitted by the  $^{55}\text{Fe}$  radioactive source are capable of fluorescing all elements up to vanadium. (chromium can be fluoresced by the manganese  $K\beta$  x-rays) Several of these elements are metals and can be bought in a very pure form, others like phosphorus and sulphur are powders and therefore had to be "fixed" to be suitable for holding. Paraffin wax was chosen to fix the powder specimens since this was composed of only carbon and hydrogen and these could not be detected using a conventional detector. Elements which were not stable had to be fluoresced as a compound. These compounds were chosen so that the extra elements could not be detected due to their absorption in the beryllium window. Lithium chloride and calcium carbonate were used in this way to obtain chlorine and calcium respectively. Argon was fluoresced as a gas.

## APPENDIX TWO

### Computation and Software.

This appendix outlines the methods by which the computer analysis was performed on the x-ray spectra. The computer system used is explained briefly and the various computer programs used in relation to this work are explained.

#### A2.1 X-Ray acquisition hardware.

As previously mentioned in section 3.10 all hardware used to acquire and process the x-ray spectra was that developed by Link Analytical. Within the solid state group there are two Link systems currently in use, these being the Link 860/LDOS mk.1 and the more recently developed Link AN10000. Although these two systems have many similar features they rely upon different operating systems. This causes a slight problem since spectra acquired on any particular system are not automatically compatible with the other. Fortunately, a conversion program was available which allowed conversion from 860/LDOS to AN10000 format and the converse. The AN10000, being far superior to the older 860, was the system used for all computation and the majority of the data acquisitions. The AN10000 uses an analyser program called AN10 for the spectral acquisitions. AN10 contains a menu of simple spectrum manipulations to assist in analysis of the spectra. These manipulations allow a spectrum to be compared, added or subtracted to another spectrum.

X-ray spectra are stored within the computers memory as an array of numbers (integers). These arrays can be either 1024 or 2048 elements long. Each array element stores a number which is characteristic of the x-ray intensity at the particular energy the array element represents. Array elements are more commonly known as channels. Each channel differs from the next by a given amount of energy. This value of energy is

determined by the external hardware (an amplifier gain) and is assigned to a particular spectrum in the process of writing to memory. Spectra are stored in integer form using a series of data blocks. Each data block contains 256 words of information, with one word being required to store a 16-bit integer (numbers less than 65535). In this way 4 data blocks are required to store a 1024 channel array of 16-bit data. If the numbers become very big (greater than 65535) then they are stored as 32-bit data, this requires 2 words per array element, so the number of blocks therefore doubles. Accompanying each set of data blocks is an additional block known as the header block. This header block is used to contain all the information about the data that the AN10000 requires. Most of this information is used to set a series of flags which the AN10000's operating system requires in order to recognise the type of spectra, the number of array elements and whether the data is 16 or 32-bit. The header block is automatically written to disk by the system when saving a spectrum.

## A2.2 Programming on the AN10000.

The AN10000 has a Fortran compiler which enables the user to write programs for spectrum manipulations and general numerical computation. The programs have to be written in a special type of Fortran devised by Link Analytical. This is basically a variation of Fortran-66 which has been modified by Link so that the various input-output statements are controlled by a series of subroutines written specially for this purpose. The programs themselves are quite simply a series of number manipulations on the array of data elements. However, when writing to memory the appropriate information required by the header block has to be used.

## A2.3 Software.

The software used during this project is now briefly explained. This software is partially a set of programs written by Drs. Adam and Nicholson which have been

converted to AN10000 type Fortran. This conversion was done by Mr. Khalid Khan and debugged by Dr. Nicholson and myself. Some of the programs used were written by Dr. Nicholson others by Khalid Khan and the remainder were written by myself. This joint collaboration was required since the AN10000 system was new to our group and no one had any first hand experience with this type of programming. The various programs used are now summarised:

**MBHBG:** This program generates a theoretical MBH background for any desired element, at any electron energy and for any bremsstrahlung angle. It can also be used for multi-element specimens if the atomic fractions are known. The program generates the bremsstrahlung cross-section as a function of photon energy and take-off angle for any energy interval between 100 eV and the maximum energy. These cross-section values are then scaled up to a large value ( $10^9$ ) to maintain digital precision during the various manipulations carried out. It is usual to make the energy range consistent with the spectrum to which the background shall be compared. The original version of this was written by Dr. Nicholson. This program's algorithm was tested thoroughly on several different computer systems.

**EFFIC:** This program allows various absorption corrections to be performed upon the theoretical background. It allows for a beryllium window absorption correction, using the Beer's Law type "slab" model. This option can also be used to calculate the absorption when slabs of other materials are encountered, such as the gold layer or the silicon dead layer. This program can also be used to calculate the self absorption for thin specimens tilted by some angle towards the detector. The self absorption correction is that proposed by Zaluzec (1979).

This program requires files containing mass absorption coefficients to be able to calculate the absorption. These coefficients are stored in data files which are called when required. This program is based upon one written by Dr. P F Adam (Adam, 1985) and was modified by Khalid Khan.

**MACW:** This program calculates the mass absorption coefficients using the model

proposed by Heinrich (1987). The values are scaled up by  $10^4$  and stored on disk. This program was written solely by Khalid Khan.

**GPEAK:** This program calculates a Gaussian peak for any detector resolution. It positions the Gaussian in a channel which is required for the peak to be fitted. The resolution for the desired peak is input directly to the program.

**FRACSHIFT:** This program shifts a spectrum, real or theoretical, by a fraction of a channel either up or down. This is useful when trying to fit Gaussian peaks to spectra which are slightly mis-calibrated.

**SHIFT:** This program shifts spectra by a whole number of channels, either up or down.

**COMP1:** This program was used to generate a theoretical background to the ICC shape. It generates an exponential function for a given value. It then convolutes this exponential with a Gaussian. Finally it scales this to the real ICC background over a specified range.

**ABSN1:** This program calculates the absorption undergone by PEB photons escaping from the detector or from a fluoresced target. This calculation is based upon the Reed and Ware (1972) equation for the escape peak intensity.

## APPENDIX THREE

### Fluorescence sources.

#### A3.1 Americium variable x-ray source.

The variable x-ray source used in this work was manufactured by Amersham International. This source comprises of a 0.1  $\mu\text{C}$  americium 241 ( $^{241}\text{Am}$ ) radioactive source which is used to fluoresce secondary x-rays from single element targets. These targets being; copper ( $Z = 29$ ), rubidium ( $Z = 37$ ), molybdenum ( $Z = 42$ ), silver ( $Z = 47$ ), barium ( $Z = 56$ ) and terbium ( $Z = 65$ ). The energy range of the characteristic photons varies from copper  $K\alpha$  at 8.4 keV to terbium  $K\beta_2$  at 51 keV.

$^{241}\text{Am}$  is an alpha emitter and also emits several different gamma rays during an internal conversion process. The principal emission is a 59.6 keV photon which makes up 36% of the output flux. There is also a 26.3 keV photon making up 2.5% of the output flux and several x-rays associated with the daughter product  $^{237}\text{Np}$ .

The entire source is encased in stainless steel for safety purposes and to collimate the source. The stainless steel also absorbs all the alpha particles. The Am source is mounted on an annular ring and the targets are rotated into a position directly above the Am. The secondary x-rays escape through the hole in the annular ring. The emergent beam of x-rays being highly collimated for safety reasons. Figures A3.1 through A3.6 show an x-ray spectrum from each of the target elements. Many stray peaks can be seen, some of these are from the stainless steel the others are from the other targets. These do not pose any problems however.

The low energy end of each spectrum is dominated by a large Compton distribution. This is due to Compton scattered photons escaping the detector leaving behind a Compton electron to be detected. In the spectra from the low  $Z$  targets most of this Compton profile is associated with the Compton scattered gamma ray from the source. This can be subtracted out of the respective spectra by obtaining a Compton

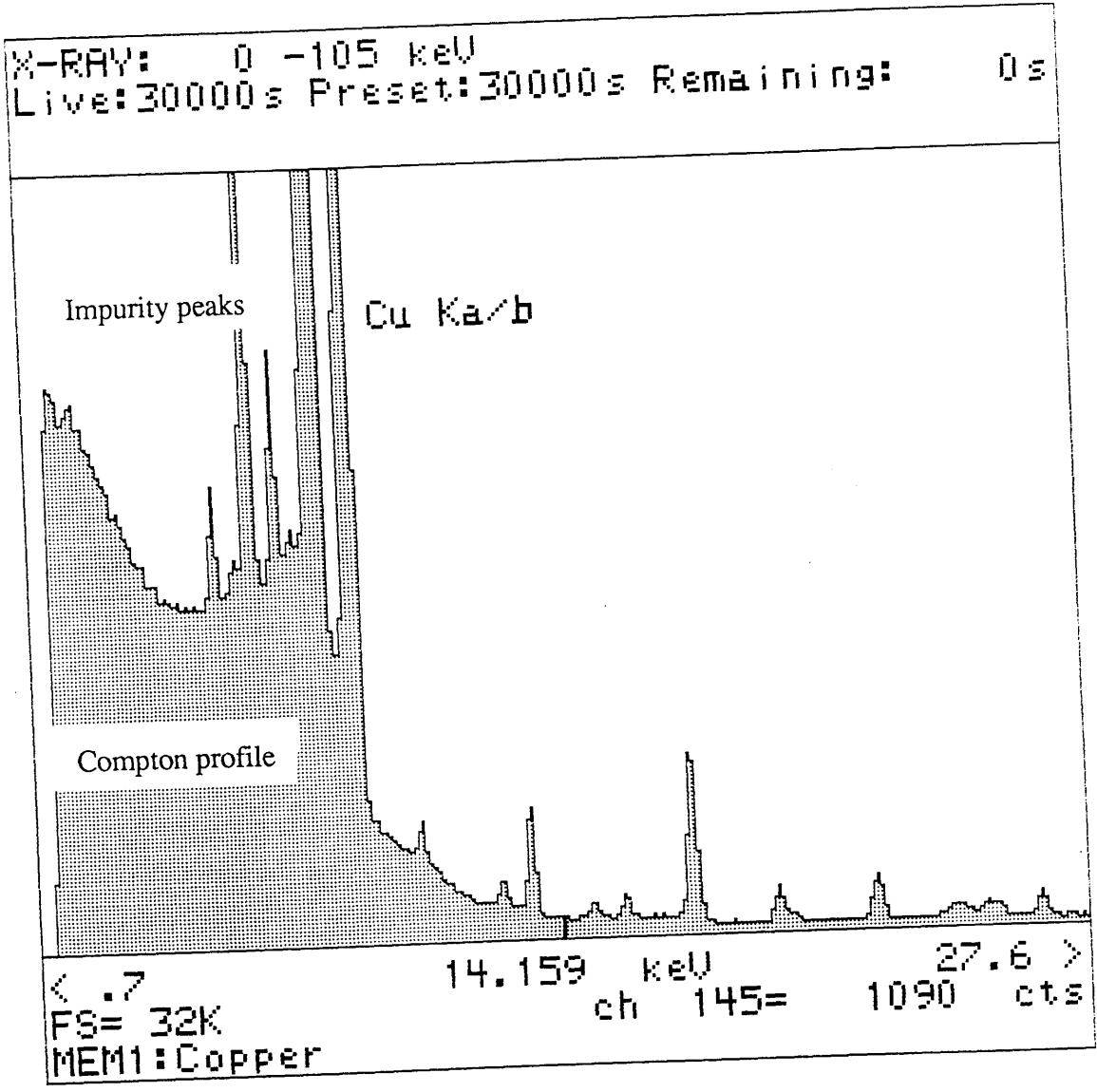


Fig. A3.1 Fluoresced copper target, showing the effects of the high energy Compton background

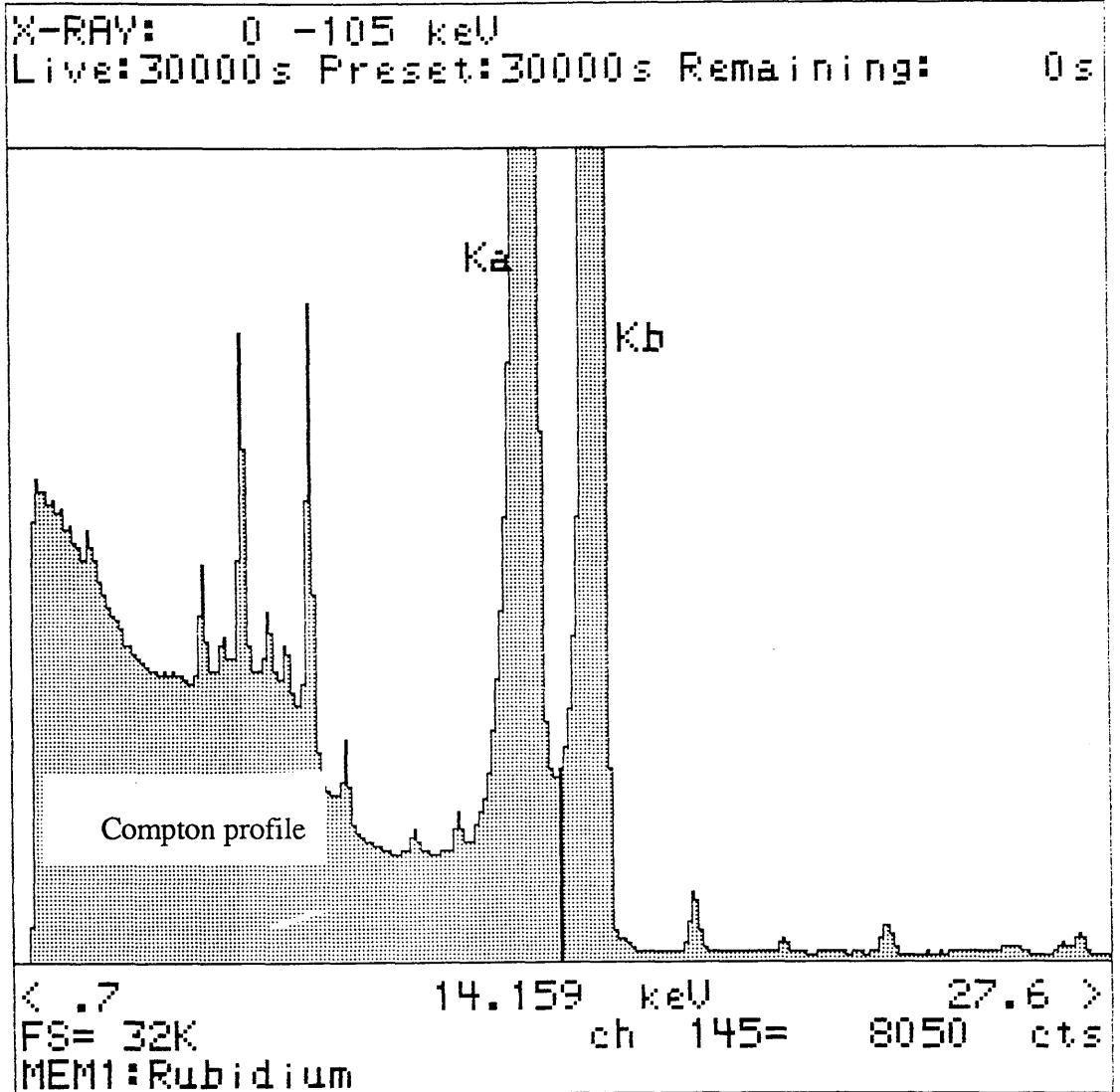


Fig. A3.2 Fluoresced rubidium target, showing the effects of the high energy Compton background.

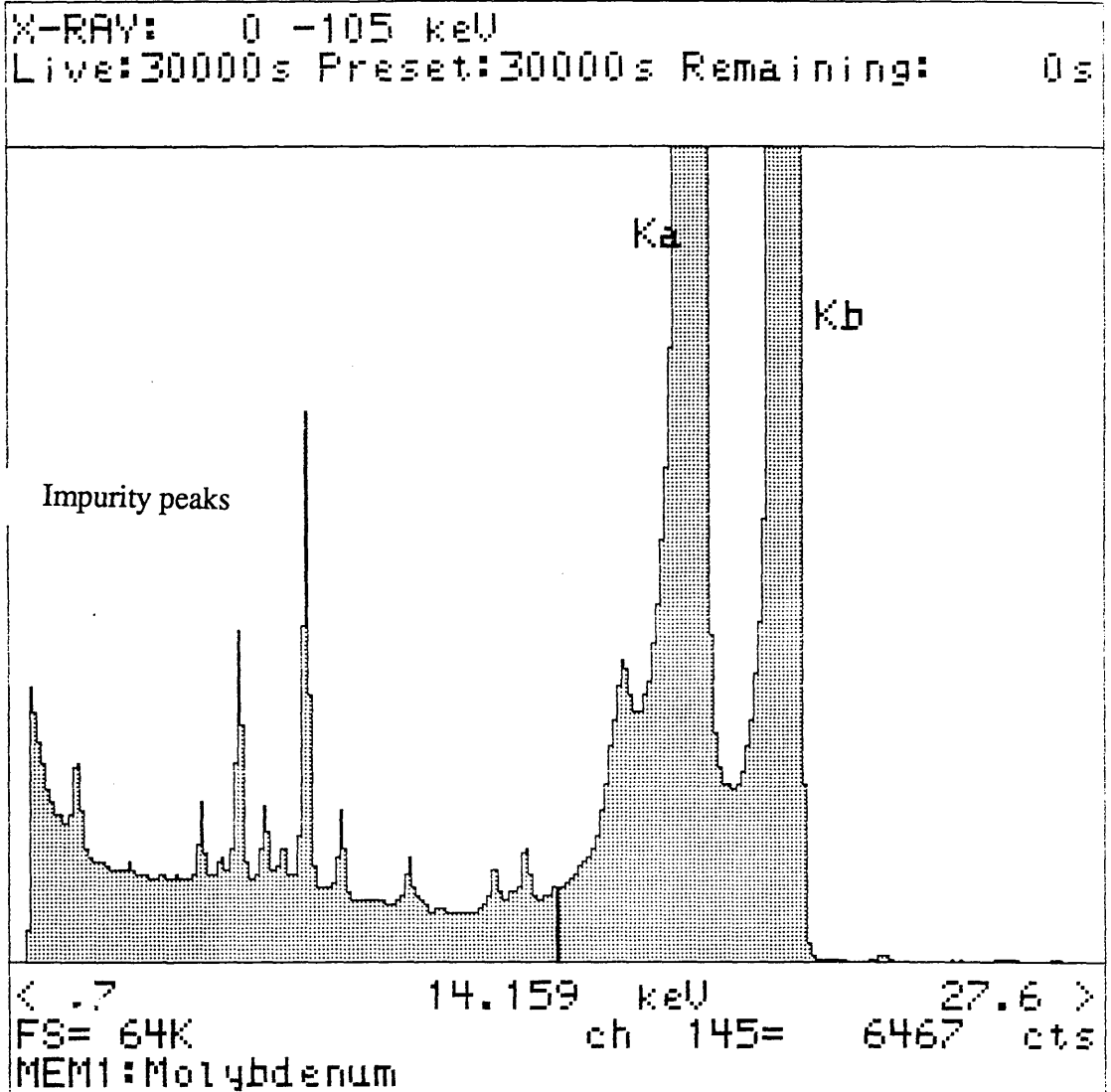


Fig. A3.3 Fluoresced molybdenum target, showing the effects of the high energy Compton background.

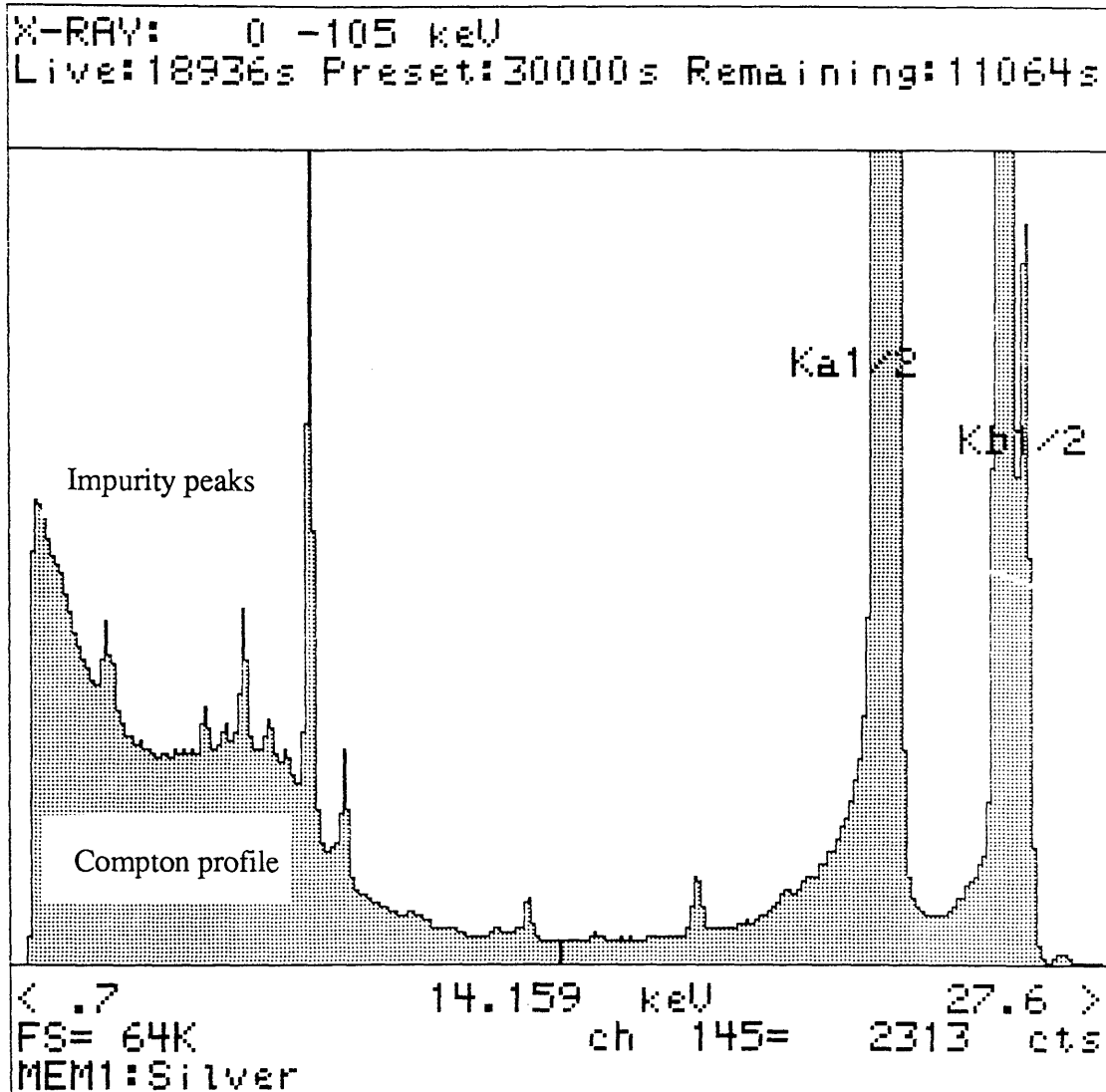
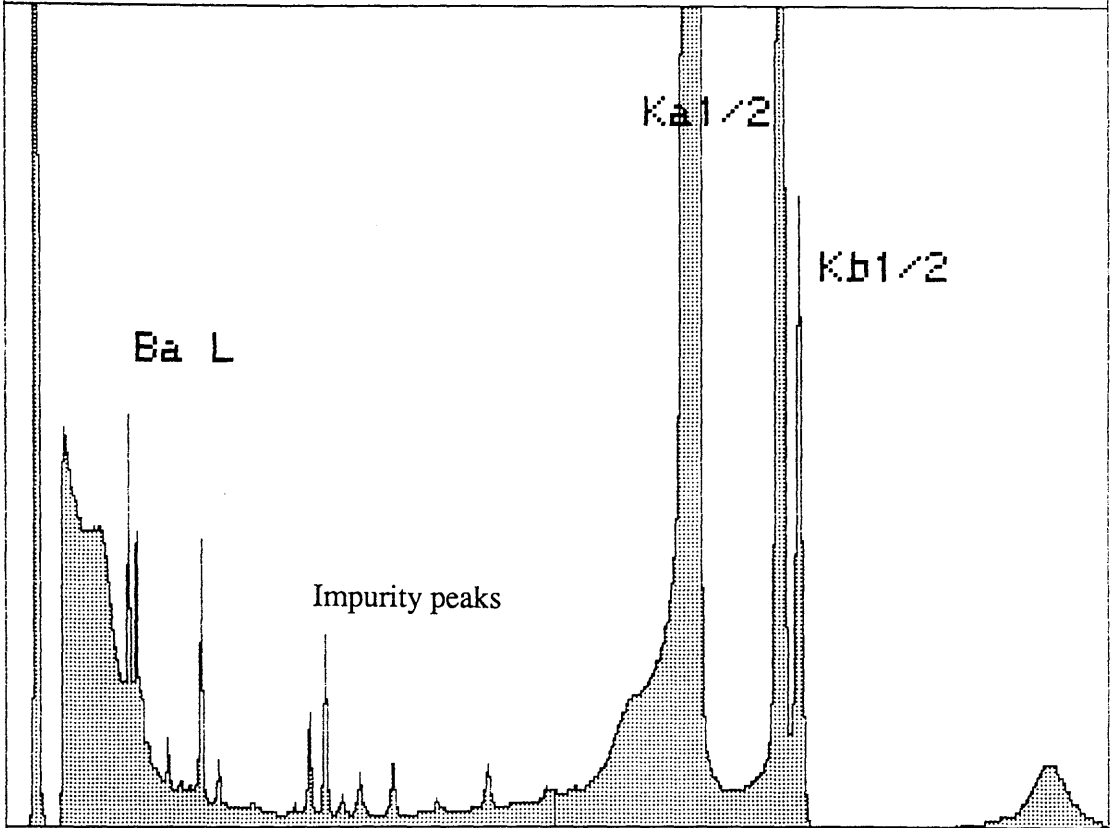


Fig. A3.4 Fluoresced silver target, just showing the effects of the high energy Compton background.

X-RAY: 0 -105 keV  
Live:30000s Preset:30000s Remaining: 0s



25.382 keV 52.2 >  
ch 252= 13187 cts  
FS=256K  
MEM1:Barium

Fig. A3.5 Fluoresced barium target.

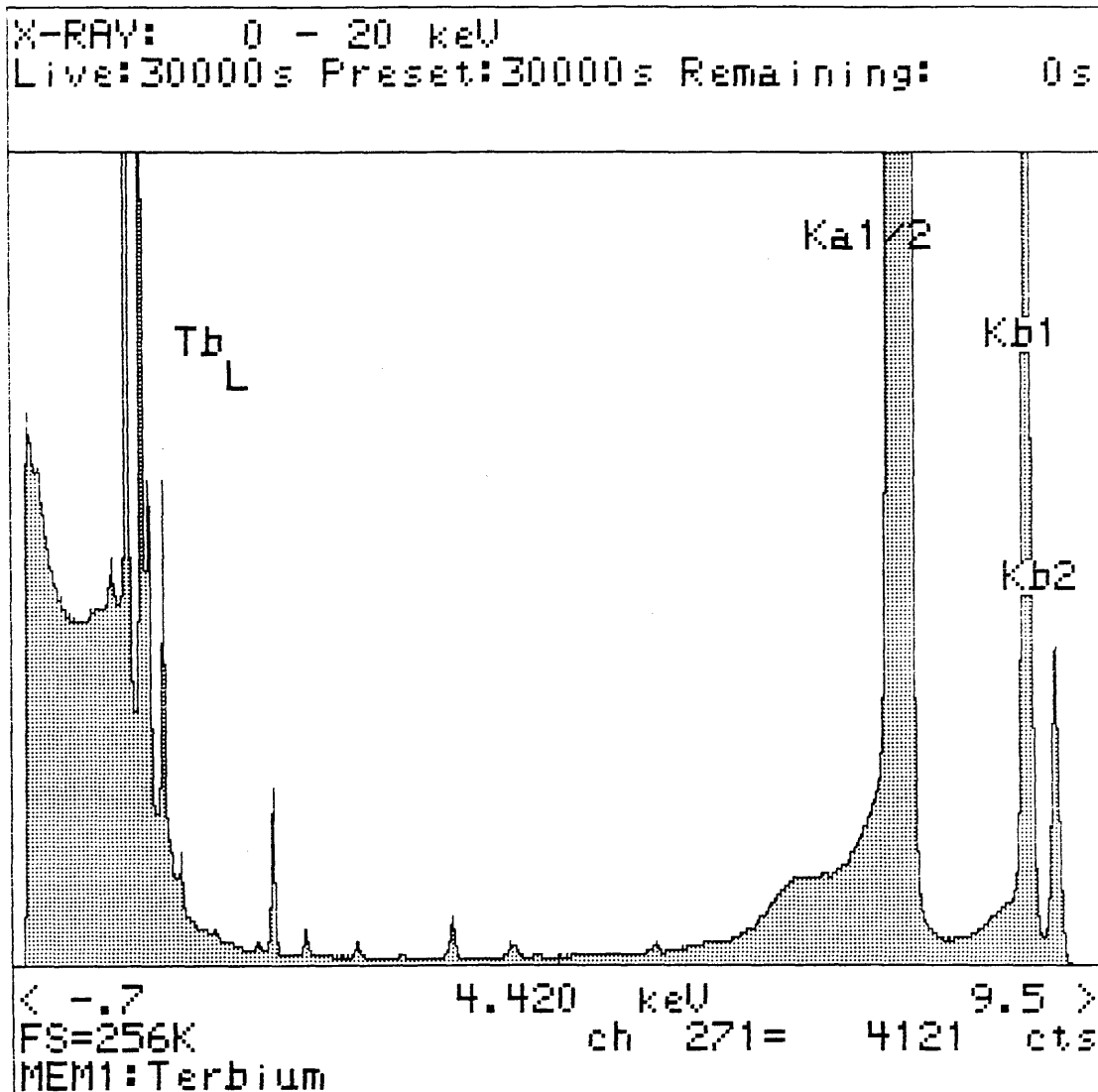


Fig. A3.6 Fluoresced terbium target.

profile for the gamma ray. This was done by irradiating the copper target in the normal way, the output photons were then blocked by a sheet of aluminium, 2mm thick. The aluminium absorbs all the copper x-rays and only the high energy components can reach the detector. Figure A3.7 shows this spectrum. The Compton distribution in the spectra from barium and terbium targets is due more to the Comptoning of the characteristic x-rays than from the background.

This source was used extensively in the detector damage experiments since it provided a convenient source of high energy photons.

### A3.2 Iron 55 radioactive source.

$^{55}\text{Fe}$  was the most widely used source of x-rays in this project. It is the established standard for estimation of the detector resolution and was also used to fluoresce secondary targets.  $^{55}\text{Fe}$  decays by electron capture and emits manganese K x-rays. The source also emits a very high energy gamma ray at 217 keV. This gamma produces electrons as it interacts with matter and these electrons give rise to a low level background source of bremsstrahlung radiation. The  $^{55}\text{Fe}$  source is plated onto an annular ring of copper and is then nickel plated for safety purposes. The source used in the majority of experiments was one which was originally 10 mCuries and had undergone approximately two half-lives.

The  $^{55}\text{Fe}$  source was contained within a small copper cylinder which was designed for general safety purposes, to allow suitable collimation to be made possible and to hold any targets which were to be fluoresced by the  $^{55}\text{Fe}$  source. This copper holder was designed by Dr. Nicholson. Figure A3.8 shows the source/source holder in the configuration used for the collection of manganese x-rays. The source/detector distance was kept at a distance of 15 mm apart. The source internal collimator was used to reduce the direct count rate. The external collimator on the detector governed to collection solid angle. Figure A3.9 shows the source/detector configuration for the acquisition of fluoresced x-rays. Here the collimation is governed by the source collimator, seen facing the detector. It was usual to fluoresce the targets under vacuum.

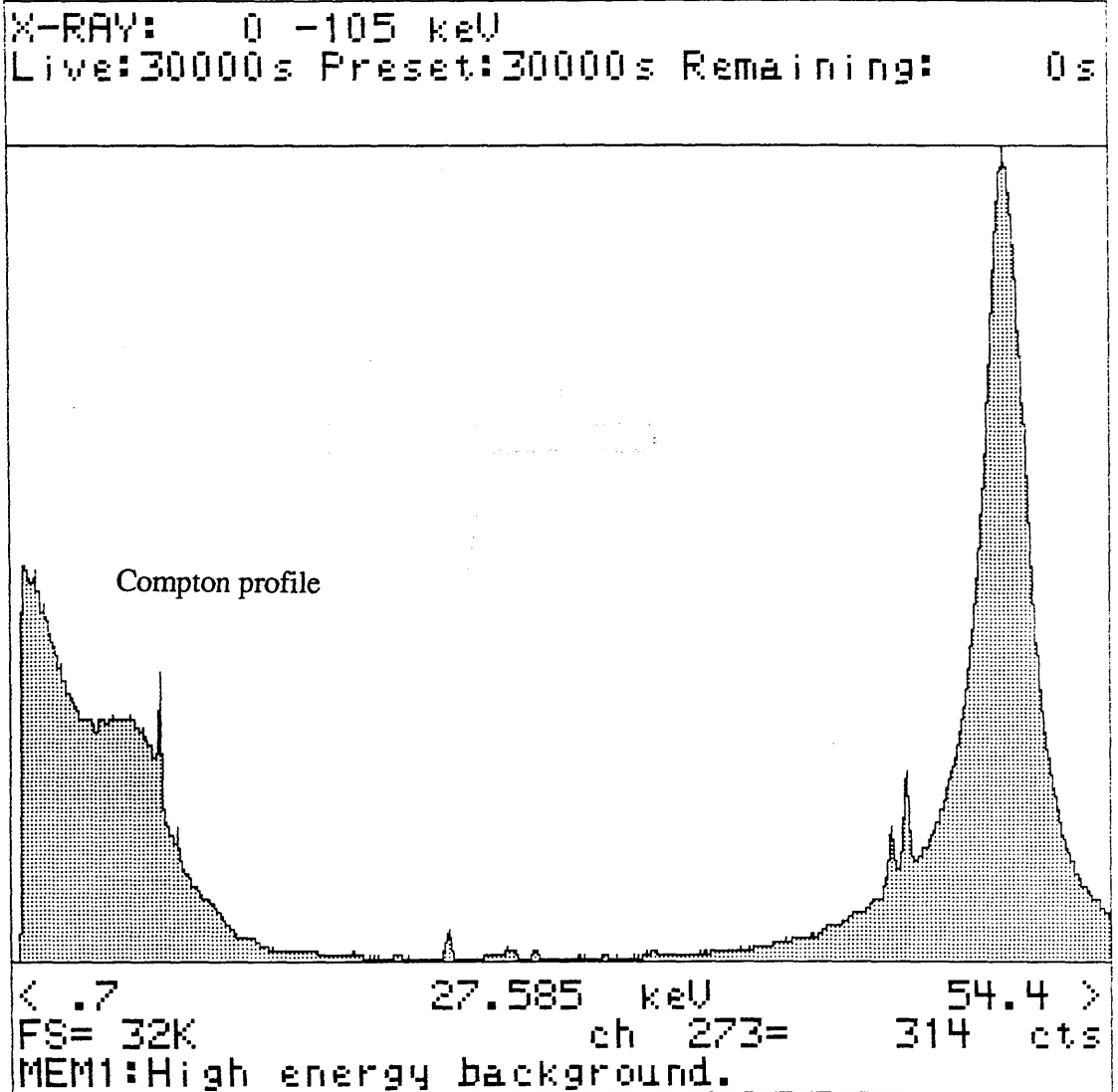


Fig. A3.7 High energy background contribution. This shows the low energy Compton profile and the high energy Compton scattered gamma ray.

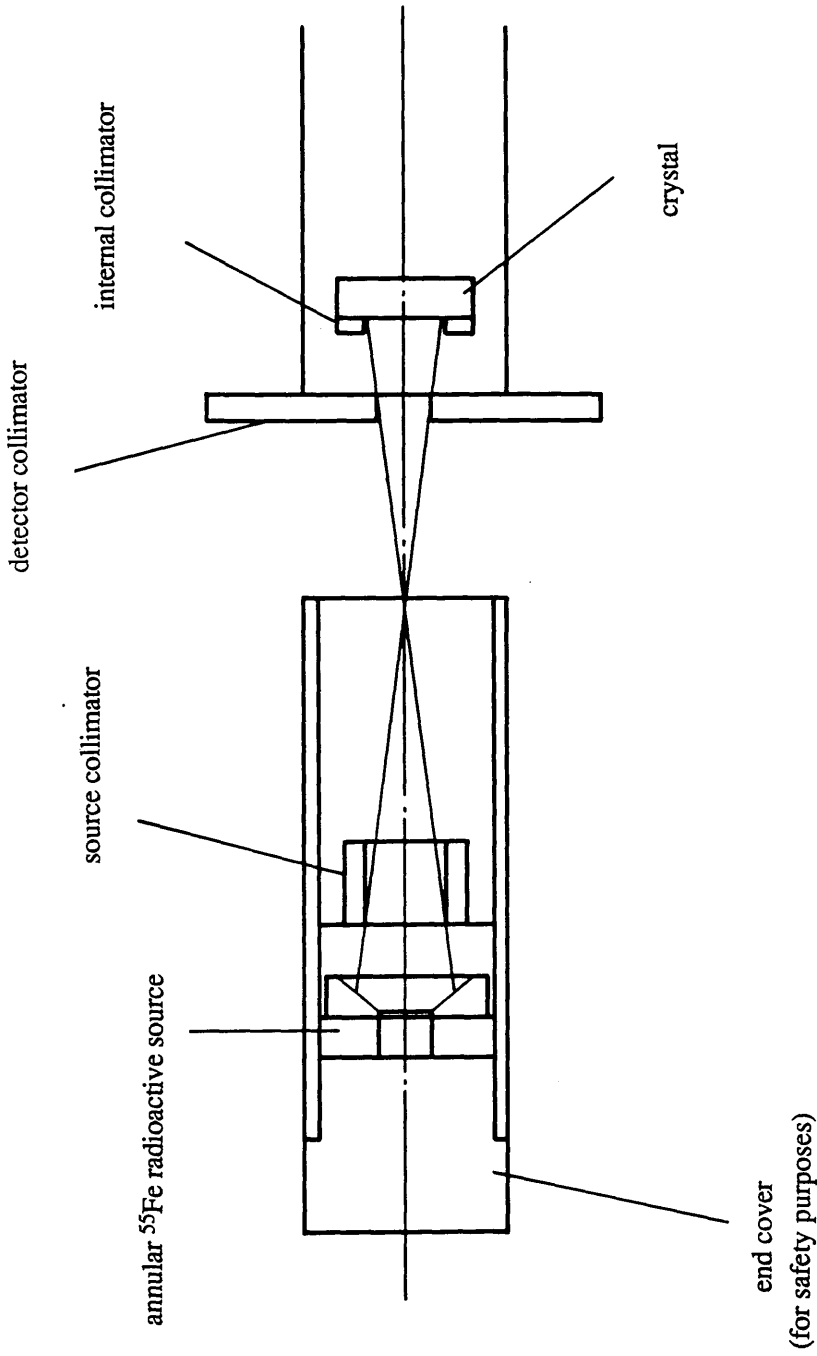


Fig. A3.8 Cross-sectional view of the  $^{55}\text{Fe}$  radioactive source holder. The source holder is shown in the experimental set-up used for manganese irradiation.

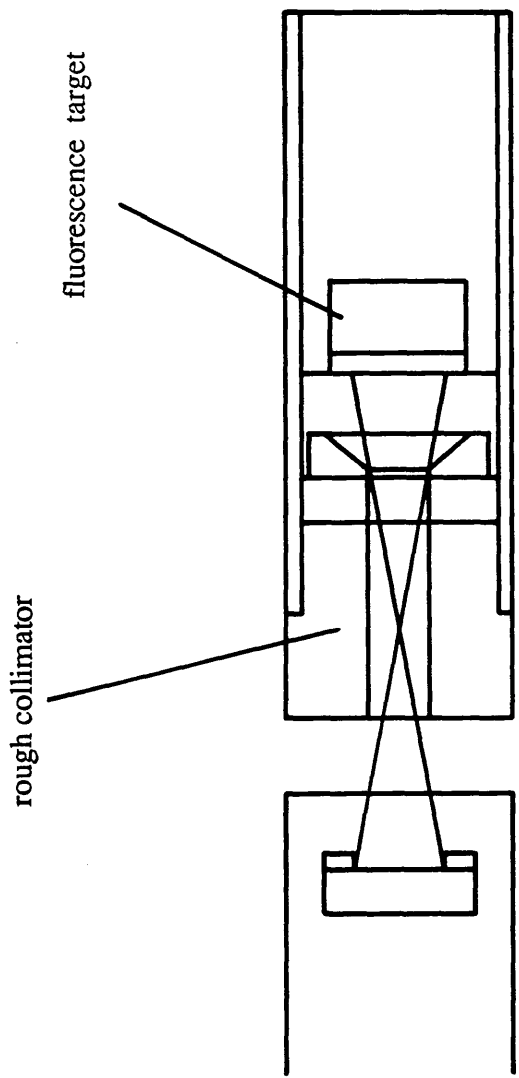


Fig. A3.9 Experimental set-up for the collection of fluoresced x-rays.

## APPENDIX FOUR

### Setting up of the Pulse Processor for Acquisition.

#### A4.1 Introduction.

At present there are several different types of pulse processor available manufactured by Link. The model used throughout this work was the 2020 pulse processor, this being one suitable for a windowless type detector. This particular model is designed to deal more efficiently with the low energy signals present with a windowless detector.

The basic operation of the pulse processor has been outlined in section 3.5, this appendix explains in more detail the exact way in which the pulse processor is set up so that the spectra acquired is done so in the most accurate fashion. The ideal set-up for the pulse processor is described in the relevant manuals supplied by Link Analytical. The pulse processor is designed for a user with little or no knowledge of the relevant electronics. In this way the setting up procedure is quick and simple to do. The set-up recommended by Link, which is considered to be best for acquiring electron generated spectra with this particular model of processor, requires both the fast and slow recognition channels to have a small noise level present. This is to ensure that no useful information is electronically removed. A consequence of having this noise in the system is that a noise peak is visible in every spectrum. This is purely the result of the noise signal being processed as if it represented a detected photon signal. This noise can however be suppressed by a low threshold setting control on the pulse processor. In addition the noise peak can also be removed by the software. Neither of these methods are particularly desirable for any work where the ICC is being studied. This is because both methods remove useful information, particularly for spectra having severe ICC; these spectra having a larger fraction of counts in the very low energy region. It was eventually realised that this noise contribution must be left in so as to obtain all the

information possible. This meant a set-up procedure which is slightly different to that in the Link manual.

The low energy end of the spectra all begin to show an intensity "roll-off" below 240 eV. This is caused by an electronic "roll-off" in the pulse processor. The various Link pulse processor's all exhibit this "roll-off" (some at even higher energies). We were not sure if this low energy electronic "roll-off" could be affected by the noise settings, or if the noise settings affected the level change (see section 7.6) seen in the manganese spectra at around 2.0 keV. An experiment was performed which tested what were the best set-up conditions and in addition allowed us to study the "roll-off" and level change as the various noise setting's changed. This experiment involved changing the various noise setting's on both the fast and slow channels and observing what differences, if any, this had on the spectra. Noise setting's of 0, 50, 100, 150, 250 and 500 c/s were used for both channels. All permutations of these values were tried. The results showed that for the count rates being used in this work, generally less than 1500 c/s, no major differences in the spectra could be seen for the range of noise setting's being tried. Setting the slow channel at values greater than 150 c/s had the effect of adding extra counts in the region below the roll-off. This meant that the noise peak merged into the spectrum. This would have the effect of adding extraneous counts to the spectrum. The level change at 2.0 keV or the minimum in the background intensity at 1.14 keV (see section 7.6) were not affected in any way. Fig. A4.1 shows a selection of these test spectra indicating that there is no observable differences to the spectra other than the extra counts below the "roll-off" position.

In all future experiments the pulse processor was set-up for a noise setting of 100 c/s on the slow channel and 50 c/s on the fast channel.

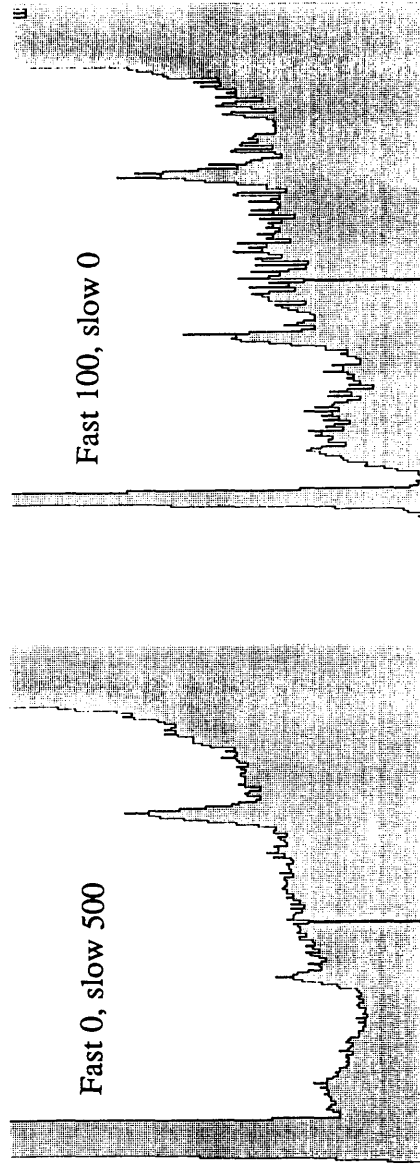
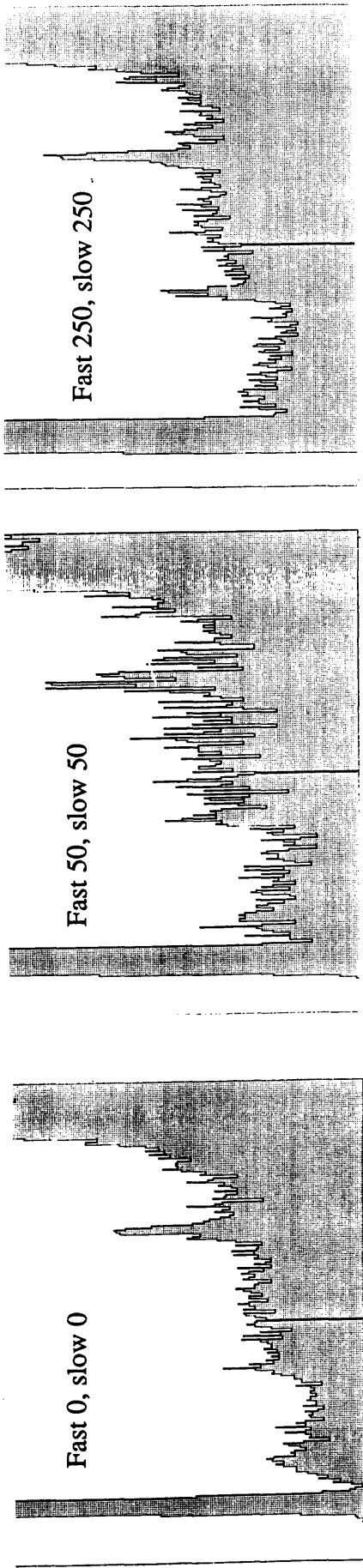


Fig. A4.1 A selection of the test spectra taken for the various noise level setting of the fast and slow channels on the 2020 pulse processor.

## REFERENCES

P F Adam (1986), Ph.D. Thesis, University of Glasgow.

D W Aitken (1968), IEEE Trans. Nuc. Sci. **NS-15**, 10.

A Alberigi Quaranta, M Martini, G Ottaviani (1968), in "Semiconductor Detectors", ed. G Bertolini and A Coche, North Holland Publishing Company-Amsterdam. p. 53.

H A Bethe (1930), Ann. der Phys. **5**, 325.

H A Bethe, W Heitler (1934), Proc. Roy. Soc., London, **A146**, 83.

E H S Burhop (1952), in "The Auger Effect and Other Radiationless Transitions", Cambridge.

J L Campbell, B M Millman, J A Maxwell, A Perujo, W J Teesdale (1985), Nuc. Instr. and Meth. in Phys Res. **B9**, 71.

J N Chapman, C C Gray, B W Robertson, W A P Nicholson (1983), X-Ray Spectrom. **12**, 153.

J N Chapman, W A P Nicholson, P A Crozier (1984), J. Micros. **136**, 179.

J P Chevalier (1988), in Proc. of the NSF/CNRS Workshop, Aussois 1988, p. 231.

A Coche, P Siffert (1968), in "Semiconductor Detectors", ed. G Bertolini and A Coche, North Holland Publishing Company-Amsterdam. p. 149.

D D Cohen (1987), X-ray Spectrom. **16**, 237.

C E Cox, B G Lowe, R A Sareen (1988), IEEE Trans. Nuc.Sci.Vol. NS-35, no.1.

A J Craven, P F Adam, R Howe (1985), in Proc. EMAG 1985, Inst. Phys. Conf. Series no. 78, 189.

A J Craven, C P McHardy, W A P Nicholson (1987), in Proc. EMAG 1987, Inst. Phys. Conf. Series no. 90, 345.

A J Craven, C P McHardy, K A Pears (1989), Ultramicroscopy, **28**, 157.

A J Craven, K A Pears, J P Chevalier (1989) in Proc. EMAG 1989, Inst. Phys. Conf. Series no. 98, 307.

A J Craven, W A P Nicholson (1990), in press.

A J Craven (1988), private communication.

P A Crozier (1986), Ph.D. Thesis, University of Glasgow.

C M Davisson, R D Evans (1952), Revs. Mod. Phys. **24**, 79.

G Dearnaley, D C Northrop (1966), Semiconductor Counters for Nuclear Radiations, (1) p. 89 . (2) p. 91.

G Dearnaley, A B Whitehead (1961), Nuc. Inst. Meth. **12**, 205.

N A Dyson (1973), X-Rays in Atomic and Nuclear Physics, Longmans.  
(1) p. 80. (2) p.7. (3) p.80.

E Elad, C N Inskeep, R A Sareen, P Nestor (1973), IEEE Trans. Nuc. Sci. **20**, 534.

R D Evans (1958), in "Handbuck der Physik", ed. S Flugge, Springer Verlag (Belgium), p. 218.

R W Fink (1981), in Proc. of Workshop on EnergyDispersive X-Ray Spectroscopy, NBS special publication 604, p. 5.

C E Fiori, R L Myklebust, K F J Heinrich, H Yakowitz (1976), Anal. Chem. **48**(1), 172.

C E Fiori, D E Newbury (1978), in "Scanning Electron Microscopy 1978" Vol.1. (O. Johari ed.) published by SEM Inc, Chicago, p. 251.

H J Fitting (1974), Phys. Stat. Sol. **26a** 525.

A J Garratt-Reed, W Furdanowicz (1987), in EMAG 87, Proc. of Workshop, p. 7.

A J Garratt-Reed (1989), private communication.

F S Goulding (1977), Nuc. Instr. Meth. **142**, 213.

F S Goulding, J M Jaklevic (1977), Nuc. Instr. Meth. **142**, 323.

C C Gray (1981), Ph.D. Thesis, University of Glasgow.

C C Gray, J N Chapman, W A P Nicholson, B W Robertson, R P Ferrier (1983), X-Ray Spectrom. **12**, 163.

R Guye, P Jarron (1987), Nuc. Inst. Meth. Phys. Res. **A253**, 319.

E E Haller (1982), IEEE Trans. Nuc. Sci. NS-29, 1109.

J Heckel, W Scholz (1987), X-ray Spectrom. 16, 181.

K F J Heinrich (1966), in "The Electron Microprobe", (T.D. McKinley, K.F.J. Heinrich, D.B. Wittry eds.) John Wiley, New York, p. 296.

K F J Heinrich (1987), from National Bureau of Standards, Gaithersburg, Md20899.

Y Inagaki, K Shima, H Maezawa (1987), Nuc. Instr. Meth. Phys. Res. B27, 353.

J M Jaklevic, F S Goulding (1971), IEEE Trans. Nuc. Sci. NS-18, 187.

J M Jaklevic, J T Walton, R E McMurray, N W Madden, F S Goulding (1988), Nuc. Instr. Meth. Phys. Res. A266, 598.

D C Joy (1985), Rev. Sci. Instr. 56, 1772.

K Kandiah, A J Smith, G White (1975), IEEE Trans. Nuc.Sci. Vol. NS-22, no.5.

KeveX (1989), Super Quantum, Detector information.

K M Khan, W A P Nicholson (1989), private communication.

K M Khan (1990), Ph.D. Thesis, University of Glasgow, in preparation.

O Klein, Y Nishina (1929), Z. Physik 52, 853.

H W Koch, J W Motz (1959), Rev. Mod. Phys. 31, 920.

H A Kramers (1923), Phil. Mag. 46, 836.

C M Lee, L Kissel, H K Tseng, R H Pratt (1976), *Phys. Rev. A.* **13**, 1714.

Link Analytical (1989), Pulse Processor Division, Link Analytical,  
High Wycombe, private communication.

Link Systems 2020 Pulse Processor Instruction Manual, Link Analytical,  
High Wycombe.

Link Systems Detector Information Manual, Link Analytical,  
High Wycombe.

J Llacer, E E Haller, R C Cordi (1977), *IEEE Trans. Nuc. Sci.* **24**, 53.

A R Long (1988), private communication.

B G Lowe (1988), private communication.

B G Lowe (1989), *Ultramicroscopy*, **28**, 150.

B G Magorrian, N M Allinson (1988), *Nuc. Inst. Meth. Phys. Res.* **A273**, 599.

C P McHardy, A J Craven, K A Pears, B Lowe, W A P Nicholson (1988) *Inst. Phys.*  
*Conf. Ser.* no. 93, vol.1, 135.

H G J Moseley (1914), *Phil. Mag.* **27**, 763.

R G Musket (1981), in *Proc. of Workshop on Energy Dispersive X-Ray Spectroscopy*,  
NBS special publication 604, p. 97.

W A P Nicholson (1988), private communication.

J H Paterson (1988), Ph.D. Thesis, University of Glasgow.

G W Phillips, K W Marlowe (1976), *Nuc. Instr. Meth.* **137**, 525.

R H Pratt, H K Tseng, C M Lee, L Kissel, C MacCallum, M Riley (1977),  
*At. Data and Nuc. Data Tables* **20**, 175.

R H Pratt, H K Tseng (1980), private communication.

T S Rao-Sahib, D B Wittry (1975), *J. Appl. Phys.* **45**, 5060.

S J B Reed, N G Ware (1972), *J. Phys.* **E5**, 582.

G Restelli (1968), in "Semiconductor Detectors", ed. G Bertolini and  
A Coche, North-Holland Publishing Company-Amsterdam. p. 14.

F K Richtmyer (1921), *Phys. Rev.* **18**, 13.

B W Robertson (1979), Ph.D. Thesis, University of Glasgow.

W Schockley (1961), *Czech. J. Phys.* **B11**, 81.

K Shima, S Nagai, T Mikumo, S Yasumi (1983), *Nuc. Instr. Meth.* **217**, 515.

M Siegbahn (1914), *Physik. Zeits.* **15**, 753.

A Sommerfeld (1931), *Ann. der Phys.* **11**, 257.

G Springer, B Nolan (1976), *Canadian J. Spectros.* **21**, 134.